

FALSE ALARMS IN THE FORECASTING OF
SOLAR ENERGETIC PARTICLE EVENTS

BILL SWALWELL

A THESIS SUBMITTED IN PARTIAL FULFILMENT
OF THE REQUIREMENTS FOR THE DEGREE OF
DOCTOR OF PHILOSOPHY

Jeremiah Horrocks Institute for Maths, Physics and Astronomy
University of Central Lancashire

January 2018

Abstract

Solar Energetic Particles (SEPs) are known to be accelerated by high-energy events in the Sun’s corona: coronal mass ejections (CMEs) with high speed, solar flares with high peak emission in soft X-rays, or a combination of the two. SEPs, however, are not detected following all fast CMEs or intense flares. Those large solar events, which might reasonably have been expected to produce SEPs at Earth but which failed to do so, may be termed “false alarms”.

In this work, two simple SEP forecasting algorithms are defined: one (algorithm A.1) is based upon the observation of a magnetically well-connected CME with a speed of 1,500 km/s or greater (a “fast CME”), and the other (algorithm A.2) is based upon the observation of a magnetically well-connected X class flare. The algorithms were applied to historical data sets to ascertain which produced an enhancement of >40 MeV protons, and which were false alarms.

The algorithms have been evaluated using standard verification scores. Both algorithms correctly forecast approximately the same percentage of SEP events (47% and 49% respectively); the false alarm ratio for algorithm A.1, however, was much lower than for A.2 (29% and 51% respectively). Both algorithms failed to forecast almost the same number of SEP events (53% for A.1, and 51% for A.2).

The parameters of the false alarms were compared to those of the SEP-producing events. False alarm fast CMEs tended to be associated with flares of class less than M3; X class flares which were either not associated with any CME, or were associated with a CME slower than 500 km/s, were false alarms.

A third forecasting algorithm, based upon these results, was defined. This algorithm, which takes into account parameters of both CMEs and flares, performed better than either A.1 or A.2, correctly forecasting a significantly greater percentage of SEP events than both (68%), having a false alarm ratio similar to A.1 (30%), but missing a significantly lower percentage (32%) of SEP events.

A small number of case studies were carried out. It was found that for accurate forecasting of SEP events it may not be sufficient simply to consider the accelerating events, but that the location of the heliospheric current sheet relative to the site of the solar event and of the Earth's footpoint may be an important consideration.

SEP forecasts produced by the SPARX simulation were evaluated with a view to providing a benchmark against which future versions of the model may be tested.

Contents

DECLARATION	ii
Abstract	iii
Acknowledgements	xxii
1 Introduction	1
1.1 Space weather	1
1.2 Solar flares	3
1.3 Coronal Mass Ejections	4
1.4 Radio bursts	4
1.5 Solar Energetic Particles	6
1.6 Forecasting SEP events	9
1.7 Existing forecasting tools	10
1.8 Objectives	11
1.9 Organisation of the thesis	13
2 Physical processes affecting SEPs	15
2.1 Particle acceleration in flares	15
2.1.1 Acceleration by direct electric fields	15
2.1.2 Stochastic acceleration	16
2.1.3 Shock acceleration in flares	17

2.2	Acceleration by CME driven shocks	18
2.2.1	Shock drift acceleration	18
2.2.2	Diffusive shock acceleration	21
2.3	Particle acceleration in realistic scenarios	22
2.4	Particle escape	22
2.5	Propagation through interplanetary space	25
2.5.1	Magnetic field line connection to Earth	25
2.5.2	Particle flux and energetic storm particles	27
2.6	Modelling particle transport	30
2.6.1	The focused transport equation	30
2.6.2	A three dimensional approach	31
2.7	The heliospheric current sheet	32
3	Observations	36
3.1	CME observations	36
3.1.1	Speed	38
3.1.2	Acceleration	40
3.1.3	Width	40
3.1.4	Position angle	41
3.1.5	Timing	43
3.2	Flare observations	44
3.2.1	Class	44
3.2.2	Duration	45
3.2.3	Heliographic co-ordinates and active region numbers	46
3.3	SEP observations	46
3.4	Choice of data sources	47
4	Methodology	52

4.1	Associating CME and flare events	52
4.2	Definition of “false alarm”	53
4.3	SEP forecasting algorithms	54
4.4	Definition of “SEP event”	55
4.5	Associating solar events and SEP events	57
4.6	Numbers of SEP and solar events	60
4.6.1	SEP events	60
4.6.2	Solar events	61
4.7	Algorithm evaluation scores	63
5	Forecasting algorithms and associated false alarms	65
5.1	Evaluation of the forecasting algorithms	65
5.1.1	Evaluation of A.1 and A.2 over time range 1	65
5.1.2	Evaluation of A.2 over time range 2	68
5.2	Parameters of A.1 events (time range 1)	68
5.2.1	CME speed and associated flare class	68
5.2.2	CME width	70
5.2.3	Magnetic connection between the CME and the Earth’s foot- point	70
5.3	Parameters of A.2 events (time range 1)	72
5.3.1	Flare class and associated CME speed	73
5.3.2	Flare duration	75
5.3.3	Associated CME width	75
5.3.4	Magnetic connection between the flare and the Earth’s footpoint	76
5.4	Parameters of A.2 events (time range 2)	78
5.4.1	Flare class	78
5.4.2	Flare duration	81
5.4.3	Magnetic connection between the flare and the Earth’s footpoint	81

5.5	Discussion	83
5.5.1	Evaluation	83
5.5.2	Algorithms A.1 and A.2 together	85
5.5.3	Algorithm A.1	86
5.5.4	Algorithm A.2 in time range 1	87
5.5.5	Algorithm A.2 in time range 2	89
5.6	An improved SEP forecasting algorithm	90
6	Case studies	93
6.1	False alarms common to both algorithms	93
6.1.1	Event on 24 November 1998	94
6.1.2	Event on 18 March 2003	97
6.1.3	Event on 13 September 2005	98
6.2	Intense flare false alarms	100
6.3	The ground level enhancement of 17 May 2012	101
6.4	Discussion	104
7	SPARX validation	108
7.1	Description of the SPARX model	108
7.2	Methodology	110
7.3	Validation	111
7.4	Discussion of the SPARX forecasts	114
8	Conclusions	120
8.1	SEP forecasting	120
8.2	Overview	121
8.3	Results summary	122
8.4	Further work	124

A	Choice of CME and flare catalogues	142
A.1	CME catalogues	142
A.1.1	Speed	143
A.1.2	Acceleration	148
A.1.3	Width	150
A.1.4	Position angle	151
A.1.5	Discussion	152
A.2	Flare catalogues	154
A.3	SEP data	156
B	Flare and CME associations	158
C	Algorithm 1 false alarms in time range 1	162
D	Algorithm A.2 false alarms in time range 1	165
E	Algorithm A.2 false alarms in time range 2	170
F	Swalwell <i>et al.</i> (2017a)	175
G	Swalwell <i>et al.</i> (2017b)	205
H	Battarbee <i>et al.</i> (2017)	209
I	Dalla <i>et al.</i> (2017)	221

List of Tables

1.1	A summary of the differences believed to pertain to the two different types of solar flare. Adapted from Kallenrode (1998).	4
1.2	A summary of the differences believed to pertain to the two different types of SEP event. Adapted from Kallenrode (1998).	7
3.1	A list of the GOES satellites and their operational periods. Column 1 states the name of the spacecraft, column 2 the date when it first became operational and column 3 the date when it was taken out of service.	45
3.2	Instruments used to obtain data on proton intensity, the dates between which data from that instrument was used, and the energy channels which have been analysed. Column 1 gives the name of the spacecraft from which the data was taken, column 2 the date from which those data began to be used, and column 3 the date when their use ceased. Column 4 shows the range of proton energies measured by the instrument which has been used, and column 5 whether the data were raw or had been cleaned by the SEPTEM team.	51

4.1	The numbers of SEP events during each of the two time ranges the subject of this study. Column 1 specifies the time range, column 2 the number of SEP events in that time range, column 3 the number of those events for which coordinates could be determined (after removal of events discarded due to data gaps, detectors still recording previous events, or other reasons), and column 4 the number of events which had their origin west of E20.	61
4.2	Numbers of solar events the subject of this study. Column 1 shows the time range over which data have been analysed, column 2 the type of solar event considered, column 3 the total number of solar events within the period investigated, column 4 the number of events for which coordinates were determined (after removal of events discarded due to data gaps, detectors still recording previous events, or other reasons) and column 5 the number of events which occurred west of E20.	62
5.1	Forecast verification scores for the 2 SEP forecasting algorithms. Column 1 gives the score type, column 2 the scores for algorithm A.1 in time range 1, and column 3 the scores for algorithm A.2 in time range 1, and column 4 the scores for algorithm A.2 in time range 2. The figures in brackets are the scores if the missed eastern events were to be taken into account.	67
5.2	Numbers of western X class flares which were false alarms during solar cycles 21 to 24. Column 1 contains the class of the flare to which the numbers refer, and columns 2 to 5 the numbers of each type of event which were false alarms for solar cycles 21 to 24 inclusive.	81
5.3	A summary of the evaluation scores for algorithm A.3 in the same format as Table 5.1.	92

6.1	List of false alarms common to both forecasting algorithms. Column 1 shows the date of the event, column 2 the start time of the flare, column 3 its class, and column 4 its coordinates. Columns 5, 6, and 7 give the time that the associated CME was first reported, its speed, and its width respectively.	94
7.1	Contingency table for SPARX forecasts for X class flares between 1 September 1997 and 30 April 2017 which exceed the SEP threshold, $I_{\text{thr}} = 10$ pfu.	112
7.2	Contingency table for SPARX forecasts for X class flares between 1 September 1997 and 30 April 2017 which exceed the SEP threshold, $I_{\text{thr}} = 1$ pfu.	113
7.3	Forecast verification scores for the SPARX SEP simulation. Column 1 gives the score type, and columns 2 and 3 the scores for the SPARX simulation for $I_{\text{thr}} = 10$ pfu and $I_{\text{thr}} = 1$ pfu respectively.	113
A.1	Table comparing CME speeds as reported by the 3 catalogues. Column 1 gives the name of the catalogue; column 2 shows the number of CMEs (having a width exceeding 20°) reported by that catalogue; column 3 gives the average speed of those CMEs; and column 4 the speed of the fastest reported CME.	144

A.2	Table comparing fast CME speeds as reported by the 3 catalogues. Column 1 gives the name of the catalogue which was used as a base for the analysis, and column 2 shows the number of fast CMEs reported in that catalogue. Column 3 gives the corresponding number of CMEs in the CACTus catalogue; column 4 the number of corresponding CMEs in the SEEDS catalogue; and column 5 number of corresponding CMEs in the CDAW catalogue. In columns 3, 4, and 5 the number in brackets indicates the number of CMEs which were fast CMEs.	147
C.1	Algorithm A.1 false alarms in time range 1. Column 1 gives the time the CME was first reported, column 2 its speed, and column 3 its acceleration all as reported by CDAW. Column 4 is the position angle at which the height-time measurements had been made (called by CDAW the “measurement position angle”). Column 5 is the CME width. Columns 6 to 10 give the parameters of the associated flare: its start time, heliographic latitude, heliographic longitude, class, and duration.	163
D.1	Algorithm A.2 false alarms in time range 1 in the same format as Table C.1.	165
E.1	Algorithm A.2 false alarms in time range 2. Columns 1 gives the start time of the flare, columns 2 and 3 its heliographic latitude and longitude, column 4 its class, and column 5 its duration.	170

List of Figures

1.1	Schematic of a spectrograph showing the major types of radio burst following a large solar flare. Taken from the Culgoora Solar Observatory website.	5
1.2	The probabilities of the occurrence of an SEP event according to (a) flare class and (b) CME speed. Taken from Dierckxsens <i>et al.</i> (2015)	9
2.1	Cartoon depicting a model of an eruptive prominence. Taken from Mann <i>et al.</i> (2006)	18
2.2	An illustration as to how a fast shock may produce an increase in magnetic field strength. Field lines bent away from the shock normal are closer together downstream of the shock. Taken from Aschwanden (2005).	20
2.3	An illustration of particle drift due to a magnetic field gradient. The magnetic field is directed upwards (shown in cyan), with the longer arrows suggesting increasing field strength; the path taken by a proton (moving left) is shown in blue, and by an electron (moving right) in yellow. Image courtesy of NASA's Scientific Visualization Studio. . .	21
2.4	An illustration of how magnetic field lines would appear during the solar eclipse of 21 August 2017. Open field lines emanate from the solar poles; closed field lines loop back on to the Sun. Image credit: the National Solar Observatory	23

2.5	A loop arcade seen on 8 September 2005 by TRACE. Image credit: TRACE	24
2.6	A visualisation of magnetic field lines emanating from the Sun. The view is down on to the Sun’s north pole. Taken from Owens and Forsyth (2013).	26
2.7	An illustration of the energetic particle flux in 3 different energy channels as observed from 3 different longitudinal locations. Taken from Reames (1999)	28
2.8	An illustration of an energetic storm particle event. The x-axis shows time, and the y-axis proton intensities seen in 6 different energy channels for an event which occurred on 19 October 1989. The parent solar event was an X13 flare at S27E10. The vertical purple dashed line shortly before midday on 20 October shows the start of the storm particle event, and the vertical magenta dashed line at about 16:45 on 20 October shows the time of passing of the shock. Adapted from Reames (1999).	29
2.9	An example source surface synoptic chart for $r = 2.5R_{\odot}$ resulting from a potential field source surface model for Carrington rotation 1912. Blue regions are areas of positive magnetic field, and red regions areas of negative magnetic field. The contours show differences in the strength of the magnetic field in μT . The black line is where the heliographic current sheet lies. Data were provided by the Wilcox Solar Observatory.	34

2.10	A representation of the HCS produced by a simulation of Carrington rotation 1912 (Odstrcil <i>et al.</i> (2004)). The HCS is “wavy”, extending about $\pm 10^\circ$ from the equator. The thick black line shows the Earth’s orbit showing that it crossed the HCS on at least 6 occasions. The thinning of the black line in the top left corner indicates a period when the Earth “skimmed” the HCS - there may have been multiple crossings of the HCS as a result of a fine scale structure not shown in the simulation. Taken from Owens and Forsyth (2013)	35
3.1	Images taken by the C2 coronagraph on 17 May 2012 showing a coronal mass ejection (downloaded from the Helioviewer website). The black circle in the centre of the image is caused by the coronagraph’s occulting disc.	39
3.2	Difference images of a CME on 3 May 2012 - the width of the CME is shown in red. The images illustrate how a CME’s width may increase over time. The angle shown in blue is the CME’s position angle, and this remains relatively constant over the lifetime of the CME.	42
3.3	A “halo” CME which occurred on 21 March 2012.	43
4.1	Heliographic latitude versus heliographic longitude for all fast CMEs and X class flares (for which coordinates could be determined) which occurred between 1 May 1980 and 31 March 2013 (Figure 4.1a) and for those solar events (whether or not they were a fast CME or an X class flare, and for which coordinates could be determined) in the same period which produced SEPs at Earth (Figure 4.1b).	56
4.2	Energetic (40 - 80 MeV) proton intensity between 28 October 2003 and 1 November 2003 as measured by the GOES EPS	59

5.1	The numbers of correctly forecast SEP events, false alarms and SEP events which were not forecast for the two forecasting algorithms during time range 1.	66
5.2	Flare class versus associated CME speed for those fast CMEs which were correctly forecast by algorithm A.1 to produce SEPs in time range 1 (top left, blue circles); for A.1 false alarms (top right, red squares); for A.1 missed events (bottom left, green diamonds); and for all events together (bottom right).	69
5.3	$\Delta\delta$ versus heliographic longitude for those western fast CMEs which produced SEPs at Earth in time range 1 (top plot) and for those which were false alarms (bottom plot). The size of the marker represents peak SXR intensity of the flare: for example, the point at S20W95 in the top plot was an M1.8 flare, whereas the point at S21E08 in the same plot was an X17.2 flare. The colour of the marker represents CME width.	71
5.4	Histograms of the distribution of $\Delta\delta$ in 10° bins for algorithm A.1. The left histogram (in blue) shows the distribution for the fast CMEs which were correctly forecast to produce SEPs at Earth, and the left histogram (in red) the distribution of the false alarms.	72
5.5	Histograms of the heliographic longitude of solar events in time range 1 of algorithm A.1 SEP events (top left); of algorithm A.1 false alarms (top right); of SEP events missed by algorithm A.1 (bottom left); and of all SEP events (bottom right)	73

5.6	Flare class versus associated CME speed for those X class flares which were correctly forecast by algorithm A.2 to produce SEPs in time range 1 (top left, blue circles); for A.2 false alarms (top right, red squares); for A.2 missed events (bottom left, green diamonds); and for all events together (bottom right).	74
5.7	Histograms of flare duration in minutes for X class flares. Those which produced SEPs are shown in the left plot in blue, and the false alarms in the right plot in red. Bin size is 30 minutes.	76
5.8	$\Delta\delta$ versus heliographic longitude for those X class flares which were correctly forecast by algorithm A.2 to produce SEPs in time range 1 (top plot) and for those which were false alarms (bottom plot). The size of the marker represents the relative duration of the flare:for example, the flare marked at S18W33 in the top plot had a duration of ten minutes, whereas the flare at S03W38 in the same plot lasted 120 minutes. The colour of the marker represents CME width.	77
5.9	Histograms of the distribution in 10° bins of $\Delta\delta$ for A.2 SEP-producing events (left plot, in blue) and for A.2 false alarms (right plot, in red).	78
5.10	Histograms of the heliographic longitude of solar events in time range 1 of algorithm A.2 SEP events (top left); of algorithm A.2 false alarms (top right); of SEP events missed by algorithm A.2 (bottom left); and of all SEP events (bottom right).	79
5.11	A plot of flare class versus time for algorithm A.2 over time range 2. Blue dots represent the X class flares which were correctly forecast to produce SEPs; red squares are the false alarms; green diamonds show the SEP events missed by the algorithm. The horizontal dashed line is the X class threshold; the vertical dashed lines are the boundaries between the different solar cycles.	80

5.12	Histograms of flare duration for X class flares in time range 2 which produced SEPs (left plot, in blue) and which were false alarms (right plot, in red). Bin size is 30 minutes.	82
5.13	Histograms of $\Delta\delta$ for X class flares in time range 2 which were correctly forecast by algorithm A.2 to produce SEPs (left plot, in blue); A.2 false alarms (right plot, in red). Bin size is 10 degrees.	82
5.14	Histograms of heliographic longitude for X class flares in time range 2 which produced SEPs (left plot, in blue) and which were false alarms (right plot, in red). Bin size is 10 degrees.	84
5.15	Plot of $\Delta\delta$ versus time for the algorithm A.2 over time range 2. Blue dots represent the SEP events correctly forecast by the algorithm, and red squares the false alarms. The size of the marker is proportional to the duration of the flare: the range is from 8 minutes to 8 hours 48 minutes. The dashed horizontal line is at 0° ; the vertical dashed lines represent the boundaries between different solar cycles.	85
5.16	The numbers of correctly forecast SEP events, false alarms and SEP events which were not forecast for algorithm A.3 during time range 1.	91
6.1	A synoptic source surface map for the 24 November 1998 event. Blue regions show areas of positive magnetic field and red regions areas of negative magnetic field. The contours are separated by $\pm 0.5, 1.0, 2.5, 5.0, 10.0,$ and $15.0 \mu\text{T}$. The vertical purple line is the position of the central meridian, the green circle the Earth's footpoint and the yellow star the location of the flare site.	96
6.2	A synoptic source surface map for the 18 March 2003 event in the same format as Figure 6.1.	98

6.3	The energetic proton and SXR flux for the 13 September 2005 event. The red curve is the SXR flux from the GOES 1 - 8 Å channel, the orange curve the flux of protons in the 9 - 15 MeV energy channel, and the blue curve the flux of protons in the 40 - 80 MeV energy channel.	99
6.4	A synoptic source surface map for the 13 September 2005 event in the same format as Figure 6.1.	100
6.5	A synoptic source surface map for the 17 May 2012 ground level enhancement event in the same format as Figure 6.1.	102
6.6	Relative locations of the Earth and different spacecraft at the time of an SEP event which occurred on 17 May 2012. The direction of the CME is shown by the arrow. Taken from Battarbee <i>et al.</i> (2017c) . . .	103
6.7	Energetic particle intensities for an event which occurred on 17 May 2012 as observed by several different spacecraft. Taken from Battarbee <i>et al.</i> (2017c)	104
7.1	Peak flux of >10 MeV protons as forecast by the SPARX model versus observed peak >10 MeV proton flux as measured by the GOES EPS for the 40 X class flares which were correctly forecast by SPARX to produce an SEP event exceeding 1 pfu. The colour of the marker represents the longitude of the flare site. The blue dotted line is the 1:1 correlation between SPARX forecast and actual observation. . . .	115
7.2	Peak proton flux plotted against heliographic longitude for observed SEP events (green dots), SPARX correct forecasts (blue dots) and SPARX false alarms (red dots) for $I_{\text{thr}} = 1$ pfu. The purple horizontal dotted line is the 10 pfu threshold.	116

7.3	Time interval in hours between flare peak SXR flux and >10 MeV proton flux as forecast by SPARX versus flare peak SXR flux and observed >10 MeV proton flux for the 52 X class flares which produced an SEP event exceeding 1 pfu. The colour of the marker represents the longitude of the flare site, and the blue dotted line is the 1:1 correlation.	118
A.1	Histograms of the speed of CMEs (in km/s) as reported by the 3 CME catalogues.	145
A.2	A comparison of how the 3 different catalogues report the speed of the same CME. Figure A.2a takes CACTus as its base catalogue, Figure A.2b uses SEEDS as its base, and the base for Figure A.2c is CDAW. In all plots, CACTus data are shown by green dots, SEEDS by purple dots, and CDAW by brown dots.	150
A.3	Histogram of distribution of fast CME acceleration as reported by the CDAW catalogue.	151
A.4	Histograms of the widths of the fast CMEs (in degrees) as reported by the 3 CME catalogues. The results for CACTus are shown at the top in green, SEEDS in the middle in purple, and CDAW at the bottom in brown. Bin size is 30 degrees.	152
A.5	Distribution of position angle measurements of the fast CMEs (in degrees) as reported by the 3 CME catalogues. The results for CACTus are shown at the top in green, SEEDS in the middle in purple, and CDAW at the bottom in brown. Bin size is 30 degrees.	153
A.6	Proton intensities in the 40 to 51 MeV channel of ERNE channel (orange line) and in the 40 to 80 MeV channel of GOES 10 EPS (blue line) instruments between 2 March 2000 and the end of 4 March 2000.	157

Acknowledgements

Silvia Dalla has supervised my transformation from lawyer and amateur astronomer to fledgling scientist. That I have been able to come as far as I have is entirely due to her expertise and patience. She has always been ready to talk when I needed help (which has been often), has gently steered me in the right direction, and given invaluable advice. I shall be eternally grateful to her.

I have also learned much from other members of the particles' group at the JHI: Timo Laitinen and Markus Battarbee have both always been willing to give guidance, and my fellow students, Peter Zelina and Don Doran, have been very kind to me and helped me whenever I needed it. My second supervisor, Robert Walsh, whilst not a member of the particles' group has, nevertheless, taken a keen interest in the work I have been doing, and has managed to fit in meetings with his very busy schedule. My sincere thanks go to all of them.

Danny Lee and Andrew Walker encouraged me to join them in outreach sessions for the university. I have very much enjoyed all my activities as a STEM Ambassador including the planetarium talks at Alston and the school visits, and both Danny and Andrew have been instrumental in showing me the ropes. Both became good friends, and I thank them for all the help they gave to me.

When I first arrived in Maudland room 208 in October 2014 I was, at times quite literally, lost. Kate Pattle and David Bresnahan took me under their wings and looked after me from our very first meeting. Both have given me invaluable advice during my time at the JHI. At later times I was joined in MB208 by Dave

Capstick, Adam Clarke, Raeesa Parker, and Tracey Friday. It has been a lovely place to carry out my research with never a cross word, and it has been a real pleasure to meet and work with all these people.

During my 3 years here, I have been involved in the marking of papers submitted by the distance learning students for Aimilia Smyrli, and I thank her for all the understanding she has shown to me. It has been a genuinely rewarding experience to work for her. She is always smiling, and every encounter with her brightens the day.

Most importantly, however, I want to thank my wife, Sandra. She has supported me throughout my time at the JHI, provided me with encouragement when it has been needed, and given me much help and support. It is difficult to express the extent of my gratitude to her.

It is, of course, also the case that my research relies heavily upon work which others, whom I have never met, have done. I have used CME data taken from the CDAW catalogue which is generated and maintained at the CDAW Data Center by NASA and The Catholic University of America in cooperation with the Naval Research Laboratory; my flare data have been taken from the GOES SXR Flare List and from the SolarSoft Latest Events Flares List (gevloc); proton intensity data were downloaded from the SEP-EM website; and data for the solar source surface maps were obtained from the Wilcox Solar Observatory. I am very grateful to all those who maintain these data repositories as this work could not have been completed without them.

I have also used videos taken by the EIT instrument on board the SOHO spacecraft, and the AIA instrument on board the SDO spacecraft. SOHO is a project of international cooperation between ESA and NASA. I acknowledge the work which has been done by the AIA, EVE, and HMI science teams to produce these images.

I also extend my gratitude to the JHI itself for helping, a little at least, with

meeting the financial burden of life as a student.

Chapter 1

Introduction

1.1 Space weather

During the course of the 12th March 1989, engineers working for Hydro-Québec, the major electricity supplier for the Canadian province of Québec, began to see fluctuations in voltage across the transmission grid. Despite efforts to maintain stability, at 02.44 local time on 13th March 1989, the grid's protection systems were triggered and within less than a minute the province suffered a power blackout which lasted for 9 hours. Costs of repair to the grid and to the Canadian economy were estimated at over \$13 million.

The cause of the voltage fluctuations in the transmission grid had been currents which had been induced into the conductors by large and rapid changes in the Earth's magnetic field. This geomagnetic disturbance had resulted in irreparable damage to the electrical transformers. Engineers ultimately traced the events responsible for the geomagnetic disturbance, and hence for the blackout, to events which had occurred near the surface of the Sun in the days and hours prior to the power loss.

At 13:54 UTC on the 6th March 1989 an extremely intense solar flare had been observed. Within hours the energetic particle sensors on board the two Geostationary Orbital Environmental Satellites (GOES) which were operational at the time

CHAPTER 1

began to record increased fluxes of protons with high energy. Over the following days several more high intensity solar events occurred, including an Earth-directed Coronal Mass Ejection (CME) on 10th March. The plasma ejected by the eruption arrived at Earth on 12th March, and it was this which caused the geomagnetically induced currents which finally led to the power loss. The space weather storm was so intense that it led to the *Aurora Borealis* or Northern Lights being seen at latitudes as far south as Cuba.

Other solar events have had similarly important consequences: in October and November 2003 the “Halloween storms” caused power outages in Sweden, resulted in aircraft being re-routed away from polar regions and damaged satellites; on the 14th July 2000 (the “Bastille Day Event”) some satellites suffered short circuits and communications systems failed; in December 2006 signals from the Global Positioning Satellite system were disrupted.

There have also been some notorious “near misses”. In April 1972 the Apollo 16 crew returned to Earth, with the next moon landing due in December of the same year, just 8 months later. However in August 1972, a severe solar storm occurred which, had it happened when an astronaut was walking on the moon, would have delivered a life-threatening dose of radiation.

Events such as these represent the extremes of what has become known as “space weather”. Radiation levels in near-Earth space can change significantly on time scales of just a few minutes, yet they can cause substantial harm to humans in space (Hoff *et al.* (2004)) and in high-flying aircraft especially those at high latitudes (Beck *et al.* (2005)), may significantly damage satellites and ground-based electrical system (Feynman and Gabriel (2000)), and make high-frequency radio communications either difficult or impossible (Hargreaves (2005)). Because of the potentially serious consequences of extreme space weather events, and because steps can be taken to mitigate their worst effects given sufficient warning, space weather forecasting has

CHAPTER 1

become a vital area for research.

Solar Energetic Particles (SEPs) are a significant component of space weather. They are mainly electrons, protons and helium nuclei, but they do include some heavier ions. Energies of tens of millions of electronvolts (MeV) can be imparted to protons; in some events protons with energies of a billion electronvolts (GeV) have been observed.

The question of what type of solar event could be responsible for accelerating these particles to such high energies has been the subject of considerable debate. Even today, there is no settled consensus on the answer, although the possible acceleration mechanisms are generally believed to be magnetic reconnection which occurs in (amongst other places) solar flares, shocks driven by CMEs, or a combination of the two.

1.2 Solar flares

A solar flare is a temporary brightening across the whole of the electromagnetic spectrum from within a small spatial region in the Sun's corona. Flares are classified according to their peak emission in soft X-rays (SXR) as measured by the 1 - 8 Å channel of the GOES X-ray sensor (XRS) instruments. Class X flares have the highest peak in SXR emission, followed by classes M, C, B, and A.

Flares endure on scales of a few minutes to several hours, and Pallavicini *et al.* (1977) suggested that they could be divided into two types. Class I (as they then described them) occur low in the corona, are compact, have a higher energy density, are of relatively short duration (~ 10 minutes), and have fast rise and decay times; class II flares occur higher in the corona, have a larger volume, a lower energy density, endure longer (\sim hours) and have longer rise and decay times. Cane *et al.* (1986) called the two classes of flare “impulsive” and “long-duration”: the term “impulsive” has stuck, although what Cane *et al.* named “long-duration events” are

CHAPTER 1

Table 1.1: A summary of the differences believed to pertain to the two different types of solar flare. Adapted from Kallenrode (1998).

Property	Impulsive	Gradual
Flare duration	< 1 hr	> 1 hr
Decay time	< 10 mins	> 10 mins
Height in corona	$\leq 10^7$ m	$\sim 5 \times 10^7$ m
Volume	$\sim 10^{20} - 10^{21}$ m ³	$\sim 10^{22} - 10^{23}$ m ³
Energy density	$\sim 10 - 100$ Pa	$\sim 1 - 10$ Pa

now more often referred to as “gradual” events. Table 1.1, adapted from Kallenrode (1998), sets out a summary of some of the differences the two types of flare are said to have.

1.3 Coronal Mass Ejections

A CME is a large ejection of plasma from the solar corona. Typically the ejecta have speeds of a few hundred kilometres per second, but in large events CMEs have been recorded with speeds in excess of 2,000 km/s. Very often CMEs, particularly fast ones, are seen to occur in close spatial and temporal association with solar flares.

1.4 Radio bursts

Both flares and CMEs have been associated with emission in radio wavelengths of the electromagnetic spectrum, and such emission is classed into different types. Type I is simply the Sun’s normal continuous emission at radio wavelengths. Type II

CHAPTER 1

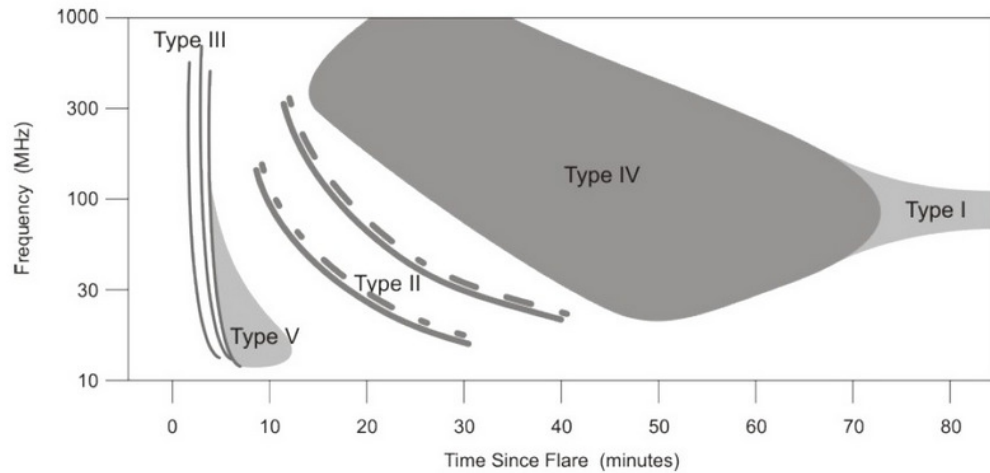


Figure 1.1: Schematic of a spectrograph showing the major types of radio burst following a large solar flare. Taken from the Culgoora Solar Observatory website.

radio bursts were first described by Wild and McCready (1950), and are associated with magnetohydrodynamic (MHD) shocks in the solar corona caused by CMEs (Gopalswamy *et al.* (2001)). Typically they begin with a frequency of around 100 MHz and they drift relatively slowly to lower frequencies. Type III bursts, which are associated with flares (Reid and Vilmer (2017)), begin typically with frequencies of a few hundred MHz and they drift much more quickly to lower frequencies. Radio bursts of types IV and V are continuous emission following type II and type III bursts respectively.

Figure 1.1 is a schematic of a spectrograph taken from the Australian Bureau of Meteorology’s Culgoora Solar Observatory website¹ which shows typical examples of the different types of radio burst. Time is displayed on the x-axis, and radio frequency in MHz on the y-axis.

¹http://www.sws.bom.gov.au/World_Data_Centre/1/9/7

1.5 Solar Energetic Particles

Historically, SEP events, like flares, have been divided into two types, and it is possible to trace this division back at least as far as the 1960s. For example, Wild *et al.* (1963) suggested that there were separate mechanisms for the acceleration of electrons and protons, and Lin (1970) put forward evidence to suggest that some enhancements of > 40 keV electrons were accompanied by enhancements of > 15 MeV protons, whereas others were not. According to Lin, the two classes of event were caused by different types of solar flare. It was argued that the “electron-only” events followed small solar flares and produced, *inter alia*, type III radio bursts at metre and decametre wavelengths, whereas the proton events were generated by larger flares and were accompanied by type II and type IV radio emission.

Other differences between the two types of SEP event began to emerge. Observations were first made of some particle events which had a relatively large abundance of ^3He (e.g. Hsieh and Simpson (1970); Dietrich (1973); Serlemitsos and Balasubrahmanyan (1975)). The ratio of $^3\text{He} / ^4\text{He}$ in the solar wind was observed to be $\sim 5 \times 10^{-4}$ (Coplan *et al.* (1984)), yet in these particle events that ratio was observed to be up to 2,000 times greater.

The ^3He -rich events also proved to have enhancements of other ions, with, for example, the ratio of iron (Fe) over oxygen (O) in some events being measured to be more than 10 times the ratio found in the solar corona (Mason *et al.* (1986)). Not only was the Fe / O ratio enhanced, but the charge states (Q) of iron were found to be different in the different types of SEP event: for the ^3He -rich events, Q_{Fe} was found to be $\sim +20$, whereas for the ^3He -poor events it was $\sim +14$ (Klecker *et al.* (1983); Luhn *et al.* (1987)).

The electron-rich events with high abundances of ^3He and Fe were said to be “impulsive” SEP events (following the description of the flare which was believed to be responsible for the acceleration), whereas the proton-rich events with coronal

CHAPTER 1

Table 1.2: A summary of the differences believed to pertain to the two different types of SEP event. Adapted from Kallenrode (1998).

Property	³ He-rich (“Impulsive”)	³ He-poor (“Gradual”)
³ He / ⁴ He	~1	~5 x 10 ⁻⁴
Fe / 0	~1.234	~0.15
Duration	some hours	some days
Particles	electron rich	proton rich
Radio emission	Types III and V	Types II and IV
Longitudinal extent	<30°	≤180°

levels of ³He and Fe were described as “gradual” SEP events (see *e.g.* Reames (1999)). Table 1.2, also adapted from Kallenrode (1998), sets out some of the properties which the two types of SEP event were believed to have.

The fact that there seemed to be two types of particle event suggested that there were different acceleration processes in play. The general idea behind the impulsive/ gradual SEP event picture was that it was the solar flare which was responsible for the acceleration of particles in impulsive SEP events. The relative abundances of different ions and their charge states relate to the location of, and the higher temperatures (~10 million Kelvin) found in, solar flares (Reames (1999)). Furthermore, because the spatial extent of the flare (and hence of the acceleration site) was relatively small, the SEPs were believed to adhere closely to the magnetic field lines connected to the flare site, meaning that they would spread little as they propagated through space.

Gradual SEP events, on the other hand, were believed to be accelerated by shocks driven by CMEs (Kahler *et al.* (1984)). These shocks have a much wider extent

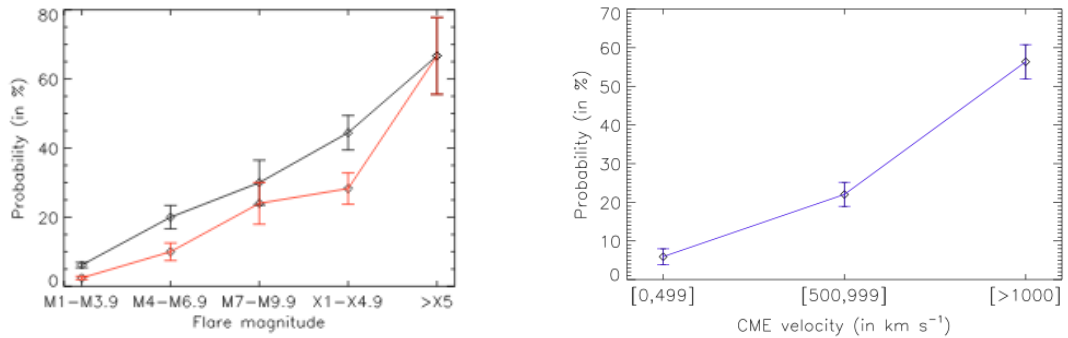
CHAPTER 1

than a solar flare and consequently were able to accelerate particles over a much wider longitudinal range. Furthermore, because a shock was able to accelerate ions (particularly protons) more efficiently than electrons, the model was able to explain why the gradual SEP events were proton rich. The abundances and charge states are typical of the outer corona (about 2 solar radii as measured from the centre of the Sun, or $2R_{\odot}$) where temperatures are around 2 million Kelvin.

However, the distinction between the two types of SEP event is not as clear-cut as was once thought. In a study of high-energy (>20 MeV) proton events, Cane *et al.* (2002) found that all were preceded by type III radio bursts; abundance enhancements similar to those in impulsive events have been observed in large gradual events (Cohen *et al.* (1999)); some impulsive events have been seen to be associated with CMEs (Nitta *et al.* (2006)).

It is thus clear that the simple impulsive / gradual division of SEP events, the former being accelerated by flares and the latter by shocks driven by CMEs, cannot be sustained. Some go as far as to argue that solar flares play no part in the acceleration (e.g. Gosling (1993); Reames *et al.* (1996)); others suggest that solar flares have an important rôle (Klein *et al.* (1999)).

The argument is not one of purely academic interest. The forecasting of SEP events is only likely to improve if it is known whether the parameters of just one type of solar event have to be considered, or whether information from both flares and CMEs ought to be taken into account. The processes which may be at work in accelerating particles in the solar corona are discussed further in Sections 2.1 and 2.2.



(a) Probability of SEP event according to flare class

(b) Probability of SEP event according to CME speed

Figure 1.2: The probabilities of the occurrence of an SEP event according to (a) flare class and (b) CME speed. Taken from Dierckxsens *et al.* (2015)

1.6 Forecasting SEP events

Figure 1.2, taken from Dierckxsens *et al.* (2015), shows that the probability of an SEP event being detected at Earth increases with flare class and CME speed. Consequently, many existing space weather forecasting tools attach great significance to the observation of high-energy solar events (e.g. Garcia (2004); Balch (2008)).

The difficulty with this approach, however, is that it is not the case that SEPs are detected at Earth following all large flares and fast CMEs (e.g. Klein *et al.* (2011)). The result is that many of these forecasting algorithms too often warn of possible SEP flux enhancements when none occur (e.g. Kahler *et al.* (2007); Núñez (2011)). A solar event which might reasonably have been expected to produce SEPs at Earth and yet which failed to do so, may be termed a “false alarm”. Furthermore, some SEP events may follow smaller solar events, so that these are “missed events” for SEP forecasting algorithms based upon the observation of intense flares and / or fast CMEs.

1.7 Existing forecasting tools

Given the number of factors which affect whether or not SEPs arrive at Earth, and given that few are completely understood, it is unsurprising that the accurate forecasting of SEP events remains a challenge.

Many SEP forecasting tools base their prediction upon the observation of intense solar flares and/or radio bursts. For example, the Proton Prediction System proposed by Smart and Shea (1989) makes a forecast based upon flare intensity and position. It produces almost equal numbers of correct forecasts, false alarms and missed events (Kahler *et al.* (2007)).

The “Protons” SEP forecasting system used by the National Oceanic and Atmospheric Administration (NOAA) Space Weather Prediction Center (SWPC) (Balch (1999)) uses the detection of intense flares and radio bursts as the basis of the forecast, although the issue of an SEP event warning follows only after human analysis. This tool was validated over a period between 1986 and 2004 by Balch (2008) and found to have a false alarm rate of 55%.

Laurenza *et al.* (2009) developed the Empirical model for Solar Proton Events Real Time Alert (ESPERTA) method of SEP forecasting based upon flare size, flare location and evidence of particle acceleration and escape. Their emphasis was to maximise the time between the issue of an SEP event warning and the arrival of the particles, and their aim was to produce an automated forecasting tool with a view to issuing warnings of SEP events without human intervention. Whilst it is a significant improvement over the Protons tool, the false alarm rate was, nevertheless, between 30% and 42%. (Alberti *et al.* (2017)). The FORcasting Solar Particle Events and Flares (FORSPEF) model, proposed by Papaioannou *et al.* (2015), aims to make forecasts of both flares and SEPs. Its SEP forecasting algorithm is based upon a purely statistical approach, and has not yet been validated.

CHAPTER 1

The Relativistic Electron Alert System for Exploration (REleASE) SEP forecasting tool (Posner (2007)) takes an alternative approach. It relies upon the fact that electrons, being less massive, travel faster than protons, and will therefore arrive at 1au first. A forecast of expected proton flux is made based upon the real-time electron flux measurements.

Although the majority of currently operational data-based forecasting schemes make use of flare information, it is widely thought that the use of CME information would substantially improve algorithm performance. While from an operational point of view it is currently not trivial to obtain CME parameters in real time, it is important to compare the performance of flare-based versus CME-based algorithms and determine whether a combination of flare and CME parameters within a forecasting tool may be beneficial.

Along with empirical forecasting algorithms which are based upon solar observations, several physics-based space weather forecasting tools have recently been developed (e.g. the SOLar Particle ENgineering COde (SOLPENCO) (Aran *et al.* (2006)), a solar wind simulation including a cone model of CMEs (Luhmann *et al.* (2010)), and the Solar Particle Radiation SWx (SPARX) model (Marsh *et al.* (2015)). An evaluation of the SPARX model has been carried out as part of this thesis work, and the results are set out in Section 7.

1.8 Objectives

In the words of the American physicist and chemist Irving Langmuir “*The scientist is motivated primarily by curiosity and a desire for the truth*”. Simply reaching for a greater understanding of how SEPs are accelerated and how they propagate through the interplanetary medium is more than adequate justification for this work. However, there are more benefits than simple satisfaction of a natural human curiosity.

As has been seen, SEPs pose a real threat to humans in space and in high-flying

CHAPTER 1

aircraft, and may cause damage to satellites and electrical systems on the ground. False alarms cost money, and so accurate forecasting has real benefits. A better understanding of the physics behind SEP acceleration and propagation will bring with it more accurate models, which in turn will allow the formation of improved SEP forecasting algorithms.

There have been previous statistical studies of SEPs (*e.g.* Gopalswamy *et al.* (2014); Dierckxsens *et al.* (2015)), but in general these have taken the SEP event as their starting point, and then gone on to look for the possible parent solar event. In doing so, those large solar events which might have been expected to produce SEPs but which did not, the false alarms, are passed over. False alarms are, however, highly interesting from a scientific point of view, and studying them will be extremely useful to improve forecasting methodologies. This work, therefore, takes a different approach.

The analysis begins by considering not the SEP event, but a large number of highly energetic solar flares and fast CMEs. It is determined whether an SEP event was measured near Earth within a short time thereafter, and this allows the construction of lists of the false alarms. By making comparisons of the parameters of those solar events which did produce SEPs with those of the false alarms it is expected that the following objectives can be met:

- To determine which parameters of solar events are important to SEP production.
- To determine whether it sufficient for space weather forecasting simply to consider the parameters relating to one type of solar event, or whether information relating to both flares and CMEs ought to be taken into account.
- To improve the forecasting of SEP events, and provide lists of false alarms to aid further study.

1.9 Organisation of the thesis

The thesis is organised in the following way. Chapter 2 includes a discussion regarding the physical processes which are believed to affect whether or not SEPs arrive at Earth. Chapter 3 introduces the instruments which are used to observe solar events and to measure SEP enhancements. It includes a description of some of catalogues and lists of solar events, together with an explanation of the parameters of CMEs and flares which are routinely reported. Appendix A is introduced: this contains a comparison of the catalogues and lists and explains the reasoning behind some of the choices which have been made.

Chapter 4 sets out the methodology which has been employed in this work. Two simple SEP forecasting algorithms for analysis are defined, and formal definitions of other terms are described. The performance of the algorithms is then evaluated using standard verification scores. Appendix B, which is a description of a method of associating flares and CMEs automatically, is presented, as are Appendices C, D, and E, which are lists of the false alarm events.

Chapter 5 is an analysis of the two forecasting algorithms, and compares the parameters pertaining to the SEP events with those of the false alarms. A third forecasting algorithm, based upon some of the results of the analysis of the false alarms, is introduced and validated. Appendix F is a copy of Swalwell *et al.* (2017a) which includes the analysis and results contained in this Chapter.

Chapter 6 is a closer examination of some of the more surprising false alarms, and of the solar events which led to the ground level enhancement (GLE) on 17 May 2012. Appendix G is a copy of Swalwell *et al.* (2017b) which includes a discussion concerning several of these events. Appendix H is a copy of Battarbee *et al.* (2017c) (to which the author of this thesis contributed) which examines the 2012 GLE event and the proton fluxes as detected by several different, widely separated, spacecraft.

CHAPTER 1

Chapter 7 contains a validation of the SPARX model for simulating SEP propagation, and introduces Appendix I which is a copy of Dalla *et al.* (2017b) (again, to which the author of this thesis contributed). It is a description of the SPARX model and includes the verification results presented in this thesis. Finally, Chapter 8 brings together the main results of this work, and suggests further work which remains to be completed.

Chapter 2

Physical processes affecting SEPs

Whether SEPs arrive at Earth or not depends upon many factors: the physical processes behind their acceleration, whether or not the particles can escape into the interplanetary medium, and how they propagate through it are all important. Each is considered further in the following sections.

2.1 Particle acceleration in flares

The fundamental process which is believed to accelerate SEPs in solar flares is magnetic reconnection. Particles may be accelerated as a result of the direct electric field in the diffusion region, stochastically as a result of turbulence in the plasma resulting from the reconnection process, or by shocks resulting from reconnection outflows.

2.1.1 Acceleration by direct electric fields

An electric field, \mathbf{E} , may be generated in current sheets formed in magnetic reconnection regions. The Dreicer field may be defined as

$$E_D = \frac{kT}{e \lambda_{\text{Coul}}} \quad (2.1)$$

where k is Boltzmann's constant, T is temperature, e is the electric charge of the particle and λ_{Coul} is the mean free path for Coulomb collisions. For conditions found in solar flares this is approximately 10^{-5} V/cm (Petrosian (2012)).

For sub-Dreicer electric fields ($E < E_D$) and using values which are typical of the conditions found in solar flares ($\sim 10^7 K$ and a column depth of $\sim 10^{20}$ particles/cm²), particles may only be accelerated to energies well below those which are observed. For super-Dreicer electric fields ($E > E_D$) acceleration to higher energies is possible, but such large scale electric fields are difficult to sustain (Tsuneta (1985)). More realistically, current sheets will be highly dynamic and fragmented (Kliem *et al.* (2000)) and, in fact, these ‘‘islands’’ may lead to more effective acceleration than in a single sheet (Cargill *et al.* (2012)). Nevertheless, it may be that in flares direct electric field acceleration is less important than stochastic acceleration (Petrosian (2012)).

2.1.2 Stochastic acceleration

Stochastic acceleration is a process in which particles may gain or lose energy over short time scales, but gain energy overall in a longer period. Particles may encounter magnetic inhomogeneities, and in doing so they will gain energy if the collision is head-on (the particle and magnetic inhomogeneity move towards each other), but will lose energy if the collision is head-to-tail (the particle and magnetic inhomogeneity move in the same direction). Because head-on collisions are more likely (in the same way that on a road cars travelling towards you pass more frequently than cars moving in the same direction as you) overall the particles gain energy.

For particles with a velocity v moving towards a magnetic inhomogeneity which has velocity u the increase in the particle's energy in each collision is proportional

CHAPTER 2

to $(v/u)^2 D_{uu}$, where D_{uu} is the pitch angle diffusion coefficient (Zharkova *et al.* (2011)). This is known as second order Fermi acceleration.

Ideas relating to stochastic acceleration have been extended to include plasma wave turbulence or cascading MHD turbulence as the source of the acceleration. In conditions which pertain to flares, it has been shown that plasma wave turbulence may accelerate particles to the required energies within a short space of time (Miller *et al.* (1996)). There are, however, difficulties with this proposition in that it is to be expected that high-frequency waves would produce decimetre radio waves in every flare, but this emission is not observed (Benz *et al.* (2005)).

In the case of cascading MHD turbulence, magnetic compressions which move at an angle to the magnetic field cause the scattering. In order to be accelerated efficiently, the particles must have an initial speed which is greater than that of the magnetic compressions (*i.e.* comparable to the Alfvén speed). Whilst electrons may have this speed, protons do not. For protons to be accelerated efficiently, therefore, they must be pre-accelerated (which may be able to occur due to parallel propagating Alfvén waves (Miller and Roberts (1995))).

Obviously these ideas require a mechanism to produce the plasma or MHD waves in the first place. For a discussion regarding a number of recent developments which advance the understanding of stochastic acceleration see Zharkova *et al.* (2011).

2.1.3 Shock acceleration in flares

Figure 2.1 is a cartoon (taken from Mann *et al.* (2006)) of an eruptive prominence (EP). The prominence is destabilised as a result of movements in the footpoints at the photosphere causing the prominence to rise and to stretch the magnetic field lines. This results in the formation of a current sheet and reconnection can take place in the diffusion region (DR). Plasma flows into the diffusion region and is accelerated away in two oppositely directed jets (which are contained within slow

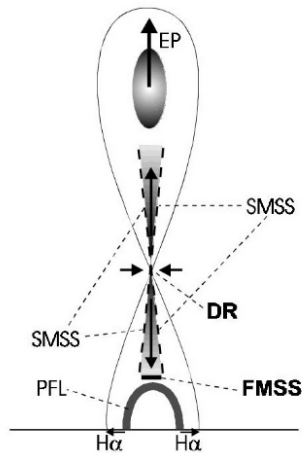


Figure 2.1: Cartoon depicting a model of an eruptive prominence.

Taken from Mann *et al.* (2006)

magnetosonic shocks (SMSS)). If the jets are super-Alfvénic a fast magnetosonic shock (FMSS) (or termination shock) is produced.

A fast magnetosonic shock may compress the magnetic field so that the particles are accelerated by shock-drift acceleration which is described in Section 2.2.1. Electrons may reach energies of up to 10 MeV (Mann *et al.* (2006)).

2.2 Acceleration by CME driven shocks

There are two different types of acceleration associated with shocks: shock-drift acceleration and diffusive shock acceleration.

2.2.1 Shock drift acceleration

In shock-drift acceleration a charged particle drifts in the induced electric field in the shock front which is described by the equation:

$$\mathbf{E} = -\frac{\mathbf{u}_u \times \mathbf{B}_u}{c} = -\frac{\mathbf{u}_d \times \mathbf{B}_d}{c} \quad (2.2)$$

CHAPTER 2

where \mathbf{u}_u is the speed of the plasma flow upstream of the shock, \mathbf{B}_u is the upstream magnetic field, \mathbf{u}_d is the speed of the (slower) plasma flow downstream of the shock, and \mathbf{B}_d is the downstream magnetic field. The direction of the electric field is along the shock front, perpendicular to both the magnetic field and the flow of the plasma.

The angle between a line perpendicular to the shock (the “shock normal”) and the direction of the upstream magnetic field is called θ_{Bn} . If $\theta_{Bn} > 45^\circ$ then the shock is described as quasi-perpendicular, whereas if $\theta_{Bn} < 45^\circ$ it is described as quasi-parallel. The induced electric field is at its maximum when the shock is perpendicular, and is zero when it is parallel.

Figure 2.2, taken from Aschwanden (2005), shows that in a fast shock magnetic field lines bend away from the shock normal resulting in a stronger magnetic field downstream than upstream ($B_d \gg B_u$). A particle passing through the shock gains velocity as a result of the conservation of magnetic moment (which is known as the first adiabatic invariant):

$$\mu = \frac{mv_u^2}{2B_u} = \frac{mv_d^2}{2B_d} = \text{constant} \quad (2.3)$$

Because the downstream magnetic field is stronger than the upstream magnetic field, the particle’s velocity must be greater downstream than upstream. However, for a particle to gain large amounts of energy it must interact with the shock front for a long time, and whether it does so depends upon its velocity and pitch angle (see Section 2.6), the speed of the shock, and θ_{Bn} . In regions with a stronger magnetic field (here, downstream), the gyroradius of the particle will be smaller; in regions where the magnetic field is weaker (here, upstream) the gyroradius will be greater. The net effect is that the particle drifts along the shock front.

Figure 2.3 is an illustration of the how magnetic gradient drift occurs. The magnetic field is directed upwards (shown in cyan) with the longer arrows indicating

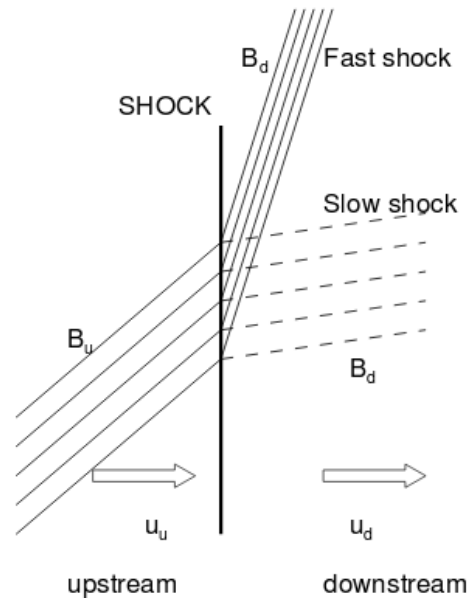


Figure 2.2: An illustration as to how a fast shock may produce an increase in magnetic field strength. Field lines bent away from the shock normal are closer together downstream of the shock. Taken from Aschwanden (2005).

increasing field strength; the path taken by a proton is shown in blue, and by an electron in yellow. In regions where the magnetic field is of lower strength the gyroradius of each particle is less tight, resulting in drift.

The direction of the drift is dependent upon the charge of the particle: in Figure 2.3 the proton (blue dot) is moving towards the left and the electron (yellow dot) is moving towards the right.

Eventually, once the particle has gained sufficient energy, it will escape from the shock front either back upstream or downstream - which is heavily dependent upon its velocity and pitch angle.

In addition to needing time at the shock front to be accelerated to the observed energies, particles need to encounter the shock more than once. However regions in the vicinity of shock fronts are likely to be turbulent, and such turbulence will

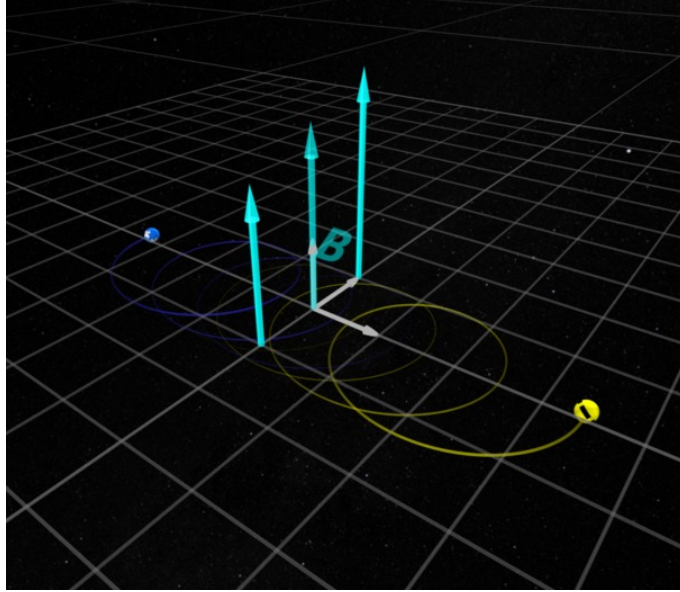


Figure 2.3: An illustration of particle drift due to a magnetic field gradient. The magnetic field is directed upwards (shown in cyan), with the longer arrows suggesting increasing field strength; the path taken by a proton (moving left) is shown in blue, and by an electron (moving right) in yellow. Image courtesy of NASA’s Scientific Visualization Studio.

be able to scatter downstream particles back upstream allowing possibly multiple interactions with the shock.

2.2.2 Diffusive shock acceleration

Diffusive shock acceleration occurs when the shock is quasi-parallel, meaning that the induced electric field is small and consequently shock-drift acceleration is negligible. The acceleration occurs as a result of many collisions both upstream and downstream.

On each side of the shock the magnetic field is turbulent, and the amount of

CHAPTER 2

pitch-angle scattering (see Section 2.6) is given by the diffusion coefficient upstream and downstream (D_u and D_d) (or, equivalently, the upstream and downstream mean-free-paths, λ_u and λ_d). Upstream collisions will be head-on resulting in an increase in particle speed, but collisions downstream will be head-to-tail causing a decrease in speed. But the speed of the flow upstream is faster than the flow downstream, so the increase in speed is greater than the decrease.

The amount of energy which the particle gains depends upon the component of the particle's velocity which is parallel to the magnetic field, and therefore is also dependent upon its pitch angle.

2.3 Particle acceleration in realistic scenarios

The traditional view of particle acceleration, as exemplified in the two class paradigm discussed in Section 1.5, was that impulsive SEP events result from acceleration by flares, and gradual SEP events from acceleration by CME driven shocks. However, in realistic scenarios the distinction between the different types of acceleration becomes blurred. Increasingly flares and CMEs are viewed as two different, but complementary, manifestations of energy release and all basic acceleration mechanisms may play a rôle to a variable degree.

2.4 Particle escape

A second important factor in determining whether or not SEPs may be detected at Earth is whether or not the particles have access to open magnetic field lines, and may therefore be able to escape into interplanetary space.

Figure 2.4 is an illustration of how magnetic field lines would appear during the solar eclipse of 21 August 2017 according to a model based on measurements from the National Solar Observatory Integrated Synoptic Program. In the figure,

CHAPTER 2

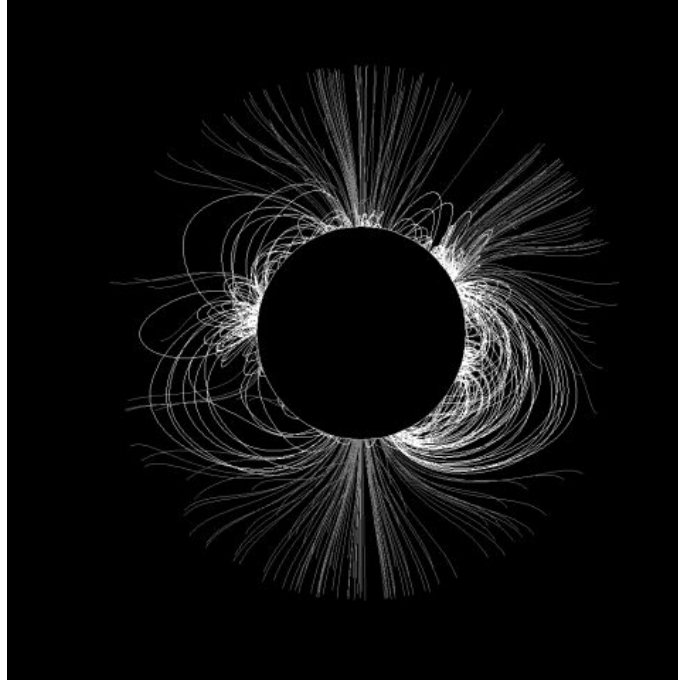


Figure 2.4: An illustration of how magnetic field lines would appear during the solar eclipse of 21 August 2017. Open field lines emanate from the solar poles; closed field lines loop back on to the Sun. Image credit: the National Solar Observatory

the solar disc has been occulted so as to show only the structure of the magnetic field around the limb. The figure clearly shows the complex structure of the coronal magnetic field. The field lines which emanate from the solar poles and which do not return to the Sun are called “open” field lines, whereas those where the field lines loop back on to the Sun (and which appear closer to the solar equator) are said to be “closed”.

Figure 2.5 shows an arcade of loops which was observed by the Transition Region And Coronal Explorer (TRACE, a mission of the Stanford-Lockheed Institute for Space Research, and part of the National Aeronautics and Space Administration (NASA) Small Explorer program). These loops are formed by plasma which follows

CHAPTER 2

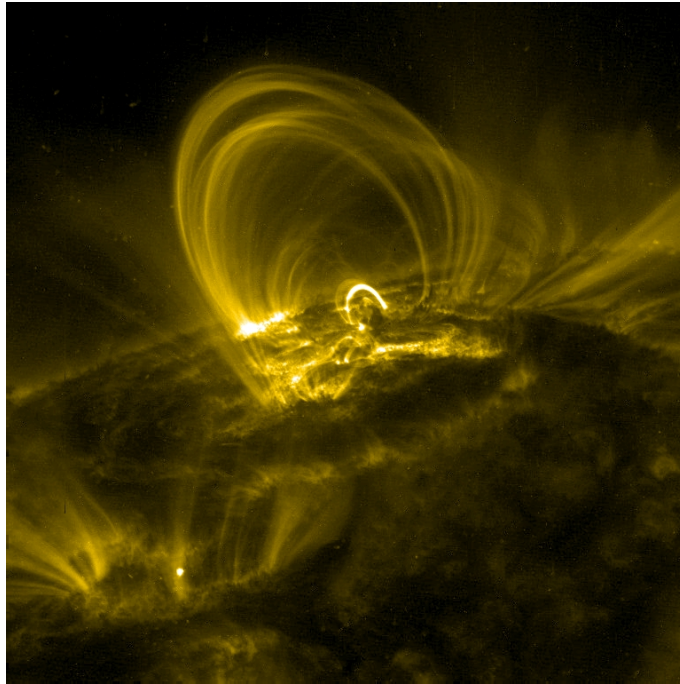


Figure 2.5: A loop arcade seen on 8 September 2005 by TRACE. Image credit: TRACE

the magnetic field lines.

The loops can have a height of $0.2R_{\odot}$ (DeForest (2007)). However it was seen in Section 1.2 that solar flares occur at heights above the solar surface of between ~ 1 and 5×10^7 m (0.014 and $0.07 R_{\odot}$). This means that it may be the case that a flare can occur in a region relatively close to the surface of the Sun, with magnetic field lines arching over the top of them.

Wang and Zhang (2007) made a study of 4 “confined” X class flares (which are defined as those flares which were not associated with a CME), and 4 “eruptive” X class flares (*i.e.* those which were associated with a CME). They found that confined events occurred closer to the magnetic centre of the source active region, whereas for eruptive events they occurred closer to its edge. They conclude that in some events, magnetically strong overlying arcades may prevent the release of energy from the

solar corona resulting in a flare but not a CME. Consequently any particles which might have been accelerated by the flare would not have access to open magnetic field lines and could not, therefore, escape into interplanetary space.

Klein *et al.* (2010) investigated a small number of these “CME-less” flares further, and argued that no SEP event might be expected following a flare which shows high peak emission in soft X-rays but which does not exhibit radio emission at decimetre and longer wavelengths (as such radio emission is a reliable indicator that particles accelerated in a flare do have access to the high corona and interplanetary space).

2.5 Propagation through interplanetary space

2.5.1 Magnetic field line connection to Earth

Alfvén’s theorem states that for a plasma with infinite electrical conductivity the magnetic field is “frozen in” to the plasma, and moves along with it. In interplanetary space, whilst electrical conductivity is not infinite, resistivity is low enough for the theorem to be applied approximately. The result is that interplanetary magnetic field (IMF) lines are pulled into a spiral shape (called the “Parker spiral”) by a combination of the outward flow of the solar wind and the rotation of the Sun (Parker (1958)). Figure 2.6 (taken from Owens and Forsyth (2013)) is a visualisation of the magnetic field lines in the ecliptic plane as they emanate from the Sun. The view is down on to the Sun’s north pole, and the Parker spiral shape is very clear outside a distance of a few solar radii. How tightly wound are the spirals is determined by the speed of the solar wind: a faster wind will result in a less tightly wound spiral.

The “central meridian” is where a straight line between the centre of the Sun and the centre of the Earth intersects with the source surface (see Section 2.7. The “Earth’s footpoint”, Φ_s , is the point on the source surface where the magnetic field line which directly connects the Earth to the Sun is seated. Because the tightness

CHAPTER 2

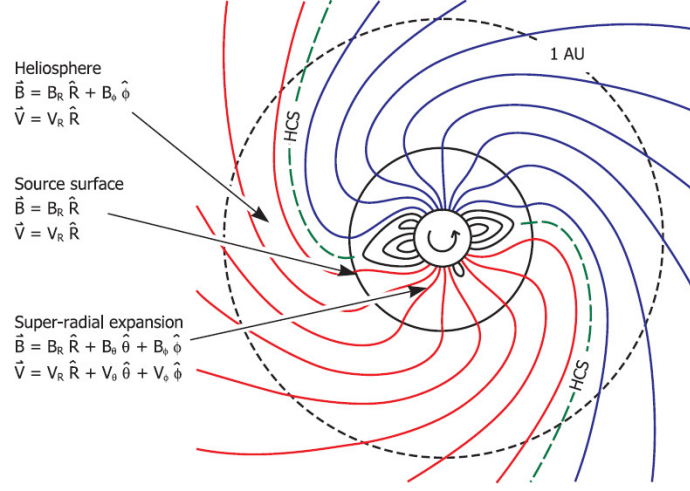


Figure 2.6: A visualisation of magnetic field lines emanating from the Sun. The view is down on to the Sun's north pole. Taken from Owens and Forsyth (2013).

of the Parker spiral is dependent upon solar wind speed, so is the location of the Earth's longitudinal footprint. It is given by (Parker (1961)):

$$\Phi_S = \Phi_{(1\text{au})} + \frac{\Omega}{v_{\text{sw}}}(1\text{au} - R_S) \quad (2.4)$$

where Ω is the rotation rate of the Sun (and which can be taken to be 2.87×10^{-6} rad/s), v_{sw} is the solar wind speed, 1au is $\sim 1.5 \times 10^8$ km, and R_S is the source surface radius (taken to be $2.5R_{\odot}$). $\Phi_{(1\text{au})}$ is the longitude of the spiral at 1au . As all the data used in this thesis have been obtained from instruments in Earth orbit, $\Phi_{(1\text{au})}$ can be taken to be at the central meridian, *i.e.* zero. Φ_S is positive west of the central meridian. For a typical solar wind speed of $v_{\text{sw}} = 450$ km/s, $\Phi_S \approx 55^\circ$.

The Sun's axis of rotation is tilted with respect to the Earth's orbit, meaning that the Earth's footprint also varies latitudinally between $+7.2^\circ$ and -7.2° over a six monthly cycle.

It has long been known that solar events which occur with a longitude between about W20 and W80 have a much greater likelihood of producing SEPs at Earth

CHAPTER 2

than solar events outside this range (Van Hollebeke *et al.* (1975)), and the reason for this can now be seen. Because SEPs broadly follow the magnetic field lines (Jian *et al.* (2015)), those which have an origin in the eastern side of the solar disc (as observed from Earth) will tend to be guided away from the Earth, whereas those from the western side will be guided towards the Earth. These western events are said to be “magnetically well-connected”, and the result is that such events are much more likely to produce SEPs at Earth than eastern events.

That is not to say that solar events which have a poor magnetic connectivity to Earth cannot produce SEPs at Earth: some SEP events have been seen from spacecraft which have been separated by nearly 360° (*e.g.* Dresing *et al.* (2012); Wiedenbeck *et al.* (2013)), and the reasons why this may happen are discussed in Section 2.6.2.

2.5.2 Particle flux and energetic storm particles

The location of the observer relative to the source of SEPs at the Sun is relevant to the observed energetic particle flux. Figure 2.7 (taken from Reames (1999)) is an illustration of the energetic particle flux in 3 different energy channels as observed from 3 different longitudinal locations. An observer who is located towards the east of the source region will see the acceleration site to the west. She will have been very well magnetically-connected to the CME shock when it was close to the Sun, but by the time it reaches 1au she is much less well connected. She sees a rapid rise in energetic particle flux, but then a slow decline.

An observer at a central location sees a slower initial rise in flux (since he is less well-magnetically connected early in the event) but as the CME approaches he becomes better and better connected, and so the energetic particle flux profile shows a levelling off until it begins to decline. An observer located west of the shock always has the shock to the east. She sees a slow rise and observed the peak flux only after

CHAPTER 2

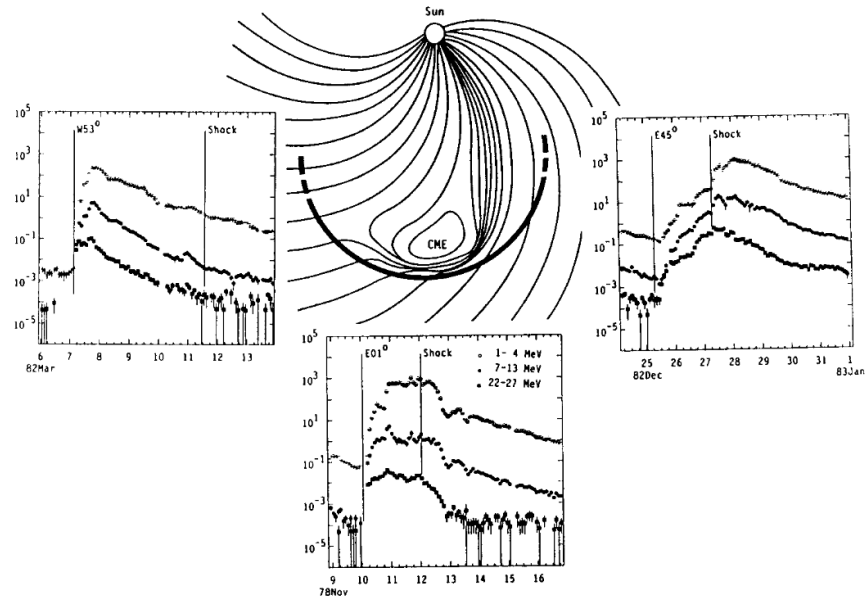


Figure 2.7: An illustration of the energetic particle flux in 3 different energy channels as observed from 3 different longitudinal locations. Taken from Reames (1999)

the shock has passed.

A rise in proton intensity may be observed with the passing of the shock: such rises are called energetic storm particle (ESP) events. An illustration of an ESP event is shown in Figure 2.8. The x-axis of the plot shows time, and the y-axis proton intensities seen in 6 different energy channels for an event which occurred on 19 October 1989. The parent solar event was an X13 flare at S27E10. The profile of the curves is essentially flat until the passing of the shock. The vertical purple dashed line shortly before midday on 20 October shows the start of the ESP event, and the vertical magenta dashed line at about 16:45 on 20 October shows the time of the passing of the shock.

It is notable that the rise in proton intensity begins some hours before the actual arrival of the shock, but that peak intensities occur close to the time the shock passes the observer. Once the shock has passed the intensities begin to decline.

CHAPTER 2

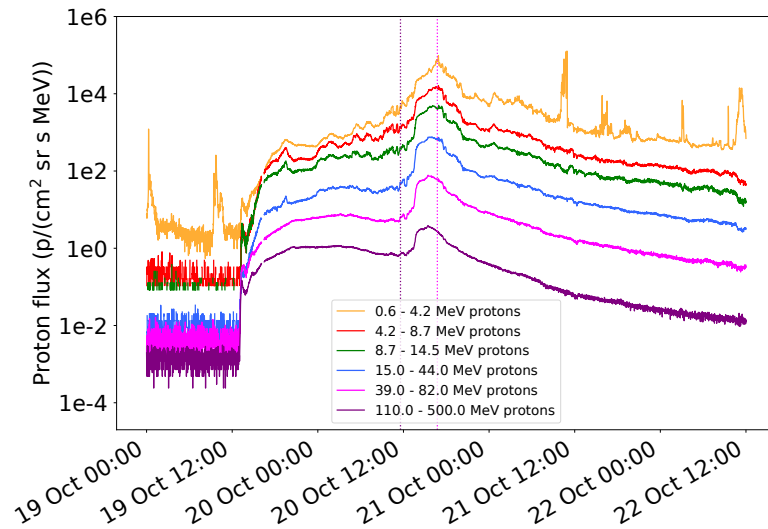


Figure 2.8: An illustration of an energetic storm particle event. The x-axis shows time, and the y-axis proton intensities seen in 6 different energy channels for an event which occurred on 19 October 1989. The parent solar event was an X13 flare at S27E10. The vertical purple dashed line shortly before midday on 20 October shows the start of the storm particle event, and the vertical magenta dashed line at about 16:45 on 20 October shows the time of passing of the shock. Adapted from Reames (1999).

ESPs can be helpful in identifying interplanetary CMEs (ICMEs) which may have strong geomagnetic effects. The acceleration of ESPs takes place not at the Sun, but by the ICME in interplanetary space.

2.6 Modelling particle transport

2.6.1 The focused transport equation

Historically, SEP transport has been modelled by finding solutions to a focused transport equation (e.g. Zank *et al.* (2000); Lee (2005)). The equation includes terms for the propagation of the particle parallel to the magnetic field including focusing and pitch angle scattering.

In order to understand what is meant by “focusing”, a particle’s pitch angle, α , is defined as

$$\alpha = \tan^{-1}\left(\frac{v_{\perp}}{v_{\parallel}}\right) \quad (2.5)$$

where v_{\perp} and v_{\parallel} are the components of the particle’s velocity perpendicular and parallel to the magnetic field line respectively. Furthermore, the particle’s magnetic moment is conserved:

$$\mu = \frac{mv_{\perp}^2}{2B} = \text{constant} \quad (2.6)$$

Because the strength of the interplanetary magnetic field falls as distance from the Sun increases, it follows that smaller values of B require a smaller value for v_{\perp} for μ to remain constant. Then, from Equation 2.5, it can be concluded that smaller values of v_{\perp} mean that the pitch angle is also smaller. A particle may have a large pitch angle when close to the Sun which will be much reduced by the time the particle reaches Earth’s orbit. It is this effect of pitch angle reduction which is called focusing.

The dependence of pitch angle upon the strength of the magnetic field also explains magnetic mirroring. If a particle travels towards an *increasing* magnetic field, its pitch angle must increase. The consequence of this is that v_{\perp} also increases, and therefore v_{\parallel} decreases. Eventually, as the pitch angle approaches 90° , v_{\parallel} approaches

CHAPTER 2

zero and the particle is reflected back along the field line.

Rather than being involved in large-angle interactions (in which the particle is reflected by 180°), particles are more likely to be affected by small-angle interactions. If a particle were to encounter a magnetic inhomogeneity, the direction of its guiding centre may change, but, crucially, the magnitude of its velocity remains the same: it is the ratio of v_\perp to v_\parallel which changes, and, according to Equation 2.5, this means a change in pitch angle. This “pitch angle scattering”, or “pitch angle diffusion” as it sometime called, is associated with turbulence in interplanetary space.

The focused transport equation is essentially one dimensional: it describes how particles travel along a magnetic field line, the only spatial variable being the distance along the magnetic field line. The difficulty, however, is that that SEPs with a very wide longitudinal (*e.g.* Dresing *et al.* (2012); Wiedenbeck *et al.* (2013); Batarbee *et al.* (2017c)) and latitudinal (*e.g.* Dalla *et al.* (2003)) spread have been observed, and these observations suggest that SEPs are able to propagate across the magnetic field.

2.6.2 A three dimensional approach

A 3-dimensional approach may better explain how SEPs may be observed at distant locations. There are 3 possible mechanisms for 3-dimensional SEP transport: field line meandering, perpendicular diffusion, and particle drift.

The smooth magnetic field lines shown in Figure 2.6 represent the ideal case, but the field lines are disrupted by turbulence caused by the solar wind, CMEs and other factors. The result is that locations which are not well magnetically-connected to the Sun by the application of the simple Parker spiral model may in fact be well connected as a result of the “meandering” of the field lines (Laitinen *et al.* (2013, 2016)).

Perpendicular diffusion of SEPs refers to the tendency of charged particles to

CHAPTER 2

diffuse in lateral directions (*i.e.* perpendicularly to the magnetic field lines). Diffusion is a stochastic process, resulting from many random collisions. The effect of diffusion has been included in transport models (*e.g.* Dröge *et al.* (2014); He (2015)), and, although determination of diffusion coefficients is difficult, attempts have been made to derive realistic estimates from first principles (Strauss *et al.* (2017)).

Following recent test particle studies, it has become clear that a particle's guiding centre may be subject to a drift which is associated with the gradients and curvature of the interplanetary magnetic field. This drift can produce transport both in longitude and latitude within the heliosphere (Dalla *et al.* (2013)). Particles which undergo drift are decelerated in the process (Dalla *et al.* (2015)).

The extent of the drift is greater for particles which have a large mass over charge ratio, and consequently is particularly relevant for SEP heavy ions which are partially ionised. Such particles have been shown in simulations to travel to locations which are not well magnetically connected to the region at which they are injected, and this drift produces a decrease over time in the ratios of heavy ion SEPs, *e.g.* iron over oxygen (Dalla *et al.* (2017a)); such decreases have been observed (*e.g.* Zelina *et al.* (2017)).

The direction of drift is dependent upon the polarity of the magnetic field in which the particle propagates: in locations where the magnetic field is positive, the drift is directed towards the south; where the magnetic field is negative, the drift is north-directed.

2.7 The heliospheric current sheet

The Parker spiral shape becomes apparent outside a distance of a few solar radii from the Sun. Inside that boundary, however, the picture is rather different. Relatively close to the solar surface it is the magnetic field which dominates over the plasma meaning that it undergoes non-radial or super-radial expansion; at the boundary

CHAPTER 2

(which is called the “source surface”) the plasma pressure becomes dominant, and the magnetic expansion is radial.

A potential field source surface (PFSS) model (Hoeksema *et al.* (1983)) may be used to produce a synoptic map of the magnetic field at the source surface. Figure 2.9 shows an example of such a map (taking the source surface to be at $r = 2.5R_{\odot}$) for Carrington rotation 1912 (produced from data downloaded from the Wilcox Solar Observatory website¹). The model assumes a radial magnetic field at the source surface. Blue shading represents regions with a positive magnetic field, and red shading regions with a negative magnetic field. The contours show differences in the strength of the magnetic field in μT with boundaries at ± 0.5 , 1.0, 2.5, 5.0, 10.0, and 15.0 μT .

Between the positive and negative magnetic fields there is a region where the strength of the field falls to zero, the magnetic neutral line. This region is shown in Figure 2.9 as a black line. Its extension into the heliosphere is a 3-dimensional surface called the heliospheric current sheet (HCS). It was first discovered in 1965 through magnetic field measurements at 1au (Wilcox and Ness (1965)) and is so called because a small electric current (about 10^{-10} A/m²) flows through it. At 1au the HCS is about 10,000 km thick.

Figure 2.10 (taken from Owens and Forsyth (2013)) is a representation of the HCS produced by a simulation of Carrington rotation 1912 (Odstrcil *et al.* (2004)). As can be seen from Figure 2.9, during this rotation the HCS was located mostly along the solar equator. Nevertheless, the current sheet is “wavy” because the Sun’s axis of rotation is tilted with respect to the ecliptic. The red and blue colours shown in Figure 2.10 illustrate this “waviness”.

The black line shown in Figure 2.10 represents the orbit of the Earth as it travelled through the undulating current sheet. On one side the solar magnetic field

¹<http://wso.stanford.edu/>

CHAPTER 2

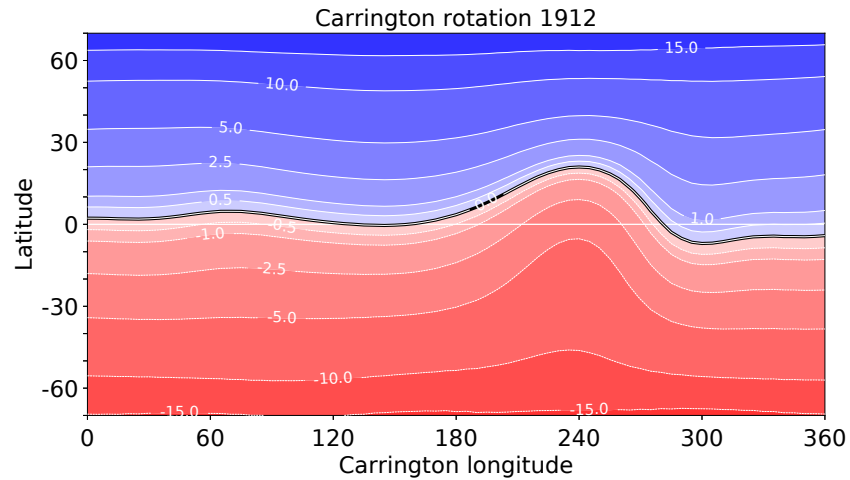


Figure 2.9: An example source surface synoptic chart for $r = 2.5R_{\odot}$ resulting from a potential field source surface model for Carrington rotation 1912. Blue regions are areas of positive magnetic field, and red regions areas of negative magnetic field. The contours show differences in the strength of the magnetic field in μT . The black line is where the heliographic current sheet lies. Data were provided by the Wilcox Solar Observatory.

points towards the Sun; on the other it points away. This point is also made clear by the red and blue colours of the magnetic field lines shown in Figure 2.6: in that figure the two colours are separated by dotted green lines which represent the HCS.

The existence of the current sheet has an effect upon the way that SEPs propagate through the interplanetary medium. Models have shown that a flat equatorial HCS in the inner heliosphere can inhibit the crossing of protons into the opposite hemisphere (Battarbee *et al.* (2017a)).

CHAPTER 2

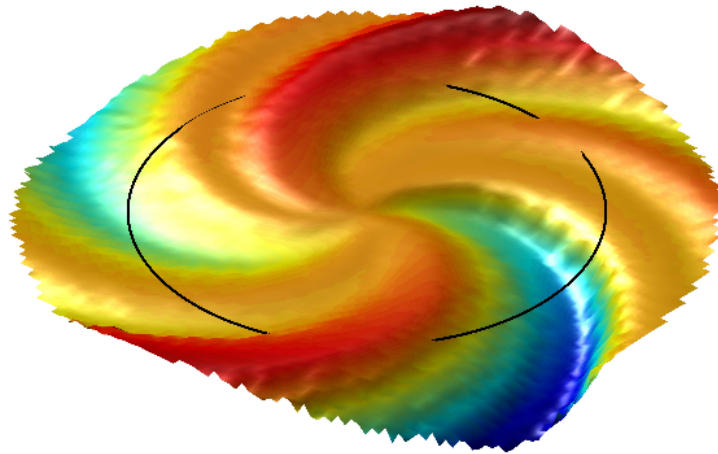


Figure 2.10: A representation of the HCS produced by a simulation of Carrington rotation 1912 (Odstrožil *et al.* (2004)). The HCS is “wavy”, extending about $\pm 10^\circ$ from the equator. The thick black line shows the Earth’s orbit showing that it crossed the HCS on at least 6 occasions. The thinning of the black line in the top left corner indicates a period when the Earth “skimmed” the HCS - there may have been multiple crossings of the HCS as a result of a fine scale structure not shown in the simulation. Taken from Owens and Forsyth (2013)

Chapter 3

Observations

This chapter provides an introduction to some of the instruments which may be used to observe solar events and to measure SEP enhancements. It includes a description of some of the parameters of CMEs and flares which may have an influence upon whether SEPs are detected at Earth or not.

3.1 CME observations

CMEs are detected by coronagraphs. In essence, a coronagraph is an instrument which has in the centre of its imaging plane an occulting disc. This disc hides the radiation from the central star, allowing details in the regions close to the star to be observed. Coronagraphs are used in astronomy to image extra-solar planets and circumstellar discs, but in the field of solar physics they are used to observe the Sun's corona.

Currently there are only two spacecraft in active service which carry coronagraphs. The Solar and Heliospheric Observatory (SOHO) is a joint project run by the European Space Agency (ESA) and NASA. It was launched in 1996, and amongst the instruments on board it carries the Large Angle and Spectrometric COronagraph (LASCO). LASCO consists of three coronagraphs, C1, C2, and C3,

CHAPTER 3

but sadly C1 had to be disabled shortly after the launch of the spacecraft. SOHO is stationed at the L1 Lagrange point which is about 150 million kilometres from Earth.

The C2 coronagraph has a field of view between about 1.5 and 6 solar radii (R_{\odot}), although the lowest height at which detection of the corona can be made is about 2 R_{\odot} (Brueckner *et al.* (1995)). C3 has a field of view between about 3.7 and 30 R_{\odot} (*ibid.*). Apart from short periods, data from these coronagraphs are available for a period exceeding 20 years.

The second spacecraft with coronagraphs on board is the Solar Terrestrial Relations Observatory (STEREO). There were two nearly identical spacecraft in this mission which were designed to orbit the Sun at the same distance as Earth. One was to travel ahead of the Earth (STEREO-A), and the other to trail behind it (STEREO-B). The spacecraft were launched in 2006, but contact was lost with STEREO-B on 1 October 2014. Communications were re-established in August 2016, but it was not possible to regain control, and contact was lost again in September 2016. Further attempts to communicate with STEREO-B have recently re-commenced as the spacecraft approaches Earth once more.

Each STEREO spacecraft carried two coronagraphs, COR-1 and COR-2. COR-1 has a field of view between 1.3 and 4 R_{\odot} (Thompson *et al.* (2003)), and COR-2 from about 2 R_{\odot} out to 15 R_{\odot} (Eyles *et al.* (2007)). There are data from STEREO-A from 2006 until the present, and from STEREO-B from 2006 until September 2014.

For this work, the coordinates of the site of origin of the CME need to be known. The STEREO spacecraft are both moving relative to the Earth, and consequently calculating the heliographic coordinates of an event as seen by one of the STEREO craft adds an unnecessary level of complexity. Furthermore, solar flare data are only available for flares which occurred on the front side of the Sun as observed from Earth. For these reasons in this work it has been data obtained by the SOHO /

CHAPTER 3

LASCO coronagraphs which have been used.

There are four currently maintained catalogues which list CMEs detected by the SOHO / LASCO coronagraphs: the Computer Aided CME Tracking (CACTus) catalogue (Robbrecht and Berghmans (2004)) publishes data from May 1997; the Solar Eruption Event Detection System (SEEDS) catalogue (Olmedo *et al.* (2008)) covers from January 1996; the Coronal Image Processing (CORIMP) catalogue (Morgan *et al.* (2012); Byrne *et al.* (2012)) begins in January 2000; and the Co-ordinated Data Analysis Workshop (CDAW) catalogue (Gopalswamy *et al.* (2009)) currently covers between January 1996 and June 2016. The first three of these are automated systems with the catalogue being produced without any human intervention, whereas the last is produced manually.

Typically each catalogue publishes data on various parameters relating to the CME, and these are discussed in the following sections.

3.1.1 Speed

All of the coronagraphs which are currently in service produce images in white light: what is observed is the Thomson-scattered emission from the electrons within a CME. A typical example of an image of a CME taken in white light by the C2 coronagraph, downloaded from the Helioviewer website¹ (Hughitt *et al.* (2011)), is shown in Figure 3.1. The black circle in the centre of this image is caused by the occulting disc of the coronagraph.

Estimates of the speed of a CME may be made by the comparison of a least two, and ideally many more, images. A measure is taken of how far the leading edge (or “front”) of the CME has travelled in the time between the taking of the images, and its speed is thereby derived.

A real difficulty in estimating CME speed is that the coronagraphs produce a

¹<https://helioviewer.org/>

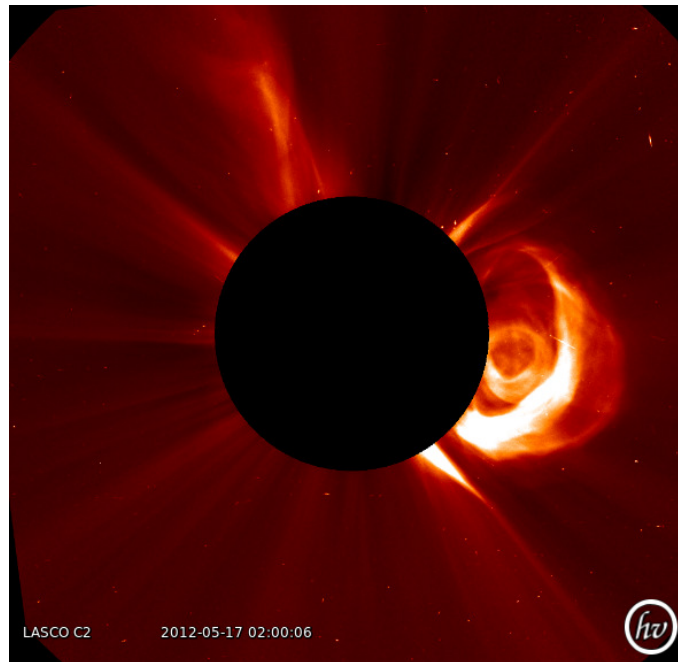


Figure 3.1: Images taken by the C2 coronagraph on 17 May 2012 showing a coronal mass ejection (downloaded from the Helioviewer website). The black circle in the centre of the image is caused by the coronagraph’s occulting disc.

2-dimensional image of a 3-dimensional effect - in order to make this clear, very often CME speed is quoted as the “plane-of-the-sky” speed. For CMEs which have their origin close to the edge (or “limb”) of the solar disc (as observed from Earth) the estimate of speed may be relatively accurate; for those which have their origin elsewhere on the solar disc the estimate of speed can only ever be an under-estimate.

There are several methods of calculating CME speed from the coronagraph images and each of the CME catalogues employs a different one. The CACTus catalogue publishes 4 parameters relating to CME speed: v , the median velocity of all different structures within the CME; $minv$, the minimum velocity detected within the CME; $maxv$, the maximum velocity detected within the CME; and dv , the variation of velocity over the width of the CME. The method used by CACTus to

CHAPTER 3

determine CME speed requires a number of coronagraph images, and it is therefore impossible to determine the speed of CMEs which move too rapidly through the coronagraph’s field of view: the limit is approximately 2,000 km/s.

SEEDS gives one value for CME speed which is calculated by applying a linear fit to height-time measurements; CDAW reports a value for CME speed which is calculated in the same way, although the position within the CME of where the height measurement is made is slightly different in each case. CDAW also publishes two other measures of speed based upon a second-order polynomial fit to the height-time measurements.

CORIMP publishes two values for CME speed, a “median” speed and a “maximum” speed, and each of these are calculated using different techniques again, as described in Byrne *et al.* (2013).

3.1.2 Acceleration

An estimate can also be made from the height-time measurements as to whether a CME has increased or decreased in speed (or maintained a constant speed) whilst it is visible in the LASCO coronagraph fields of view. At least three observations of the CME are required in order to make an estimate of acceleration, but the more observations there are, the more accurate the estimate is likely to be. Of the catalogues under consideration here, only SEEDS and CDAW publish a value for CME acceleration.

3.1.3 Width

The width of a CME is a measure of its plane-of-the-sky angular extent - *i.e.* the number of degrees from one edge of the CME to the other. The concept is illustrated by a CME which occurred on 3 May 2012 and is shown in Figure 3.2. These images are “difference” images: one image is subtracted from the next so as to enhance

CHAPTER 3

the way that the image has changed in the time between the two images. Overlaid on the coronagraph’s occulting disc are difference images from the Atmospheric Imaging Assembly (AIA) which is on board the Solar Dynamics Observatory (SDO) spacecraft.

In these images the width of the CME is represented by the angle shown in red. While some CMEs do not continue to expand as they leave the Sun, others do. It is apparent that the time at which the width of the CME is measured must be specified: for example, if the width of the CME were to be measured from the image in Figure 3.2a the result would be much lower than that obtained had the image in Figure 3.2d been used. Different CME catalogues may publish different values for the width of CMEs.

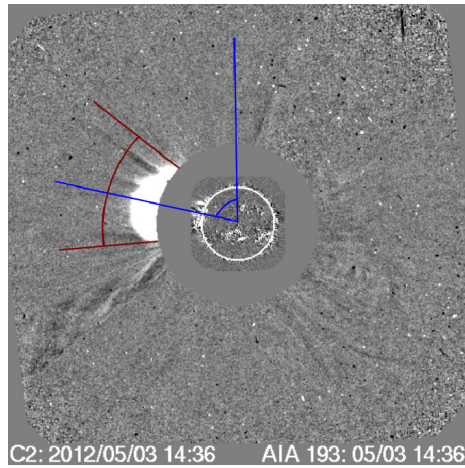
Some CMEs may widen to such an extent that the ejecta appear to surround the solar disc. Such a case is illustrated in Figure 3.3, and in these circumstances the CME is said to be a “halo”.

3.1.4 Position angle

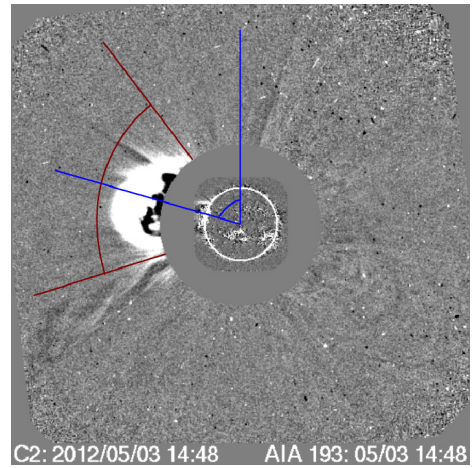
The position angle of a CME is an indication of its direction. It is measured in degrees anti-clockwise from solar north (at 0°) to the centre of the CME. This is illustrated by the blue angle shown in Figure 3.2. Whilst a decision must be taken as to where, within the width of the CME, the centre lies, it can be seen that generally the position angle is likely to remain relatively constant throughout the lifetime of the CME.

CDAW publishes two values for position angle, the first measured when the CME makes its first appearance in the C2 images, and the second (which is called the “measurement position angle”, or “MPA”) calculated when the height-time measurements are made. Ideally the two should be the same, although it is possible for a CME to move non-radially so that the measurements can differ. If a CME is

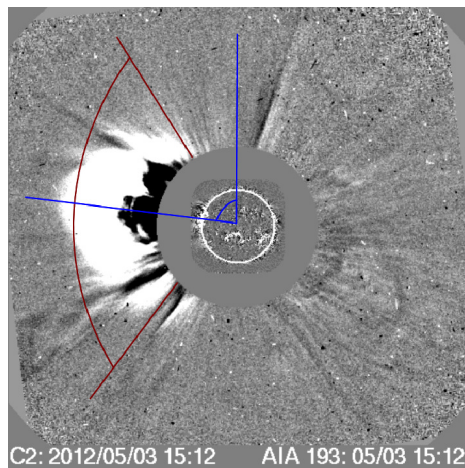
CHAPTER 3



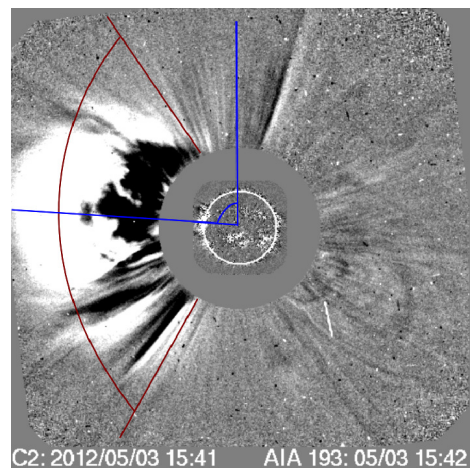
(a) Image taken at 14:36 UTC



(b) Image taken at 14:48 UTC



(c) Image taken at 15:12 UTC



(d) Image taken at 15:42 UTC

Figure 3.2: Difference images of a CME on 3 May 2012 - the width of the CME is shown in red. The images illustrate how a CME's width may increase over time. The angle shown in blue is the CME's position angle, and this remains relatively constant over the lifetime of the CME.

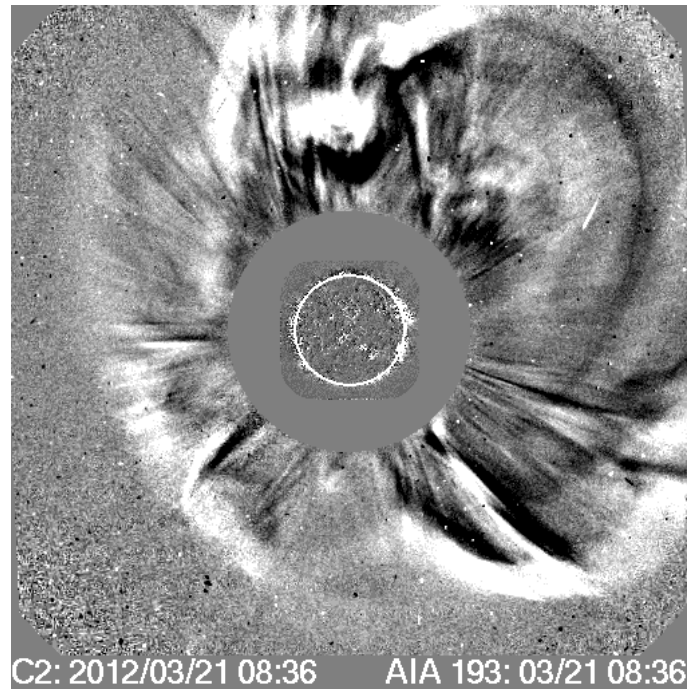


Figure 3.3: A “halo” CME which occurred on 21 March 2012.

reported by CDAW to be a halo (as is the case for most fast CMEs) then only the measurement position angle is published.

3.1.5 Timing

The time at which the CME may be said to be ejected from the solar surface is often referred to as the “lift-off” time, t_o . However, the time of the CME as reported in the CME catalogues will be different from t_o for a number of reasons. First, the CME must travel at least $1 R_{\odot}$ (if its origin lies close to the limb), and possibly as far as $2 R_{\odot}$ (if its origin is close to the centre of the solar disc), before it can be detected by the SOHO C2 coronagraph. For a CME with a speed of 2,000 km/s which has its origin at the solar limb, nearly six minutes will pass before it can possibly be detected by C2; for slower CMEs, and for those which occur closer to the centre of the solar disc, the delay will be (possibly significantly) greater.

Secondly, detection of the CME is affected by the cadence of the coronagraph.

CHAPTER 3

For C2, that cadence is no better than 12 minutes, and is sometimes rather longer. Thus, a CME may have travelled much further than $2 R_{\odot}$ before it is first detected.

Thirdly, the SOHO spacecraft is in orbit at the Lagrangian L1 point which is about 99% of the Sun-Earth distance: hence it will take approximately 8 minutes for the electromagnetic radiation to reach the detector.

3.2 Flare observations

The GOES series of satellites has been operational since January 1976, and each of them has carried a Space Environment Monitor (SEM) suite of instruments. The XRS provides information in two wavelength bands - 0.5 to 4 Å and 1 to 8 Å. Their design has changed little over the years (Garcia (1994)). Table 3.1 sets out a list of the GOES satellites and their operational periods. It should be noted that no data were recovered from GOES 4.

The GOES spacecraft are in geosynchronous orbit which means that they have an unobstructed view of the Sun for the entire year, apart from the few hours when the Earth eclipses the Sun.

3.2.1 Class

As was seen in Chapter 1, solar flares are classified according to their peak emission in SXR as measured in the 1 - 8 Å channel of the GOES XRS instruments. The scale is logarithmic: SXR peak fluxes below 10^{-7} W m^{-2} are of class A; between 10^{-7} W m^{-2} and 10^{-6} W m^{-2} they are of class B; and so on to classes C, M and X. There is no class above X, and so if a flare is seen to have a peak SXR flux of, say, $1.5 \times 10^{-3} \text{ W m}^{-2}$ then it is said to be of class X15.

CHAPTER 3

Table 3.1: A list of the GOES satellites and their operational periods. Column 1 states the name of the spacecraft, column 2 the date when it first became operational and column 3 the date when it was taken out of service.

Satellite name	Start date	End date
GOES 1	January 1976	May 1978
GOES 2	August 1977	May 1983
GOES 3	July 1978	August 1980
GOES 5	January 1983	February 1982
GOES 6	May 1983	November 1994
GOES 7	March 1987	August 1996
GOES 8	January 1995	June 2003
GOES 9	April 1996	July 1998
GOES 10	July 1998	December 2009
GOES 11	July 2000	February 2011
GOES 12	January 2003	August 2010
GOES 13	April 2010	In operation
GOES 14	December 2009	Limited service
GOES 15	September 2010	In operation

3.2.2 Duration

The National Centers for Environmental Information (NCEI) define the start of a solar flare as when 4 consecutive values in the 1-minute X-ray data meet all 3 of the following conditions:

- (a) All 4 values are above the B1 threshold and,
- (b) All 4 values are strictly increasing and,

CHAPTER 3

- (c) The last value is greater than 1.4 times the value which occurred 3 minutes earlier.

The flare ends when the X-ray flux returns to one half of the peak flux, and in this context “peak” is the sum of the flux at maximum plus the value of the flux at the start of the event².

3.2.3 Heliographic co-ordinates and active region numbers

The location of a particular site on the solar surface may be specified by heliographic latitude and longitude, with the origin of the system being the intersection of the solar equator with the central meridian as observed from Earth. Convention has it that the hemisphere to the left of the central meridian as seen from Earth is east, and west is to the right. Thus if a flare is reported to have heliographic co-ordinates of -5 -20, it occurred 5 degrees east of the solar meridian and 20 degrees south of the equator. This is sometimes shown as E05S20.

The National Oceanic and Atmospheric Administration (NOAA) gives numbers to sunspot groups (which may include more than 1 sunspot). Active region numbers are assigned sequentially, and if an active region survives an entire solar rotation the next time it appears it is assigned a new number³.

3.3 SEP observations

There are a number of different instruments on board currently-operating spacecraft which are capable of detecting SEPs. The Energetic and Relativistic Nuclei and Electron (ERNE) detector is on board the SOHO spacecraft which is in orbit at the Lagrangian L1 point (Torsti *et al.* (1995)). It measures electrons, protons and

²<https://www.ngdc.noaa.gov/stp/solar/solarflares.html>

³https://hesperia.gsfc.nasa.gov/sftheory/questions.htm#AR_numbers

CHAPTER 3

heavier elements over a range of energy channels: for protons the lowest range is between 1.6 to 1.8 MeV, and the highest range is between 101.0 to 131.0 MeV.

The Advanced Composition Explorer (ACE) spacecraft was launched on 25th August 1997, and is also in orbit at the L1 point. It carries (*inter alia*) the Electron, Proton and Alpha Monitor (EPAM) instrument (Gold *et al.* (1998)) and the Solar Isotope Spectrometer (SIS) (Stone *et al.* (1998)).

The range of EPAM extends to about 5 MeV; SIS provides isotopically resolved measurements of the elements from lithium to zinc over the energy range 10 - 100 MeV per nucleon.

The GOES satellites also have a particle detector on board as part of their SEM. The Energetic Particle Sensor (EPS) also measures the flux of electrons, protons, and helium nuclei. For protons there are a number of energy channels, the lowest ranging from 0.6 to 4.0 MeV and the highest from 165.0 to 500 MeV.

SEPs may also be detected indirectly by ground-based neutron monitors, but this will only be the case for the most energetic events: if such an event is detected by neutron monitors it is called a ground level enhancement (GLE), but there have only been 72 GLEs since the mid 1940s. The last occurred shortly before submission of this thesis, on 10 September 2017.

3.4 Choice of data sources

Section 3.1 describes four of the different catalogues which publish parameters relating to CMEs. Whilst some discrepancy between the published values is to be expected, it may be thought that there would be some correlation between the catalogues. Unfortunately, this does not seem to be the case.

Appendix A is a comparison of the different parameters as published by three of the different catalogues (CORIMP had to be excluded from analysis because its data were not published in a suitable format). The main conclusions following that

CHAPTER 3

analysis are as follows:

- There is a wide variation in the number of CMEs reported by each of the 3 catalogues: between 17 May 1997 and 31 March 2013 CACTus reported 7,528 CMEs with a width exceeding 20° , SEEDS 14,372, and CDAW 13,566.
- Comparison of reported speeds is difficult because of the different methods used for determining speed (as described in Section 3.1.1). That said, the variation in speed values as published by the catalogues is large: average speed for CMEs with a width exceeding 20° is 774 km/s according to CACTus, 284 km/s according to SEEDS, and 418 km/s according to CDAW.
- The fastest CME according to CACTus had a speed of 2,027 km/s; for SEEDS it was 7,671 km/s; and for CDAW it was 3,387 km/s
- There were no cases where the 3 catalogues agreed on whether a CME was a fast CME (*i.e.* had a speed equal to or exceeding 1,500 km/s). CACTus reported 1,055 fast CMEs, SEEDS just 66, and CDAW 141.
- CME width estimates varied widely between catalogues. For fast CMEs both CACTus and SEEDS suggested that the width was likely to be less than 60° , whereas in the CDAW catalogue a fast CME was overwhelmingly likely to be reported as a halo.
- CME position angle for fast CMEs seems to be reported mostly as is to be expected (with peaks in distribution around 90° and 270°) by all 3 catalogues. However SEEDS reported 326 CMEs (including 2 fast ones) to have a position angle exceeding 360° which is plainly impossible.

Because the catalogues publish very different values for the same parameters it is very difficult to make a decision as to which should be used as a source of data for this work. There are, however, good reasons to believe that the SEEDS catalogue is

CHAPTER 3

not as reliable as CACTus and CDAW. The suggestion that there have been only 66 CMEs which exceeded 1,500 km/s in a period extending over nearly 16 years must be questionable, and the report that one of them had a speed exceeding 7,500 km/s must also cast doubt upon reliability. Finally, reports of CMEs with a position angle exceeding 360° must, by definition, be in error.

The CACTus catalogue, as noted in Section 3.1.1, is not able to measure accurately the speed of a CME exceeding 2,000 km/s and this is a major handicap for this work given the intention to confine the analysis to high-energy events. Furthermore, just as intuitively it may be thought that SEEDS reports too few fast CMEs, reports of over 1,000 such CMEs may be too many.

CDAW is by no means a perfect choice. The CDAW catalogue is produced manually, and this fact alone brings with it the dangers of subjectivity. The catalogue has been produced since 1996, and presumably it has not been the same person in charge of its production over the whole of that time. Therefore, what may have been regarded as a CME by one person may not be looked upon similarly by another; where a CME front lies may be interpreted differently by different people, meaning that the calculations of CME speed and acceleration may be inconsistent over the years.

Furthermore, because of the way that it is produced, the CME catalogue is not published until several months after the solar events have occurred. This means that it cannot be used for real-time forecasting of SEPs.

Nevertheless, because of the problems associated with the use of both CACTus and SEEDS, it has been decided to use the CDAW CME catalogue as the source of the CME data for this work. The measurement of speed used in this work is the one obtained by the straight line fit to the height-time measurements. It should always be borne in mind, however, that there are other catalogues, and that these publish very different data.

CHAPTER 3

For flare data, the GOES SXR Flare List has been used. Again, there is a comparison of different flare lists in Appendix A, but for flares there is only this one catalogue which both has data going back to 1980 and publishes values for peak SXR flux.

The GOES EPS has been used as the basis of energetic proton data, and this has been downloaded from the European Space Agency’s Solar Energetic Particle Environment Monitor (SEP-EM) website (Crosby *et al.* (2010))⁴. Again, the justification for making this choice is set out in Appendix A.

There has not been a single GOES spacecraft in operation throughout the period covered by this work. A number of different instruments have therefore been used, and the energy channels for each instrument have changed slightly. Table 3.2 shows the name of each spacecraft together with the time periods over which each has been used, and the energy channel considered to establish the occurrence of an SEP event. There are slight differences in the energy channels, particularly in the case of GOES 2, but the view is taken that the differences are so small as to have a negligible effect upon the results. From 1 April 1987 onwards the data had been cleaned and intercalibrated by the SEP-EM team; prior to that date their raw data were used.

⁴<http://dev.sepem.oma.be/>

CHAPTER 3

Table 3.2: Instruments used to obtain data on proton intensity, the dates between which data from that instrument was used, and the energy channels which have been analysed. Column 1 gives the name of the spacecraft from which the data was taken, column 2 the date from which those data began to be used, and column 3 the date when their use ceased. Column 4 shows the range of proton energies measured by the instrument which has been used, and column 5 whether the data were raw or had been cleaned by the SEPTEM team.

Spacecraft	Start date	End date	Energy channel (MeV)	Raw data / Cleaned
GOES 2	1 May 1980	31 December 1983	36.0 - 500.0	Raw data
GOES 6	1 January 1984	31 March 1987	39.0 - 82.0	Raw data
GOES 7	1 April 1987	28 February 1995	39.0 - 82.0	Cleaned
GOES 8	1 March 1995	7 January 2003	40.0 - 80.0	Cleaned
GOES 12	8 January 2003	31 December 2009	40.0 - 80.0	Cleaned
GOES 11	1 January 2010	31 December 2010	40.0 - 80.0	Cleaned
GOES 13	1 January 2011	31 March 2013	38.0 - 82.0	Cleaned

Chapter 4

Methodology

No large scale study has previously been made of large solar events which failed to produce SEPs at Earth, yet false alarms are highly interesting from a scientific point of view. By studying them, and by comparing their parameters with those of the solar events which did produce SEPs, answers to the questions posed in Section 1.8 may be determined.

Before setting out a formal definition of what is meant by the term “false alarm”, there is one other important matter which needs to be dealt with: CME-flare associations.

4.1 Associating CME and flare events

Very often, particularly for the higher energy events, CMEs and flares occur from the same active region in close temporal proximity: such events may be said to be “associated”. Finding such associations is important for two reasons:

1. CME catalogues do not publish data relating to the coordinates on the solar disc of their source active regions, whereas flare catalogues often include coordinate information. For cases where flare coordinates were not given in

the catalogues, they may be determined by one of the methods set out in Appendix A.2. If an association between CME and flare can be established, the coordinates of the CME may be inferred from the flare data.

2. This work is aimed at reaching an understanding of the type of solar events which produce SEPs. It is therefore essential to know whether that solar event consists of a CME alone, a flare alone, or a CME associated with a flare.

There is no standard approach, and so a method for making these associations automatically has been developed as part of this thesis work. It is described in Appendix B. The method produces correct associations in over 90% of cases from a total of 179 associations made. In an attempt to increase accuracy further movies of each solar event in 195Å (obtained by the Extreme ultraviolet Imaging Telescope (EIT) on board SOHO) and 193Å (obtained by the AIA on board SDO) were viewed. The associations made by the automatic method were confirmed in 156 cases; in 6 cases they were altered, and in a further 17 cases it was not possible to verify the automatically-made associations because EIT or AIA images were not available.

4.2 Definition of “false alarm”

A false alarm may simply be defined as “a solar event which is predicted by a forecasting algorithm to produce SEPs at Earth but which fails to do so”. The definition requires specification of:

- An SEP forecasting algorithm. This must include the criteria by which a solar event is assigned a high likelihood of producing SEPs at Earth. Typically this will include identification of the type of solar event (e.g. flare or CME) expected to produce SEPs, of a requirement on the intensity of the event (e.g. a flare with peak SXR flux, f_{SXR} , which exceeds a specified threshold intensity, f_{thr} , or a CME with a speed v_{CME} which is faster than a threshold speed v_{thr}),

CHAPTER 4

of a positional requirement (e.g. an event with a source region west of a given longitude), and possibly of other parameters.

- The criteria by which it is determined that an SEP event has occurred or not. These will typically include specification of the instrument being used to measure particle flux intensity, of the species of particle examined and its energy range, and of the SEP intensity threshold, I_{thr} , used to establish whether an SEP event was detected following a particular solar event.
- The method by which the solar event is associated with the SEP event.

Each of these requirements is considered in the following sections.

4.3 SEP forecasting algorithms

It is clear from Figure 1.2 that the more energetic the solar event, the greater the likelihood of that event producing SEPs at Earth (Dierckx *et al.* (2015)). It is also the case, as explained in Section 2.5.1, that heliographic longitude is an important parameter in determining the likelihood that a solar event will produce SEPs at Earth.

Based upon these premises two simple SEP forecasting algorithms may be defined as follows:

- A.1 A CME with a reported speed of $1,500 \text{ km s}^{-1}$ or greater (a “fast CME”) occurring west of E20 on the solar disc will result in an SEP event being detected at Earth.
- A.2 An X class flare occurring west of E20 on the solar disc will result in an SEP event being detected at Earth.

The threshold values $v_{\text{thr}} = 1,500 \text{ km/s}$ and $f_{\text{thr}} = \text{X class}$ have been chosen because there is a general anecdotal understanding within the community that events

CHAPTER 4

above such thresholds are highly likely to produce SEPs. However the actual performance of algorithms using these threshold values has not so far been evaluated.

The positional requirement is based upon Figure 4.1. Figure 4.1a shows the heliographic latitude and longitude of all fast CMEs and X class flares for which coordinates could be determined which occurred between 1 May 1980 and 31 March 2013. As is to be expected, there is no dependence upon longitude. Figure 4.1b, on the other hand, shows the same information over the same time period for those solar events for which coordinates could be determined (whether or not they were a fast CME or X class flare) which produced SEPs at Earth.

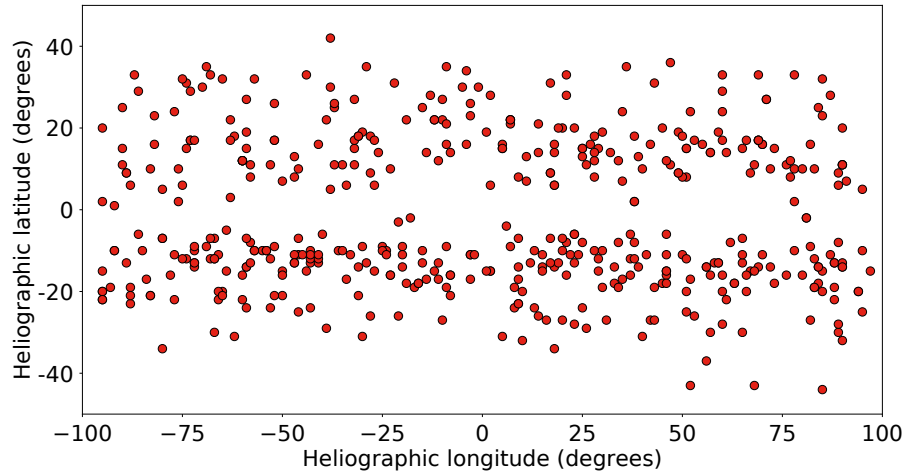
There are 171 points in Figure 4.1b of which 86.5% (148/171) are west of E20. Whilst the spatial requirement could have been chosen to be anywhere between about 0° and E30, the choice which has been made results in the vast majority of SEP events being included without a concomitant disproportionate increase in the number of false alarms.

4.4 Definition of “SEP event”

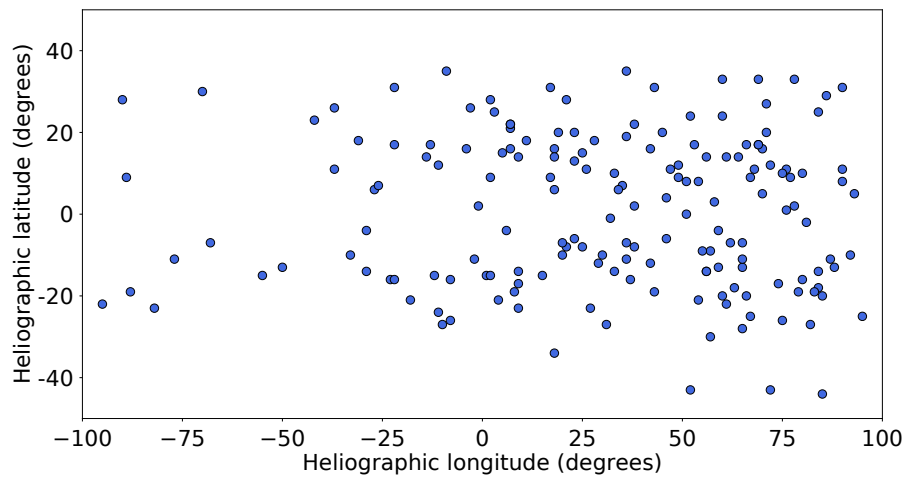
The definition of an SEP event will typically include specification of the instrument being used to measure particle flux, of the species of particle examined and its energy range, and of the SEP intensity threshold, I_{thr} used to establish whether an SEP event was detected following a particular solar event.

Particles accelerated by solar events include electrons, protons, and heavier ions, but in this work high energy (>40 MeV) protons have been analysed. The threshold considered is a little higher than the >10 MeV threshold used by NOAA, making the event list less biased towards interplanetary shock-accelerated events. This choice also avoids proton enhancements caused by magnetospheric effects.

All instruments which detect proton intensities are subject to slight fluctuations, and not all of these can properly be said to be SEP events. The definition of intensity



(a) All fast CMEs and X class flares.



(b) Those solar events which produced SEPs at Earth.

Figure 4.1: Heliographic latitude versus heliographic longitude for all fast CMEs and X class flares (for which coordinates could be determined) which occurred between 1 May 1980 and 31 March 2013 (Figure 4.1a) and for those solar events (whether or not they were a fast CME or an X class flare, and for which coordinates could be determined) in the same period which produced SEPs at Earth (Figure 4.1b).

threshold, I_{thr} , must be high enough so as to exclude the normal fluctuations in measurements, but low enough to ensure that rises which are genuinely due to solar events are included. In this work I_{thr} is set to be a 2.5-fold increase in proton intensity over the quiet-time background level as recorded by the GOES EPS.

4.5 Associating solar events and SEP events

In order to make a determination as to whether a particular solar event had produced an SEP event, the start time of the the solar event was taken: for CMEs not associated with a flare, the time the CME was first reported in the CDAW catalogue was used; for CMEs which were associated with a flare and for all flares, the reported start time of the flare was used.

The GOES proton data $\sim 40 - 80$ MeV energy channel was then searched for an SEP event which may have commenced thereafter. In most cases the SEP enhancement, if there was one, began before another solar event was reported, in which case the association between the solar event and the SEP enhancement was made.

In some instances, however, a new solar event was reported to have begun before the SEP enhancement commenced. For these cases it was assumed that it was this new solar event which accelerated the particles unless that event was so close in time to the arrival of the SEPs (~ 20 minutes) that it was unlikely that the new event could have been the cause.

To confirm the point, the kinetic energy of a particle is given by

$$E_{\text{kin}} = \frac{1}{2}mv^2 \quad (4.1)$$

Thus, for a proton which has a mass of 1.67×10^{-27} kg, a charge of 1.60×10^{-19} C, and an energy of, say, 50 MeV:

CHAPTER 4

$$v = \sqrt{\frac{2 \times E_{\text{kin}}}{m}} \quad (4.2)$$

$$v = \sqrt{\frac{2 \times 1.60 \times 10^{-19} \text{ C} \times 50 \times 10^6 \text{ V}}{1.67 \times 10^{-27} \text{ kg}}} \quad (4.3)$$

$$v \approx 9.79 \times 10^7 \text{ m s}^{-1} \quad (4.4)$$

Taking a typical Parker spiral distance to Earth of 1.1au (Masson, S. *et al.* (2012)), at this speed the particle arrives no earlier than about 28 minutes after it left the Sun. Bearing in mind the fact that it takes ~ 8 minutes for the electromagnetic radiation carrying the information about the solar event to travel from the Sun to the Earth, 50 MeV protons which begin to arrive at Earth within 20 minutes of a report of a solar event could not have been accelerated in that event: they must have been accelerated in some earlier event.

There were some cases where the GOES EPS was still recording an enhancement of energetic protons from a previous event when the fast CME or X class flare occurred. The problem is well illustrated by events which happened at the end of October 2003 - the following is a list of the most salient events:

1. An X17.2 flare began at 09:51 on 28 October 2003
2. An X10.0 flare began at 20:37 on 29 October 2003
3. A CME of speed 2,126 km/s was first reported at 04:26 on 31 October 2003

Figure 4.2 shows a plot of ~ 40 - 80 MeV proton intensity between 28 October 2003 and 2 November 2003. It can be seen that there was an SEP event which began very shortly after the X17.2 class flare on 28 October. The SEP event can be attributed to the flare.

CHAPTER 4

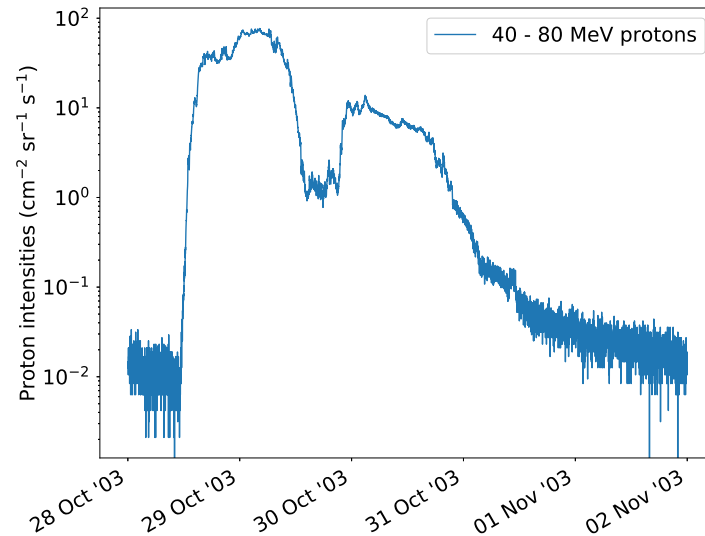


Figure 4.2: Energetic (40 - 80 MeV) proton intensity between 28 October 2003 and 1 November 2003 as measured by the GOES EPS

By the time of the X10.0 class flare on 29 October the energetic proton intensity had not returned to within within 2.5 times the background level. Nevertheless, there was a very clear additional rise in intensity which began very shortly after the start time of the flare: it can properly be said that this was a new SEP event, and that it can be attributed to the X10.0 flare.

Proton intensity was still not back to within 2.5 times the background level by the time of the fast CME on 31 October. There is no obvious rise in intensity following this CME, but it would be wrong to designate it as a false alarm as it may have been responsible for some increase in proton intensity which is simply not apparent in the plot. This event therefore must be disregarded altogether.

As well as disregarding a number of solar events because they coincided with periods when the GOES EPS was still recording an enhancement of energetic protons from a previous event, other solar events had to be disregarded because they

CHAPTER 4

happened when there were gaps in the SEP data: it therefore could not be known whether or not they had produced an SEP enhancement. However, if there had been short outages in SEP data (~ 3 hours), and there was no evidence of an SEP event either side of the outage, the solar event has been counted as a false alarm.

Some of the SEP events did not occur as a result of a fast CME or an X class flare but were produced by less energetic solar events. For each of these events, the CME and flare catalogues were searched for the last solar event (or associated events) which had occurred. Unless that event had occurred so close in time to the SEP event that it was unlikely that this event had been the driver of the SEPs (~ 20 minutes), that event was regarded as the source of the SEPs. If there had been an event within ~ 20 minutes of the start of the arrival of the SEPs, the previous solar event was regarded as the cause.

4.6 Numbers of SEP and solar events

The CDAW CME catalogue includes data since January 1996 when the LASCO coronagraphs became operational. Flare data have been available since 1976. It has therefore been possible to analyse both CMEs and flares between 1 January 1996 and 31 March 2013 (“time range 1”); for flares alone, a longer period between 1 May 1980 and 31 March 2013 (“time range 2”) has been considered.

4.6.1 SEP events

During time range 2, there had been 221 flux enhancements in the GOES >40 MeV proton channel which satisfied the definition of an SEP event. This is lower than the number of events identified by Belov *et al.* (2005) and Cane *et al.* (2010), with the difference being explained by the fact that each of those authors were investigating protons in different energy channels and using different values of I_{thr} .

CHAPTER 4

Table 4.1: The numbers of SEP events during each of the two time ranges the subject of this study. Column 1 specifies the time range, column 2 the number of SEP events in that time range, column 3 the number of those events for which coordinates could be determined (after removal of events discarded due to data gaps, detectors still recording previous events, or other reasons), and column 4 the number of events which had their origin west of E20.

Time range	Number of SEP events	Events for which coordinates could be found	SEP events from sources west of E20
1	107	86	79
2	221	171	148

Solar events were associated with all of the 221 proton events which were identified. In some cases the associated flare was of a class smaller than X and/or the associated CME was not a fast one according to our definition. Of these 221 events, the coordinates of the parent solar event could not be identified in 50 cases. The event was a western one in 86.5% (148/171) of the remaining cases.

107 of the 221 SEP events occurred during time range 1. Coordinates for 86 of these events were found, of which 91.9% (79/86) had their origin west of E20. These numbers are summarised in Table 4.1.

4.6.2 Solar events

Table 4.2 sets out the numbers of solar events which have been examined in this study. Some have had to be excluded from our analysis because of data gaps, because the SEP detector was still recording enhancements from a previous event, or because it was not possible to determine the heliographic co-ordinates of the source.

CHAPTER 4

Table 4.2: Numbers of solar events the subject of this study. Column 1 shows the time range over which data have been analysed, column 2 the type of solar event considered, column 3 the total number of solar events within the period investigated, column 4 the number of events for which coordinates were determined (after removal of events discarded due to data gaps, detectors still recording previous events, or other reasons) and column 5 the number of events which occurred west of E20.

Time range	Event type	Total number of events	Events for which coordinates were determined	Analysed events west of E20
Time range 1	Fast CMEs	143	93	52
	X class flares	140	139	79
Time range 2	X class flares	403	377	197

Of the 143 fast CMEs in time range 1 the coordinates for 93 were determined. This may be considered a high proportion: because the observation of a CME is made by examination of LASCO coronagraph images, and because these images show Thomson-scattered radiation whether the CME originated from the front side of the Sun or from behind its limb, it is to be expected that approximately half of the CMEs would be from the front-side of the Sun.

There are two possible reasons why the proportion of CMEs for which the coordinates could be determined is greater than one half. First, for 11 of the CMEs their associated flare was either reported or estimated to have occurred from behind the limb although it was still visible in the EIT or AIA images. Furthermore, when a flare occurs close to the limb of the Sun, accurate determination of its coordinates is not easy: in 7 cases the flare was said to have occurred within 5 degrees of the

CHAPTER 4

limb, and, given the uncertainties, it is entirely possible that some or all of these in fact had their origin from behind the limb.

Secondly, 15 of the fast CMEs were from 5 separate active regions each of which produced 3 fast CMEs each. It cannot be known whether this is serendipitous or whether there was similar numbers of multiple fast-CME-producing active regions from behind the limb.

Fifty of the 143 fast CMEs in time range 1 produced an SEP event, and of these, 8 were not associated with a visible flare. Having viewed EIT and AIA movies of each of these 8 events it is believed that they at least 6 originated from behind the west limb, and it was impossible to determine the location of the origin of the other 2 as a result of data gaps. It has not been possible to determine the coordinates of one of the remaining 42 events: of the others, 37 were western events and 4 were eastern events.

Of the 140 X class flares which occurred in time range 1, 45 produced SEPs. Four of the SEP-producing X class flares coincided with gaps in the LASCO data and so it could not be known whether or not they were associated with a CME: all of the remaining 41 were associated with a CME. 39 of the 45 SEP-producing X class flares were western events, and 6 were eastern events.

4.7 Algorithm evaluation scores

To evaluate the effectiveness of forecasting algorithms A.1 and A.2 introduced in Section 4.3, several evaluation scores are considered. The number of SEP events which are forecast by an algorithm to occur, and which did in fact occur (the “hits”) is named α ; the number of SEP events which are forecast to occur but which did not do so (the “false alarms”) is named β ; and the number of SEP events which occurred but which had not been forecast (the “missed events”) is called γ .

There are a number of standard verification scores for forecasting systems: in

CHAPTER 4

this work, four are used. The BIAS score is simply a measure of the ratio of the frequency of forecast events to the frequency of observed events. It is given by

$$BIAS = \frac{\alpha + \beta}{\alpha + \gamma} \quad (4.5)$$

The BIAS score does not measure how well the forecast corresponds to the observations, but it does give an indication as to whether the algorithm has a tendency to under-forecast (BIAS <1) or over-forecast (BIAS >1) events.

The probability of detection (POD) gives the fraction of forecast events which were correct. It is defined as

$$POD = \frac{\alpha}{\alpha + \gamma} \quad (4.6)$$

The “perfect” score is 1. The POD is sensitive to hits, but ignores false alarms, and so it should be used in conjunction with the false alarm ratio (FAR).

The FAR is the fraction of forecast events which were false alarms. It is defined as

$$FAR = \frac{\beta}{\alpha + \beta} \quad (4.7)$$

The “perfect” score is 0. The FAR is obviously sensitive to false alarms, but it takes no account of the missed events.

Finally, the critical success index (or threat score) shows how well the forecast “yes” events corresponded to the observed “yes” event. It is defined as

$$CSI = \frac{\alpha}{\alpha + \beta + \gamma} \quad (4.8)$$

The “perfect” score is 1. The CSI may be considered as the accuracy of the forecast.

Chapter 5

Forecasting algorithms and associated false alarms

5.1 Evaluation of the forecasting algorithms

5.1.1 Evaluation of A.1 and A.2 over time range 1

This section includes an analysis of the effectiveness of the forecasting algorithms using the evaluation scores which were introduced in Section 4.7. The algorithms are, by definition, only able to forecast SEP events which have their origin in solar events which occurred west of E20. The question therefore arises as to whether or not those SEP events which occurred from east of E20 should be counted as “missed events” for forecast validation purposes. It has been decided, because these eastern events could never have been forecast by the algorithms, that they should not be counted. In fact, the verification scores change very little by the inclusion of the eastern events, but, for the avoidance of doubt, how the BIAS, POD, and CSI scores would change if those eastern events had been included is shown in brackets after each score in the text, and also in Table 5.1.

Figure 5.1 shows the results of applying the two SEP forecasting algorithms to

CHAPTER 5

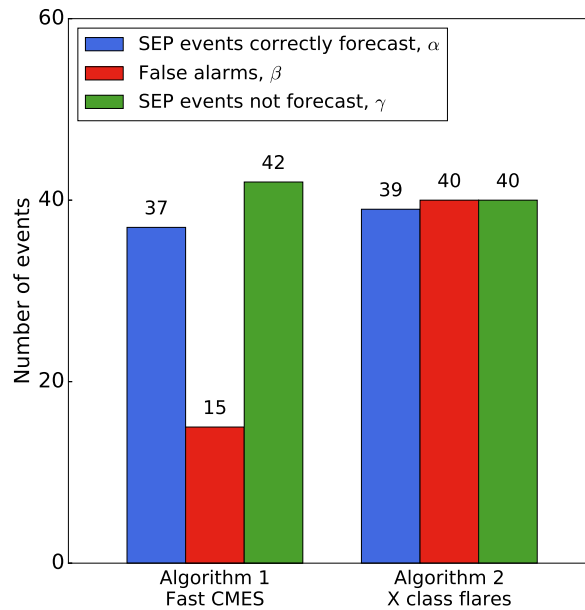


Figure 5.1: The numbers of correctly forecast SEP events, false alarms and SEP events which were not forecast for the two forecasting algorithms during time range 1.

the data set for time range 1. The number of correctly forecast SEP events is shown by the blue bar (α); the number of false alarms is represented by the red bar (β); and the number of missed events is shown by the green bar (γ).

Algorithm A.1 considers western fast CMEs. There were 52 such events during time range 1, and 71.2% (37/52) produced SEPs at Earth. Thus the FAR was 28.8% (15/52) but the algorithm failed to forecast 53.2% (42/79) of SEP events for which the parent solar event was a western one (or 57.0% (49/86) of *all* SEP events (*i.e.* including eastern events) for which coordinates could be determined).

The BIAS score for A.1 was 0.66 (0.60) suggesting that the algorithm has a tendency to under-forecast SEP events; the POD score was 0.47 (0.43), and the CSI 0.39 (0.37).

Algorithm A.2 uses western X class flares as the basis for the forecast. There

CHAPTER 5

Table 5.1: Forecast verification scores for the 2 SEP forecasting algorithms. Column 1 gives the score type, column 2 the scores for algorithm A.1 in time range 1, and column 3 the scores for algorithm A.2 in time range 1, and column 4 the scores for algorithm A.2 in time range 2. The figures in brackets are the scores if the missed eastern events were to be taken into account.

Score type	Algorithm A.1 (time range 1)	Algorithm A.2 (time range 1)	Algorithm A.2 (time range 2)
BIAS	0.66 (0.60)	1.00 (0.92)	1.33 (1.15)
POD	0.47 (0.43)	0.49 (0.45)	0.52 (0.45)
FAR	0.29	0.51	0.61
CSI	0.39 (0.37)	0.33 (0.31)	0.29 (0.26)

were 79 such flares in time range 1, and 49.4% (39/79) produced SEPs at Earth. The FAR was therefore 50.6% (40/79) and the algorithm failed to forecast 50.6% (40/79) of SEP events for which the parent solar event was a western one (or 54.7% (47/86) of *all* SEP events (*i.e.* including eastern events) for which coordinates could be determined).

The BIAS score for A.2 was 1.00 (0.92) suggesting that the algorithm forecasts almost exactly the correct number of SEP events (but, of course, not all of those forecasts were correct); the POD score was 0.49 (0.45), and the CSI 0.33 (0.31).

Table 5.1 summarises the scores for the algorithms. Appendices C and D provide the list of false alarms for algorithms A.1 and A.2 respectively in time range 1.

5.1.2 Evaluation of A.2 over time range 2

In time range 2 there were 197 western X class flares, of which 39.1% (77/197) produced SEPs at Earth. The FAR was therefore 60.9% (120/197). The algorithm failed to forecast 48.0% (71/148) of SEP events for which the parent solar event was a western one (or 55.0% (94/171) of *all* SEP events (*i.e.* including eastern events) for which coordinates could be determined).

The BIAS score for A.2 over time range 2 was 1.33 (1.15) suggesting that for this time range the algorithm tended to forecast more SEP events than actually occurred; the POD score was 0.52 (0.45), and the CSI 0.29 (0.26).

The list of false alarms according to algorithm A.2 over time range 2 is set out in Appendix E.

5.2 Parameters of A.1 events (time range 1)

Algorithm A.1 bases its forecasts upon the observation of a western fast CME. It is analysed over time range 1, which is the period between 1 January 1996 and 31 March 2013. Of the 50 SEP-producing fast CMEs in this period, 42 were from the front-side of the Sun and all of these were associated with a flare. 37 were western events.

Factors relating to the acceleration of particles are considered in Sections 5.2.1 and 3.1.3. Those factors which relate to how the particles may propagate through the interplanetary medium are analysed in Section 5.2.3.

5.2.1 CME speed and associated flare class

In Figure 5.2 the peak SXR intensity of the fast CME's associated flare is plotted against its speed for those solar events which produced SEPs at Earth (top left, blue circles); for those events in the same period which were false alarms according

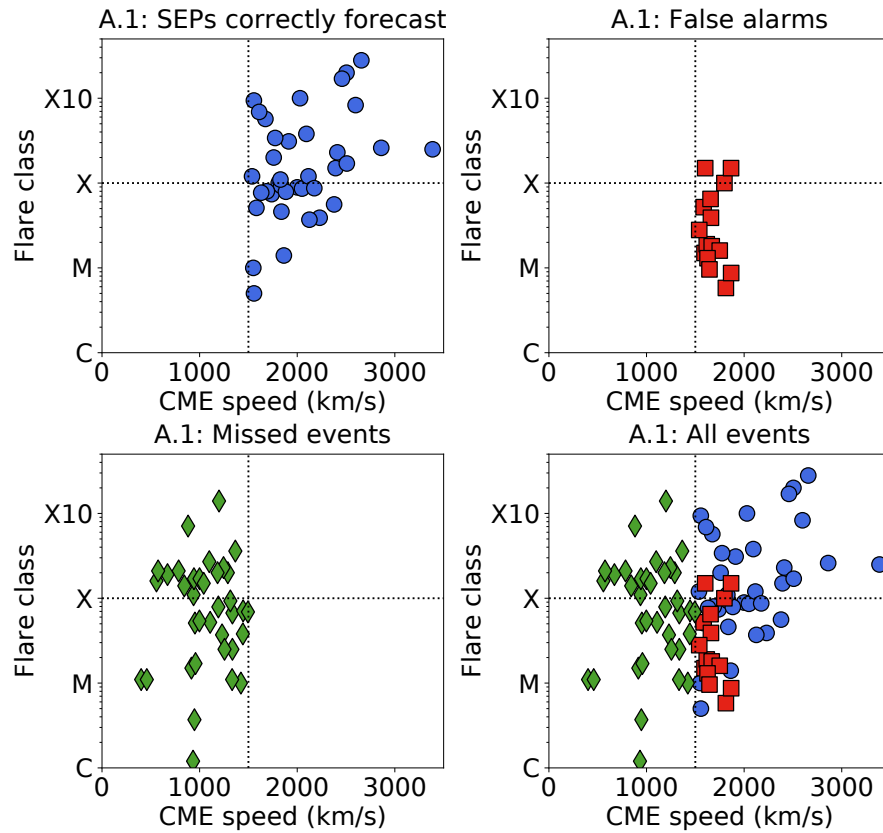


Figure 5.2: Flare class versus associated CME speed for those fast CMEs which were correctly forecast by algorithm A.1 to produce SEPs in time range 1 (top left, blue circles); for A.1 false alarms (top right, red squares); for A.1 missed events (bottom left, green diamonds); and for all events together (bottom right).

to algorithm A.1 (top right, red squares); for SEP events missed by algorithm A.1 (bottom left, green diamonds); and for all events together (bottom right).

Many of the fast CME false alarms occur close to the threshold speed, v_{thr} , and so increasing the threshold would reduce the number of false alarms, although it would also increase the number of missed events. A significant fraction of SEP events were associated with CMEs of reported speed much slower than 1500 km/s: *i.e.* even though the algorithm produces a low number of false alarms, it misses a

CHAPTER 5

significant number of SEP events. It is also clear that many of the false alarms have a flare intensity $<M3$.

It is to be noted that all CMEs faster than 1,867 km/s produced SEPs, although all of these events were associated with a flare of class at least M3.7.

5.2.2 CME width

The parameter $\Delta\delta$ is defined as the difference in latitude between the latitude of the flare and the latitude of the Earth's footpoint. Use of the Earth's footpoint in this definition takes into account the tilt of the Sun's axis of rotation with respect to the Earth's orbit.

In Figure 5.3 $\Delta\delta$ is plotted against the longitude of the 37 western fast CMEs which produced an SEP event in time range 1. In this plot the size of the marker reflects the peak SXR intensity of the associated flare: in the top plot, for example, the point at S20W95 was an M1.8 flare whereas the point at S21E08 was an X17.2 flare. The colour of the marker is representative of the width of the CME. The bottom plot gives the same information, but for the false alarms according to algorithm A.1.

It is clear that CME width is an important parameter for SEP production. Of the 37 SEP-producing CMEs, 86.5% (32/37) were reported to be haloes by the CDAW catalogue. By contrast, for the algorithm A.1 false alarms, only 46.7% (7/15) were haloes.

5.2.3 Magnetic connection between the CME and the Earth's footpoint

The last two sections dealt with factors relevant to the question of how SEPs may be accelerated. In this section it is the efficiency with which they may travel to Earth which is considered. In the following analysis the coordinates of the fast CME's

CHAPTER 5

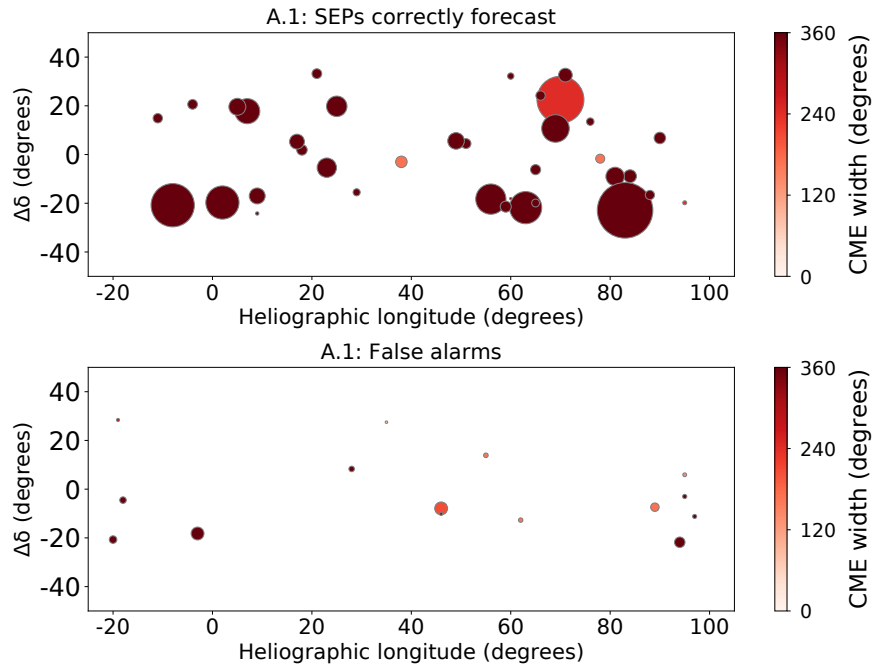


Figure 5.3: $\Delta\delta$ versus heliographic longitude for those western fast CMEs which produced SEPs at Earth in time range 1 (top plot) and for those which were false alarms (bottom plot). The size of the marker represents peak SXR intensity of the flare: for example, the point at S20W95 in the top plot was an M1.8 flare, whereas the point at S21E08 in the same plot was an X17.2 flare. The colour of the marker represents CME width.

associated flare are taken as a proxy for the location of the acceleration site.

Gopalswamy *et al.* (2014) studied major solar eruptions during the first 62 months of solar cycle 24 and suggested that, among other things, the separation in latitude between the flare and the footpoint to Earth may be an important factor in determining whether high-energy particle events are detected.

In Figure 5.4, histograms of the distribution for $\Delta\delta$ are shown for algorithm A.1. The events correctly forecast to produce SEPs are presented in the left histogram (shown in blue), and the false alarms in the right (shown in red). There is no

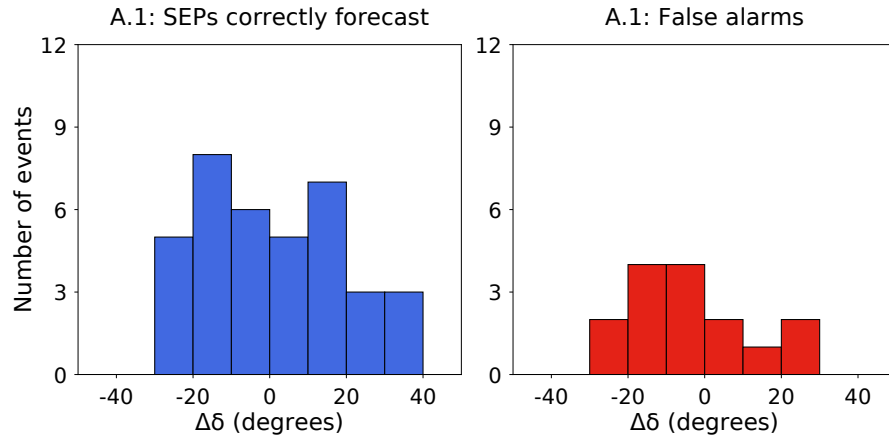


Figure 5.4: Histograms of the distribution of $\Delta\delta$ in 10° bins for algorithm A.1. The left histogram (in blue) shows the distribution for the fast CMEs which were correctly forecast to produce SEPs at Earth, and the left histogram (in red) the distribution of the false alarms.

significant difference in the shape of the distributions of SEP-producing events and the false alarms.

Figure 5.5 shows histograms of the heliographic longitude of solar events in time range 1 correctly forecast by algorithm A.1 to produce an SEP event (top left), of algorithm A.1 false alarms (top right), of SEP events missed by algorithm A.1 (bottom left), and of all SEP events (bottom right). There is a peak of SEP-producing fast CMEs between W50 and W90, and also a smaller peak between 0 and W30. The false alarms for algorithm A.1 are relatively evenly distributed, as are the SEP events not forecast by A.1.

5.3 Parameters of A.2 events (time range 1)

Algorithm A.2 bases its forecasts upon the observation of a western X class flare. Again it is analysed for time range 1. Of the 45 X class flares which produced SEPs during this period, all (barring 4 for which no data were available) were associated

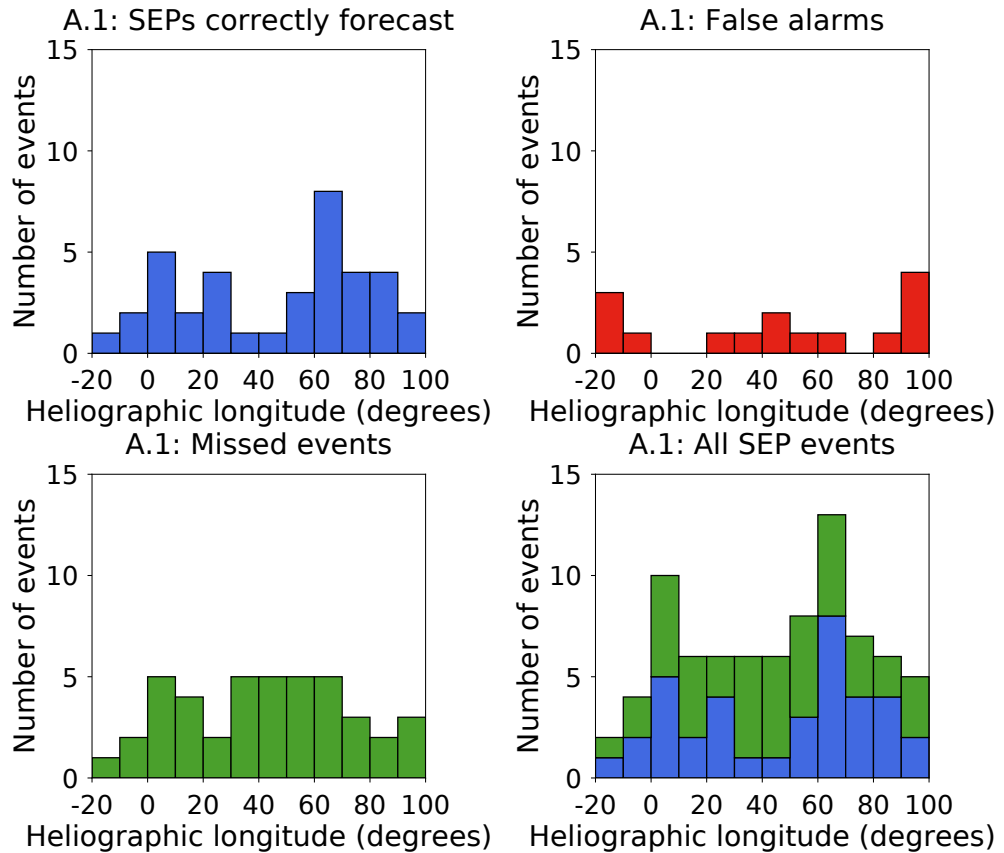


Figure 5.5: Histograms of the heliographic longitude of solar events in time range 1 of algorithm A.1 SEP events (top left); of algorithm A.1 false alarms (top right); of SEP events missed by algorithm A.1 (bottom left); and of all SEP events (bottom right)

with a CME. Thirty-nine were western events.

Sections 5.3.1, 5.3.2, and 5.3.3 consider factors relating to the acceleration of particles. Those factors which relate to how the particles may propagate through the interplanetary medium are analysed in Section 5.3.4.

5.3.1 Flare class and associated CME speed

In Figure 5.6 the peak SXR intensity of the flare is plotted against the speed of its associated CME in the same format as in Figure 5.2. There is some symmetry with

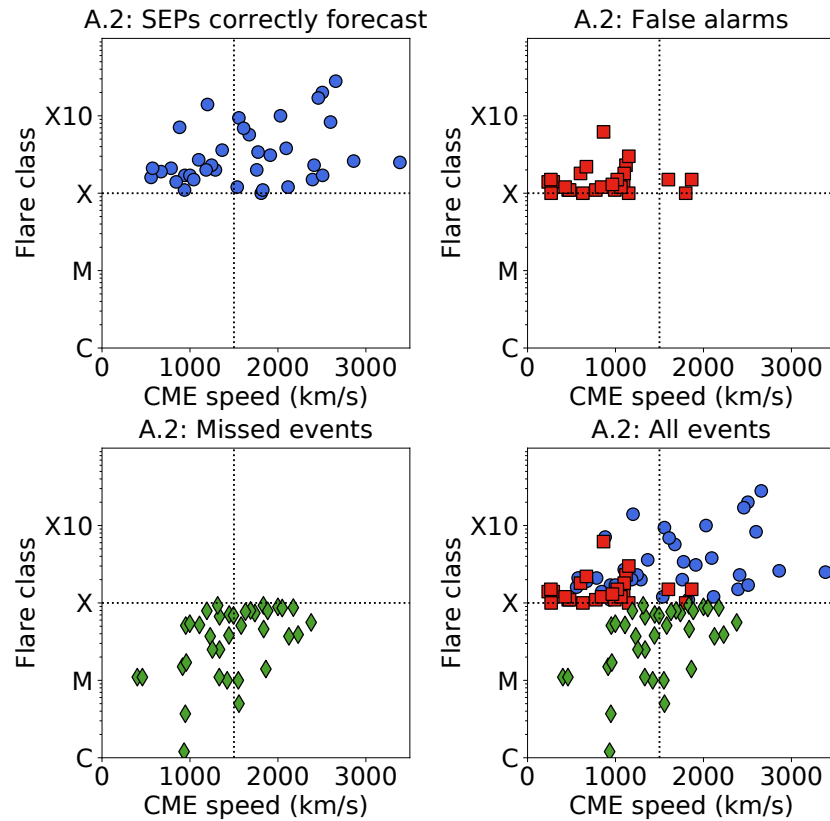


Figure 5.6: Flare class versus associated CME speed for those X class flares which were correctly forecast by algorithm A.2 to produce SEPs in time range 1 (top left, blue circles); for A.2 false alarms (top right, red squares); for A.2 missed events (bottom left, green diamonds); and for all events together (bottom right).

Figure 5.2 in that many of the false alarms fall close to the chosen threshold, and a significant number of SEP events were missed. Many of these missed events also occurred close to the chosen threshold.

It should be noted that not all of the false alarms above the A.2 threshold have an associated CME. Of the 122 X class flares which occurred in time range 1 (and which did not coincide with a LASCO data gap), 14.8% (18/122) had no associated CME. However the percentage of A.2 false alarms which did not have an associated CME is 26.5% (9/34) (6 of the X class flare false alarms occurred at times which

CHAPTER 5

coincided with LASCO data gaps, and so it cannot be known if those flares were associated with a CME). By contrast, all of the SEP-producing X class flares had an associated CME.

Seven of the false alarms were flares which were associated with a CME with a speed less than 500 km/s, whereas all of the SEP-producing X class flares were associated with a CME with a speed greater than 500 km/s. It may also be noted that 33 of the X class flare false alarms were of class <X2; 5 were between class X2 and <X3; 1 was of class X3.0 and the last of class X6.2. These last two events are analysed further in Section 6.2.

5.3.2 Flare duration

Figure 5.7 shows histograms of the duration of the X class flares which produced SEPs (left, in blue) and those which were false alarms (right, in red). Shorter X class flares were more likely to be false alarms than produce SEPs. Average flare duration for the SEP-producing X class flares was 46.3 minutes, and 25.6% were longer than 60 minutes (“long duration flares”). For the false alarms, average flare duration was 24.9 minutes, and only 5.0% (2/40) were long duration flares.

5.3.3 Associated CME width

Figure 5.8 is a plot of $\Delta\delta$ versus heliographic longitude for algorithm A.2 events: the correctly forecast SEP events are shown in the top plot, and the false alarms in the bottom plot. For this plot, the size of the marker represents the relative duration of the flare: for example, in the top plot the flare marked at S18W33 had a duration of ten minutes, whereas the flare at S03W38 lasted 120 minutes. The colour of the marker is representative of the width of the flare’s associated CME.

Of the 39 western X class flares which produced SEPS at Earth, 37 were definitively associated with a CME (the other 2 occurring during times when LASCO did

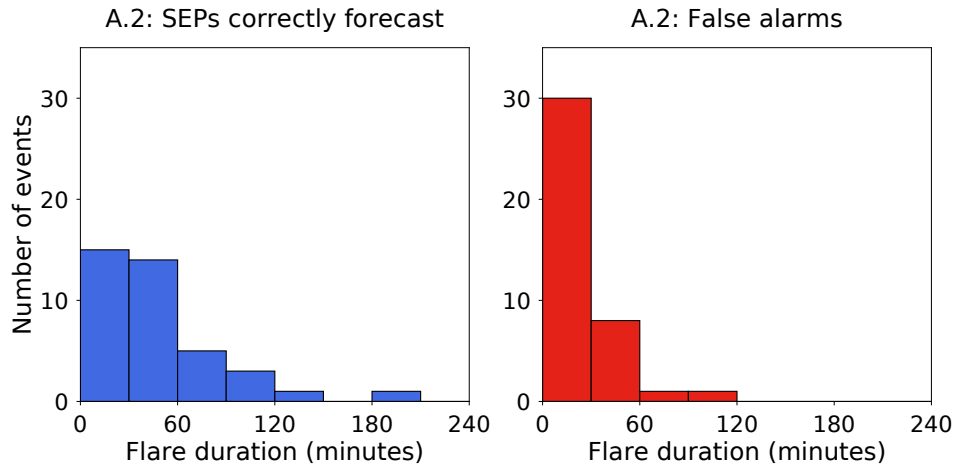


Figure 5.7: Histograms of flare duration in minutes for X class flares. Those which produced SEPs are shown in the left plot in blue, and the false alarms in the right plot in red. Bin size is 30 minutes.

not produce any data). Of those 37, 86.5% (32/37) were halo CMEs. In contrast, for the false alarms associations with CMEs were apparent in 25 cases: of these 25, only 44.0% (11/25) were haloes.

It is interesting to note the longitudinal distribution of the halo CME false alarms apparent in Figure 5.8. For the SEP-producing X class flares, the 5 non-halo associated CMEs were evenly spread between about 0° and 90° , whereas for the false alarms almost all those events which occurred between -20° and 40° were seen as haloes, and almost all those between 40° and 90° were seen as non-haloes.

5.3.4 Magnetic connection between the flare and the Earth's footpoint

Figure 5.9 shows histograms of the distribution of $\Delta\delta$ in 10° bins for A.2 hits (blue bars, left) and A.2 false alarms (red bars, right). For the fast CMEs there did not appear to be any distinction to be made in the distributions for SEP-producing events and the false alarms (see Figure 5.4); in the case of algorithm A.2, however,

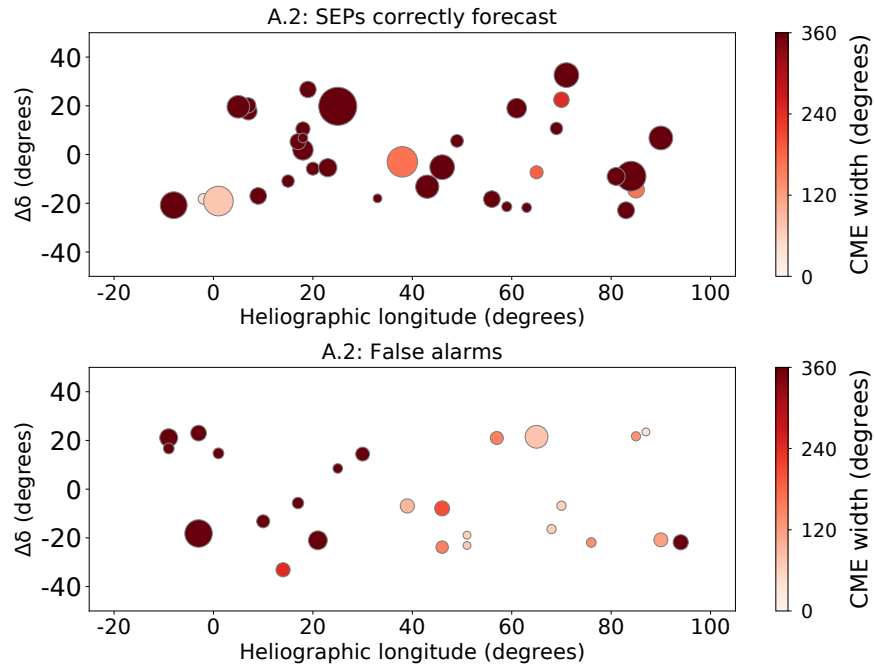


Figure 5.8: $\Delta\delta$ versus heliographic longitude for those X class flares which were correctly forecast by algorithm A.2 to produce SEPs in time range 1 (top plot) and for those which were false alarms (bottom plot). The size of the marker represents the relative duration of the flare: for example, the flare marked at S18W33 in the top plot had a duration of ten minutes, whereas the flare at S03W38 in the same plot lasted 120 minutes. The colour of the marker represents CME width.

there does appear to be difference. The distribution for the false alarms shows two separate peaks at between -30° and -10° , and between $+10^\circ$ and $+30^\circ$.

Figure 5.10 shows histograms of the heliographic longitude of solar events in time range 1 for algorithm A.2 in the same format as Figure 5.5. There appears to be no significant difference in the longitudinal distribution of western X class flares which produced an SEP event and those which were false alarms, but in this case there is a clear peak between 20° and 80° in the SEP events missed by algorithm A.2.

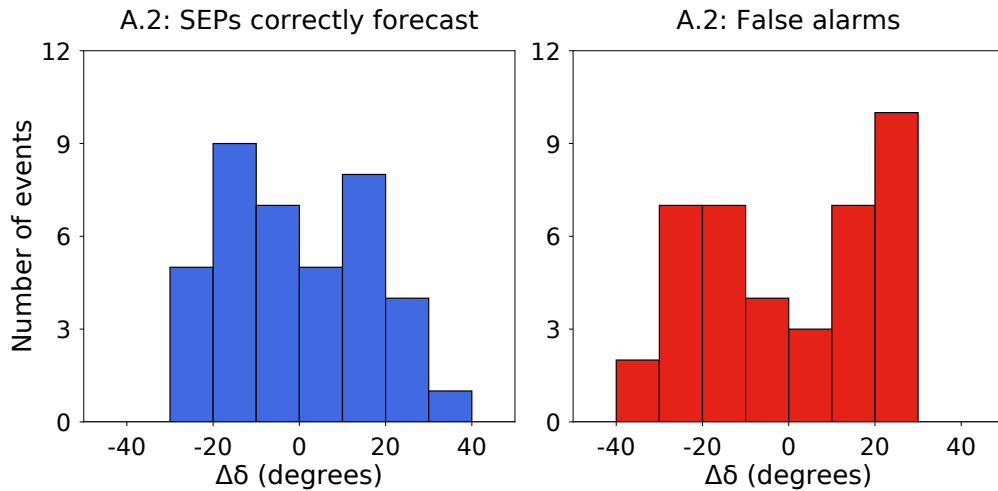


Figure 5.9: Histograms of the distribution in 10° bins of $\Delta\delta$ for A.2 SEP-producing events (left plot, in blue) and for A.2 false alarms (right plot, in red).

5.4 Parameters of A.2 events (time range 2)

Because there are data from the GOES satellites going back to the mid-1970s, it has been possible to examine X class flares over the longer time range 2. For the purposes of this analysis solar cycle 21 was taken to end on 31 December 1986; solar cycle 22 was taken to last from 1 January 1987 until 31 December 1995; solar cycle 23 was taken to last from 1 January 1996 until 31 December 2009; and solar cycle 24 has been taken to be from 1 January 2010 onwards.

Factors relating to the acceleration of particles are considered in Section 5.4.1 and 5.4.2. Those factors which relate to how the particles propagate through the interplanetary medium are analysed in Section 5.4.3.

5.4.1 Flare class

Figure 5.11 is a plot of flare class versus time for algorithm A.2 over time range 2. As before, blue dots represent those X class flares which were correctly forecast to

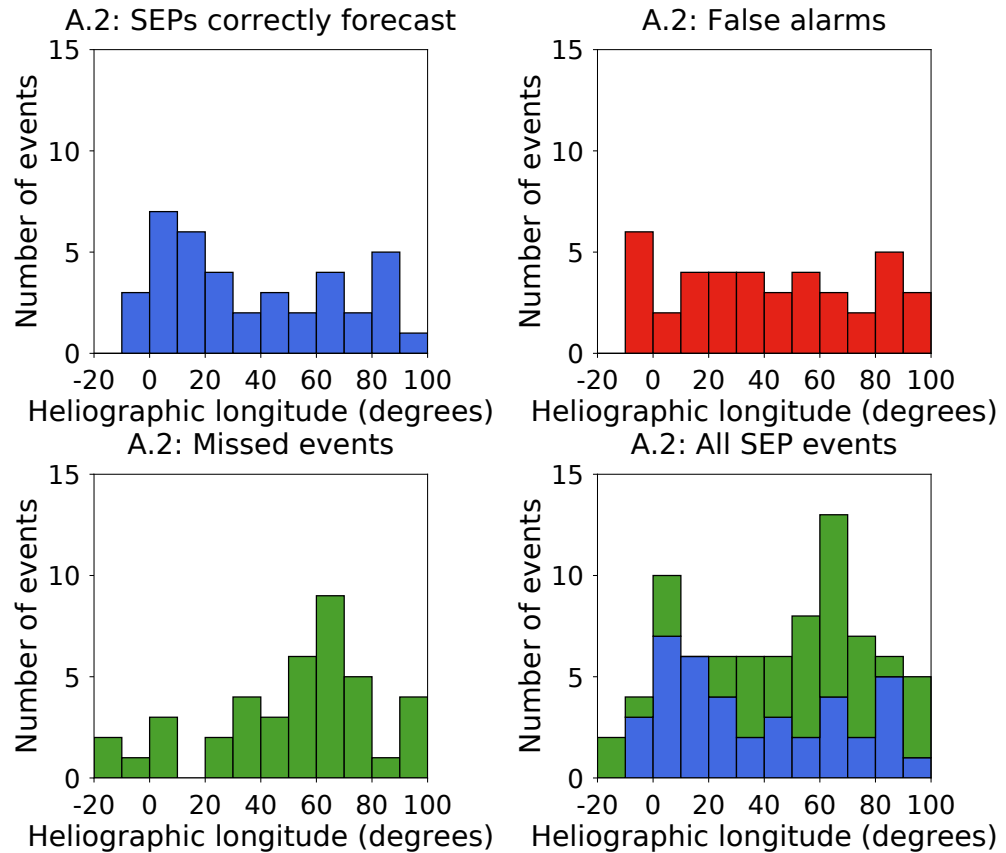


Figure 5.10: Histograms of the heliographic longitude of solar events in time range 1 of algorithm A.2 SEP events (top left); of algorithm A.2 false alarms (top right); of SEP events missed by algorithm A.2 (bottom left); and of all SEP events (bottom right).

produce SEPs, red squares the false alarms, and green diamonds the SEP events missed by the algorithm. The horizontal dashed line is the X class threshold; the vertical dashed lines are the boundaries between the different solar cycles.

There are two points to be made. First, for solar cycles 23 and 24 (which have already been considered as time range 1), the number of SEP-producing events correctly forecast by A.2 and the number of false alarms it produced were almost equal (39 and 40 respectively). That cannot be said for cycles 21 and 22.

In solar cycle 21 there were 43 western X class flares remaining to be considered

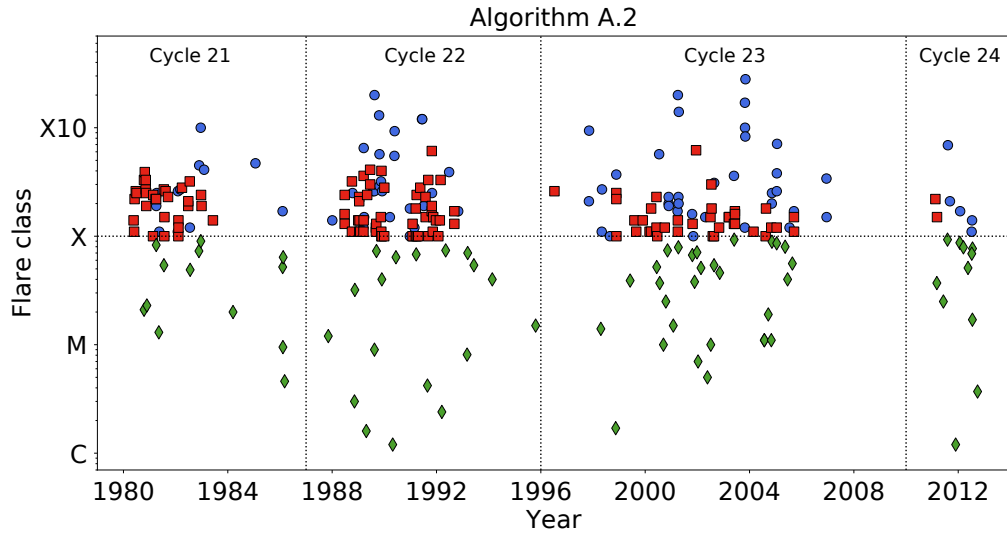


Figure 5.11: A plot of flare class versus time for algorithm A.2 over time range 2. Blue dots represent the X class flares which were correctly forecast to produce SEPs; red squares are the false alarms; green diamonds show the SEP events missed by the algorithm. The horizontal dashed line is the X class threshold; the vertical dashed lines are the boundaries between the different solar cycles.

after the removal of those events which coincided with data gaps or because the SEP detector was still recording an enhancement from a previous event. Of these, 13 produced SEPs and 30 were false alarms. In cycle 22 there were 75 western X class flares remaining after removal of events for similar reasons. Of these 75, 25 produced SEPs and 50 were false alarms.

The second point arising from Figure 5.11 is that for cycles 21 and 22 flares of class $>X2$ were more likely to be false alarms. Table 5.2 shows the numbers: column 1 contains the class of the flare to which the numbers refer, and columns 2 to 5 the numbers of each type of event for solar cycles 21 to 24 inclusive.

For cycle 21, 60% (18/30) of the false alarms were from flares with a class greater or equal to class X2.0: in cycle 23 that percentage was just 15.8% (6/38). In cycle

CHAPTER 5

Table 5.2: Numbers of western X class flares which were false alarms during solar cycles 21 to 24. Column 1 contains the class of the flare to which the numbers refer, and columns 2 to 5 the numbers of each type of event which were false alarms for solar cycles 21 to 24 inclusive.

Flare class	Cycle 21	Cycle 22	Cycle 23	Cycle 24
<X2	12	34	32	2
\geq X2, <X3	14	8	4	0
\geq X3	4	8	2	0

22, 16% (8/50) of the false alarms were from flares of class X3.0 or higher; in cycle 23 that percentage was just 5.3% (2/38).

5.4.2 Flare duration

Figure 5.12 shows histograms of the duration of those X class flares in time range 2 which produced SEPs (left, in blue) and which were false alarms (right, in red). There is a contrast with Figure 5.7 in which it is shown that most (75% (30/40)) of the X class flare false alarms had a duration of less than 30 minutes. For the false alarms over this longer time range, only 37% (44/120) had a duration of less than 30 minutes; the majority (63.3% (76/120)) endured for longer (some very much longer), and the reasons why this is the case are explored in Section 5.5.5.

5.4.3 Magnetic connection between the flare and the Earth's footpoint

Figure 5.13 presents histograms of $\Delta\delta$ for western X class flares in time range 2. Correctly forecast SEP events are shown in the left hand plot in blue, and the false alarms in the right hand plot in red.

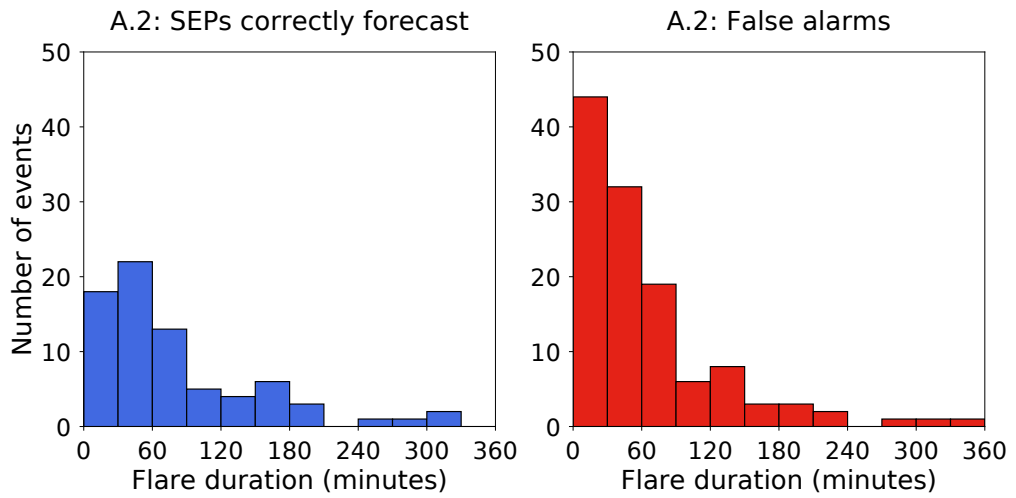


Figure 5.12: Histograms of flare duration for X class flares in time range 2 which produced SEPs (left plot, in blue) and which were false alarms (right plot, in red). Bin size is 30 minutes.

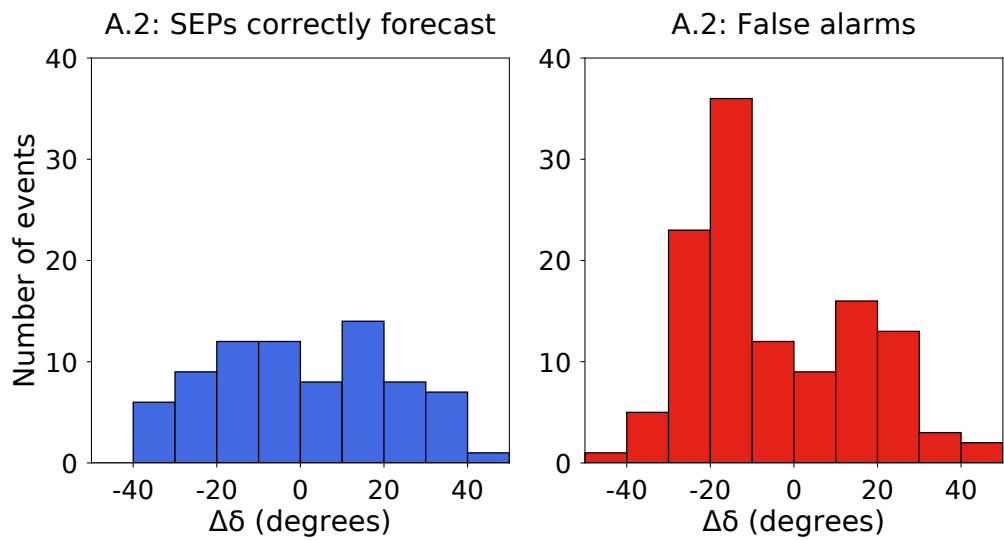


Figure 5.13: Histograms of $\Delta\delta$ for X class flares in time range 2 which were correctly forecast by algorithm A.2 to produce SEPs (left plot, in blue); A.2 false alarms (right plot, in red). Bin size is 10 degrees.

CHAPTER 5

For the SEP-producing events there does not appear to be any dependence upon the value of $\Delta\delta$, but in the case of the false alarms there are the two peaks which can also be seen in Figure 5.9. There is a very large over-abundance of false alarms with negative values of $\Delta\delta$, and the reasons for this are also discussed in Section 5.5.5.

Figure 5.14 shows histograms for the longitudinal distribution of the algorithm’s correctly forecast SEP events (top left, in blue), false alarms (top right, in red), missed events (bottom left, in green), and all SEP events together (bottom right, in blue and green). Again, there seems to be no longitudinal dependence for the false alarms in this time range.

There is a similarity with Figure 5.10 in that there is a peak in the missed events histogram around W70. It may be argued that there is a peak around W30 in the “hits” histogram, and that consequently there are two peaks in the histogram which shows all the SEP events, but if that be so, the peaks are not at all distinct.

Figure 5.15 is a plot of $\Delta\delta$ versus time for SEP-producing western X class flares (blue dots) and A.2 false alarms (red squares) in time range 2. In this plot, the size of the marker is proportional to flare duration (ranging from 8 minutes to 8 hours 48 minutes). The dashed horizontal line is at 0° ; the vertical dashed lines represent the boundaries between different solar cycles.

In cycles 21 and 22 the average duration for western X class flares which produced SEPs was ~ 136 minutes, and for false alarms was ~ 85 minutes; for cycles 23 and 24 the averages were ~ 47 minutes and ~ 24 minutes respectively.

5.5 Discussion

5.5.1 Evaluation

Four different forecasting evaluation scores have been considered. Over time range 1 algorithm A.1 (based upon the observation of a western fast CME) performs better

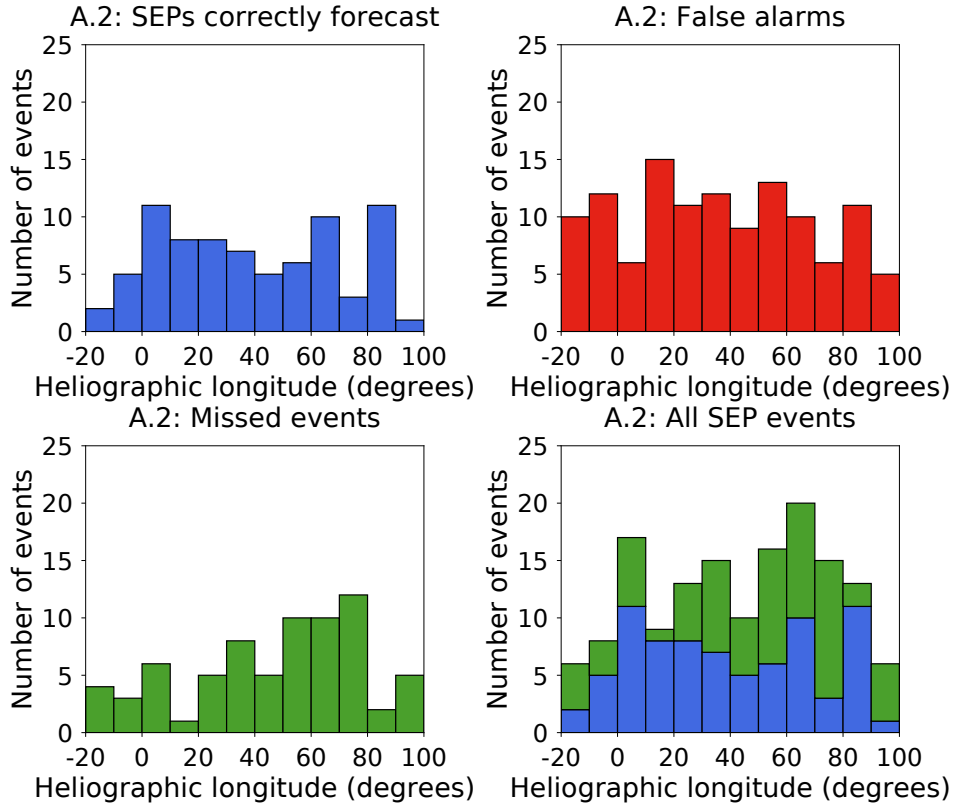


Figure 5.14: Histograms of heliographic longitude for X class flares in time range 2 which produced SEPs (left plot, in blue) and which were false alarms (right plot, in red). Bin size is 10 degrees.

than algorithm A.2 (based upon the observation of a western X class flare).

The BIAS score for algorithm A.1 (0.60) indicates that it under-estimates the number of SEP events - indeed it forecasts just 52 events whereas in fact there were 79 SEP events from western origins. Algorithm A.2 has a BIAS score of exactly 1: it forecast that there would be 79 SEP events, and there were exactly that number. However this illustrates how reliance on the BIAS score may be misleading, as it does not contain any information as to how many of the forecasts turned out to be correct.

The two algorithms correctly forecast almost the same number of SEP events (37 and 39 respectively) and hence have very similar POD scores. However, A.1 has

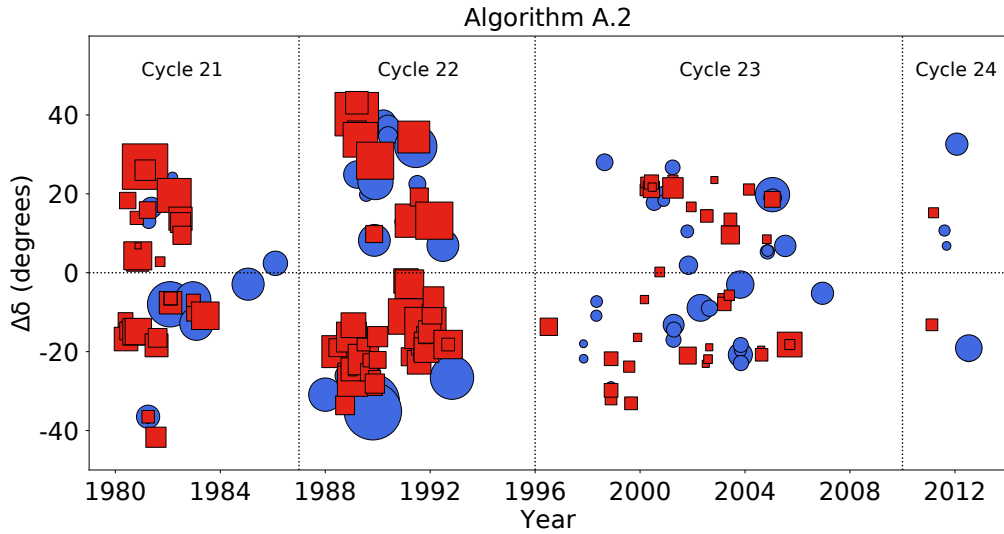


Figure 5.15: Plot of $\Delta\delta$ versus time for the algorithm A.2 over time range 2. Blue dots represent the SEP events correctly forecast by the algorithm, and red squares the false alarms. The size of the marker is proportional to the duration of the flare: the range is from 8 minutes to 8 hours 48 minutes. The dashed horizontal line is at 0° ; the vertical dashed lines represent the boundaries between different solar cycles.

a much lower FAR (0.29 (15/52)) as opposed to 0.51 (40/79) for A.2), and this is reflected in the CSI, which suggests that A.1 performs better than A.2.

In time range 2, the FAR for A.2 is somewhat higher than that obtained over time range 1, and the reasons for this are considered in Section 5.5.5. Its POD score is very similar to (albeit slightly higher than) that for time range 1, but because of the increased number of false alarms the CSI, at 0.29, is lower than for time range 1.

5.5.2 Algorithms A.1 and A.2 together

Considering both algorithms together, the important points are:

- Of the 50 SEP-producing fast CMEs, 42 were from the front-side of the Sun and all of these were associated with a flare.

CHAPTER 5

- Of the 45 X class flares which produced SEPs, all (barring 4 for which no data were available) were associated with a CME.

These results suggest strongly that for a solar event to produce protons with an energy of at least 40 MeV it needs to consist of both a flare and a CME.

Of course, such a result does not shed light on what the acceleration processes might have been. It is, for example, possible that in all of these events it was a CME-driven shock which accelerated the particles, and that the flare was simply a by-product of the restructuring of the magnetic field. Similarly, it may be argued that the acceleration had occurred in the flare, and the occurrence of the CME was incidental.

Neither of those proposals seem attractive. If it really were the case that only a CME or only a flare had accelerated the particles it must surely be expected that at least one SEP-producing event which consisted of only one type of solar event might have been found. The fact that there have been none is, it is submitted, indicative of the fact that both types of event contribute to the acceleration and escape of the particles. It was pointed out in Section 2.3 that conditions in the solar corona are so complex that to expect one solution which covers all eventualities is unrealistic: it seems likely that in each event a combination of acceleration processes is at work.

5.5.3 Algorithm A.1

The following main conclusions can be drawn from a comparison of the parameters relating SEP-producing western fast CMEs with those which were false alarms:

- Many SEP events were produced by CMEs of a speed slower than v_{thr} - in other words, the algorithm misses a significant number of SEP events. Reducing the threshold speed to produce an algorithm which catches these events will not, however, improve the algorithm's overall performance: whilst the number of

CHAPTER 5

missed events will certainly fall, the number of false alarms will increase. On the other hand, increasing v_{thr} results in a reduction in the number of false alarms, but increases the number of missed SEP events.

- Nine of the 12 fast CMEs which were associated with a flare of class <M3 were false alarms.
- CME width is an important parameter when considering the likelihood of whether SEPs will be produced or not. The vast majority of SEP-producing fast CMEs were seen as haloes, whereas fewer than 50% of the false alarms were haloes. This result is consistent with the findings of Park *et al.* (2012) who reported that solar events which had the highest probability of producing 10 MeV protons were full halo CMEs with a speed exceeding 1,500 km/s.

5.5.4 Algorithm A.2 in time range 1

The following main conclusions can be drawn from a comparison of the parameters relating SEP-producing western X class flares with those which were false alarms:

- Many of the missed SEP events were produced by flares very close to the X class threshold - in other words, the algorithm misses a significant number of SEP events. However a reduction of the threshold to, say, M9 or M8, will increase the false alarm ratio.
- X class flares which were not associated with a CME, or which were associated with a CME of speed <500 km/s were all false alarms.
- Only 2 of the flares which were of class X3 or greater failed to produce SEPs. The reasons why these intense flares were false alarms are examined in Section 6.2.

CHAPTER 5

- The duration of the X class flare appears to be a parameter relevant to SEP production. It has, however, previously been shown that there is an association between long duration flares and CMEs (Yashiro *et al.* (2006)), and therefore it may be said that the trend with duration may be connected with the fact that large flares without CMEs are more likely to be false alarms. The longer the flare, the more likely it is to have associated with it a CME.

It has already been seen that X class flares without a CME did not produce SEPs, and so if a flare is short (and thus being less likely to be associated with a CME) the less likely it is to produce SEPs. However, if only the 25 X class flare false alarms which were associated with a CME are considered, 20 had a duration of less than 30 minutes, 3 had a duration of between 30 minutes and 1 hour, and only 2 lasted for more than 1 hour. This seems to counter the argument that the dependence of SEP production upon flare duration is simply a consequence of the flare's association with a CME.

- The width of the flare's associated CME is clearly also relevant. An X class flare associated with a CME which is not a halo is much more likely to be a false alarm.
- There is, however, possibly a peak in the histogram for correctly forecast SEP events around W15, and certainly a peak around W70 in the histogram for the missed events.

This suggests that the higher class flares are more likely to produce SEPs between E20 and W30, and that it is lower class flares which are more likely to produce SEPs from between W50 and W90. This result may be connected to the distribution of the associated non-halo CMEs for the false alarms which tended to occur between W40 and W90.

5.5.5 Algorithm A.2 in time range 2

Time range 2 covers most of solar cycle 21, all of cycles 22 and 23, and half of cycle 24. From the point of view of SEP production solar cycles 21 and 22 differ significantly from cycles 23 and 24 in five respects.

- For cycle 23 there were 38 western X class flare false alarms and 34 SEP-producing western X class flares; for cycle 24 the numbers (up to the end of March 2013) were 2 and 5 respectively. On the other hand, in cycles 21 and 22 there were twice as many false alarms as western SEP-producing events.
- In cycles 23 and 24 a well magnetically-connected flare of class X2 or greater was highly likely to produce SEPs, but in cycles 21 and 22 there was a much greater chance that such flares would be false alarms.
- Figure 5.12 shows that there is a difference in the duration of X class flares for events pre 1996 compared to events post 1996. In cycles 21 and 22 the average duration of a western X class flare which failed to produce SEPs was ~ 85 minutes, but in cycles 23 and 24 the average duration for false alarms was ~ 24 minutes. A similar difference can be seen in the duration of SEP-producing X class flares. The results relating to flare duration presented in Section 5.3.2 suggest that X class flares of short duration (≤ 30 minutes) in time range 1 had a high likelihood of being a false alarm; the duration of the false alarm flares in the longer time range is greater (see Figure 5.12).
- In Figure 5.13 there is seen a very large peak of false alarms with values of $\Delta\delta$ around -20° . In solar cycles 21, 23 and 24 there were almost equal numbers of false alarms from each hemisphere. However, in cycle 22 there were 50 false alarms, 40 of which occurred in the southern hemisphere.

The GOES flare dataset is derived from observations from different satellites, and

CHAPTER 5

it is possible that there may be instrumental reasons for these trends. Alternatively it is possible that the effect may be due to real physical differences in solar activity.

There is certainly some question as to how well the data from the pre-GOES 8 satellites match those from GOES 8 and later. The information file for the GOES X-ray Sensor Measurements¹ begins with the warning that “*for GOES 8-15, the archived fluxes have had SWPC scaling factors applied*”, although the document goes on to say that “*no adjustments are needed to use the GOES 8-15 fluxes to get the traditional C, M, and X alert levels*”.

Correspondence has been entered into with Dr Janet Machol at NCEI (who is the author of that document), and she has given the assurance that an X class flare which was reported pre-1996 has the same peak SXR flux as an X class flare reported post 1996. It seems, therefore, that instrument change is not a contributory cause of the differences.

Dr Machol is not aware, either, of any change in the way in which flare duration has been calculated, and the website which sets out how that calculation is done² does not give any indication that the definition is different now from previous times. It seems as though this possibility, too, may be discounted.

At present, therefore, the causes of the observed patterns remain unclear.

All of the aforementioned analysis and results are included in Swalwell *et al.* (2017a). This paper is included as Appendix F.

5.6 An improved SEP forecasting algorithm

It is possible to define a third SEP forecasting algorithm based upon the main results:

A.3 A front-side CME with a reported speed of 1,500 km/s or faster and which is

¹https://www.ngdc.noaa.gov/stp/satellite/goes/doc/GOES_XRS_readme.pdf

²<https://www.ngdc.noaa.gov/stp/solar/solarflares.html>

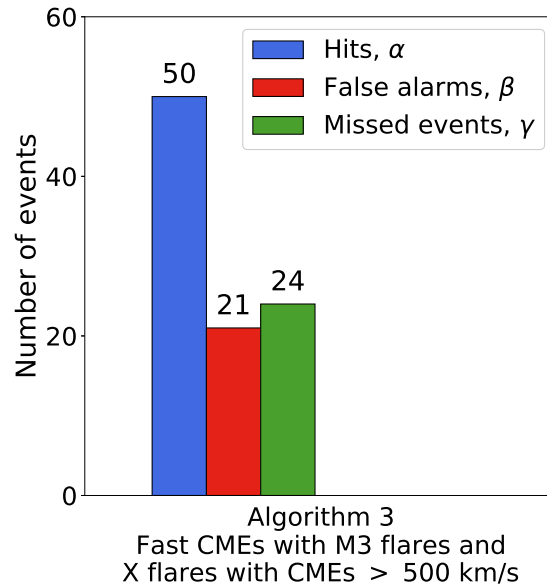


Figure 5.16: The numbers of correctly forecast SEP events, false alarms and SEP events which were not forecast for algorithm A.3 during time range 1.

associated with a flare of class M3 or greater . . . , **or**

An X class flare which is associated with a CME of speed >500 km/s . . .

. . . which occurs west of E20 on the solar disc will result in an SEP event being detected at Earth.

There were 71 such events in time range 1 and 70.4% (50/71) produced SEPs at Earth. Thus the false alarm rate was 29.6% (21/71). Five of the SEP events in this time range occurred during a period when there were no data from the LASCO coronagraph, and so have been disregarded for the purposes of evaluating this algorithm. Thus the algorithm missed 32.4% (24/74) of SEP events. Figure 5.16 (which is in the same format as Figure 5.1) illustrates these results.

For the purposes of the verification scores, only those SEP events which could possibly have been forecast by this algorithm have been counted (*i.e.* 74 events), but for comparison purposes the scores which would have resulted had all SEP events

CHAPTER 5

Table 5.3: A summary of the evaluation scores for algorithm A.3 in the same format as Table 5.1.

Score type	Algorithm A.3 (time range 1)
BIAS	0.96 (0.83)
POD	0.68 (0.58)
FAR	0.30
CSI	0.53 (0.47)

been counted (*i.e.* 86 events) are shown in brackets.

The algorithm had a BIAS score of 0.96 (0.83), showing a slight tendency to under-forecast events; the POD was 0.68 (0.58); the FAR was 0.30; and the CSI was 0.53 (0.47). All of these results are summarised in Table 5.3 (which is in the same format as Table 5.1).

Thus the algorithm correctly forecasts a much higher number of SEP events than either algorithm based upon the observation of simply one type of solar event, has a FAR very similar to A.1, but it misses far fewer SEP events than either A.1 or A.2.

Chapter 6

Case studies

A number of the false alarms follow very large solar events, and it is a worthwhile exercise to consider each of these with a view to reaching a better understanding of why they failed to produce SEPs at Earth. In Section 6.1 the three events which were false alarms according to both algorithms A.1 and A.2 are examined, and Section 6.2 looks at the 2 false alarms which followed the flares of class X3.0 and X6.2. Finally, by way of contrast, Section 6.3 examines the solar events which led to the acceleration of particles to such high energies that their effects were detected at ground level. Four of these events were also looked at by Swalwell *et al.* (2017b), and that paper is reproduced as Appendix G.

6.1 False alarms common to both algorithms

The main details of the three solar events which were false alarms according to both forecasting algorithms are set out in Table 6.1. Column 1 shows the date of the event, column 2 the start time of the flare, column 3 its class, and column 4 its coordinates. Columns 5 and 6 give the time that the associated CME was first reported and its speed respectively.

CHAPTER 6

Table 6.1: List of false alarms common to both forecasting algorithms. Column 1 shows the date of the event, column 2 the start time of the flare, column 3 its class, and column 4 its coordinates. Columns 5, 6, and 7 give the time that the associated CME was first reported, its speed, and its width respectively.

Date	Flare data			CME data		
	Start time	Class	Coordinates	First report	Speed (km/s)	Width (degrees)
1998-11-24	02:07	X1.0	S20W94	02:30	1,798	360
2003-03-18	11:51	X1.5	S15W46	12:30	1,601	209
2005-09-13	19:19	X1.5	S11E03	20:00	1,866	360

6.1.1 Event on 24 November 1998

The first of these events was an X1.0 flare which began at 02:07 on 24 November 1998, and which was associated with a CME of speed 1,798 km/s. It had a duration of 30 minutes. The coordinates of the flare were not reported by the GOES SXR flare list, and so have been estimated following the viewing of images obtained by the SOHO EIT at 195Å. It appears to be an event which occurred from just behind the western limb, and, as not all of the flaring region is visible, it is possible that the actual intensity of the flare may have been greater than X1.0.

In fact, this X class flare was the last in a series of 4 all from the same active region. The others were: an X3.7 flare at 06:30 on 22 November which had a duration of 19 minutes; an X2.5 flare at 16:10 on 22 November (22 minutes' duration); an X2.2 flare at 06:28 on 23 November (30 minutes' duration). Unfortunately it cannot be known whether these three were associated with a CME as the LASCO coronagraphs were not operational at the time. Only the first produced an SEP event in the 40 -

CHAPTER 6

80 MeV energy channel, and even that was extremely small.

The flare at 02:07 was clearly not confined given that it was accompanied by a fast CME. Indeed, there is present only one of the factors identified in Section 5 as likely to produce a false alarm - the flare was a short one, at 30 minutes (although this is at the boundary of what might be considered “short”).

It is the case that the event occurred from just behind the limb, but in the dataset there were 8 fast CMEs from behind the limb which produced SEPs, and consequently this, too, may not provide a satisfactory explanation as to why it failed to produce SEPs.

A possible answer may lie in Figure 6.1. This is a synoptic source surface map of the type introduced in Section 2.7. In this plot, blue regions correspond to areas of positive magnetic field and red regions to areas of negative magnetic field, and they are separated by the thick black line which represents the HCS. The contours are separated by $\pm 0.5, 1.0, 2.5, 5.0, 10.0,$ and $15.0 \mu\text{T}$.

The Earth’s footpoint and central meridian were introduced in Section 2.5.1. The solar wind speed at the time of this event was 495 km/s (data taken from https://omniweb.gsfc.nasa.gov/form/omni_min.html); thus the Earth’s footpoint was $\sim 50^\circ$ to the west of the central meridian (see Equation 2.4). Its latitude, calculated using the Python “sunpy.coordinates” module (Inglis *et al.* (2017)), was $+1.7^\circ$.

In Figure 6.1 the vertical purple line shows the position of the central meridian, the green circle the Earth’s footpoint, and the yellow star the location of the flare site. It should be noted that because of the time of the event and the site of the flare, the plot was produced from data from the last half of Carrington rotation 1942 and the first half of Carrington rotation 1943.

It was said in Section 2.7 that according to models described by Battarbee *et al.* (2017a) a current sheet between the flare site and the Earth’s footpoint may inhibit particles crossing into regions of opposite polarity. For this event it does appear

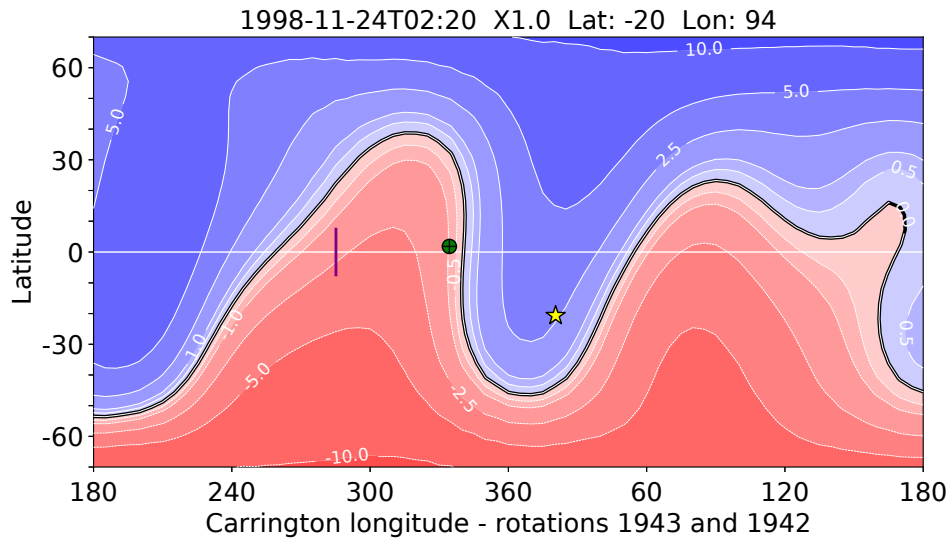


Figure 6.1: A synoptic source surface map for the 24 November 1998 event. Blue regions show areas of positive magnetic field and red regions areas of negative magnetic field. The contours are separated by ± 0.5 , 1.0, 2.5, 5.0, 10.0, and 15.0 μT . The vertical purple line is the position of the central meridian, the green circle the Earth's footpoint and the yellow star the location of the flare site.

that the flare site and Earth footpoint are indeed on opposite sides of the HCS, and this may have contributed to the fact that SEPs were not detected by the GOES EPS. There are, however, three *caveats* to be entered:

- The model described by Battarbee *et al.* (2017a) is based upon a flat current sheet. As can be seen from Figure 6.1 that is far from the case here.
- The source surface map may not truly represent the actual configuration at the solar surface, and given that the Earth's footpoint is shown to be relatively close to the HCS it may be that in fact it was on the same side of it as the flare.

CHAPTER 6

- There may be errors in the positioning of the markers: see the discussion in Section 6.4.

Nevertheless, taking all of these factors together (the short duration of the flare, the fact that the event occurred from behind the limb, and the fact that the flare and Earth's footpoint may not have been on the same side of the HCS) may explain why this event was a false alarm.

6.1.2 Event on 18 March 2003

In many ways it is quite remarkable that the event of 18 March 2003 did not produce particles. It was an X1.5 flare associated with a CME of speed 1,601 km/s, and it was extremely well magnetically-connected to Earth having occurred at W46. The event had been preceded by another X1.5 flare (which had begun at 18:50 on 17 March 2003) and which was associated with a CME of speed 1,020 km/s. That, too, was a false alarm. At the time of this event the solar wind was very high at 817 km/s, leading to the Earth's footpoint being $\sim 30^\circ$ west of the central meridian; its latitude was -7.1° .

As can be seen from the synoptic source surface map shown in Figure 6.2, the flare location and Earth's footpoint were very close, and both were on the same side of the HCS. The possible explanation for the 18 November 1998 event being a false alarm cannot apply here.

There are, however, two features present which have been identified as being likely to produce a false alarm: the CME was not a halo, and the flare was relatively short at 29 minutes. It may be the case that these two factors together were sufficient to result in the acceleration of so few particles as not to register in the GOES EPS.

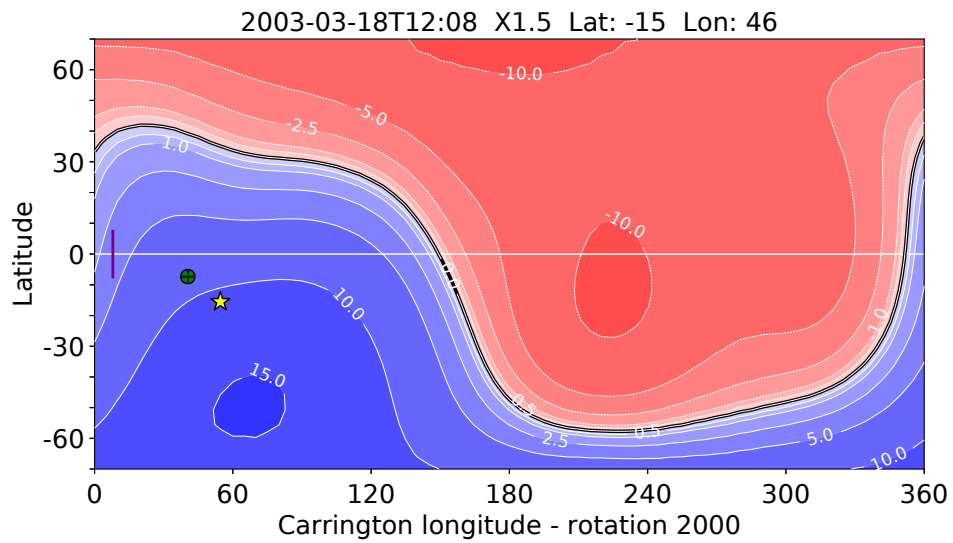


Figure 6.2: A synoptic source surface map for the 18 March 2003 event in the same format as Figure 6.1.

6.1.3 Event on 13 September 2005

This event has none of the features previously identified as being likely to produce a false alarm: the flare was intense (X1.5) and long (1 hour 38 minutes); the CME was very fast (1,866 km/s) and a halo. However, in this instance it is instructive to look at the plots of the SXR flux and the energetic proton flux. They are shown in Figure 6.3: in this plot the red curve is the SXR flux, and the orange and blue curves are the fluxes of protons in the 9 - 15 MeV and 40 - 80 MeV energy channels respectively.

It can be seen that the X1.5 flare which has been treated as a false alarm was followed only four hours later by a flare of class X1.7. This second flare was much shorter than the first (it endured for just 15 minutes); it was associated with a CME reported to have a speed of 999 km/s and a width of 170°. The (small) rise in flux in the 40 - 80 MeV energy channel follows that second flare and CME, and consequently it has been those events which have been treated as the ones which

CHAPTER 6

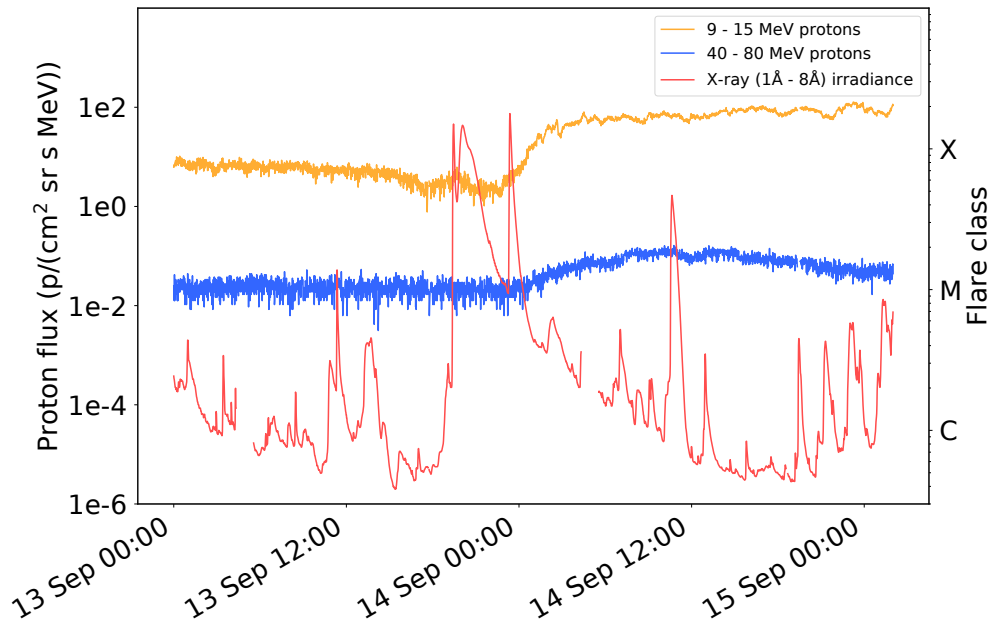


Figure 6.3: The energetic proton and SXR flux for the 13 September 2005 event. The red curve is the SXR flux from the GOES 1 - 8 Å channel, the orange curve the flux of protons in the 9 - 15 MeV energy channel, and the blue curve the flux of protons in the 40 - 80 MeV energy channel.

produced the particles.

Based on the >40 MeV data the first event was classed as a false alarm, but, given that there were two X class flares and the particle signatures are unclear (See Figure 6.3), there is some ambiguity as to this association.

The synoptic source surface map for the events is shown in Figure 6.4. The solar wind speed was 666 km/s, and so the Earth's footpoint was $\sim 37^\circ$ west of the central meridian; its latitude was $+7.2^\circ$. Even taking into account the possible errors in the map and in the positioning of the symbols, it is very likely that the site of the flare and the Earth's footpoint were on opposite sides of the HCS. The fact of the

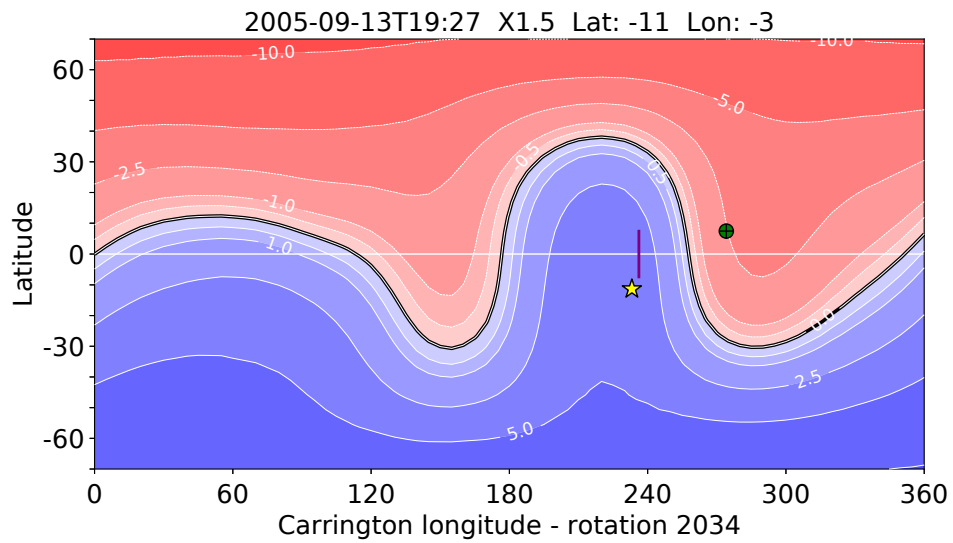


Figure 6.4: A synoptic source surface map for the 13 September 2005 event in the same format as Figure 6.1.

matter is that some particles did arrive at Earth (whether as a result of the first event or the second, or both) and consequently there is some evidence here that the HCS was crossed, although (given that the SEP event was very small) it may well have been a significant inhibiting factor.

6.2 Intense flare false alarms

There were two flares of class X3.0 or greater in time range 1 which failed to produce SEPs at Earth. They were an X3.0 which occurred on 15 July 2002, and an X6.2 flare which occurred on 13 December 2001. Both were associated with a halo CME. How is it, then, that neither produced particles at Earth?

There are a number of possible reasons. First, whilst the CMEs were haloes, neither was particularly fast: for the X3.0 flare the speed was 1,151 km/s; for the X6.2 flare the speed was 864 km/s. Secondly, both flares were very short - each was

reported to have a duration of just 15 minutes. Thirdly, both were on the edge of the region of good magnetic connectivity to Earth: the X3.0 flare had coordinates of N19W01, and the X6.2 flare coordinates of N16E09.

It may be that it is the combination of these three factors taken together which may go some way to explaining why these very intense flares were false alarms.

6.3 The ground level enhancement of 17 May 2012

Finally, it is interesting to consider a solar event which was not a false alarm, but which produced particles of such energy that their effects were detected in neutron detectors at ground level. Such events are called “ground level enhancements” (GLEs) and are relatively rare: this one, which occurred on 17 May 2012, was the 71st such event since the 1940s.

The parent solar event was a class M5.1 flare which occurred at N11W76 and which endured for 49 minutes. It was associated, according to CDAW, with a CME which had a reported speed of 1,582 km/s. It is notable that the flare was relatively small for an event which produced particles of such energies, although it was not a short duration flare, and it was above the threshold of M3; as might be expected for an SEP producing event, CDAW reported the CME to be a halo.

The synoptic source surface map for the event (in the same format as that in Figure 6.1) is shown in Figure 6.5. At the time of the flare the solar wind speed was 366 km/s meaning that the Earth’s footpoint was $\sim 67^\circ$ west of the central meridian. The solar event and Earth were well magnetically-connected and both the flare and the Earth’s footpoint were on the same side of the HCS.

This event occurred at a time when it was possible to observe it not only by the LASCO coronagraphs, but also by the coronagraphs on board STEREO-A and STEREO-B. Shen *et al.* (2013) used observations from each of these instruments and were able to identify not one but two separate eruptions which produced two

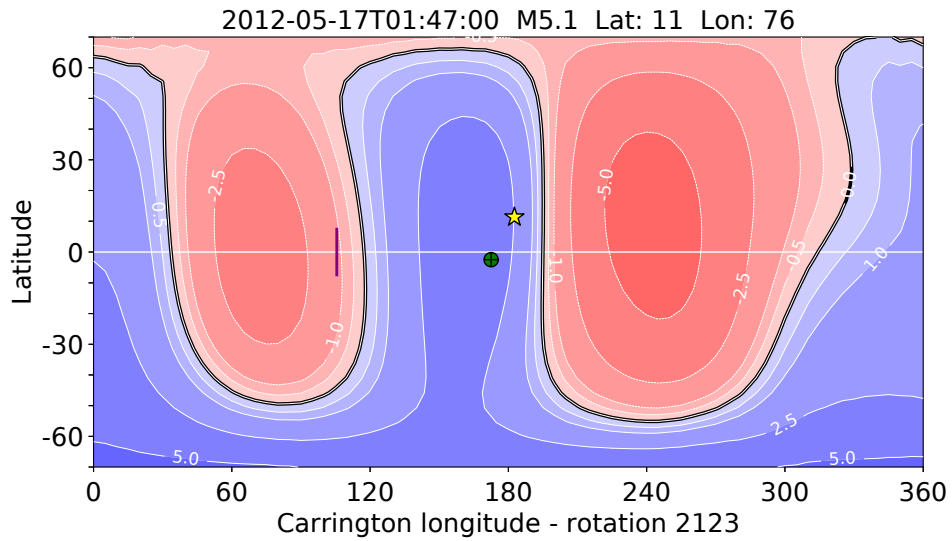


Figure 6.5: A synoptic source surface map for the 17 May 2012 ground level enhancement event in the same format as Figure 6.1.

separate CMEs within about two minutes of each other. Li *et al.* (2012) have suggested that more efficient particle acceleration may occur if two CMEs erupt in sequence from the same active region during a short period of time. Furthermore, Firoz *et al.* (2015) reported that, whilst the CME-driven shock may have played the leading rôle in accelerating the particles, components of the preceding flare may also have contributed to the shock. Both of these factors may therefore have played a part in the acceleration of the particles.

It was also possible to measure the effects of these solar events by instruments on widely separated spacecraft within the inner heliosphere. Energetic particle data from STEREO-A, STEREO-B, SOHO, and GOES (which were all located at about 1au), together with data from the MErcury Surface, Space Environment, Geochemistry and Ranging (MESSENGER) neutron spectrometer (Lawrence *et al.* (2016)) and the Mars Science Laboratory (MSL) Radiation Assessment Detector (RAD) (Hassler *et al.* (2012)) were examined by Battarbee *et al.* (2017c). The author

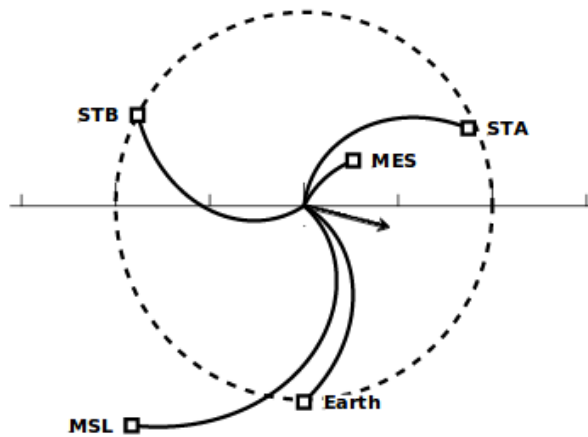


Figure 6.6: Relative locations of the Earth and different spacecraft at the time of an SEP event which occurred on 17 May 2012. The direction of the CME is shown by the arrow. Taken from Battarbee *et al.* (2017c)

of this thesis was involved in the collaboration which resulted in this paper, and provided information on the solar eruptive events associated with this and several other events where enhanced proton fluxes were detected by MSL/RAD. The paper is reproduced as Appendix H.

The relative locations of the various spacecraft at the time of the event are shown in Figure 6.6, and the direction of the CME is shown by the arrow. Figure 6.7 shows the proton intensities as recorded by each instrument.

It is to be noted that there was an enhancement in proton flux observed by all the spacecraft even though they were widely separated in longitude. The two spacecraft which observed the solar event as an eastern one (STEREO-A and MESSENGER) see a slow rise in flux, whereas the well-connected spacecraft see a sharp rise, as may be expected.

On each plot is marked a green vertical line which marks the start of the SEP event, whilst the grey vertical lines indicate possible ESP events (see Section 2.5.2).

CHAPTER 6

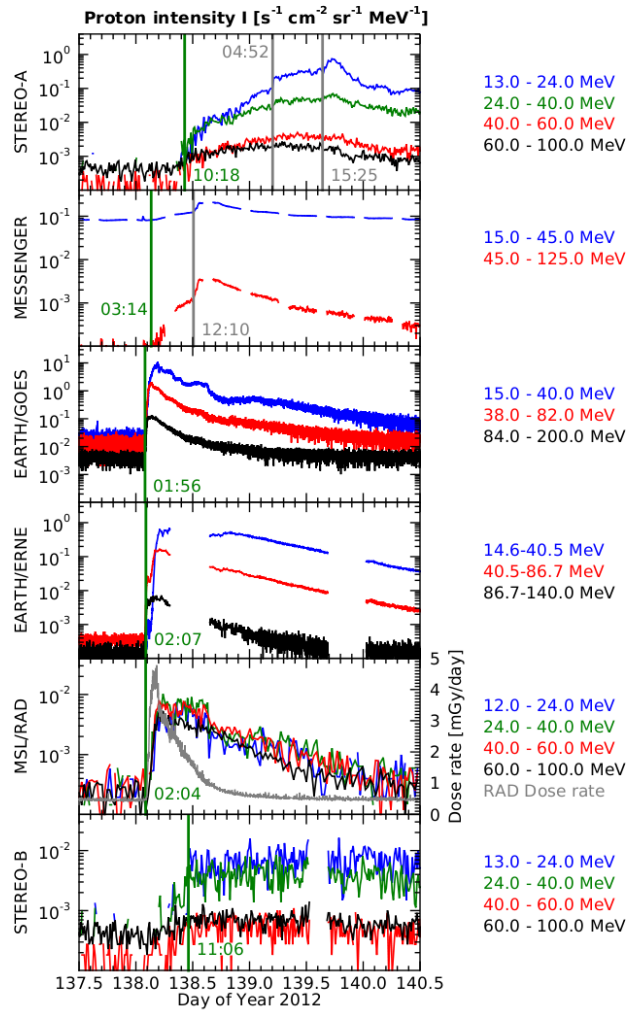


Figure 6.7: Energetic particle intensities for an event which occurred on 17 May 2012 as observed by several different spacecraft. Taken from Battarbee *et al.* (2017c)

6.4 Discussion

As an aid to reaching an understanding as to why some of the most energetic solar events were false alarms, synoptic source surface maps have been examined. Some caution needs to be exercised when considering these maps.

CHAPTER 6

The position of the Earth's footpoint relative to the central meridian is calculated from the measurement of the strength of the solar wind (Equation 2.4) on the basis of a field line following an ideal Parker spiral. Solar wind speed has been taken from the Goddard Space Flight Center's Omniweb website which provides data from instruments on board several different spacecraft, but there is no estimate of error provided.

It is sometimes the case that there is no reported value for solar wind speed for considerable periods of time (occasionally for many days) and in these instances an estimate of solar wind speed (usually taken to be ~ 500 km/s) has to be used. Additionally, as was seen in Section 2.6.2, magnetic field lines are likely to be disrupted, which in this context means that the Earth's footpoint may actually be some distance from its calculated position - see *e.g.* Ippolito *et al.* (2005).

It is consequently the case that there is likely to be an error in the calculation of the position of the Earth's footpoint, although it is difficult to quantify the extent of that uncertainty.

Apart from the difficulties in determining the Earth's footpoint, SEP events usually occur when the Sun is at its most active, and therefore when the magnetic field is at its most changeable. The result is that the HCS is likely to be extremely complex, and determination of its exact position relative to the Earth's footpoint and flare site is also subject to some uncertainty.

Additional work needs to be undertaken to quantify the uncertainties involved in using synoptic source surface maps, but on the basis of these case studies it is suggested that there is at least some evidence to support the contention that a current sheet may inhibit particles crossing from a region of one magnetic polarity to another.

The case studies do illustrate the difficulties inherent in the forecasting of SEP events. There were 3 events which were false alarms according to both forecasting

CHAPTER 6

algorithms A.1 and A.2, and the reasons why each was a false alarm may be different in each case.

For the first there were 3 inhibiting factors to the arrival of SEPs at Earth: it was a short duration flare; there was relatively poor magnetic connectivity; and the flare and Earth's footpoint were probably on opposite sides of the HCS. For the second, the events were well magnetically-connected to Earth and the Earth's footpoint was on the same side of the HCS as the flare. However the flare was short and the CME not a halo. The third was the most complicated of all, with two X class flares in quick succession with the result that it is very difficult to disentangle the events. Whilst a small enhancement in proton flux was seen after the second of the flares, the fact that the events were on the opposite side of the HCS to the Earth's footpoint may well have been a significant inhibiting factor to SEP arrival at Earth.

For the intense flare false alarms, both were associated with relatively slow CMEs, both flares were short, and both were on the edge of good magnetic-connectivity. The combination of these three factors together may explain why the events failed to produce SEPs at Earth.

Finally the GLE of 17 May 2012 provides an interesting contrast. In this otherwise fairly unremarkable solar event several factors favourable to SEP acceleration and propagation occurred together: the flare, whilst modest at class M5.1, endured for a relatively long time and may have contributed to the shock process; there were two separate CMEs within a very short space of time resulting in more efficient acceleration of the particles; at least one of those CMEs was reported to be a halo; and the solar events and the Earth's footpoint were on the same side of the HCS. The result was to accelerate particles to such high energies that it was possible to detect them in neutron monitors at ground level.

It is interesting to note that following this event SEPs were detected not only

CHAPTER 6

at Earth, but by widely separated spacecraft. The profiles of the energetic proton flux as measured by the different instruments are very much as might have been expected from the points made in Section 2.5.2 and Figure 2.7.

Chapter 7

SPARX validation

Up to this point, the forecasting algorithms which have been considered are simple empirical algorithms based upon the observation of a particular type of solar event. However there are, as was mentioned in Section 1.7, other methods of forecasting the arrival of SEPs. In particular, there is a number of physics-based space weather forecasting tools. In this section such a tool, SPARX, which was developed at the University of Central Lancashire, is described. The database of flares and SEP events obtained for this thesis has been used to evaluate the performance of the model. The results of this evaluation are included in Dalla *et al.* (2017b) which is reproduced as Appendix I.

7.1 Description of the SPARX model

The Solar Particle Radiation SWx (SPARX) is a fully 3-D physics-based model for simulating SEP propagation for Space Weather forecasting purposes (Marsh *et al.* (2015)). The model takes a full-orbit test particle approach. In the simulation large numbers of particles are injected instantaneously at $2R_{\odot}$ from an extended region consisting of “tiles” with a size of $6^{\circ} \times 6^{\circ}$ (or any multiple thereof). This aims to represent a CME-driven shock in the corona. Particle velocities are randomly

CHAPTER 7

distributed in a semi-hemisphere and in a direction outwards from the Sun. The particles are injected with a power law energy spectrum $E^{-\gamma}$ (where γ can be chosen) over an energy range of 10 - 400 MeV.

The model takes into account turbulence in the heliosphere by the introduction of scattering which is isotropic in velocity space. The level of scattering is determined by a chosen mean free path, λ . For each particle, its equation of motion is integrated up to a scattering event at which point the direction of the particle's velocity vector is changed randomly, and then the integration proceeds until the next scattering (Marsh *et al.* (2013)).

The time when a particle crosses a sphere at 1au is recorded and output, as is its longitude, latitude, kinetic energy, and pitch angle; this output may then be used to produce a profile of the particle flux which would have been observed by a spacecraft situated at 1au.

Results from the model show that, especially in the case of partially ionised heavy ions and protons at the high end of the SEP energy range, drifts have an important rôle to play in particle propagation (Marsh *et al.* (2013)). This has the additional effect of strongly decelerating particles (Dalla *et al.* (2015)) meaning that a particle may arrive at 1au with much less energy than when it left the Sun. SPARX naturally takes this deceleration into account.

A user may input the location of a given event manually, but SPARX may also be used in the context of real-time space weather forecasting. The “Coronal Mass Ejections and Solar Energetic Particles: forecasting the space weather impact” (COMESSEP) project developed a space weather alert system which runs without human intervention, and which uses the output of SPARX. A forecast is currently triggered by the real-time observation of a flare by the Flaremail tool¹, and the time of the particle injection is taken to be that of the flare's peak emission in SXR. Data

¹sidc.oma.be/products/flaremail

CHAPTER 7

for the speed of CMEs is not easily available over real-time forecasting timescales, and therefore within the present version of SPARX only flare information is input to the model.

Because it is computationally impractical to run SPARX each time an event is detected, a database of results obtained by using various injection locations has been generated, and this database may then be queried in near-real time, and the required tiles are combined to simulate a large extended region of particle injection.

7.2 Methodology

The aim was to evaluate the performance of the SPARX model by running it over a historical dataset of flares, and comparing SPARX forecasts with GOES EPS data so as to assess how well the predictions matched the observed events. Flare data were taken from the GOES SXR Flare List. As a basis for the validation 125 X class flares which had occurred between 1 September 1997 and 30 April 2017 were examined. It should be noted that a further 36 X class flares had to be disregarded either because there were available no GOES data for proton flux, or because it was impossible to determine whether the flare had produced SEPs due to the GOES EPS still recording an enhancement from a previous event.

For the purposes of this evaluation, two different definitions of SEP event have been adopted:

1. >10 MeV proton flux exceeds a threshold, $I_{\text{thr}} = 10$ particle flux units (pfu)
i.e. $10 \text{ particles cm}^{-2} \text{ s}^{-1} \text{ sr}^{-1}$
2. >10 MeV proton flux exceeds a threshold, $I_{\text{thr}} = 1$ pfu.

The first definition matches that used by NOAA and the second is examined with a view to discovering whether SPARX performs better for the higher or lower energy events.

CHAPTER 7

For the SEP data, plots of integrated > 10 MeV proton flux (as measured by the GOES EPS instruments) were downloaded from <https://solarmonitor.org> and estimates of SEP onset and peak times were made visually. If there were two peaks in SEP data the second of which was likely to have resulted from the passing of a shock, then it was the higher of the two peaks which has been noted.

SPARX was run manually for each of the 125 X class flares and the output noted for (*inter alia*) (a) the peak in >10 MeV proton flux and (b) the time between the flare peak and the SEP peak. The output from SPARX produces a value for proton flux in every case: if that forecast was greater than I_{thr} , then this was treated as a forecast of an SEP event; if the forecast was that the flare would produce a flux less than I_{thr} then this was treated as a negative forecast.

Consequently, if SPARX forecast a proton flux $> I_{\text{thr}}$ but in fact there was no enhancement in the GOES data which passed I_{thr} , then this was treated as a false alarm; on the other hand, if SPARX forecast a proton flux $< I_{\text{thr}}$ but in fact there was a GOES enhancement which passed I_{thr} , then this was treated as a missed event. There are, of course, other “misses”, *i.e.* SEP events which followed flares of a lower class and / or CMEs, but as these events could not have been forecast by SPARX they have not been included in the validation scores. Had they been included, the false alarm ratio would be unaffected, but all the other scores would change (albeit not to any great degree).

7.3 Validation

Using a value for I_{thr} of 10 pfu, there were 40 SEP events resulting from X class flares in the time period under investigation. SPARX correctly forecast 20 of these events, produced 27 false alarms, missed 20 of the SEP events, and correctly forecast that 58 of the X class flares would not produce SEPs. A contingency table for the SPARX forecasts, summarising these results, is shown in Table 7.1.

CHAPTER 7

Table 7.1: Contingency table for SPARX forecasts for X class flares between 1 September 1997 and 30 April 2017 which exceed the SEP threshold, $I_{\text{thr}} = 10$ pfu.

		Observed		Total
		Yes	No	
Forecast	Yes	hits = 20	false alarms = 27	47
	No	misses = 20	correct negatives = 58	78
Total		40	85	125

For $I_{\text{thr}} = 1$ pfu, there were 52 SEP events. For this threshold SPARX produced 40 hits and 31 false alarms. It missed 12 of the SEP events, and correctly forecast that 42 of the X class flares would not produce SEPs. A contingency table for these results, is shown in Table 7.2.

Section 4.7 introduced a number of verification scores for forecasting algorithms. Using X class flares as the selection criterion for the forecast and a value of $I_{\text{thr}} = >10$ pfu, for the SPARX model the BIAS score was 1.18, the POD score was 0.50, the FAR was 0.57, and the CSI was 0.30. For $I_{\text{thr}} = >1$ pfu the BIAS score was 1.37, the POD score was 0.77, the FAR was 0.44, and the CSI was 0.48. These results are summarised in Table 7.3.

For both SEP thresholds the BIAS score shows that SPARX has a tendency to over-forecast SEP events. It performs rather better with a threshold of $I_{\text{thr}} >1$ pfu than $I_{\text{thr}} >10$ pfu: the POD and CSI scores are both higher, and the FAR lower.

CHAPTER 7

Table 7.2: Contingency table for SPARX forecasts for X class flares between 1 September 1997 and 30 April 2017 which exceed the SEP threshold, $I_{\text{thr}} = 1$ pfu.

		Observed		
		Yes	No	Total
Forecast	Yes	hits = 40	false alarms = 31	71
	No	misses = 12	correct negatives = 42	54
Total		52	73	125

Table 7.3: Forecast verification scores for the SPARX SEP simulation. Column 1 gives the score type, and columns 2 and 3 the scores for the SPARX simulation for $I_{\text{thr}} = 10$ pfu and $I_{\text{thr}} = 1$ pfu respectively.

Score type	SPARX	SPARX
	($I_{\text{thr}} = 10$ pfu)	($I_{\text{thr}} = 1$ pfu)
BIAS	1.18	1.37
POD	0.50	0.77
FAR	0.57	0.44
CSI	0.30	0.48

7.4 Discussion of the SPARX forecasts

Figure 7.1 is a plot for the 40 X class flares which were forecast by SPARX to produce an SEP event in excess of the 1 pfu threshold. The x-axis is the observed peak in >10 MeV proton flux as measured by the GOES EPS, and the y-axis the peak flux as forecast by the SPARX model. In the plot, the colour of the marker represents the longitude of the flare site; for ease of identification, the different colours represent different 20° bins. The dotted blue line shows the 1:1 correlation between SPARX forecast and actual observation.

There are relatively few events which appear close to the 1:1 correlation. The SPARX forecasts almost appear in horizontal bands across the plot: events with a longitude $>W50$ tend to be forecast to have a peak flux of about 100 pfu or higher. Events from between $\sim W10$ and $\sim W50$ are often forecast to have a peak flux between about 10 and 100 pfu; and those events from between $\sim E10$ and $\sim W10$ tend to be forecast to have a peak flux between about 1 and 10 pfu. Only 2 events which occurred east of E10 were forecast to have a peak flux exceeding the $I_{\text{thr}} = 1$ pfu threshold.

The reason for this distribution is the way in which SPARX makes its forecasts, and this is best explained by reference to Figure 7.2. In this plot peak proton flux is plotted against heliographic longitude: green dots show the observed SEP events, blue dots the correct SPARX forecasts and red dots the SPARX false alarms ($I_{\text{thr}} = 1$ pfu).

It is clear from Figure 7.2 that SPARX forecasts that the best magnetically-connected events (*i.e.* those events between about W20 and W70) will produce SEPs with a peak flux of ~ 100 pfu (or possibly $\sim 1,000$ pfu for events between W50 and W70). Events west of $\sim W70$ are forecast to have lower peak flux.

For events which occur east of $\sim W20$ there is a rapid fall of forecast peak flux.

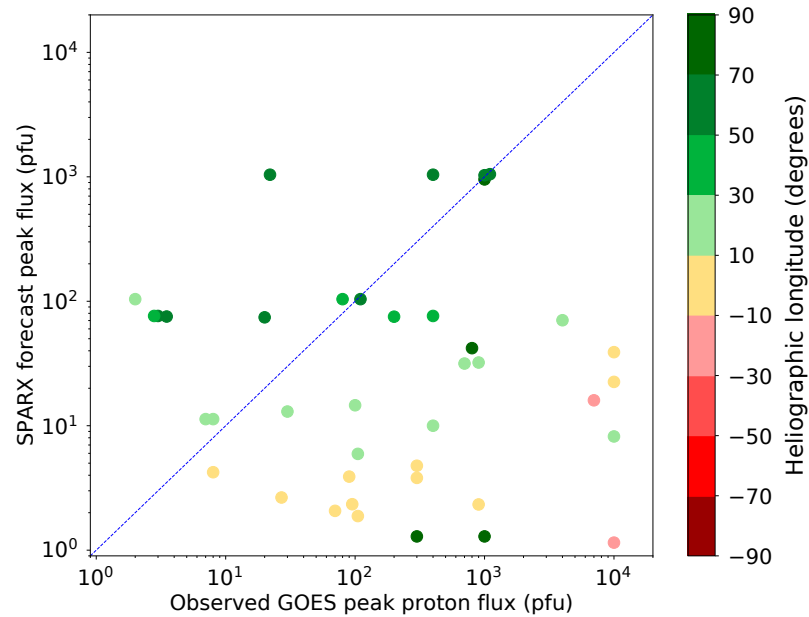


Figure 7.1: Peak flux of >10 MeV protons as forecast by the SPARX model versus observed peak >10 MeV proton flux as measured by the GOES EPS for the 40 X class flares which were correctly forecast by SPARX to produce an SEP event exceeding 1 pfu. The colour of the marker represents the longitude of the flare site. The blue dotted line is the 1:1 correlation between SPARX forecast and actual observation.

These events are less well magnetically-connected to Earth, but particles are nevertheless forecast by SPARX to arrive at Earth as a result of the effects of co-rotation and particle drift. The result is that SPARX forecasts that very few events which occur east of \sim W10 will produce a peak proton flux in excess of the NOAA 10 pfu threshold. Events between \sim W10 and \sim E25 are usually forecast by SPARX to produce a small SEP event, and events east of \sim E25 are forecast not to produce any enhancement (above the $I_{\text{thr}} = 1$ pfu threshold) of energetic protons.

Figure 7.2 may also go some way to explaining why SPARX performs better

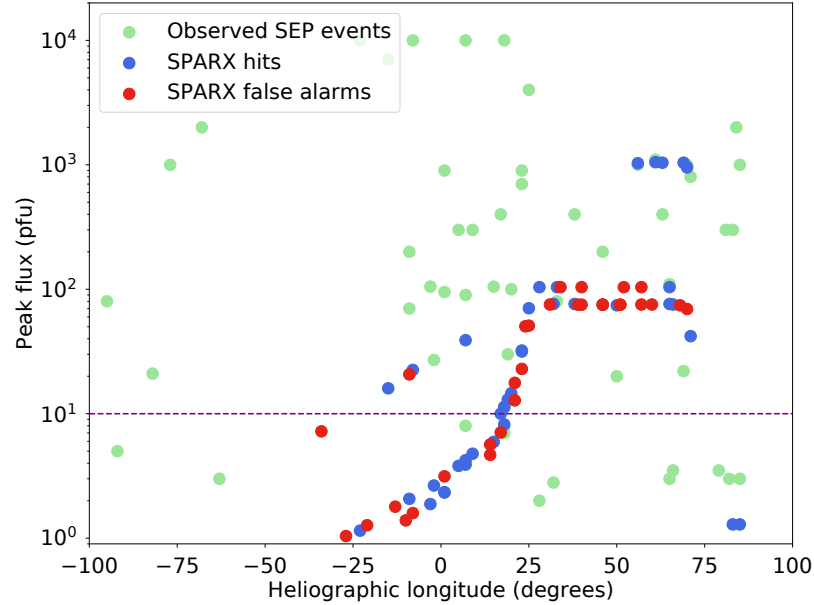


Figure 7.2: Peak proton flux plotted against heliographic longitude for observed SEP events (green dots), SPARX correct forecasts (blue dots) and SPARX false alarms (red dots) for $I_{\text{thr}} = 1$ pfu. The purple horizontal dotted line is the 10 pfu threshold.

with a lower SEP event threshold. As can be seen by the green dots, there is a considerable number of observed >10 pfu SEP events which occur from longitudes east of W20, but because of the way the SPARX simulation is set up, very few of these events are forecast to reach fluxes in excess of the 10 pfu threshold. Essentially this means that almost all >10 MeV SEP events which occur from longitudes east of W20 are missed by SPARX.

Solar events which occur between \sim E25 and \sim W20 generally are forecast by SPARX to produce a small SEP event (*i.e.* above the 1 pfu threshold but below the 10 pfu threshold). Thus these SEP events are less likely to be missed if the >1 pfu threshold is adopted.

A direct comparison between the accuracy of the SPARX forecasts and that of the

CHAPTER 7

three of the simple forecasting algorithms considered in Chapter 5 must be treated with caution because of the different definitions of “SEP event”. Different proton energies are considered, and there are different methods employed for determining the occurrence of an SEP event.

That *caveat* having been entered, a comparison of Table 7.3 with Table 5.1 suggests that with a value of I_{thr} of 10 pfu SPARX performs less well than all three of the algorithms, but that with a value of I_{thr} of 1 pfu it has a better CSI score than both A.1 and A.2. There are at least two reasons for its relatively poor performance using the 10 pfu threshold.

First, by design, SPARX does not use CME data. It was always intended that SPARX would be used as an operational tool and real-time CME data are not available. As has been seen, forecasting SEP events based upon the observation of only one type of solar event is likely to be less accurate than using parameters of both flares and CMEs. In fact, the verification scores for SPARX with I_{thr} equal to 10 pfu are broadly similar to those of algorithm A.2 (which also uses only flare data to make its forecasts).

Secondly, SPARX is in its early days of development, and the models of SEP propagation which it uses are constantly being improved. Following on from the flat current sheet model described by Battarbee *et al.* (2017a), SEP propagation in the presence of a “wavy” current sheet has now been modelled (Battarbee *et al.* (2017b)) and the results will be included into future versions of SPARX. Improved models will lead to improved forecasting, and the verification of SPARX which has been carried out in this work serves only as a benchmark against which later versions of the simulation can be tested.

Figure 7.3 is a plot of the 52 X class flares which were observed to produce SEPs exceeding the 1 pfu threshold. On the x-axis is plotted the time interval (in hours) between peak flare SXR intensity and the peak of >10 MeV proton flux as observed

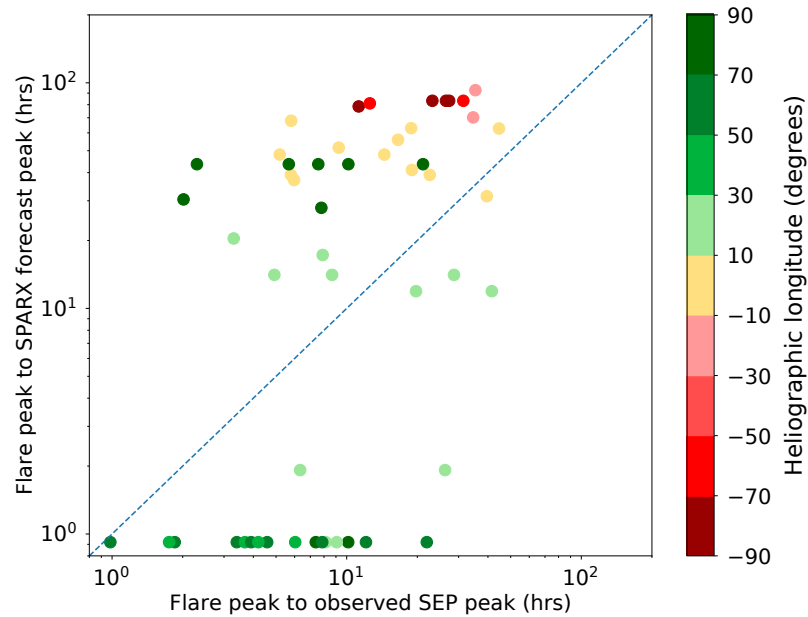


Figure 7.3: Time interval in hours between flare peak SXR flux and >10 MeV proton flux as forecast by SPARX versus flare peak SXR flux and observed >10 MeV proton flux for the 52 X class flares which produced an SEP event exceeding 1 pfu. The colour of the marker represents the longitude of the flare site, and the blue dotted line is the 1:1 correlation.

by the GOES EPS. On the y-axis is the time interval between peak flare SXR flux and the peak of >10 MeV proton flux as forecast by SPARX. In this plot also, the longitude of the flare site is represented by the colour of the marker in bins 20° wide, and the blue dotted line represents a 1:1 correlation.

There is a considerable population of magnetically well-connected events which SPARX forecasts to produce an SEP event which reaches its peak within an hour of the peak of the flare. For all but one of these events, these are under-estimates of the time it actually took for the SEP event to reach its peak. There is a separate band of events from a longitude exceeding $\sim 70^\circ$ which SPARX forecasts would reach

CHAPTER 7

their peak in ~ 40 hours, whereas in fact these events in general took less than ~ 10 hours. This trend of SPARX over-estimating the time that it took for an SEP event to reach its peak continues for less well magnetically-connected events.

Chapter 8

Conclusions

8.1 SEP forecasting

In 2011 for the first time the UK government added severe solar storms to the National Risk Register of Civil Emergencies. In 2013 the Department for Business, Innovation and Skills made available the sum of £4.6 million for the establishment of an operational space weather prediction centre in the UK. The consequence was the creation of the Met Office Space Weather Operations Centre (MOSWOC) in Exeter.

For the reasons which were expounded in Section 1.1, accurate space weather forecasting, including the forecasting of SEP events, is vital. MOSWOC issues daily space weather forecasts to, amongst others, the armed forces, the electricity industry, satellite operators, and the aviation industry.

Space weather forecasting, of course, is not simply a UK enterprise. There are now many countries which have their own space weather services including Australia, China, Indonesia, Belgium, Brazil, and Canada. The International Space Environment Service has been involved in the international coordination of space weather services since the 1960s and now has 16 Regional Warning Centres around the globe, of which MOSWOC is one.

CHAPTER 8

The American equivalent of MOSWOC, the Space Weather Prediction Centre (SWPC) which is based in Boulder, Colorado, also provides space weather forecasts to similar interested parties. The U.S Federal Aviation Administration takes the space weather predictions issued by SWPC very seriously: it will divert flights which are planned to follow polar route on the basis of a warning that space weather will interfere with high-frequency communications. Estimated costs of such a diversion may be as high as \$100,000 per flight. Thus each false alarm may bring with it a high financial cost.

It is expected that this large sample study will provide useful information to aid the understanding of the acceleration processes behind, and the interplanetary propagation of, SEPs. Understanding the reasons why some large solar events fail to produce SEPs at Earth will result in improved forecasting algorithms and reduce false alarm rates.

8.2 Overview

The basic particle acceleration mechanisms which are described in Sections 2.1 and 2.2 may all have a rôle to play to some degree or other. Determining which were dominant in any one solar event, however, is not easy because each may occur in close temporal connection with the other.

The picture is further complicated by the question as to whether or not the particles have access to open magnetic field lines, and therefore whether they are able to escape into interplanetary space, as described in Section 2.4.

Should they escape, SEPs broadly travel along magnetic field lines (Section 2.5), but the actual path taken by SEPs may be affected by several factors, including the meandering of the field lines and particle drift (Section 2.6).

Within this complex picture of particle acceleration, escape, and propagation,

there is the enigma of the false alarm. Why is it that some very well magnetically-connected solar events, which clearly have released large amounts of stored energy by a magnetic reconnection event in a flare, by the ejection of significant amounts of mass at high speed, or by both, produce no SEPs at Earth? Reaching an understanding as to why some solar events fail to produce SEPs will ultimately produce better modelling and more accurate forecasts.

This work analyses these events by formulating a robust definition of a “false alarm”. Two simple SEP forecasting algorithms were applied to historical data sets, and lists of the false alarms they generate have been derived. The performance of the forecasting algorithms was validated using a number of standard verification scores with a view to monitoring their performance, and providing a method of determining whether and by how much they may be improved.

The parameters of the false alarms were then compared with those of the solar events which did produce SEPs at Earth so as to determine which are important to SEP production. A number of very high-energy false alarms were studied individually with a view to determining whether the reasons why they failed to produce SEPs could be determined. Additionally, an event which produced particles of such high energy that they were detected on the ground was also examined.

Finally a validation of the SPARX SEP simulation was carried out using standard verification scores; the forecast peak flux was compared to observed peak flux, and the forecast time to peak flux was also compared to observation.

The lists of the false alarms which have been derived are made available for further study. It is hoped that they will be useful to others in the field.

8.3 Results summary

The main results found by this work are as follows:

CHAPTER 8

- A forecasting algorithm based solely upon the observation of a well-connected fast CME has a relatively low false alarm ratio, but misses a significant number of SEP events; an algorithm based solely upon the observation of a well-connected X class flare has a higher false alarm ratio, and misses a similar number of SEP events.
- A forecasting algorithm which is based upon the parameters of both CMEs and flares performs better than one which is based upon the parameters of just one type of solar event.
- Many of the fast CME false alarms were associated with flares of class lower than M3. All of the front-side CMEs which produced SEPs were associated with a flare. CME width is important to SEP production, in that if a fast CME was not reported to be a halo, then it was more likely to be a false alarm. X class flares which were not associated with a CME, or which were associated with a CME slower than 500 km/s were all false alarms. The width of the flare's associated CME is also important: those associated with a CME which was not reported to be a halo were more likely to be false alarms. In time range 1 the duration of an X class flare was an important factor in SEP production.
- There was a trend for X class flares prior to 1996 to have a longer duration than those post 1996. It is suspected that this may be due either to the use of different instrumentation, or to a different method of determining flare duration.
- Investigation of the case studies suggests that for accurate forecasting of SEPs it may not be sufficient simply to consider the accelerating events, but that the location of the heliospheric current sheet relative to the site of the solar event and the Earth's footpoint may be of relevance.

- The evaluation of the SPARX simulation sets a benchmark against which future versions of model can be tested. Currently SPARX tends to under-forecast SEP peak flux. There is also a number of very well magnetically connected events which SPARX suggests will produce SEPs within an hour, but which do not in fact reach their peak until much later.

8.4 Further work

There are several different avenues open to further exploration.

- This work has concentrated on energetic protons, but protons are only one of many species of particle which make up an SEP event. However particle drift, which was introduced in Section 2.6.2, is particularly strong for SEP heavy ions as a result of them having a large mass to charge ratio (they will have been partially ionised at the Sun).

It may be that particle drift is an important phenomenon in determining whether or not these heavy ions arrive at Earth. Carrying out an analysis similar to the one described in this thesis for heavy ions will shed light on just how important drift is for such particles. For similar reasons, it may also prove enlightening to consider very high energy protons, in, say, the GOES 100 - 900 MeV energy channel.

- The forecasting algorithms considered in this work produce a purely binary outcome: will this solar event produce particles or not? This is not, however, the question posed by many forecasters today. The preference is for “probabilistic” forecasts: what is the probability that this solar event will produce particles? Algorithms which seek to answer this question are likely to prove useful, and it may be possible to improve the forecasting algorithms discussed in this work were they to be rephrased as a probabilistic forecast.

CHAPTER 8

It may be possible to achieve this by employing a method akin to the Drake Equation. Each term of the equation may be based upon the importance which different parameters of solar events have to SEP production: for example good magnetic connectivity would lead to a high probability of SEPs being detected; the lower the class of the flare would reduce that probability; the higher the speed of the associated CME would increase the probability, and so on. This type of method is highly amenable to machine learning. The relative importance of each parameter may be adjusted as the amount of available data increases.

Similarly, the SPARX simulation output is an estimate of the peak flux of >10 MeV protons, but this is a definite forecast: no attempt is made to assess how likely a solar event will produce SEPs. SPARX is, primarily, a simulation of how particles behave, but if it is to be used for forecasting purposes then it may be appropriate to phrase its output as a probability of SEP arrival at a given location.

- In their work on real-time SEP forecasting using the K-cor coronagraph at the Mauna Loa Solar Observatory in Hawaii, St. Cyr *et al.* (2017) express in their conclusions some optimism as to the levels of success enjoyed by automatic CME detection systems. However, in the light of Section 3.4 and Appendix A, that optimism is not shared: there are simply too many differences between the results produced by the automated systems to know which are reliable. That said, the detection algorithms will surely improve with time.

This work has based its conclusions upon the CDAW CME catalogue. It would be interesting to investigate whether different conclusions would be reached by using data from different catalogues.

The first of the suggestions will lead to a better understanding of the physics

CHAPTER 8

behind the acceleration, escape and propagation of energetic particles. Three-dimensional modelling of SEPs, which, as was seen in Section 2.6.2, must be the most promising way forward, will only improve when the processes involved in particle drift and deceleration are fully taken into account. Robust information as to how drift may affect the arrival of heavy-ions and high-energy protons at Earth will provide information useful to those involved in modelling SEPs.

The second and third suggestions are important for SEP forecasting purposes. Probabilistic forecasting is now the norm, and finding a way of describing forecasts as a probability is essential. But equally important from a real-time forecasting point of view is gaining an understanding of false alarm rates if the automated CME detection systems were to be used.

It has been shown in this work that if SEP forecasting algorithms based upon the observation of a solar event are to be improved, the parameters of both flares and CMEs need to be taken into account. This demands accurate data relating to CMEs being available in real-time, and consequent reliance on the automatic detection of CMEs. For SEP forecasting purposes, research into the numbers of false alarms and missed events generated by algorithms using these systems is vital.

Bibliography

- Alberti, T., Laurenza, M., Cliver, E. W., Storini, M., Consolini, G., and Lepreti, F. (2017). Solar activity from 2006 to 2014 and short-term forecasts of solar proton events using the esperta model. *Astrophys. J.*, 838(1):59.
- Aran, A., Sanahuja, B., and Lario, D. (2006). SOLPENCO: A solar particle engineering code. *Advances in Space Research*, 37:1240–1246.
- Aschwanden, M. J. (2005). *Physics of the Solar Corona*.
- Balch, C. C. (1999). Sec proton prediction model: verification and analysis. *Radiation measurements*, pages 231–250.
- Balch, C. C. (2008). Updated verification of the Space Weather Prediction Center’s solar energetic particle prediction model. *Space Weather*, 6:S01001.
- Battarbee, M., Dalla, S., and Marsh, M. (2017a). Solar energetic particle transport near a heliospheric current sheet. *Astrophys. J.*, 836(1):138.
- Battarbee, M., Dalla, S., and Marsh, M. S. (2017b). Modelling Solar Energetic Particle transport near a wavy Heliospheric Current Sheet. [ArXiv e-prints](#).
- Battarbee, M., Guo, J., Dalla, S., Wimmer-Schweingruber, R., Swalwell, B., and Lawrence, D. J. (2017c). Multi-spacecraft observations and transport simulations of solar energetic particles for the May 17th 2012 GLE event. [submitted to *Astronomy and Astrophysics*](#).

- Beck, P., Latocha, M., Rollet, S., and Stehno, G. (2005). TEPC reference measurements at aircraft altitudes during a solar storm. *Advances in Space Research*, 36:1627–1633.
- Belov, A., Garcia, H., Kurt, V., Mavromichalaki, H., and Gerontidou, M. (2005). Proton enhancements and their relation to the X-ray flares during the three last Solar Cycles. *Solar Physics*, 229:135–159.
- Bentley, R. D., Csillaghy, A., Aboudarham, J., Jacquy, C., Hapgood, M. A., Bocchialini, K., Messerotti, M., Brooke, J., Gallagher, P., Fox, P., Hurlburt, N., Roberts, D. A., and Duarte, L. S. (2011). HELIO: The Heliophysics Integrated Observatory. *Advances in Space Research*, 47:2235–2239.
- Benz, A. O., Grigis, P. C., Csillaghy, A., and Saint-Hilaire, P. (2005). Survey on solar X-ray flares and associated coherent radio emissions. *Solar Physics*, 226:121–142.
- Brueckner, G. E., Howard, R. A., Koomen, M. J., Korendyke, C. M., Michels, D. J., Moses, J. D., Socker, D. G., Dere, K. P., Lamy, P. L., Llebaria, A., Bout, M. V., Schwenn, R., Simnett, G. M., Bedford, D. K., and Eyles, C. J. (1995). The Large Angle Spectroscopic Coronagraph (LASCO). *Solar Physics*, 162:357–402.
- Byrne, J. P., Long, D. M., Gallagher, P. T., Bloomfield, D. S., Maloney, S. A., McAteer, R. T. J., Morgan, H., and Habbal, S. R. (2013). Improved methods for determining the kinematics of coronal mass ejections and coronal waves. *Astron. Astrophys.*, 557:A96.
- Byrne, J. P., Morgan, H., Habbal, S. R., and Gallagher, P. T. (2012). Automatic detection and tracking of coronal mass ejections. II. Multiscale filtering of coronagraph images. *Astrophys. J.*, 752:145.
- Cane, H. V., Erickson, W. C., and Prestage, N. P. (2002). Solar flares,

- type III radio bursts, coronal mass ejections, and energetic particles. *Journal of Geophysical Research (Space Physics)*, 107:1315.
- Cane, H. V., McGuire, R. E., and von Roseninge, T. T. (1986). Two classes of solar energetic particle events associated with impulsive and long-duration soft X-ray flares. *Astrophys. J.*, 301:448–459.
- Cane, H. V., Richardson, I. G., and von Roseninge, T. T. (2010). A study of solar energetic particle events of 1997-2006: their composition and associations. *Journal of Geophysical Research (Space Physics)*, 115:8101.
- Cargill, P. J., Vlahos, L., Baumann, G., Drake, J. F., and Nordlund, Å. (2012). Current fragmentation and particle acceleration in solar flares. *Space Sci. Rev.*, 173:223–245.
- Cohen, C. M. S., Mewaldt, R. A., Leske, R. A., Cummings, A. C., Stone, E. C., Wiedenbeck, M. E., Christian, E. R., and von Roseninge, T. T. (1999). New observations of heavy-ion-rich solar particle events from ACE. *Geophys. Res. Lett.*, 26:2697–2700.
- Coplan, M. A., Ogilvie, K. W., Bochsler, P., and Geiss, J. (1984). Interpretation of He-3 abundance variations in the solar wind. *Solar Physics*, 93:415–434.
- Crosby, N. B., Glover, A., Aran, A., Bonnevie, C., Dyer, C., Gabriel, S., Hands, A., Heynderickx, D., Jacobs, C., Jiggins, P., King, D., Lawrence, G., Poedts, S., Sanahuja, B., and Truscott, P. (2010). SEP-EM -Solar Energetic Particle Environment Modelling. In *38th COSPAR Scientific Assembly*, volume 38 of *COSPAR Meeting*, page 4.
- Dalla, S., Balogh, A., Krucker, S., Posner, A., Müller-Mellin, R., Anglin, J. D., Hofer, M. Y., Marsden, R. G., Sanderson, T. R., Tranquille, C., Heber, B., Zhang,

- M., and McKibben, R. B. (2003). Properties of high heliolatitude solar energetic particle events and constraints on models of acceleration and propagation. *Geophys. Res. Lett.*, 30:8035.
- Dalla, S., Marsh, M. S., Kelly, J., and Laitinen, T. (2013). Solar energetic particle drifts in the Parker spiral. *Journal of Geophysical Research (Space Physics)*, 118:5979–5985.
- Dalla, S., Marsh, M. S., and Laitinen, T. (2015). Drift-induced deceleration of solar energetic particles. *Astrophys. J.*, 808:62.
- Dalla, S., Marsh, M. S., Zelina, P., and Laitinen, T. (2017a). Time dependence of Fe/O ratio within a 3D solar energetic particle propagation model including drift. *Astron. Astrophys.*, 598:A73.
- Dalla, S., Swalwell, B., Battarbee, M., Marsh, M., Laitinen, T., and Proctor, S. (2017b). Application of test particle simulations to solar energetic particle forecasting. *Accepted by IAU Symposium 335 Proceedings*.
- DeForest, C. E. (2007). On the size of structures in the solar corona. *Astrophys. J.*, 661:532–542.
- Dierckxsens, M., Tziotziou, K., Dalla, S., Patsou, I., Marsh, M. S., Crosby, N. B., Malandraki, O., and Tsiropoula, G. (2015). Relationship between solar energetic particles and properties of flares and CMEs: statistical analysis of Solar Cycle 23 events. *Solar Physics*, 290:841–874.
- Dietrich, W. F. (1973). The differential energy spectra of solar-flare ^1H , ^3He , and ^4He . *Astrophys. J.*, 180:955–974.
- Dresing, N., Gómez-Herrero, R., Klassen, A., Heber, B., Kartavykh, Y., and Dröge, W. (2012). The large longitudinal spread of solar energetic particles during the 17 January 2010 solar event. *Solar Physics*, 281:281–300.

- Dröge, W., Kartavykh, Y. Y., Dresing, N., Heber, B., and Klassen, A. (2014). Wide longitudinal distribution of interplanetary electrons following the 7 February 2010 solar event: observations and transport modeling. *Journal of Geophysical Research (Space Physics)*, 119:6074–6094.
- Eyles, C., Davis, C., Harrison, R., Waltham, N., Halain, J.-P., Mazy, E., Defise, J.-M., Howard, R., Moses, D., Newmark, J., and Plunkett, S. (2007). In-orbit verification, calibration, and performance of the Heliospheric Imager on the STEREO mission. In *Solar Physics and Space Weather Instrumentation II*, volume 6689 of *Proceedings of SPIE*, page 668907.
- Feynman, J. and Gabriel, S. B. (2000). On space weather consequences and predictions. *J. Geophys. Res.*, 105:10543–10564.
- Firoz, K. A., Gan, W. Q., Li, Y. P., and Rodríguez-Pacheco, J. (2015). An interpretation of a possible mechanism for the first ground-level enhancement of solar cycle 24. *Solar Physics*, 290(2):613–626.
- Garcia, H. A. (1994). Temperature and emission measure from GOES soft X-ray measurements. *Solar Physics*, 154:275–308.
- Garcia, H. A. (2004). Forecasting methods for occurrence and magnitude of proton storms with solar hard X rays. *Space Weather*, 2:S06003.
- Gold, R. E., Krimigis, S. M., Hawkins, III, S. E., Haggerty, D. K., Lohr, D. A., Fiore, E., Armstrong, T. P., Holland, G., and Lanzerotti, L. J. (1998). Electron, Proton, and Alpha Monitor on the Advanced Composition Explorer spacecraft. *Space Sci. Rev.*, 86:541–562.
- Gopalswamy, N., Xie, H., Akiyama, S., Mäkelä, P. A., and Yashiro, S. (2014). Major solar eruptions and high-energy particle events during Solar Cycle 24. *Earth, Planets, and Space*, 66:104.

- Gopalswamy, N., Yashiro, S., Kaiser, M. L., Howard, R. A., and Bougeret, J.-L. (2001). Characteristics of coronal mass ejections associated with long-wavelength type II radio bursts. *Journal of Geophysical Research (Space Physics)*, 106(A12):29219–29229.
- Gopalswamy, N., Yashiro, S., Michalek, G., Stenborg, G., Vourlidas, A., Freeland, S., and Howard, R. (2009). The SOHO/LASCO CME Catalog. *Earth Moon and Planets*, 104:295–313.
- Gosling, J. T. (1993). The solar flare myth. *J. Geophys. Res.*, 98:18937–18950.
- Hargreaves, J. K. (2005). A new method of studying the relation between ionization rates and radio-wave absorption in polar-cap absorption events. *Annales Geophysicae*, 23:359–369.
- Harrison, R. A. and Bewsher, D. (2007). A benchmark event sequence for mass ejection onset studies. A flare associated CME with coronal dimming, ascending pre-flare loops and a transient cool loop. *Astronomy and Astrophysics*, 461:1155–1162.
- Hassler, D. M., Zeitlin, C., Wimmer-Schweingruber, R. F., Böttcher, S., Martin, C., Andrews, J., Böhm, E., Brinza, D. E., Bullock, M. A., Burmeister, S., Ehresmann, B., Epperly, M., Grinspoon, D., Köhler, J., Kortmann, O., Neal, K., Peterson, J., Posner, A., Rafkin, S., Seimetz, L., Smith, K. D., Tyler, Y., Weigle, G., Reitz, G., and Cucinotta, F. A. (2012). The Radiation Assessment Detector (RAD) Investigation. *Space Sci. Rev.*, 170:503–558.
- He, H.-Q. (2015). Perpendicular diffusion in the transport of solar energetic particles from unconnected sources: the counter-streaming particle beams revisited. *Astrophys. J.*, 814:157.

- Hess, P. and Colaninno, R. C. (2017). Comparing automatic CME detections in multiple LASCO and SECCHI catalogs. *Astrophys. J.*, 836:134.
- Hoeksema, J. T., Wilcox, J. M., and Scherrer, P. H. (1983). The structure of the heliospheric current sheet - 1978-1982. *J. Geophys. Res.*, 88:9910–9918.
- Hoff, J. L., Townsend, L. W., and Zapp, E. N. (2004). Interplanetary crew doses and dose equivalents: variations among different bone marrow and skin sites. *Advances in Space Research*, 34:1347–1352.
- Hsieh, K. C. and Simpson, J. A. (1970). The relative abundances and energy spectra of ^3He and ^4He from solar flares. *Astrophys. J. Letters*, 162:L191.
- Hughitt, V. K., Ireland, J., and Mueller, D. (2011). Helioviewer.org: simple solar and heliospheric data visualization. *AGU Fall Meeting Abstracts*.
- Inglis, A., Bobra, M., Christe, S., Hewett, R., Ireland, J., Mumford, S., Martinez Oliveros, J. C., Perez-Suarez, D., Reardon, K. P., Savage, S., Shih, A. Y., Ryan, D., Sipocz, B., and Freij, N. (2017). SunPy 0.8 - Python for Solar Physics. In *AAS/Solar Physics Division Meeting*, volume 48 of *AAS/Solar Physics Division Meeting*, page 115.06.
- Ippolito, A., Pommois, P., Zimbardo, G., and Veltri, P. (2005). Magnetic connection from the Earth to the solar corona, flare positions and solar energetic particle observations. *Astron. Astrophys.*, 438:705–711.
- Jian, Y., Lai, M., and Ding, L.-Q. (2015). A statistical study on the ascending times of solar energetic particle events. *Chinese Astronomy and Astrophysics*, 39:225–237.
- Kahler, S. W., Cliver, E. W., and Ling, A. G. (2007). Validating the proton prediction system (PPS). *Journal of Atmospheric and Solar-Terrestrial Physics*, 69:43–49.

- Kahler, S. W., Sheeley, Jr., N. R., Howard, R. A., Michels, D. J., Koomen, M. J., McGuire, R. E., von Rosenvinge, T. T., and Reames, D. V. (1984). Associations between coronal mass ejections and solar energetic proton events. *J. Geophys. Res.*, 89:9683–9693.
- Kallenrode, M.-B. (1998). *Energetic Particles in the Heliosphere*, pages 187–210. Springer Berlin Heidelberg, Berlin, Heidelberg.
- Klecker, B., Hovestadt, D., Moebius, E., Scholer, M., Gloeckler, G., and Ipavich, F. M. (1983). Direct determination of the ionic charge distribution of heavy ions in Fe-rich solar energetic particle events. *International Cosmic Ray Conference*, 10:330–333.
- Klein, K.-L., Chupp, E. L., Trotter, G., Magun, A., Dunphy, P. P., Rieger, E., and Urpo, S. (1999). Flare-associated energetic particles in the corona and at 1 AU. *Astron. Astrophys.*, 348:271–285.
- Klein, K.-L., Trotter, G., and Klassen, A. (2010). Energetic particle acceleration and propagation in strong CME-less flares. *Solar Physics*, 263:185–208.
- Klein, K.-L., Trotter, G., Samwel, S., and Malandraki, O. (2011). Particle acceleration and propagation in strong flares without major solar energetic particle events. *Solar Physics*, 269:309–333.
- Kliem, B., Karlický, M., and Benz, A. O. (2000). Solar flare radio pulsations as a signature of dynamic magnetic reconnection. *Astron. Astrophys.*, 360:715–728.
- Laitinen, T., Dalla, S., and Marsh, M. S. (2013). Energetic particle cross-field propagation early in a solar event. *Astrophys. J. Letters*, 773:L29.
- Laitinen, T., Kopp, A., Effenberger, F., Dalla, S., and Marsh, M. S. (2016). Solar energetic particle access to distant longitudes through turbulent field-line meandering. *Astron. Astrophys.*, 591:A18.

- Laurenza, M., Cliver, E. W., Hewitt, J., Storini, M., Ling, A. G., Balch, C. C., and Kaiser, M. L. (2009). A technique for short-term warning of solar energetic particle events based on flare location, flare size, and evidence of particle escape. *Space Weather*, 7:4008.
- Lawrence, D. J., Peplowski, P. N., Feldman, W. C., Schwadron, N. A., and Spence, H. E. (2016). Galactic cosmic ray variations in the inner heliosphere from solar distances less than 0.5 AU: measurements from the MESSENGER Neutron Spectrometer. *Journal of Geophysical Research (Space Physics)*, 121:7398–7406.
- Lee, M. A. (2005). Coupled hydromagnetic wave excitation and ion acceleration at an evolving coronal/interplanetary shock. *Astrophys. J. Supple.*, 158:38–67.
- Li, G., Moore, R., Mewaldt, R. A., Zhao, L., and Labrador, A. W. (2012). A twin-CME scenario for Ground Level Enhancement Events. *Space Science Reviews*, 171(1):141–160.
- Lin, R. P. (1970). The emission and propagation of 40 keV solar flare electrons. I: The relationship of 40 keV electron to energetic proton and relativistic electron emission by the Sun. *Solar Physics*, 12:266–303.
- Luhmann, J. G., Ledvina, S. A., Odstrcil, D., Owens, M. J., Zhao, X.-P., Liu, Y., and Riley, P. (2010). Cone model-based SEP event calculations for applications to multipoint observations. *Advances in Space Research*, 46:1–21.
- Luhn, A., Klecker, B., Hovestadt, D., and Moebius, E. (1987). The mean ionic charge of silicon in He-3-rich solar flares. *Astrophys. J.*, 317:951–955.
- Mann, G., Aurass, H., and Warmuth, A. (2006). Electron acceleration by the reconnection outflow shock during solar flares. *Astron. Astrophys.*, 454:969–974.
- Marsh, M. S., Dalla, S., Dierckxsens, M., Laitinen, T., and Crosby, N. B. (2015).

- Sparx: A modeling system for solar energetic particle radiation space weather forecasting. *Space Weather*, 13(6):386–394. 2014SW001120.
- Marsh, M. S., Dalla, S., Kelly, J., and Laitinen, T. (2013). Drift-induced perpendicular transport of solar energetic particles. *Astrophys. J.*, 774:4.
- Mason, G. M., Reames, D. V., von Rosenvinge, T. T., Klecker, B., and Hovestadt, D. (1986). The heavy-ion compositional signature in He-3-rich solar particle events. *Astrophys. J.*, 303:849–860.
- Masson, S., Dmoulin, P., Dasso, S., and Klein, K.-L. (2012). The interplanetary magnetic structure that guides solar relativistic particles. *Astron. Astrophys.*, 538:A32.
- Miller, J. A., Larosa, T. N., and Moore, R. L. (1996). Stochastic electron acceleration by cascading fast mode waves in impulsive solar flares. *Astrophys. J.*, 461:445.
- Miller, J. A. and Roberts, D. A. (1995). Stochastic proton acceleration by cascading Alfvén waves in impulsive solar flares. *Astrophys. J.*, 452:912.
- Morgan, H., Byrne, J. P., and Habbal, S. R. (2012). Automatically detecting and tracking coronal mass ejections. I. Separation of dynamic and quiescent components in coronagraph images. *Astrophys. J.*, 752:144.
- Nitta, N. V., Reames, D. V., De Rosa, M. L., Liu, Y., Yashiro, S., and Gopalswamy, N. (2006). Solar sources of impulsive solar energetic particle events and their magnetic field connection to the Earth. *Astrophys. J.*, 650:438–450.
- Núñez, M. (2011). Predicting solar energetic proton events ($E > 10$ MeV). *Space Weather*, 9(7). S07003.
- Odstrčil, D., Pizzo, V. J., Linker, J. A., Riley, P., Lionello, R., and Mikic, Z.

- (2004). Initial coupling of coronal and heliospheric numerical magnetohydrodynamic codes. *Journal of Atmospheric and Solar-Terrestrial Physics*, 66:1311–1320.
- Olmedo, O., Zhang, J., Wechsler, H., Poland, A., and Borne, K. (2008). Automatic detection and tracking of coronal mass ejections in coronagraph time series. *Solar Physics*, 248:485–499.
- Owens, M. J. and Forsyth, R. J. (2013). The Heliospheric Magnetic Field. *Living Reviews in Solar Physics*, 10:5.
- Pallavicini, R., Serio, S., and Vaiana, G. S. (1977). A survey of soft X-ray limb flare images - The relation between their structure in the corona and other physical parameters. *Astrophys. J.*, 216:108–122.
- Papaioannou, A., Anastasiadis, A., Sandberg, I., Georgoulis, M. K., Tsiropoula, G., Tziotziou, K., Jiggins, P., and Hilgers, A. (2015). A novel Forecasting System for Solar Particle Events and Flares (FORSPEF). *Journal of Physics: Conference Series*, 632(1):012075.
- Park, J., Moon, Y.-J., and Gopalswamy, N. (2012). Dependence of solar proton events on their associated activities: coronal mass ejection parameters. *Journal of Geophysical Research (Space Physics)*, 117:A08108.
- Parker, E. N. (1958). Dynamics of the interplanetary gas and magnetic fields. *Astrophys. J.*, 128:664.
- Parker, E. N. (1961). *The Solar Wind*, page 157.
- Petrosian, V. (2012). Stochastic acceleration by turbulence. *Space Sci. Rev.*, 173:535–556.

- Posner, A. (2007). Up to 1-hour forecasting of radiation hazards from solar energetic ion events with relativistic electrons. *Space Weather*, 5(5). S05001.
- Reames, D. V. (1999). Particle acceleration at the Sun and in the heliosphere. *Space Sci. Rev.*, 90:413–491.
- Reames, D. V., Barbier, L. M., and Ng, C. K. (1996). The spatial distribution of particles accelerated by coronal mass ejection–driven shocks. *Astrophys. J.*, 466:473.
- Reid, H. A. S. and Vilmer, N. (2017). Coronal type III radio bursts and their x-ray flare and interplanetary type III counterparts. *Astron. Astrophys.*, 597:A77.
- Richardson, I. G., von Rosenvinge, T. T., and Cane, H. V. (2015). The properties of solar energetic particle event-associated coronal mass ejections reported in different CME catalogs. *Solar Physics*, 290:1741–1759.
- Robbrecht, E. and Berghmans, D. (2004). Automated recognition of coronal mass ejections (CMEs) in near-real-time data. *Astron. Astrophys.*, 425:1097–1106.
- Serlemitsos, A. T. and Balasubrahmanyam, V. K. (1975). Solar particle events with anomalously large relative abundance of He-3. *Astrophys. J.*, 198:195–204.
- Shen, C., Li, G., Kong, X., Hu, J., Sun, X. D., Ding, L., Chen, Y., Wang, Y., and Xia, L. (2013). Compound twin coronal mass ejections in the 2012 May 17 GLE event. *Astrophys. J.*, 763(2):114.
- Smart, D. F. and Shea, M. A. (1989). PPS-87 - A new event oriented solar proton prediction model. *Advances in Space Research*, 9:281–284.
- St. Cyr, O. C., Posner, A., and Burkepile, J. T. (2017). Solar energetic particle warnings from a coronagraph. *Space Weather*, 15(1):240–257. 2016SW001545.

- Stone, E. C., Cohen, C. M. S., Cook, W. R., Cummings, A. C., Gauld, B., Kecman, B., Leske, R. A., Mewaldt, R. A., Thayer, M. R., Dougherty, B. L., Grumm, R. L., Milliken, B. D., Radocinski, R. G., Wiedenbeck, M. E., Christian, E. R., Shuman, S., and von Rosenvinge, T. T. (1998). The Solar Isotope Spectrometer for the Advanced Composition Explorer. *Space Sci. Rev.*, 86:357–408.
- Strauss, R. D. T., Dresing, N., and Engelbrecht, N. E. (2017). Perpendicular diffusion of solar energetic particles: model results and implications for electrons. *Astrophys. J.*, 837:43.
- Swalwell, B., Dalla, S., and Walsh, R. (2017a). Solar energetic particle forecasting algorithms and associated false alarms. *Solar Physics*, 292(11):173.
- Swalwell, B., Dalla, S., and Walsh, R. (2017b). Forecasting solar energetic particle events and associated false alarms. *Accepted by IAU Symposium 335 Proceedings*.
- Thompson, W. T., Davila, J. M., Fisher, R. R., Orwig, L. E., Mentzell, J. E., Hetherington, S. E., Derro, R. J., Federline, R. E., Clark, D. C., Chen, P. T. C., Tveekrem, J. L., Martino, A. J., Novello, J., Wesenberg, R. P., StCyr, O. C., Reginald, N. L., Howard, R. A., Mehalick, K. I., Hersh, M. J., Newman, M. D., Thomas, D. L., Card, G. L., and Elmore, D. F. (2003). COR1 inner coronagraph for STEREO-SECCHI. In Keil, S. L. and Avakyan, S. V., editors, *Innovative Telescopes and Instrumentation for Solar Astrophysics*, volume 4853 of *Proceedings of SPIE*, pages 1–11.
- Torsti, J., Valtonen, E., Lumme, M., Peltonen, P., Eronen, T., Louhola, M., Riihonen, E., Schultz, G., Teittinen, M., Ahola, K., Holmlund, C., Kelhä, V., Leppälä, K., Ruuska, P., and Strömmer, E. (1995). Energetic Particle Experiment ERNE. *Solar Physics*, 162:505–531.

- Tsuneta, S. (1985). Heating and acceleration processes in hot thermal and impulsive solar flares. *Astrophys. J.*, 290:353–358.
- Van Hollebeke, M. A. I., Ma Sung, L. S., and McDonald, F. B. (1975). The variation of solar proton energy spectra and size distribution with heliolongitude. *Solar Physics*, 41:189–223.
- Wang, Y. and Zhang, J. (2007). A comparative study between eruptive X-class flares associated with coronal mass ejections and confined X-class flares. *Astrophys. J.*, 665:1428–1438.
- Wiedenbeck, M. E., Mason, G. M., Cohen, C. M. S., Nitta, N. V., Gómez-Herrero, R., and Haggerty, D. K. (2013). Observations of solar energetic particles from ^3He -rich events over a wide range of heliographic longitude. *Astrophys. J.*, 762:54.
- Wilcox, J. M. and Ness, N. F. (1965). Quasi-stationary corotating structure in the interplanetary medium. *J. Geophys. Res.*, 70(23):5793–5805.
- Wild, J. P. and McCready, L. L. (1950). Observations of the spectrum of high-intensity solar radiation at metre wavelengths. I. The apparatus and spectral types of solar burst observed. *Australian Journal of Scientific Research A, Physical Sciences*, 3:387.
- Wild, J. P., Smerd, S. F., and Weiss, A. A. (1963). Solar bursts. *Ann. Rev. Astron, Astrophys.*, 1:291.
- Yashiro, S., Akiyama, S., Gopalswamy, N., and Howard, R. A. (2006). Different power-law indices in the frequency distributions of flares with and without coronal mass ejections. *Astrophys. J. Letters*, 650:L143–L146.
- Zank, G. P., Rice, W. K. M., and Wu, C. C. (2000). Particle acceleration and coronal mass ejection driven shocks: A theoretical model. *J. Geophys. Res.*, 105:25079–25096.

Zelina, P., Dalla, S., Cohen, C. M. S., and Mewaldt, R. A. (2017). Time evolution of elemental ratios in solar energetic particle events. *Astrophys. J.*, 835:71.

Zharkova, V. V., Arzner, K., Benz, A. O., Browning, P., Dauphin, C., Emslie, A. G., Fletcher, L., Kontar, E. P., Mann, G., Onofri, M., Petrosian, V., Turkmani, R., Vilmer, N., and Vlahos, L. (2011). Recent advances in understanding particle acceleration processes in solar flares. *Space Sci. Rev.*, 159:357–420.

Appendix A

Choice of CME and flare catalogues

This work is aimed at discovering which of the parameters of solar events discussed in Sections 3.1 and 3.2 are important in SEP production. However it was also mentioned that there are different ways of measuring these parameters, and that there are a number of different catalogues of the different types of solar event which include values for these parameters. Consequently a decision had to be made as to which of the catalogues and SEP data should be used as a basis for this study. In Section A.1 the various CME catalogues are discussed, the flare catalogues in Section A.2, and SEP data in Section A.3.

A.1 CME catalogues

Typically each CME catalogue publishes data on, *inter alia*, the parameters mentioned in Section 3.1, although the method employed to derive the values for each of these parameters is usually not the same. Richardson *et al.* (2015) made a comparison of CME speed and width as reported in all four catalogues in respect of 145 CMEs which were said to be associated with enhancements at Earth of 25 MeV proton flux,

and reported that the published parameters can differ significantly from catalogue to catalogue. Hess and Colaninno (2017) compared the automated detection systems and concluded that, whilst they are well-correlated with each other when considering CME detection, “*the other statistics should be used with caution*”.

In order to establish which of the catalogues should be used to provide data for this work, an investigation was carried out with a view to discovering exactly how the parameters published in the catalogues differed from one another. The CORIMP catalogue had to be excluded from this analysis as the website does not publish their data in a suitable format.

For the three remaining catalogues, all published data between 17 May 1997 and 31 March 2013, and henceforth it is this time period which is considered. In that time CACTus reported 13,889 CMEs, SEEDS 36,028, and CDAW 19,960. However, it is known that the automatic detection systems may confuse small-scale outflows with CMEs, and so, in order to avoid this confusion, events which have a reported width equal to or less than 20° have been excluded. This approach is consistent with that adopted by Hess and Colaninno (2017). Applying this razor reduces the numbers of CMEs reported by each catalogue to 7,528, 14,372 and 13,566 respectively.

A.1.1 Speed

As discussed in Section 3.1.1, the various catalogues publish different estimates of CME speed. Both SEEDS and CDAW give a value based upon a linear fit to height-time measurements, and so it is these values which have been chosen as a basis for comparison. For the data from the CACTus catalogue, the maximum velocity value has been used (and wherever henceforth the CACTus speed is referred to, it is this maximum velocity which is intended).

Table A.1 summarises the number of CMEs reported by each catalogue which have a width greater than 20° , and gives the average speed of those CMEs together

Table A.1: Table comparing CME speeds as reported by the 3 catalogues. Column 1 gives the name of the catalogue; column 2 shows the number of CMEs (having a width exceeding 20°) reported by that catalogue; column 3 gives the average speed of those CMEs; and column 4 the speed of the fastest reported CME.

Catalogue	Number of CMEs	Average speed (km/s)	Speed of fastest CME (km/s)
CACTus	7,528	774	2,027
SEEDS	14,372	284	7,671
CDAW	13,566	418	3,387

with the fastest reported CME speed. The most notable result to be taken from this table is that SEEDS has the lowest average speed of the 3 catalogues, but reports the fastest speed at 7,671 km/s: in fact SEEDS reports 11 CMEs to have a speed in excess of 3,000 km/s. The CACTus threshold of about 2,000 km/s is also evident.

Figure A.1 show histograms of CME speed distribution as reported by the 3 catalogues (the x-axis has been curtailed at 3,000 km/s). The histogram for the CACTus catalogue has its peak between CME speeds of 400 - 500 km/s; for SEEDS and CDAW the peak is between 200 - 300 km/s.

CACTus reports a relatively high proportion of CMEs with a speed exceeding 1,000 km/s; SEEDS reports very few above that limit; CDAW reports some, but the percentage of CMEs with a speed above that threshold is much lower than that reported by CACTus.

It is already known that the faster the CME, the more likely it is that SEPs will be detected at Earth (Dierckxsens *et al.* (2015)), and consequently it is CMEs with a reported speed equal to or greater than 1,500 km/s (fast CMEs) which will be

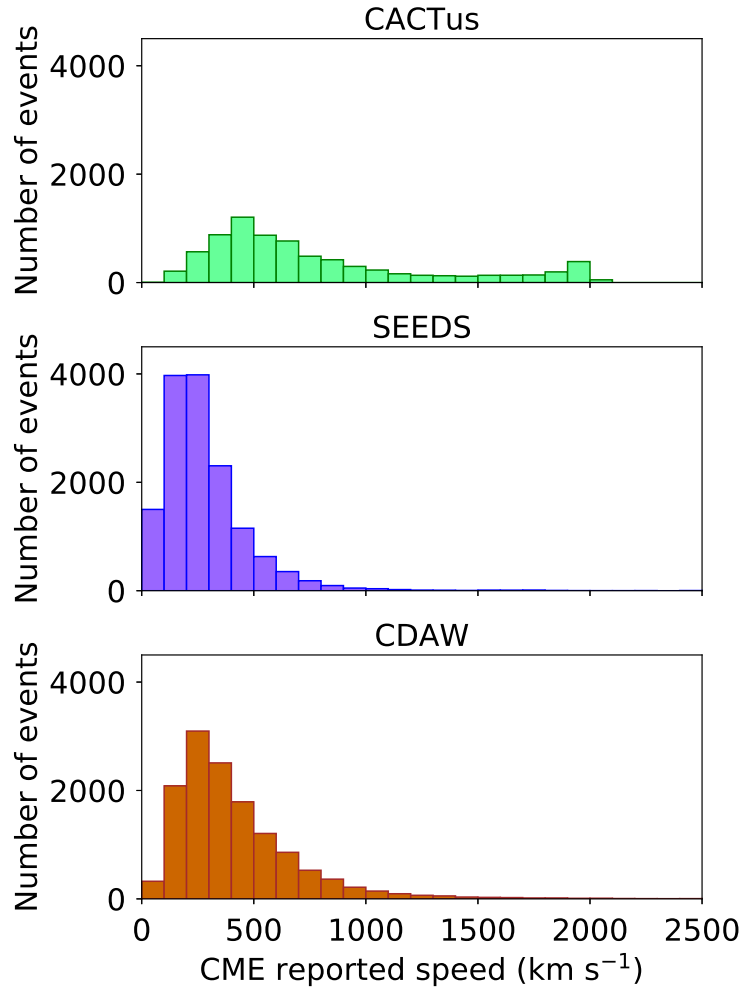


Figure A.1: Histograms of the speed of CMEs (in km/s) as reported by the 3 CME catalogues.

considered further. The question is whether a fast CME reported in, say, CACTus, is also reported to be a fast CME by the other catalogues.

In order to determine the answer, it has been assumed that if catalogues have reported a CME within 1 hour of each other it is most likely that they are reporting the same CME. Thus, the following procedure was adopted:

1. Find all the fast CMEs as reported by one of the catalogues (the “base catalogue”).

2. For each fast CME in the base catalogue, search the other two catalogues (“the searched catalogues”) for any CME which they report as having occurred within ± 1 hour (the “search period”) of the fast CME.
3. If a CME is reported by the searched catalogues to have occurred within the search period, assume that that CME corresponds to the fast CME reported in the base catalogue.
4. If no CME is reported by either or both of the searched catalogues to have occurred within the search period, then assume that those catalogues do not report the fast CME reported in the base catalogue.
5. If there is more than one CME reported in either of the searched catalogues to have occurred within the search period, assume that it is the fastest which corresponds to the fast CME reported in the base catalogue.
6. Repeat the procedure, taking each catalogue as the base catalogue in turn.

Following this algorithm, the following results were found (they are summarised in Table A.2):

- Taking CACTus as the base catalogue, it reported 1,044 fast CMEs. SEEDS reported 586 CMEs to have occurred within the search periods (of which only 4 were fast CMEs), and CDAW 581 (of which 108 were fast CMEs). Thus, there are 458 CMEs which were fast CMEs according to CACTus but which have no corresponding report in SEEDS; 463 have no corresponding report in CDAW.
- Taking SEEDS as the base catalogue, it reported just 66 fast CMEs. CACTus reported 10 CMEs to have occurred with the search periods (of which 3 were fast CMEs), and CDAW 12 (of which 0 were fast CMEs). Thus, there are

Table A.2: Table comparing fast CME speeds as reported by the 3 catalogues. Column 1 gives the name of the catalogue which was used as a base for the analysis, and column 2 shows the number of fast CMEs reported in that catalogue. Column 3 gives the corresponding number of CMEs in the CACTus catalogue; column 4 the number of corresponding CMEs in the SEEDS catalogue; and column 5 number of corresponding CMEs in the CDAW catalogue. In columns 3, 4, and 5 the number in brackets indicates the number of CMEs which were fast CMEs.

Base catalogue	Number of fast CMEs	Number of corresponding (fast) CMEs in CACTus	Number of corresponding (fast) CMEs in SEEDS	Number of corresponding (fast) CMEs in CDAW
CACTus	1,044	–	586 (4)	581 (108)
SEEDS	66	10 (3)	–	12 (0)
CDAW	141	121 (80)	108 (0)	–

56 CMEs which were fast CMEs according to SEEDS but which have no corresponding report in CACTus; 54 have no corresponding report in CDAW.

- Taking CDAW as the base catalogue, it reported 141 fast CMEs. CACTus reported 121 CMEs to have occurred within the search periods (of which 89 were fast CMEs), and SEEDS 108 (of which 0 were fast CMEs): Thus, there are 20 CMEs which were fast CMEs according to CDAW but which have no corresponding report in CACTus; 33 have no corresponding report in SEEDS.

It is surprising that there is so little correlation between the catalogues. For example, CACTus reports more than 7 times the number of fast CMEs as CDAW, and nearly 16 times as many as SEEDS. Equally troubling is that each of the catalogues reports a significant number of fast CMEs which do not appear to have been

observed by the others.

Of most concern for this work, however, is the fact that the catalogues do not agree on whether a CME is a fast CME or not. Of the 1,044 fast CMEs reported by CACTus for example, only about 10% are said to be fast CMEs by CDAW, and rather less than 1% are fast CMEs according to SEEDS.

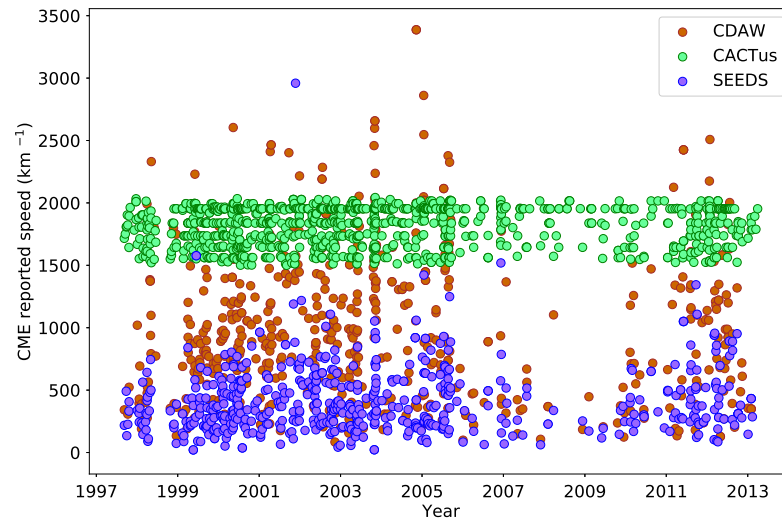
In Figure A.2 the speeds of these CMEs are plotted against time - CACTus CMEs are represented by green dots, SEEDs CMEs by purple dots, and CDAW CMEs by brown dots. These plots show, as might have been expected from Figure A.1, that the speeds of both the CACTus and CDAW fast CMEs were reported by SEEDS to be much slower. In fact, the trend appears to be that the fast CMEs reported by each catalogue are either not reported by the other catalogues at all, or are reported to have a much lower speed. The 2,000 km/s threshold for the CACTus data is shown starkly in Figure A.2a.

Interestingly, the CACTus data show that whilst there was a reduction in number of fast CMEs during solar minimum (between about 2007 and 2010), there was still a significant number of such CMEs; SEEDS and CDAW report none during those years.

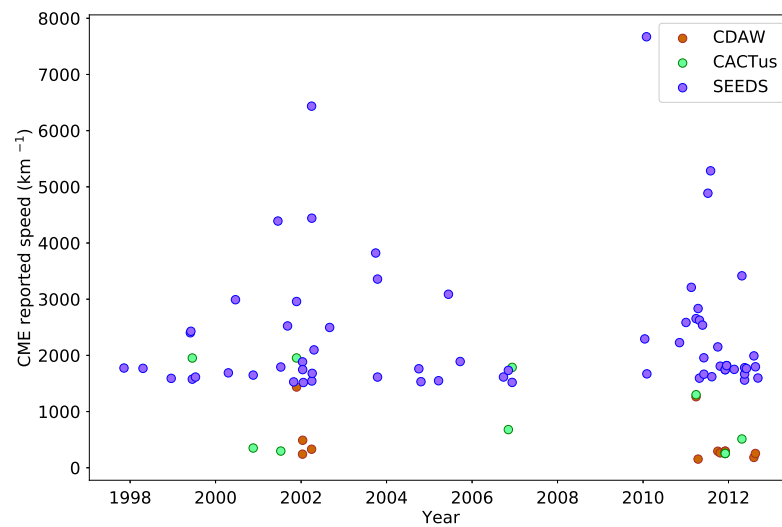
A.1.2 Acceleration

The CACTus catalogue does not publish data on whether a CME has accelerated or decelerated within the LASCO coronagraphs fields of view. Whilst SEEDS does publish data on CME acceleration, for the fast CMEs at least, those data are somewhat limited: for only 12 of the 66 fast CMEs reported by SEEDS is an estimate of acceleration given, and this number is too low for any meaningful conclusions to be drawn.

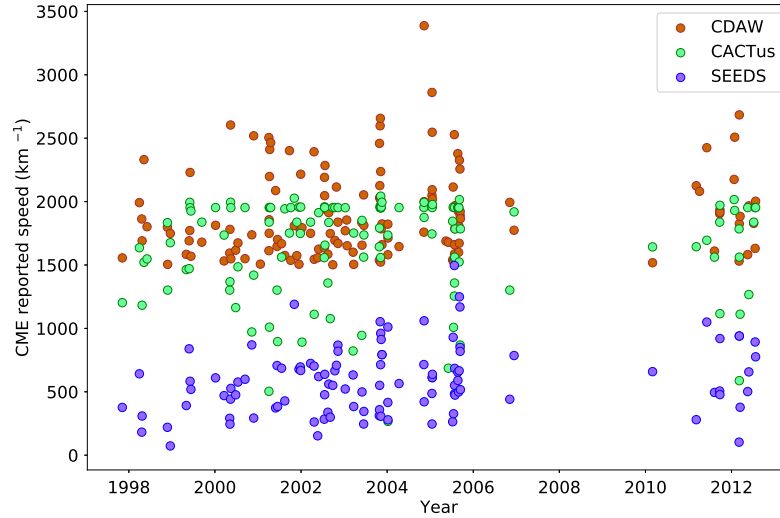
CDAW, however, publishes an estimate of the acceleration / deceleration for 136 of the 141 fast CMEs in its catalogue. Figure A.3 is a histogram for the acceleration



(a) Fast CMEs as reported by CACTus plotted against time (green dots). The speeds of the corresponding CMEs reported by SEEDS (purple dots) and CDAW (brown dots) are also plotted.



(b) Fast CMEs as reported by SEEDs plotted against time (purple dots). The speeds of the corresponding CMEs reported by CACTus (green dots) and CDAW (brown dots) are also plotted.



(c) Fast CMEs as reported by CDAW plotted against time (brown dots). The speeds of the corresponding CMEs reported by CACTus (green dots) and SEEDS (purple dots) are also plotted.

Figure A.2: A comparison of how the 3 different catalogues report the speed of the same CME. Figure A.2a takes CACTus as its base catalogue, Figure A.2b uses SEEDS as its base, and the base for Figure A.2c is CDAW. In all plots, CACTus data are shown by green dots, SEEDS by purple dots, and CDAW by brown dots.

of fast CMEs as reported by CDAW. It can be seen that most are said to not to change speed significantly as they travel through the LASCO coronagraphs fields of view.

A.1.3 Width

It was noted in Section 3.1.3 that determination of CME width is by no means straightforward, and the widths of CMEs specified in the 3 catalogues vary considerably. Figure A.4 shows histograms of the widths of the fast CMEs as reported in

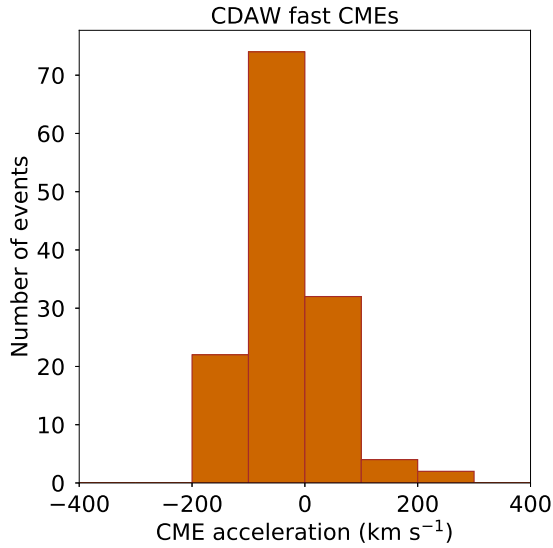


Figure A.3: Histogram of distribution of fast CME acceleration as reported by the CDAW catalogue.

each of the 3 catalogues. Bin size is 30° .

There are some similarities between the CACTus and SEEDS width distributions in that both suggest that even for fast CMEs the width of the CME is likely to be less than 60° . However for CDAW a fast CME is overwhelmingly likely to be reported as a halo.

A.1.4 Position angle

It was noted in Section 3.1.4 that CDAW published 2 values for position angle. For this analysis, it is the measurement position angle which is used.

It is to be expected that, because CMEs originate from magnetically active regions on the solar surface which tend to be located within about $\pm 40^\circ$ of the solar equator, position angles should tend to be close to 90° and 270° . Figure A.5 shows the distribution of position angles as reported by the 3 catalogues. All 3 histograms show the 2 expected peaks, although the peaks are less clear in the CACTus data.

It should be added that the SEEDS catalogue reports that 326 of the CMEs

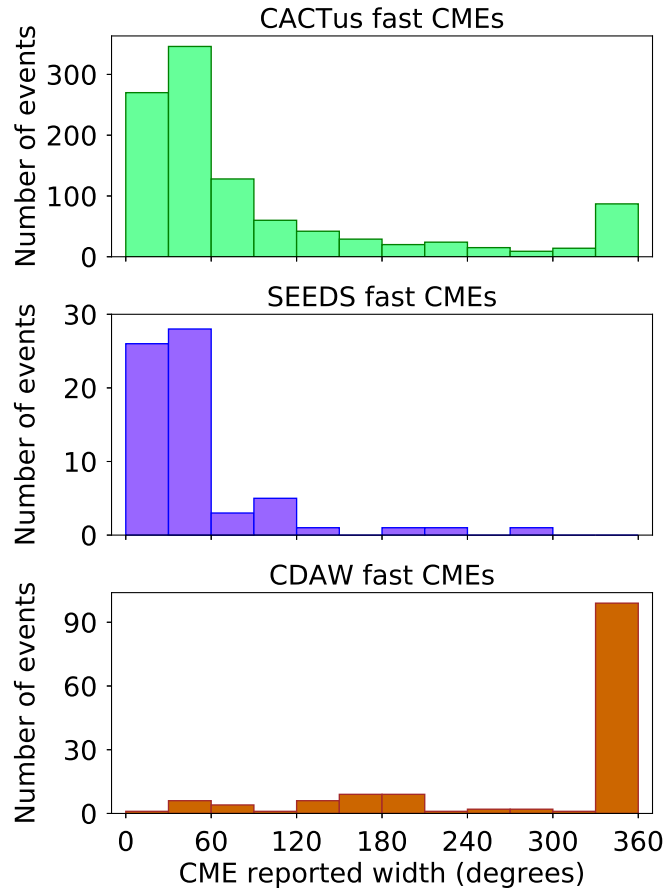


Figure A.4: Histograms of the widths of the fast CMEs (in degrees) as reported by the 3 CME catalogues. The results for CACTus are shown at the top in green, SEEDS in the middle in purple, and CDAW at the bottom in brown. Bin size is 30 degrees.

reported by them (including 2 of the fast CMEs) have a position angle exceeding 360° (one is high as 449°). Given that, by definition, a position angle can be 360° at most, this is unsettling.

A.1.5 Discussion

There is little correlation between the data published in the 3 CME catalogues which have been analysed. The catalogues do not seem to be able to agree on how many

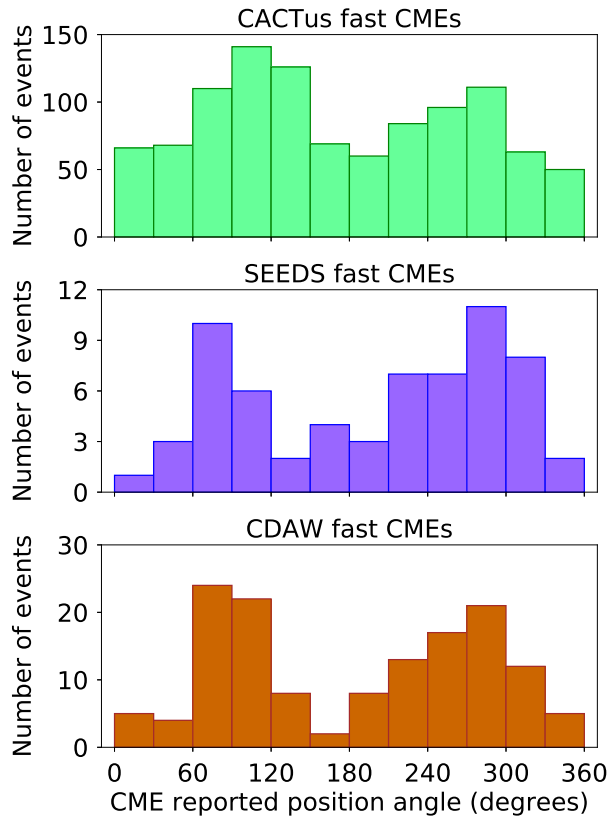


Figure A.5: Distribution of position angle measurements of the fast CMEs (in degrees) as reported by the 3 CME catalogues. The results for CACTus are shown at the top in green, SEEDS in the middle in purple, and CDAW at the bottom in brown. Bin size is 30 degrees.

CMEs have occurred, whether a CME is a fast one, nor upon how wide a CME may be. This makes the choice of which catalogue to use as the basis for this study very difficult.

It has not been possible to consider the CORIMP catalogue, and so it is not known how it compares to the other three. However, it contains data only from January 2000, and given that it is intended in this work to analyse data over as long a period as possible, its use has been excluded on this basis.

There are good reasons not to use the SEEDS catalogue: the average speed of

CMEs reported by it is very low, yet some of the speeds reported by the catalogue seem to be unfeasibly high; only 66 of the CMEs were said to be fast CMEs, but, of these, very few were reported to be fast CMEs by the other catalogues (although this is a criticism which may be levelled also at the other catalogues, it is particularly the case for SEEDS); and there are clearly errors in determination of a CME's position angle.

As far as CACTus is concerned, the inability to measure the speed of a CME which exceeds $\sim 2,000$ km/s is a major handicap, and the total number of fast CMEs which the catalogue reports (especially during solar minimum) is questionable.

CDAW is by no means the perfect choice. The catalogue is produced manually, and is therefore susceptible to the subjective interpretation of the C2 images by the person who prepares it. It may be that the catalogue has been produced by more than one person over the years, and consequently interpretation of CME features may not be consistent. Furthermore, the percentage of fast CMEs which CDAW reports as halos is extremely high. Nevertheless, given the shortcomings of the other two catalogues which have been considered, on balance it is the CDAW catalogue which has been chosen to provide the CME data for this study.

One of the aims of this work is improve the forecasting of SEP events. The choice of CDAW as the source for data on CME parameters means that it will not be possible to produce an SEP forecasting algorithm which is based upon real-time data. That said, from the analysis of the automated systems, it seems clear that automated CME detection algorithms will have to improve significantly if they are to form the basis for future real-time SEP forecasting.

A.2 Flare catalogues

Fortunately, the choice as to which of the flare catalogues to use as a source for data is rather more straightforward. According to the Heliophysics Integrated Observatory

website¹ (Bentley *et al.* (2011)), there are 7 currently active solar flare catalogues. However, only the GOES SXR Flare List and the Kanzelhöhe Solar Observatory H α Flare List give data from as long ago as the 1980s. For this work it is peak SXR flux which is the most important parameter, and the Kanzelhöhe list does not provide this information. Consequently the choice of catalogue is limited to only the GOES list.

There are, however, two difficulties with that list. The first is that prior to 28th April 1980 peak SXR flux is reported in a different format to the way it is reported after that date. It is not entirely clear exactly how that early format should be interpreted, and it therefore seems appropriate to limit the analysis in this work to flares which have occurred after 28th April 1980.

The second problem is that the GOES SXR list does not publish the heliographic co-ordinates for all the flares it reports. In these cases co-ordinates of flares have been obtained from the following sources:

1. Co-ordinates reported in the SolarSoft Latest Events Flares List (gevloc) (which may also be obtained through Helio). This list, however, only contains details of flares which have occurred since 26th September 2002 and, even then, list does not report the co-ordinates of every flare.
2. The reported co-ordinates of the active region from which the flare originated according to the GOES SXR flare list.
3. Making an estimate of co-ordinates by watching movies of 195Å images taken by Extreme ultraviolet Imaging Telescope (EIT) on board the SOHO spacecraft or of 193Å images taken by the Atmospheric Imaging Assembly (AIA) carried by the Solar Dynamics Observatory (SDO).

¹<http://hfe.helio-vo.eu/Helio/>

A.3 SEP data

As was seen in Section 3.3 there is a number of currently operational instruments which are capable of detecting SEPs. In this study high energy ($>\sim 40$ MeV) protons are analysed, and this means that the EPAM and SIS instruments must be excluded. Equally, neutron monitors do not provide information on the energy of protons which is needed. The choice is therefore between ERNE and GOES EPS.

The minimum threshold for detection of an enhancement of ~ 40 MeV protons by ERNE is $\sim 10^{-4}$ particles $\text{cm}^{-2} \text{sr}^{-1} \text{s}^{-1} \text{MeV}^{-1}$. For the GOES EPS instrument, however, it is $\sim 10^{-2}$ particles $\text{cm}^{-2} \text{sr}^{-1} \text{s}^{-1} \text{MeV}^{-1}$. It is not known whether this difference is produced by the design of the instrument, or whether the reduced sensitivity of the GOES EPS is a consequence of the fact that it is carried by a spacecraft which is in an orbit much closer to Earth, and which is therefore partially shielded from energetic particles by the Earth's magnetosphere.

Whatever the cause, the difference in sensitivity produces a difficulty which is illustrated by Figure A.6. This is a plot of proton intensities as measured by the ERNE (orange line) and GOES 10 EPS (blue line) instruments between the start of 2 March 2000 and the end of 4 March 2000. According to the ERNE instrument there are two events which show an almost 50-fold enhancement of protons in the 40.0 - 51.0 MeV channel. However the sensitivity of the GOES EPS instrument for proton intensity in the 40.0 - 80.0 MeV channel is such that the events are not seen by that instrument.

This means that choice of instrument will have an effect upon how many SEP events are detected. In many ways the natural choice would be to use the more sensitive ERNE, but there are two reasons why it has been decided to use the GOES EPS:

1. ERNE is on board the SOHO spacecraft which was launched only in 1995.

It is intended that this study will consider solar events which occurred in the

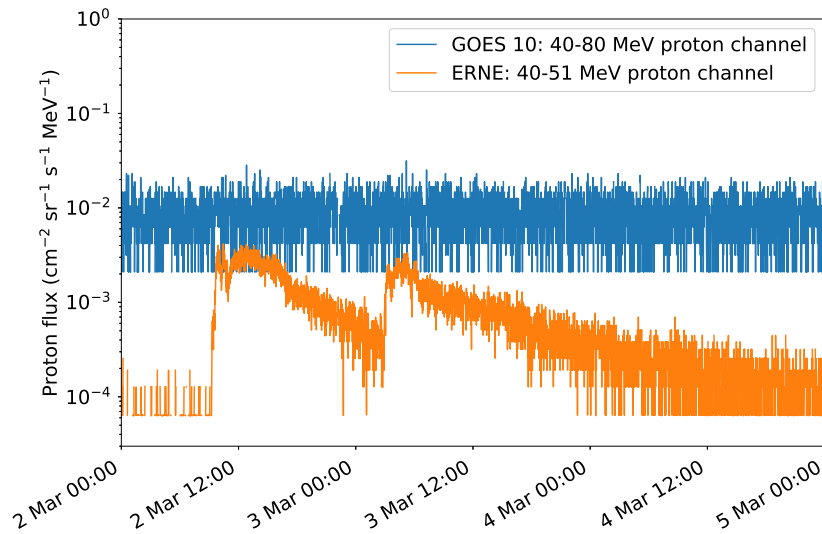


Figure A.6: Proton intensities in the 40 to 51 MeV channel of ERNE channel (orange line) and in the 40 to 80 MeV channel of GOES 10 EPS (blue line) instruments between 2 March 2000 and the end of 4 March 2000.

1980s, and consequently ERNE is not able to provide data over the whole period under investigation. Consideration was given to using the GOES EPS for events prior to the launch of SOHO, and ERNE thereafter, but consistency was regarded as paramount.

2. ERNE is subject to a number of data gaps which have become more frequent as the instrument ages. Had ERNE been used, very many solar events would have had to be discarded as it could not be known whether or not they had produced SEPs.

Appendix B

Flare and CME associations

In order to develop a method of making flare-CME associations automatically, high-energy solar events which occurred between 1 July 2011 and 31 August 2012 were analysed: that period was chosen solely because it provided a data set which was small enough to allow individual observation of each event, yet large enough to allow wider conclusions to be drawn. In this context, a “high-energy solar event” was defined to be either:

1. A CME reported by CDAW to have a speed of 1,000 km/s or faster (“a rapid CMEs”), **or**
2. A flare reported in the GOES SXR list to be of class M5 or greater (“an intense flare”).

There were 55 rapid CMEs and 32 intense flares reported in the 13 month period under investigation. Of these, 3 of the rapid CMEs and 1 of the intense flares were excluded because they coincided with data gaps. Hence there were 83 events which formed the basis of this study of CME-flare associations.

In order to set a benchmark against which any automated method of associating CMEs and flares could be judged, movies (created from data at 193Å obtained by

the AIA) of each of the 83 events were examined. Intense flares were identified by looking for increases in brightness at the time of the flare specified by the GOES SXR list; CMEs were identified by the observation of any one of the following:

1. Visual evidence of any ejected material, **or**
2. Any loop distortion, **or**
3. Any coronal dimming

If such evidence was present and consistent with a front-side event (in some events, for example, loop distortions were clearly caused by an event which had occurred from behind the solar limb), the CME was regarded as having occurred on the face of the disc; if there was no such evidence, the CME was regarded as a back-side event.

It was determined that:

- A rapid CME was associated with a flare (whether or not this was an intense flare) if there was evidence that the CME was a front-side event, that it occurred between 1 hour prior to the start of the flare and 1 hour after its end, and that its origin was consistent with the flare site.
- An intense flare was associated with a CME (whether or not this was a rapid CME) if there was evidence of a front-side CME consistent with the flare site.

As a result of making the associations manually it was found that 35 of the 52 fast CMEs were on the face of the disk. This proportion is slightly higher than might have been expected: only one side of the Sun is visible, but all CMEs are detected. Consequently it is to be expected that only half of the CMEs would be observed from the face of the disk), but can be explained by two factors: first, there were large numbers of CMEs from same active regions (two active regions produced

5 each, and one other 8) and this may slightly distort the figures; secondly 17 of the 52 events were reported to occur very close to the limb, meaning that a CME which originated from just behind the limb may have been observed.

Of the 35 rapid CMEs which occurred on the face of the disk, all were associated with a flare of some kind; 46% (16/35) were associated with an intense flare. Of the 31 intense flares, 84% (26/31) were associated with a CME.

In every instance where we had associated a solar flare with a CME, the flare was reported in the GOES SXR list as having commenced before the CME was first reported in the CDAW catalogue. It should be noted that this is not an indication of actual chronology - as an example of where there is evidence of a CME lifting off before its associated flare, see Harrison and Bewsher (2007) - but it is of significance when devising a method of automatically making associations between flares and CMEs.

CDAW reports the time of a CME as being when it is first seen in images produced by the LASCO C2 coronagraph. This instrument, however, has a field of view between about 2 and 6 solar radii (as measured from the Sun's centre) and the images used by CDAW have a cadence of, at best, 12 minutes and sometimes much longer. The combination of these factors means that the reported time of the CME may be many minutes after its actual "lift-off" time, t_o .

Any attempt to make an estimate of t_o faces a number of difficulties: there is no information as to the height of the CME when it was first ejected; no information as to whether it has accelerated or decelerated before its first appearance in the C2 images; and no information as to the direction of the CME. Nevertheless, finding a first approximation of t_o is more likely to result in accurate associations between CMEs and flares than using the time of the CME as reported by CDAW.

It was assumed that by the time the CME reaches the field of view of the C2 coronagraph it has travelled (at least) one solar radius and has undergone neither

significant acceleration nor deceleration. An estimate for t_o was then obtained by using the reported speed of the CME.

In order to take into account of the difficulties caused by the cadence of the images, an error buffer, Δt , was defined as a specified number of minutes both before the the time of the start of flare, t_{f_start} and the time of its end, t_{f_end} . Δt was thus used to specify the time interval for the flare-CME associations. For example, if $\Delta t = 12$, t_o is compared with a time window opening 12 minutes before the flare began and closing 12 minutes after it ended. Plainly, the greater Δt , the more likely it is that t_o will fall within the window, and hence the greater the number of Type I (false positive) errors.

A good correlation could be found between those flare-CME associations which had made manually and those using a value of Δt of just 30 minutes. We did investigate whether it may be possible to improve the accuracy of the method by imposing a spatial criterion, for example by requiring the position angle of the CME to agree with the latitude and longitude of the flare to within a particular number of degrees. In fact we found that overall accuracy was not improved by the imposition of such a criterion.

Thus the criterion used to make associations between flares and CMEs is simply: if the estimated lift-off time of the CME, t_o , falls within the time window:

$$(t_{f_start} - \Delta t) < t_o < (t_{f_end} + \Delta t) \quad (\text{B.1})$$

then an association is made.

There will, of course, always be a small number of (usually) Type I errors when using this automatic method given that occasionally apparently unconnected solar events sometimes occur almost simultaneously. Nevertheless, in our sample the method correctly identified 98% (60/61) associations and correctly identified 86% (19/22) non-associations, an overall success rate in 95% (79/83) of cases.

Appendix C

Algorithm 1 false alarms in time range 1

Table C.1: Algorithm A.1 false alarms in time range 1. Column 1 gives the time the CME was first reported, column 2 its speed, and column 3 its acceleration all as reported by CDAW. Column 4 is the position angle at which the height-time measurements had been made (called by CDAW the “measurement position angle”). Column 5 is the CME width. Columns 6 to 10 give the parameters of the associated flare: its start time, heliographic latitude, heliographic longitude, class, and duration.

First reported	CME parameters				Flare parameters				
	V (km s ⁻¹)	Accel. (km s ⁻²)	Mpa (degrees)	Width (degrees)	Time start	Lat	Lon	Class	Duration (hrs: mins)
1998-11-24T02:30	1798	-12.5	225	360	1998-11-24T02:07	-20	94	X1.0	00:30
2000-01-06T07:31	1813	10.7	342	67	2000-01-06T06:45	24	35	C5.8	00:21
2000-05-05T15:50	1594	-103.4	265	360	2000-05-05T15:19	-15	97	M1.5	02:09
2000-06-25T07:54	1617	-17.5	274	165	2000-06-25T07:17	16	55	M1.9	01:04
2001-07-19T10:30	1668	-11.6	252	166	2001-07-19T09:52	-8	62	M1.8	00:25
2002-03-22T11:06	1750	-22.5	259	360	2002-03-22T10:12	-10	95	M1.6	01:40
2002-05-30T05:06	1625	67.0	275	144	2002-05-30T04:24	5	95	M1.3	01:49

Continued –

Table C.1 – Continued

First reported	CME parameters				Flare parameters				
	V (km s ⁻¹)	Accel. (km s ⁻²)	Mpa (degrees)	Width (degrees)	Time start	Lat	Lon	Class	Duration (hrs: mins)
2002-08-16T12:30	1585	-67.1	121	360	2002-08-16T11:32	-14	-20	M5.2	01:35
2003-03-18T12:30	1601	-13.3	266	209	2003-03-18T11:51	-15	46	X1.5	00:29
2003-06-02T00:30	1656	42.5	248	172	2003-06-02T00:07	-8	89	M6.5	00:36
2003-11-18T08:50	1660	-3.3	206	360	2003-11-18T08:12	-2	-18	M3.9	00:47
2004-04-11T04:30	1645	-77.6	237	314	2004-04-11T03:54	-16	46	C9.6	00:41
2005-07-09T22:30	1540	-168.5	328	360	2005-07-09T21:47	12	28	M2.8	00:32
2005-09-13T20:00	1866	11.5	149	360	2005-09-13T19:19	-11	-3	X1.5	01:38
2013-02-06T00:24	1867	-8.2	31	271	2013-02-06T00:04	22	-19	C8.7	00:37

Appendix D

Algorithm A.2 false alarms in time range 1

Table D.1: Algorithm A.2 false alarms in time range 1 in the same format as Table C.1.

First reported	CME parameters			Flare parameters			
	V (km s ⁻¹)	Accel. (km s ⁻²)	Mpa (degrees)	Width (degrees)	Time start	Lat Lon Class	Duration (hrs: mins)
LASCO data gap					1996-07-09T09:01	-10 30 X2.6	00:48
Continued –							

Table D.1 – Continued

First reported	CME parameters				Flare parameters				
	V (km s ⁻¹)	Accel. (km s ⁻²)	Mpa (degrees)	Width (degrees)	Time start	Lat	Lon	Class	Duration (hrs: mins)
LASCO data gap					1998-11-22T16:10	-30	89	X2.5	00:22
LASCO data gap					1998-11-23T06:28	-28	89	X2.2	00:30
1998-11-24T02:30	1798	-12.5	225	360	1998-11-24T02:07	-20	94	X1.0	00:30
1999-08-02T22:26	292	0.9	264	157	1999-08-02T21:18	-18	46	X1.4	00:20
1999-08-28T18:26	462	1.1	221	245	1999-08-28T17:52	-26	14	X1.1	00:26
1999-11-27T12:54	235	64.2	256	68	1999-11-27T12:05	-15	68	X1.4	00:11
2000-03-02T08:54	776	0.8	233	62	2000-03-02T08:20	-11	70	X1.1	00:11
2000-03-22T19:31	478	-92.0	312	154	2000-03-22T18:34	14	57	X1.1	00:22
					2000-03-24T07:41	16	82	X1.8	00:18
					2000-06-06T13:30	22	-10	X1.1	00:16
2000-06-06T15:54	1119	1.5	47	360	2000-06-06T14:58	21	-9	X2.3	00:42

Continued –

Table D.1 – Continued

First reported	CME parameters				Flare parameters				
	V (km s ⁻¹)	Accel. (km s ⁻²)	Mpa (degrees)	Width (degrees)	Time start	Lat	Lon	Class	Duration (hrs: mins)
2000-06-07T16:30	842	59.8	309	360	2000-06-07T15:34	23	-3	X1.2	00:32
2000-06-18T02:10	629	-1.2	318	132	2000-06-18T01:52	23	85	X1.0	00:11
					2000-09-30T23:13	7	91	X1.2	00:15
					2001-04-02T10:04	17	60	X1.4	00:16
2001-04-02T11:26	992	3.0	278	80	2001-04-02T10:58	15	65	X1.1	01:07
2001-10-25T15:26	1092	-1.4	175	360	2001-10-25T14:42	-16	21	X1.3	00:46
2001-12-13T14:54	864	-11.4	37	360	2001-12-13T14:20	16	-9	X6.2	00:15
2002-07-03T02:54	265	-9.9	274	73	2002-07-03T02:08	-20	51	X1.5	00:08
2002-07-15T20:30	1151	-25.6	35	360	2002-07-15T19:59	19	1	X3.0	00:15
2002-07-18T08:06	1099	-30.2	354	360	2002-07-18T07:24	19	30	X1.8	00:25
2002-08-03T19:31	1150	-18.8	272	138	2002-08-03T18:59	-16	76	X1.0	00:12

Continued –

Table D.1 – Continued

First reported	CME parameters				Flare parameters				
	V (km s ⁻¹)	Accel. (km s ⁻²)	Mpa (degrees)	Width (degrees)	Time start	Lat	Lon	Class	Duration (hrs: mins)
2002-08-21T06:06	268	-19.6	266	66	2002-08-21T05:28	-12	51	X1.0	00:08
2002-10-31T17:06	1061	-33.4	96	43	2002-10-31T16:47	28	87	X1.2	00:08
2003-03-17T19:54	1020	-5.5	264	96	2003-03-17T18:50	-14	39	X1.5	00:26
2003-03-18T12:30	1601	-13.3	266	209	2003-03-18T11:51	-15	46	X1.5	00:29
2003-05-27T23:50	964	-9.6	67	360	2003-05-27T22:56	-7	17	X1.3	00:17
LASCO data gap					2003-06-09T21:31	12	34	X1.7	00:12
LASCO data gap					2003-06-10T23:19	10	40	X1.3	00:53
					2003-06-11T20:01	14	57	X1.6	00:26
					2004-02-26T01:50	14	14	X1.1	00:20
					2004-08-13T18:07	-13	23	X1.0	00:08
2004-08-18T17:54	602	0.5	250	120	2004-08-18T17:29	-14	90	X1.8	00:25

Continued –

Table D.1 – Continued

First reported	CME parameters				Flare parameters				
	V (km s ⁻¹)	Accel. (km s ⁻²)	Mpa (degrees)	Width (degrees)	Time start	Lat	Lon	Class	Duration (hrs: mins)
2004-10-30T12:30	427	12.4	269	360	2004-10-30T11:38	13	25	X1.2	00:12
					2005-01-15T00:22	14	-8	X1.2	00:40
2005-09-13T20:00	1866	11.5	149	360	2005-09-13T19:19	-11	-3	X1.5	01:38
					2005-09-15T08:30	-11	24	X1.1	00:16
2011-02-15T02:24	669	-18.3	189	360	2011-02-15T01:44	-20	10	X2.2	00:22
					2011-03-09T23:13	8	9	X1.5	00:16

Appendix E

Algorithm A.2 false alarms in time range 2

Table E.1: Algorithm A.2 false alarms in time range 2. Columns 1 gives the start time of the flare, columns 2 and 3 its heliographic latitude and longitude, column 4 its class, and column 5 its duration.

Flare parameters				
Time start	Lat	Lon	Class	Duration (hrs: mins)
1980-05-21T20:51	-14	15	X1.4	00:35
1980-05-28T19:24	-18	33	X1.1	01:29
1980-06-04T22:57	-14	69	X2.2	00:17
1980-06-21T01:17	20	90	X2.6	00:43

Continued –

Table E.1 – Continued

Flare parameters				
Time start	Lat	Lon	Class	Duration (hrs: mins)
1980-07-01T16:22	-12	38	X2.5	00:49
1980-10-14T05:42	-9	7	X3.3	01:52
1980-10-25T09:42	19	59	X3.9	00:28
1980-11-07T01:56	7	11	X2.7	01:19
1980-11-08T13:33	8	28	X3.3	02:05
1980-11-12T04:46	10	72	X2.5	00:06
1980-11-15T15:40	-12	83	X1.9	01:51
1981-02-17T18:12	20	20	X1	05:30
1981-02-20T06:40	19	49	X2.4	01:07
1981-03-25T20:39	9	89	X2.2	00:44
1981-04-02T11:03	-43	68	X2.2	00:25
1981-07-19T05:32	-37	56	X2.7	01:05
1981-07-26T07:57	-14	18	X1	00:35
1981-07-27T17:24	-13	-11	X1.5	01:24
1981-08-12T06:24	-10	28	X2.6	00:56
1981-09-15T21:13	10	78	X2.3	00:15
1982-02-07T12:50	-14	72	X1	01:21
1982-02-08T12:50	-13	88	X1.4	00:29
1982-02-09T03:57	-13	90	X1.2	00:26
1982-03-30T05:22	13	11	X2.8	03:04

Continued –

Table E.1 – Continued

Flare parameters				
Time start	Lat	Lon	Class	Duration (hrs: mins)
1982-06-26T00:42	16	5	X1.9	01:26
1982-06-26T19:09	15	73	X2.1	01:04
1982-07-17T10:28	14	32	X3.2	00:53
1982-12-22T08:26	-9	82	X2.4	00:31
1982-12-29T06:43	-13	12	X1.9	00:34
1983-06-06T13:31	-11	15	X1.4	02:01
1988-06-23T08:56	-19	34	X1.6	01:07
1988-06-24T04:18	-18	45	X1.3	02:43
1988-06-24T16:03	-17	52	X2.4	00:51
1988-10-03T14:53	-27	16	X3.2	00:49
1988-10-03T23:22	-27	20	X1.1	00:57
1988-12-30T17:25	-19	30	X1.4	02:23
1989-01-13T08:29	-31	5	X2.3	02:16
1989-01-14T02:54	-32	10	X2.1	02:25
1989-01-14T21:45	-29	26	X1.1	01:24
1989-01-18T07:02	-30	65	X1.4	00:11
1989-01-27T19:08	-19	-17	X1.1	01:38
1989-03-14T16:46	33	21	X1.1	05:02
1989-03-16T15:24	36	47	X3.6	01:21
1989-03-16T20:35	29	60	X1.4	00:56

Continued –

Table E.1 – Continued

Flare parameters				
Time start	Lat	Lon	Class	Duration (hrs: mins)
1989-05-05T07:23	30	-1	X2.4	03:12
1989-06-15T18:13	-21	-8	X4.1	02:28
1989-06-16T04:19	-17	-3	X3	00:26
1989-09-03T14:28	-18	-16	X1.2	00:32
1989-09-04T08:57	-18	-19	X1.1	00:49
1989-09-09T19:28	-15	67	X1.3	00:28
1989-11-12T06:21	13	39	X1.5	00:46
1989-11-19T06:19	-24	25	X1.1	00:23
1989-11-20T21:25	-27	43	X1	00:36
1989-11-21T13:32	-26	53	X4	00:59
1989-11-25T22:55	30	-5	X1	03:40
1989-12-30T04:09	-19	-9	X1	01:05
1989-12-31T09:32	-25	51	X2.8	00:45
1991-01-30T08:49	-8	34	X1	01:36
1991-01-31T01:58	-17	35	X1.3	03:21
1991-03-16T00:47	-9	-9	X1.8	00:22
1991-03-17T20:54	-10	13	X1	02:11
1991-03-29T06:42	-28	60	X2.4	00:52
1991-03-31T19:11	-22	88	X1	00:08
1991-04-20T08:27	8	50	X1	02:57

Continued –

Table E.1 – Continued

Flare parameters

Time start	Lat	Lon	Class	Duration (hrs: mins)
1991-05-18T05:06	32	85	X2.8	02:42
1991-07-31T00:46	-17	-11	X2.3	01:29
1991-08-02T03:07	25	-15	X1.5	00:52
1991-09-07T19:11	-11	50	X3.3	01:10
1991-09-08T09:06	-13	58	X1	00:43
1991-10-26T18:53	-9	-20	X1.7	04:32
1991-10-27T02:06	-11	-20	X1.9	00:51
1991-10-27T05:38	-13	-15	X6.1	01:20
1991-11-09T15:32	-16	57	X1.1	01:37
1991-11-15T22:34	-13	19	X1.5	00:43
1991-12-24T10:13	-17	-14	X1.4	01:20
1992-01-26T15:23	-16	66	X1	01:02
1992-02-16T12:32	-13	17	X1.4	01:09
1992-02-27T09:22	6	2	X3.3	03:41
1992-09-06T18:42	-11	41	X1.7	02:09
1992-09-06T20:50	-11	46	X1.3	00:26

Appendix F

Swalwell *et al.* (2017a)

SEPs are known to be energised by flares and coronal mass ejections (CMEs), processes which can take place within the same active region in close temporal association. Flares exhibiting high levels of energy emission in soft X-rays (SXR) and CMEs with high speeds have long been associated with a high likelihood of SEPs being detected at Earth (see *e.g.* Dierckxens *et al.*, 2015). The bases for making such associations are studies of large numbers of events which are directed towards demonstrating the connection between flare and CME properties, and SEP events. These studies go on to look for correlations between event parameters and the proportion of associated solar event SEPs (*e.g.* Belov *et al.*, 2005; Cliver *et al.*, 2012).

Whether SEPs are actually detected at Earth, however, may depend upon many different factors: the mechanism behind their acceleration, the energy and efficiency of that acceleration, the location of the acceleration site, whether or not the particles can escape into the interplanetary medium, and how they travel through it.

It is not the case that SEPs are detected at Earth following all large flares and fast CMEs (*e.g.* Klein *et al.*, 2011). Solar events of this type, which might reasonably be expected to produce SEPs at Earth but which do not, may be termed “false alarms”. Furthermore, some SEP events may follow smaller solar events, so that they are “missed events” for SEP forecasting algorithms based on intense flares and/or fast CMEs.

Many SEP forecasting tools base their prediction upon the observation of intense solar flares and/or radio bursts. For example, the Proton Prediction System proposed by (Smart and Shea, 1989) makes a forecast based upon flare intensity and position. It produces almost equal numbers of correct forecasts, false alarms and missed events (Kahler, Cliver, and Ling, 2007).

The National Oceanic and Atmospheric Administration (NOAA) Space Weather Prediction Center (SPWC) uses a system named “Protons” which is described by (Balch, 1999). The tool aims to forecast the arrival of SEPs near Earth following the detection of solar flares and radio bursts. Balch, 2008, validated the system over a period between 1986 and 2004, and found that its false alarm rate was 55%. The tool, however, is only used as a decision aid and the actual forecasts issued by SWPC have improved over time¹. Kahler and Ling, 2015, combine SEP event statistics with real-time SEP observations to produce a forecast which changes dynamically.

Laurenza *et al.*, 2009, developed the Empirical model for Solar Proton Events Real Time Alert (ESPERTA) method of SEP forecasting based upon flare size, flare location and evidence of particle acceleration and escape. Their emphasis was to maximise the time between the issue of an SEP event warning and the arrival of the particles, and their aim was to produce an automated forecasting tool with a view to issuing warnings of SEP events without human intervention. Whilst it is a significant improvement over the Protons tool, the false alarm rate was, nevertheless, between 30% and 42% (Alberti *et al.*, 2017). The FORcasting Solar Particle Events and Flares (FORSPEF) model, proposed by (Papaioannou *et al.*, 2015), aims to make forecasts of both flares and SEPs. Its SEP forecasting algorithm is based upon a purely statistical approach, and has not yet been validated.

Other forecasting tools use different methods. It has also been shown that type II radio bursts at decametric–hectometric (DH) wavelengths may be used to aid the forecasting of SEP events. Winter and Ledbetter, 2015, have described a statistical relationship between DH type II radio bursts, the properties of the associated type III burst, and peak proton flux. During the period they analysed (2010 to 2013) they were able to make predictions of an SEP event with a false alarm rate of 22%.

The Relativistic Electron Alert System for Exploration (REleASE) SEP forecasting tool (Posner, 2007) relies upon the fact that electrons will travel faster than protons, and will therefore

¹[http://www.swpc.noaa.gov/sites/default/files/images/u30/S1 Proton Events.pdf](http://www.swpc.noaa.gov/sites/default/files/images/u30/S1_Proton_Events.pdf)

arrive at 1 AU first. A forecast of expected proton flux is made based upon the real-time electron flux measurements.

Although the majority of currently operational data-based forecasting schemes make use of flare information, it is widely thought that the use of CME information would substantially improve algorithm performance. While from an operational point of view it is currently not trivial to obtain CME parameters in real time, it is important to compare the performance of flare-based *versus* CME-based algorithms and determine whether a combination of flare and CME parameters within a forecasting tool may be beneficial.

Along with empirical forecasting algorithms which are based upon solar observations, several physics-based space weather forecasting tools have recently been developed (*e.g.* the SOLar Particle ENgineering COde (SOLPENCO) (Aran, Sanahuja, and Lario, 2006), a solar wind simulation including a cone model of CMEs (Luhmann *et al.*, 2010), and the Solar Particle Radiation SWx (SPARX) model (Marsh *et al.*, 2015).

A catalogue of 314 SEP events and their parent solar events between 1984 and 2013 has been produced by Papaioannou *et al.*, 2016. It is expected that this database will provide a solid basis for the analysis of SEP events and the characteristics of their parent solar event. The catalogue does not, however, include information on those solar events which were false alarms. In order to improve SEP forecasting tools for space weather applications, an analysis of the characteristics of false alarm events should be carried out with a view to gaining an understanding of why SEPs were not observed.

Some statistical studies of SEP events and false alarms have been undertaken. Most take the same approach as Papaioannou *et al.* and Laurenza *et al.*, starting by considering the SEP events and then looking for the possible parent solar events. (Gopalswamy *et al.*, 2014) examined solar events during the early part of solar cycle 24, and considered why some which had very fast CMEs and large flares did not produce ground level enhancements of energetic particles as might have been expected. They suggested that poor latitudinal magnetic connectivity between the solar event and the Earth may have been an important factor.

Marqué, Posner, and Klein, 2006, examined a small number of CMEs with a speed greater than 900 km s^{-1} which had no radio signature of flare-related acceleration, and found that none produced conspicuous SEP events at Earth. Those authors argue, therefore, that a CME shock without an associated flare is not sufficient to produce SEPs.

Wang and Zhang, 2007, suggested that X-class flares not associated with any CME may occur closer to the magnetic centre of their source active region and may therefore be confined by overlying arcade magnetic fields. Klein, Trotter, and Klassen, 2010 investigated a small number of these “CME-less” flares further, and argued that no SEP event might be expected following a flare which shows high peak emission in soft X-rays but which does not exhibit radio emission at decimetre and longer wavelengths.

Most of the large sample studies described above started by considering SEP events and then looked for possible parent solar events. In this paper we take a different approach. We start our analysis by considering solar events and determining whether an SEP event was measured at Earth a short time thereafter. We focus on intense flares and fast CMES and define two possible forecasting algorithms, the first based solely on the occurrence of an intense flare and the second on that of a fast CME. The performance of the algorithms is quantified by evaluating them over historical datasets, and the characteristics of false alarms studied. In addition, missed events, *i.e.* SEP events not forecast, are also identified and studied. Finally we discuss how a new algorithm which combines flare and CME properties may be introduced, resulting in better performance.

We provide lists of false alarms based upon the forecasting algorithms in order that they may form the basis of future studies and comparisons, together with a list of the solar events which produced $>40 \text{ MeV}$ protons. We analyse the properties of the false alarm events to determine whether reasons why they did not produce SEPs at Earth can be identified.

2. False alarms and forecasting algorithms

A false alarm may simply be defined as “a solar event which is predicted by a forecasting algorithm to produce SEPs at Earth but which fails to do so”. Specification of a forecasting algorithm and determination of its associated false alarms requires identification of:

1. The criteria and observational data sets by which a solar event is assigned a high likelihood of producing SEPs at Earth. Typically this will include identification of the type of solar event (*e.g.* flare or CME) expected to produce SEPs, of a requirement on the intensity of the event (*e.g.* a flare with peak SXR flux, f_{SXR} , which exceeds a specified threshold intensity, f_{thr} , or a CME with a speed v_{CME} which is faster than a threshold speed v_{thr}), of a positional requirement (*e.g.* an event with a source region west of a given longitude), and possibly of other parameters.
2. The criteria by which it is determined that an SEP event has occurred or not. These will typically include specification of the instrument being used to measure particle flux intensity, of the species of particle examined and its energy range, and of the SEP intensity threshold, I_{thr} , used to establish whether an SEP event was detected following a particular solar event.
3. The method by which the solar event is associated with the SEP event.

We discuss each of these requirements in Sections 2.1, 2.4, and 2.5 respectively.

2.1. Solar event parameters

As our source for CME data we have used the Co-ordinated Data Analysis Workshop (CDAW) CME catalogue² (Gopalswamy *et al.*, 2009). This catalogue is produced manually, CMEs being identified visually from images obtained by the C2 and C3 coronagraphs of the *Large Angle and Spectrometric Coronagraph Experiment* (LASCO) (Brueckner *et al.*, 1995) on board the *Solar and Heliospheric Observatory* (SOHO) spacecraft.

Information is published in the catalogue on various CME parameters including, *inter alia*, the time it is first seen in the LASCO images, its width, and its position angle. CDAW publishes three values for the speed of CMEs in its catalogue, each calculated by different means: we use the first, the “linear” speed, which is obtained simply by fitting a straight line to the height-time measurements. Importantly, there is no information directly available from the catalogue as to whether the CME is Earth-directed, or from where on the solar disk it originated. This imposes serious limitations in analysing whether or not a particular CME is likely to produce SEPs at Earth.

Solar flares are classified by their peak SXR emission as measured in the 1 - 8 Å channel of the *Geostationary Observational Environmental Satellites* (GOES) (Grubb, 1975) *X-ray Sensor* (XRS) instruments. Flares with a peak flux in this energy channel above 10^{-4} W m⁻² are designated to be of class X; those with a peak flux between 10^{-5} and 10^{-4} W m⁻² are of class M; classes C, B, and A are defined in a similar fashion. No single instrument has been in continuous operation since 1975, although the design has changed little over the years (Garcia, 1994).

As our source for solar flare data we have used the GOES SXR Flare List which has been continuously maintained since 1975, and which may be downloaded from the website³ of the *Heliophysics Integrated Observatory* (Bentley *et al.*, 2011).

²http://cdaw.gsfc.nasa.gov/CME_list/index.html

³<http://www.helio-vo.eu/>

In addition to reporting the maximum SXR intensity and the time of the start, peak and end of the flare, the GOES SXR Flare List also usually reports its heliographic co-ordinates. However there is a significant number of flares for which the list does not provide this information. In these cases we have used values for co-ordinates from the following sources:

1. Co-ordinates reported in the SolarSoft Latest Events Flares List (gevloc) (which may also be obtained through Helio).
2. The reported co-ordinates of the active region (AR) from which the flare originated according to the GOES SXR flare list.
3. Making our own estimate of co-ordinates by watching movies of 195 Å images taken by **the Extreme ultraviolet Imaging Telescope** (EIT) on board the SOHO spacecraft or of 195 Å images taken by the *Atmospheric Imaging Assembly* (AIA) on board the *Solar Dynamics Observatory* (SDO).

CMEs and solar flares, particularly high energy events, often occur within a short time of each other from the same solar active region. Making associations between these solar events is required so as to gain an understanding of the type of event which did, or did not produce SEPs at Earth: it also allows an estimate to be made of the site of origin of the CME from the reported heliographic coordinates of its associated flare.

We developed a method of making associations between CMEs and flares automatically which we set out in Appendix A. Whilst we are confident that the method produces correct associations in over 90% of cases, to be sure we also viewed 195 Å (obtained by the EIT on board SOHO) and 193 Å (obtained by the AIA on board SDO) movies of each solar event. We confirmed the associations made by the automatic method in 156 cases, changed them in six cases, and were unable to confirm the associations in a further 17 cases because EIT or AIA images were not available.

2.2. Location criterion for solar events

It is well known that solar events with origin in the west of the Sun as observed by an observer on Earth are more likely to produce SEPs than those originating in the east. Therefore it is common to introduce a positional criterion within SEP forecasting algorithms. Figure 1 shows the heliographic longitude of the 171 SEP-producing events between 1 April 1980 and 31 March 2013 for which we were able to determine coordinates. Of these, 86.5% (148/171) had their origin in a solar event which occurred at a site west of E20, hence our choice of positional requirement in the forecasting algorithms. We call solar events which have their origin west of E20 “western events”.

2.3. The forecasting algorithms

The two forecasting algorithms we investigate in this work are based upon the fact that that the more energetic the solar event, the greater the likelihood of that event producing SEPs at Earth, particularly if magnetically well-connected (*e.g.* Dierckxsens *et al.*, 2015). The algorithms are:

- A.1 A frontside CME with a reported speed of 1500 km s⁻¹ or greater (a “fast CME”) occurring west of E20 on the solar disk will result in an SEP event being detected at Earth.
- A.2 An X-class flare occurring west of E20 on the solar disk will result in an SEP event being detected at Earth.

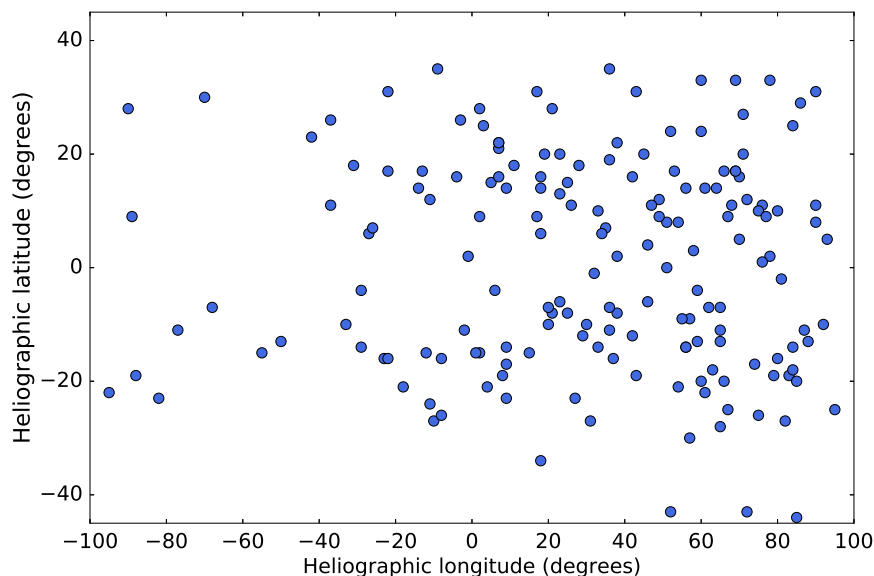


Figure 1. Heliographic longitude and latitude of solar events which produced an SEP event according to the criteria defined in Section 2.4 between 1 April 1980 and 31 March 2013.

Table 1. Numbers of solar events the subject of this study. Column 1 shows the time range over which data have been analysed, column 2 the type of solar event considered, column 3 the total number of solar events within the period investigated, column 4 the number of events for which we were able to determine coordinates (after removal of events discarded due to data gaps, saturation of detectors or other reasons) and column 5 the number of events which occurred west of E20.

Time range	Event type	Total number of events	Events for which coordinates were determined	Analysed events west of E20
Time range 1 (Jan 1996 to Mar 2013)	Fast CMEs	143	93	52
	X-class flares	140	139	79
Time range 2 (Apr 1980 to Mar 2013)	X-class flares	403	377	197

We evaluate both the forecasting algorithms over the time range from 11 January 1996 until 31 March 2013 (“time range 1”); for algorithm A.2 we are also able to examine a longer period, between 1 April 1980 and 31 March 2013 (“time range 2”). In time range 1 there were 143 fast CMEs (according to our definition set out in A.1) reported by CDAW and 140 X-class flares. In time range 2 there were 403 X-class flares.

Table 1 sets out the numbers of solar events which we have examined in this study. A number of solar events have had to be excluded from our analysis because of data gaps, the saturation of detectors or other cause, or because it was not possible to determine the heliographic co-ordinates.

2.4. SEP event parameters

The definition of an SEP event will typically include specification of the instrument being used to measure particle flux, of the species of particle examined and its energy range, and of the

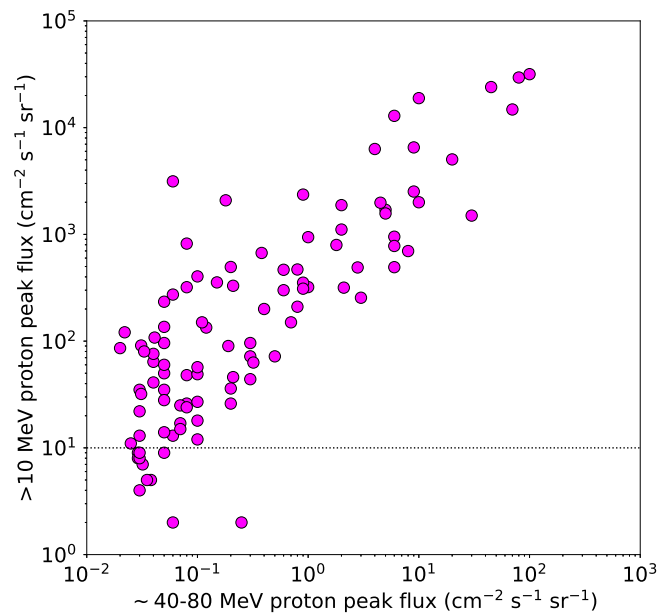


Figure 2. Peak flux of >10 MeV protons as reported by NOAA plotted against peak proton flux in the GOES ~ 40 -80 MeV energy channel in time range 1. The dotted horizontal line is at the NOAA threshold of 10 pfu.

SEP intensity threshold, I_{thr} used to establish whether an SEP event was detected following a particular solar event.

Particles accelerated by solar events include electrons, protons, and heavier ions, but we have chosen to analyse high energy (> 40 MeV) protons. The threshold considered is a little higher than the > 10 MeV threshold used by NOAA, making our event list less biased towards interplanetary shock-accelerated events. This choice also avoids proton enhancements caused by magnetospheric effects.

Because our threshold energy for protons is higher than that used by NOAA, we compared peak >40 MeV fluxes for our event sample with the peak >10 MeV fluxes for the same events. For each of our events a value for >10 MeV flux was obtained from the NOAA SEP list⁴. Eleven of the SEP events at >40 MeV did not reach the NOAA threshold of 10 pfu at >10 MeV, and for these we estimated peak flux by visual analysis of the plots of each event⁵. Figure 2 is a plot of the peak flux of >10 MeV protons plotted against peak proton flux in the ~ 40 -80 MeV energy channel of the GOES EPS instruments for the SEP events in time range 1. The dotted horizontal line is at the NOAA threshold of 10 particles $\text{cm}^{-2} \text{s}^{-1} \text{sr}^{-1}$ (pfu). The highest value for maximum peak flux at >40 MeV in time range 1 was approximately 100 pfu - the same event at >10 MeV produced 31700 pfu according to NOAA.

All instruments which detect proton intensities are subject to slight fluctuations, and not all of these can properly be said to be SEP events. The definition of intensity threshold, I_{thr} , must be high enough so as to exclude the normal fluctuations in measurements, but low enough to ensure that rises which are genuinely due to solar events are included. We set I_{thr} to be a 2.5-fold increase in proton intensity over the quiet-time background level.

⁴<ftp://ftp.swpc.noaa.gov/pub/indices/SPE.txt>

⁵Downloaded from <https://solarmonitor.org/>

Table 2. Instruments used to obtain data on proton intensity, the dates between which data from that instrument was used, and the energy channels which have been analysed. Column 1 gives the name of the spacecraft from which the data we have used was taken, column 2 the date from which we began to use those data and column 3 the date when we ceased using those data. Column 4 shows the range of proton energies measured by the instrument we have used, and column 5 whether the data was raw or had been cleaned by the SEPTEM team.

Spacecraft	Start date	End date	Energy channel (MeV)	Raw data / Cleaned
GOES 2	1 April 1980	31 December 1983	36.0 - 500.0	Raw data
GOES 6	1 January 1984	31 March 1987	39.0 - 82.0	Raw data
GOES 7	1 April 1987	28 February 1995	39.0 - 82.0	Cleaned
GOES 8	1 March 1995	7 January 2003	40.0 - 80.0	Cleaned
GOES 12	8 January 2003	31 December 2009	40.0 - 80.0	Cleaned
GOES 11	1 January 2010	31 December 2010	40.0 - 80.0	Cleaned
GOES 13	1 January 2011	31 March 2013	38.0 - 82.0	Cleaned

For this study we have used GOES SEP data because they allow us to study SEP events over a time period of more than 30 years. No one instrument has been in continuous operation during that time, and so we have had to use data from a number of different GOES satellites. Table 2 sets out which spacecraft we have used and the energy channel considered to establish the occurrence of an SEP event. There are slight differences in the energy channels, particularly in the case of GOES 2, but we take the view that the differences are so small as to have a negligible effect upon our results. We downloaded data from the European Space Agency’s *Solar Energetic Particle Environment Monitor* (SEPTEM) website (Crosby *et al.*, 2010)⁶. Data from 1 April 1987 onwards had been cleaned and intercalibrated by the SEPTEM team; prior to that date we used their raw data.

It is not always easy to determine whether an SEP event had occurred if the instrument were still recording high-energy protons from a previous event. If it were the case that the intensity level had not returned to within 2.5 times the quiet-time background level by the time of the start of the solar event we were investigating, that solar event was disregarded - it could not be known whether or not that event produced SEPs at Earth. The only exceptions were those cases where there was a clear increase in proton intensity which could only be attributed to the solar event in question, in which case it was treated as an SEP event.

We determined that, during time range 2, there had been 221 flux enhancements in the GOES > 40 MeV proton channel which satisfied our definition of an SEP event.

2.5. Association of solar events and SEP events

A criterion for associating solar events and SEP enhancements is necessary. First we took the start time of the solar event. For CMEs not associated with a flare we used the time the CME was first reported in the CDAW catalogue; for CMEs which were associated with a flare and for all flares, we used the reported start time of the flare.

We then searched the GOES proton data for a subsequent SEP event. In most cases the SEP enhancement began before another solar event was reported, in which case the association between the solar event and the SEP enhancement was made. In some instances,

⁶<http://dev.sepem.oma.be/>

however, another solar event was reported before the SEP enhancement commenced. For these cases it was assumed that it was this new solar event which accelerated the particles unless that event was so close in time to the arrival of the SEPs (~ 20 minutes) that it was unlikely that the new event could have been the cause. None of our confirmed solar event - SEP association time differences was as short as 20 minutes.

A number of solar events had to be discarded because they coincided with gaps in SEP data, meaning that it could not be known whether or not they had produced an SEP enhancement. However, if there had been short outages (~ 3 hours), and there was no evidence of an SEP event either side of the outage, the solar event has been counted as a false alarm.

We also associated solar events to all of the 221 proton events which we identified. In some cases the associated flare was of a class smaller than X and/or the associated CME was not a fast one according to our definition. Of these 221 events, we were not able to determine coordinates of the parent solar event for 50. The event was a western one in 148 of the remaining 171 cases.

3. Identification of false alarms and evaluation of the forecasting algorithms

We applied the forecasting algorithms described in Section 2.3 to the historical data sets we collected. We evaluated both algorithms over time range 1 (1996 to 2013) and in addition we evaluated algorithm A.2 over the longer time range 2 (1980 to 2013).

3.1. Algorithms A.1 and A.2 over time range 1

Figure 3 shows the results of applying the two SEP forecasting algorithms to the data set for time range 1. The number of correctly forecast SEP events is shown by the blue bar and named α ; the number of false alarms is represented by the red bar and named β ; and the number of SEP events which occurred but which were not forecast by the algorithm (the “missed events”) is shown as the green bar and named γ . There was a total of 107 SEP events in time range 1. Of the 86 SEP events for which we were able to determine the coordinates of the parent solar event, 91.9% (79/86) were western events.

Algorithm A.1 considers western fast CMEs. There were 52 such events during the period in question, and 71.2% (37/52) produced SEPs at Earth. Thus the false alarm rate was 28.8% (15/52) but the algorithm failed to forecast 53.2% (42/79) of SEP events for which the parent solar event was a western one. Of all the SEP events for which coordinates could be determined, it missed 57.0% (49/86).

Algorithm A.2 uses western X-class flares as the basis for the forecast. There were 79 such flares in time range 1, and 49.4% (39/79) produced SEPs at Earth. The false alarm rate was therefore 50.6% (40/79) and the algorithm failed to forecast 50.6% (40/79) of SEP events for which the parent solar event was a western one. Of all the SEP events for which coordinates could be determined, it missed 54.7% (47/86).

Appendix B provides the list of false alarms for the algorithm A.1, and Appendix C the false alarms for A.2 - the same lists are available electronically as supplementary material.

As well as reaching for an understanding of the underlying physical differences between those solar events which produced SEPs at Earth and the false alarms, we also look to measure the efficacy of the forecasting algorithms. A high percentage of correctly forecast SEP events (α) coupled with a low number of false alarms (β) is desirable, but not at the expense of failing to forecast a large number of the SEP events which did occur (γ). In our evaluation we use two ratios:

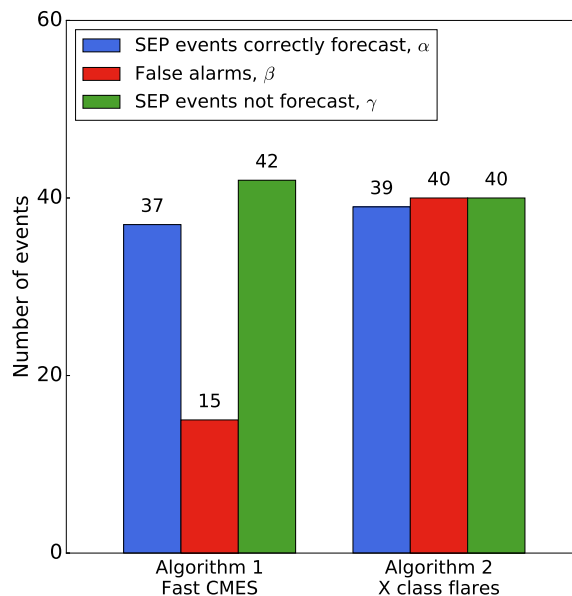


Figure 3. The numbers of correctly forecast SEP events, false alarms and SEP events which were not forecast for the two forecasting algorithms during time range 1.

1. The “false alarm ratio” (FAR) gives the fraction of forecast events which actually did occur. It is defined as:

$$\text{FAR} = \frac{\beta}{\alpha + \beta} \quad (1)$$

The FAR is sensitive to the number of false alarms, but takes no account of missed events. Possible scores range from 0 to 1, with the “perfect” score being 0.

2. The “critical success index” (CSI) is a measure of how well the forecast events correspond to the observed events. It is defined as

$$\text{CSI} = \frac{\alpha}{\alpha + \beta + \gamma} \quad (2)$$

Possible scores range from 0 to 1, with the “perfect” score being 1.

3.2. Forecasting algorithm A.1 - fast CMEs

All the CMEs in our sample were from the front-side of the Sun and had an associated flare which was used to determine the coordinates. The FAR for algorithm A.1 is 0.29 and the CSI, not taking account of the missed eastern events, is 0.39. If the eastern events were to be included within the calculation for the CSI, its value would be reduced to 0.37. The evaluation scores for this algorithm over time range 1, and for algorithm A.2 over both time ranges, are summarised in Table 3. It is not clear whether the high number of missed events is due to the fact that the

Table 3. A summary of the evaluation scores for the two forecasting algorithms: the “false alarm ratio” (FAR) and the “critical success index” (CSI) over time range 1. Algorithm A.2 is also evaluated over time range 2. Column 1 shows the forecasting algorithm being considered, column 2 the time range over which the analysis has been done, column 3 the false alarm ratio (FAR) for that algorithm, column 4 the critical success index (CSI) not taking into account the missed eastern events, and column 5 the CSI were these additional missed events to be included

Forecasting algorithm	Time range	FAR	CSI not including missed eastern events	CSI including missed eastern events
A.1 (Fast CMEs)	1	0.29	0.39	0.37
A.2 (X-class flares)	1	0.51	0.33	0.31
A.2 (X-class flares)	2	0.61	0.29	0.26

measured velocity of the CME, v_{CME} , is the plane-of-the-sky speed, whether in general the speeds measured by examination of coronagraph images are not sufficiently accurate, or whether more physics need to be included in the analysis.

In Figure 4 we plot peak SXR intensity of the CME’s associated flare against its speed for those solar events in time range 1 which produced SEPs at Earth (top left, blue circles); for those events in the same period which were false alarms according to algorithm A.1 (top right, red squares); for SEP events missed by algorithm A.1 (bottom left, green diamonds); and for all events together (bottom right). Here one can see that many of the fast CME false alarms occur close to the threshold speed, v_{thr} , and so increasing the threshold would reduce the number of false alarms, although it would also increase the number of missed events. A significant fraction of SEP events were associated with CMEs of reported speed much slower than 1500 km s^{-1} . It is also clear that many of the false alarms have a flare intensity $< \text{M3}$.

Gopalswamy *et al.*, 2014 studied major solar eruptions during the first 62 months of solar cycle 24 and suggested that, among other things, the separation in latitude between the flare and the footpoint to Earth may be an important factor in determining whether high-energy particle events are detected. Therefore we define a parameter, $\Delta\delta$, the difference between the latitude of the flare, δ_{flare} , and the latitude of the Earth’s footpoint, δ_{Earth} , *i.e.* the parameter $\Delta\delta$ takes into account the inclination of Earth’s orbit. In Figure 5 we plot $\Delta\delta$ against time for Algorithm A.1, together with histograms for $\Delta\delta$. The events correctly forecast to produce SEPs are presented in the top plots (shown in blue), and the false alarms in the bottom plots (shown in red). For fast CMEs which had their origin within ± 10 degrees of the Earth’s footpoint, 64.7% (11/17) produced SEPs; for those which had their origin outside this range, 74.3% (26/35) produced SEPs. Overall there does not appear to be a significant difference between the distribution in $\Delta\delta$ for SEP events and false alarms.

Figure 6 shows histograms of the heliographic longitude of solar events in time range 1 correctly forecast by algorithm A.1 to produce an SEP event (top left), of algorithm A.1 false alarms (top right), of SEP events missed by algorithm A.1 (bottom left), and of all SEP events (bottom right). There is a peak of SEP-producing fast CMEs between W50 and W90. The false alarms for algorithm A.1 are relatively evenly distributed, as are the SEP events not forecast by A.1.

In Figure 7 we plot $\Delta\delta$ against the longitude of the 37 western fast CMEs which produced an SEP event in time range 1. The size of the marker reflects the peak SXR intensity of the associated flare, and its colour is representative of the width of the CME. The bottom plot gives the same information, but for the false alarms according to algorithm A.1. It can be seen that, on average, the size of the markers in the middle plot is smaller than those in for the SEP-producing events. Thus, the peak SXR intensity of a fast CME’s associated flare is relevant to the question as to whether SEPs will arrive at Earth.

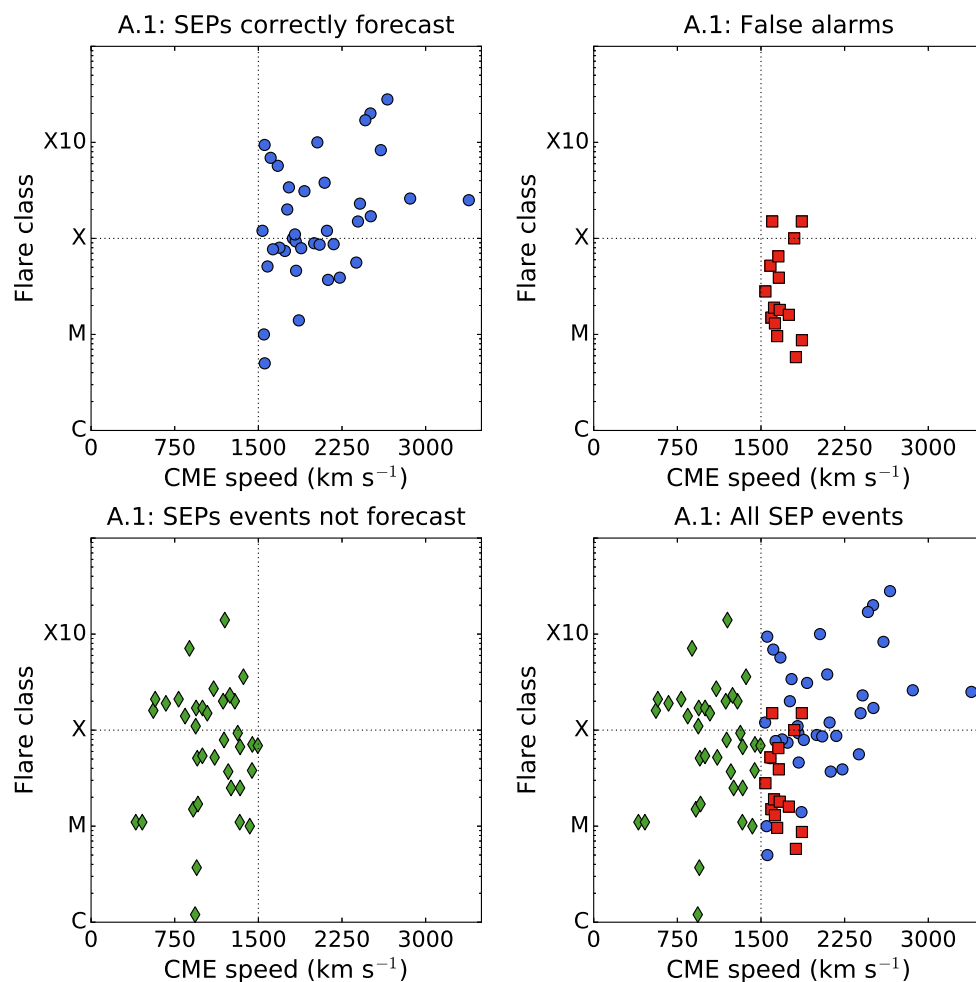


Figure 4. Flare class *versus* associated CME speed for those solar events which produced SEPs >40 MeV at Earth in time range 1 (*top left, blue circles*); for fast CMEs which were false alarms according to forecasting algorithm A.1 (*top right, red squares*); for SEP events missed by algorithm A.1 (*bottom left, green diamonds*); and for all events together (*bottom right*).

Also apparent from Figure 7 is that CME width is an important parameter. Of the 37 SEP-producing CMEs, 86.5% (32/37) were reported to be haloes by the CDAW catalogue. By contrast, for the algorithm A.1 false alarms, only 46.7% (7/15) were haloes. Therefore we find that halo CMEs are more likely to produce SEPs than non-haloes. This result is consistent with the findings of Park, Moon, and Gopalswamy, 2012 who found that solar events which had the highest probability of producing 10 MeV protons were full halo CMEs with a speed exceeding 1500 km s^{-1} .

It should be noted that Kwon, Zhang, and Vourlidas, 2015 examined 62 halo CMEs (as reported by the CDAW catalogue) which occurred between 2010 and 2012 and were observed by three spacecraft separated in longitude by nearly 180° . They found that 42 were observed to be haloes by all three spacecraft. They concluded that a CME may appear to be a halo as a result of fast magnetosonic waves or shocks, and that apparent width does not represent an accurate measure of CME ejecta size.

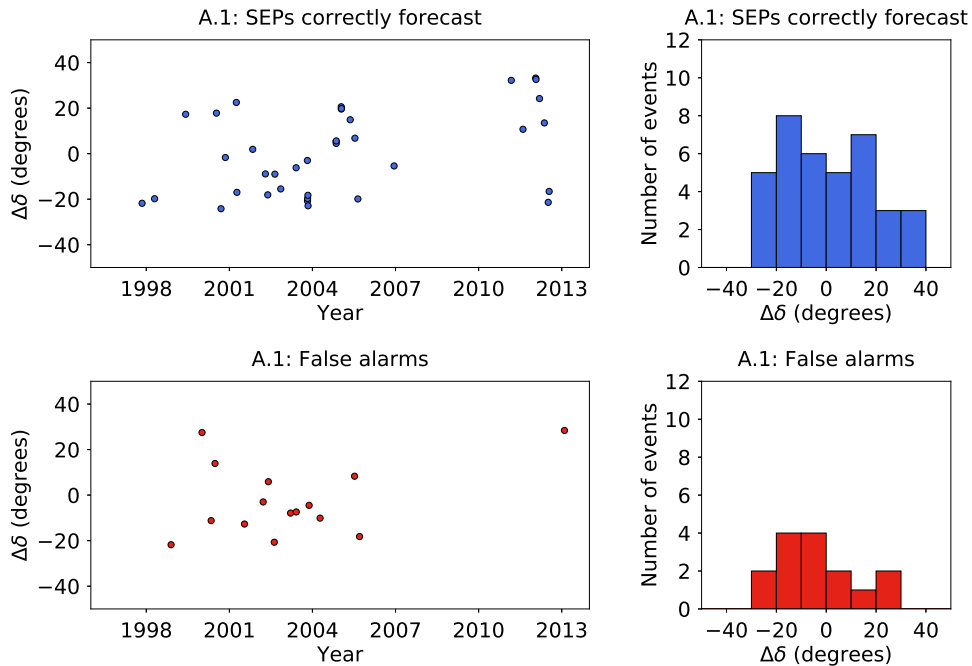


Figure 5. Plots of $\Delta\delta$ against time for algorithm A.1, together with histograms of $\Delta\delta$. The *top plots* present the results for the solar events which were correctly forecast to produce SEPs at Earth (shown in *blue*); the *bottom plots* the false alarms (shown in *red*).

3.3. Forecasting algorithm A.2 - X-class flares

Algorithm A.2 has an FAR of 0.51. Whilst it makes almost exactly the same number of correct forecasts as Algorithm A.1, the percentage of correct forecasts is lower. The proportion of missed SEP events is also relatively high, leading to a CSI of 0.33 without accounting for the missed eastern events, or of 0.31 if the missed eastern events were to be included.

In Figure 8 we plot SXR intensity for the solar flares above the threshold of A.2 against associated CME speed, and for SEP events missed by algorithm A.2 in the same format as in Figure 4. There is some symmetry with Figure 4 in that many of the false alarms fall close to the chosen threshold. It should be noted that not all events above the A.2 threshold have an associated CME. Of the 122 X-class flares which occurred in time range 1 (and which did not coincide with a LASCO data gap), 14.8% (18/122) had no associated CME. However the percentage of A.2 false alarms which did not coincide with a LASCO data gap and which did not have an associated CME is 26.5% (9/34).

In Figure 9 we show histograms of the heliographic longitude of solar events in time range 1 for algorithm A.2 in the same format as Figure 6. There appears to be no significant difference in the longitudinal distribution of western X-class flares which produced an SEP event and those which were false alarms, but in this case the SEP events which were not forecast by algorithm A.2 do have a clear peak between W20 and W80.

In the top plot of Figure 10 we plot $\Delta\delta$ against the longitude of the 39 western X-class flares which produced an SEP event in time range 1. As in Figure 7, the colour of the marker is representative of the width of the flare's associated CME as reported by CDAW, but in the case

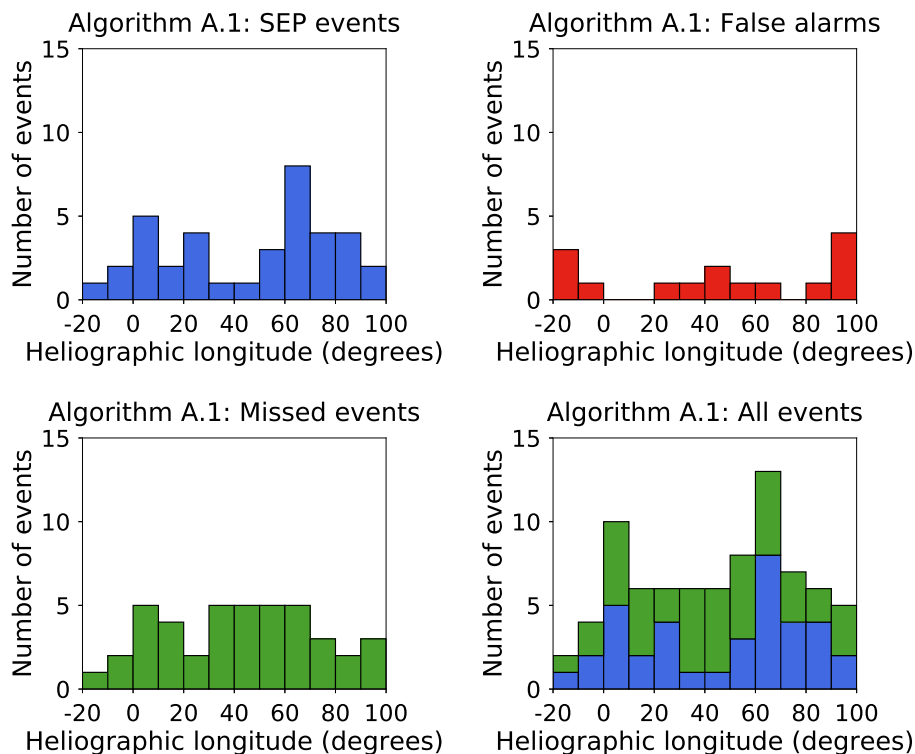


Figure 6. Histograms of the heliographic longitude of solar events in time range 1 of algorithm A.1 SEP events (*top left*); of algorithm A.1 false alarms (*top right*); of SEP events missed by algorithm A.1 (*bottom left*); and of all SEP events (*bottom right*).

of Figure 10 the size of the marker reflects the duration of the flare itself. The bottom plot gives the same information, but for the false alarms according to algorithm A.2.

X-class flares which were false alarms tended to be shorter than those which produced SEPs. Average flare duration for the SEP-producing X-class flares was 46.3 minutes, and 25.6% were longer than 60 minutes (“long duration flares”). For the false alarms, average flare duration was 24.9 minutes, and only 5.0% (2/40) were long duration flares. It has previously been shown that there is an association between long duration flares and CMEs (Yashiro *et al.*, 2006), therefore the trend with duration may be connected with the fact that large flares without CMEs are more likely to be false alarms.

In this case, too, the width of the associated CME is an important parameter. Of the 39 western X-class flares which produced SEPs at Earth, we were able definitively to associate 37 with a CME (the other two occurring during times when LASCO did not produce any data). Of those 37, 86.5% (32/37) were halo CMEs. In contrast, for the false alarms, we were able to confirm associations with CMEs in 25 cases. Of these 25, only 44.0% (11/25) were haloes.

3.4. Algorithm A.2 over time range 2

Over the longer period of time range 2, there were 197 western X-class flares which we analysed, and 39.1% (77/197) produced SEPs at Earth. The false alarm rate was thus 60.9% (120/197)

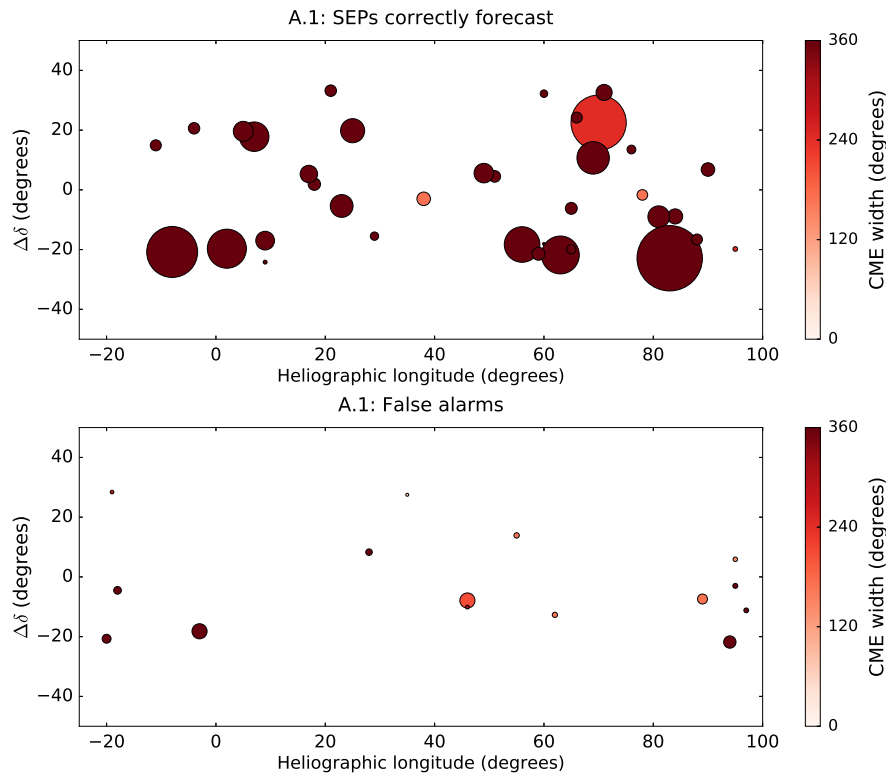


Figure 7. $\Delta\delta$ versus heliographic longitude for those western fast CMEs which produced SEPs at Earth in time range 1 (*top plot*); and for those which were false alarms according to algorithm A.1 (*bottom plot*). The size of the marker represents peak SXR intensity of the flare: for example, the point at S20W95 in the top plot was an M1.8 flare, whereas the point at S21E08 in the same plot was an X17.2 flare. The colour of the marker represents CME width.

and the algorithm failed to forecast 47.8% (71/148) of SEP events. Of all the SEP events for which coordinates could be determined, it missed 55.0% (94/171). Therefore the FAR was 0.61 and the CSI 0.29 without the missed eastern events, and 0.26 with them. The FAR is higher for this longer time period than that for time range 1. Appendix D provides the list of false alarms for the algorithm A.2 over time range 2.

In Figure 11 we plot $\Delta\delta$ against date for this longer time period together with histograms for $\Delta\delta$. In the left hand plots the duration of the flare is denoted by the size of the marker. Figure 11 shows a significant difference in the $\Delta\delta$ distribution for events which produced SEPs and false alarms. For the former the distribution is rather flat, whereas for the latter a high number of events are characterised by large $\Delta\delta$.

There was a significantly higher number of false alarms from the southern solar hemisphere during Solar Cycle 22 (taken to be 1 January 1987 until 31 December 1995) (80% - 40/50) than from the north (20% - 10/50). Furthermore, in Solar Cycle 24 (taken to be from 1 January 2010 onwards) there were only two western X-class flares which were false alarms.

It is also noted that X-class flares between 1980 and 1995 were, on average, longer than those *post* 1995. It can be seen from Table 2 that we have taken data from GOES 7 and its predecessors for dates before 1 March 1995, and from GOES 8 and its successors after that date. We are not aware of any reason why a change of instrument should produce such a result, nor are we aware of any change in the way flare duration has been measured.

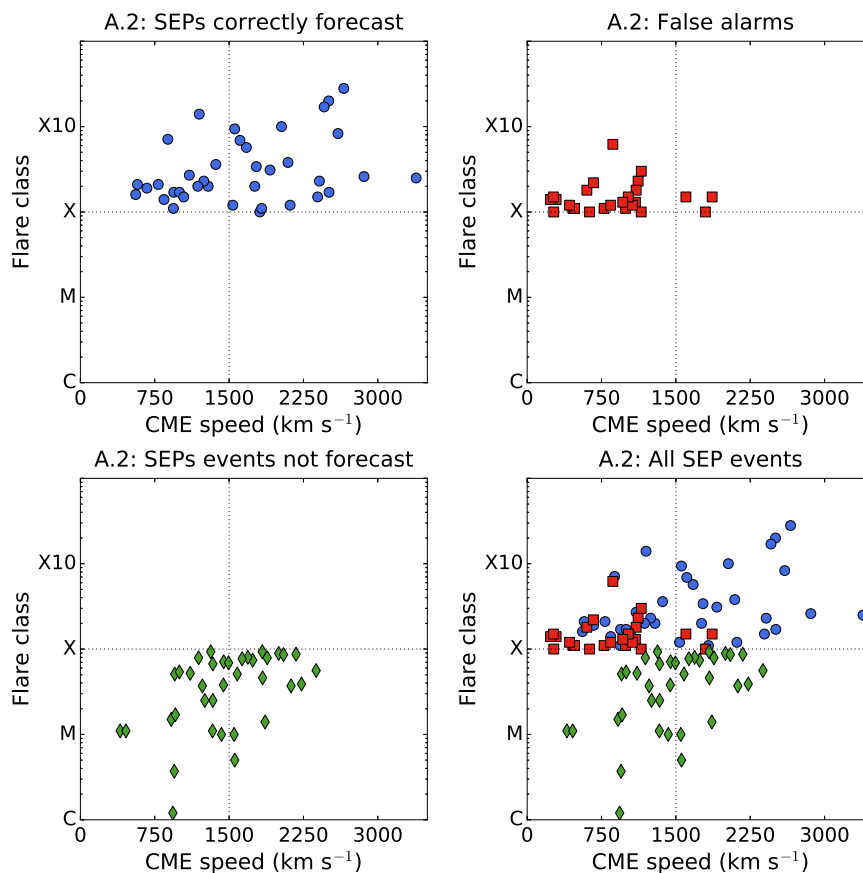


Figure 8. Flare class *versus* associated CME speed for those solar events which produced SEPs >40 MeV at Earth in time range 1 (*top left, blue circles*); for fast CMEs which were false alarms according to forecasting algorithm A.2 (*top right, red squares*); for SEP events missed by algorithm A.2 (*bottom left, green diamonds*); and for all events together (*bottom right*).

4. Improvement of the forecasting algorithms

We examined ways in which the performance of the forecasting algorithms might be improved. We note in particular the following:

1. That algorithm A.1 produced the lowest number of false alarms, and that many of these had an associated flare intensity $< M3$.
2. That X-class flares without an associated CME, or associated with a CME of speed less than 500 km s^{-1} , did not produce SEPs.

We therefore define a third forecasting algorithm as follows:

- A.3 A front-side CME with a reported speed of 1500 km s^{-1} or greater occurring west of E20 on the solar disk which is associated with a flare of class M3 or greater **or** a solar flare of class X or greater which occurs west of E 20 on the solar disk and is associated with a CME of speed greater than 500 km s^{-1} will result in an SEP event being detected at Earth.

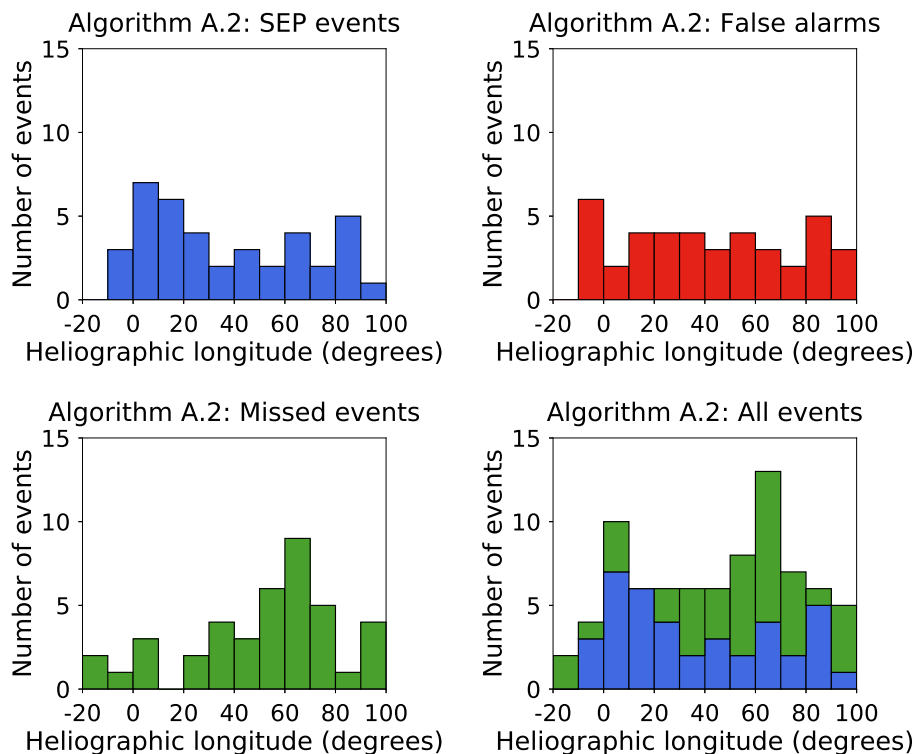


Figure 9. Histograms of the heliographic longitude of solar events in time range 1 of algorithm A.2 SEP events (*top left*); of algorithm A.2 false alarms (*top right*); of SEP events missed by algorithm A.2 (*bottom left*); and of all SEP events (*bottom right*).

Table 4. A summary of the evaluation scores for algorithm A.3 in the same format as Table 3.

Forecasting algorithm	Time range	FAR	CSI not including missed eastern events	CSI including missed eastern events
A.3	1	0.30	0.53	0.49

There were 71 such events in time range 1 and 70.4% (50/71) produced SEPs at Earth. It should be noted that for this algorithm we have had to discard five of the SEP events which occurred during a time when there were no data from the LASCO coronagraph. Thus the false alarm rate was 29.6% (21/71) and the algorithm missed 32.4% (24/74) of SEP events for which the parent solar event was a western one, or 38.3% (31/81) of all SEP events. The false alarm ratio is thus comparable to that produced by algorithm A.1, but A.3 misses far fewer SEP events and consequently the CSI is significantly higher at 0.53 not including the missed eastern events, or 0.49 were they to be included. The result is summarised in Table 4. We also show the result graphically in Figure 12 which is in the same format as Figure 3. It may be possible to formulate better forecasting algorithms, but we suggest that increased forecasting accuracy will only come if the properties of both flares and CMEs are taken into account.

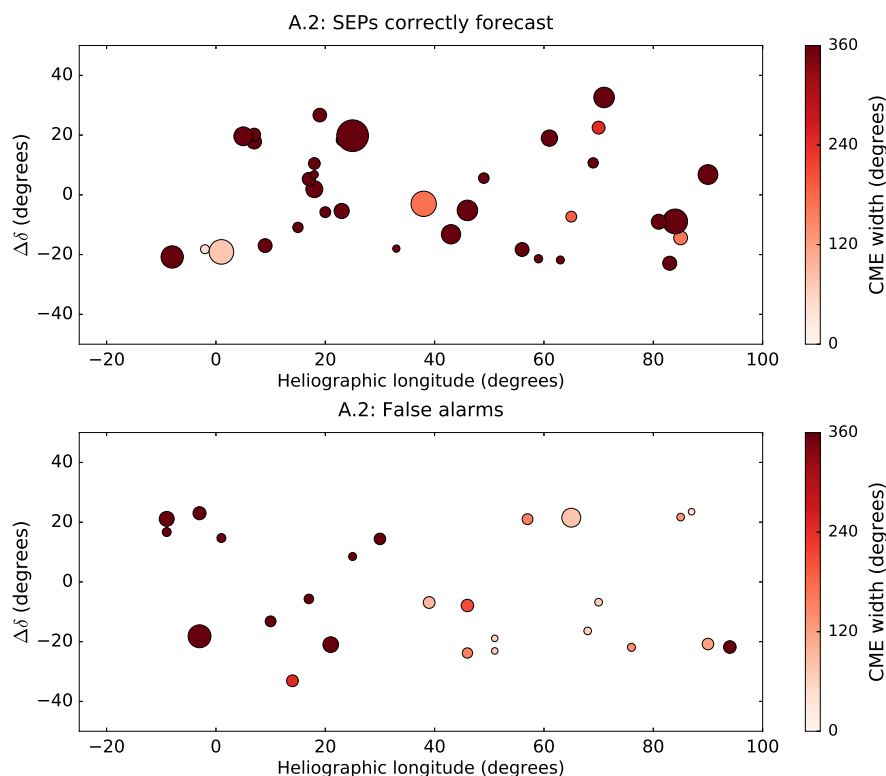


Figure 10. $\Delta\delta$ versus heliographic longitude for those western X-class flares which produced SEPs at Earth in time range 1 (*top plot*); and for those which were false alarms according to algorithm A.2 (*bottom plot*). The *size of the marker* represents the relative duration of the flare: for example, the flare marked at S18W33 in the top plot had a duration of ten minutes, whereas the flare at S03W38 in the same plot lasted 120 minutes. The *colour of the marker* represents CME width.

5. Summary and conclusions

We have used historical data sets in order to assess the efficacy of two simple SEP forecasting algorithms which were based upon the occurrence of magnetically well-connected energetic solar events: western fast CMEs and X-class flares. We used in our definition of SEP event a threshold value for proton energy of >40 MeV.

An algorithm purely based on the detection of a fast CME (A.1) performs reasonably well in terms of false alarms (having a false alarm ratio of 28.8%) but is missing a significant fraction of actual SEP events (53.1%). It is unclear whether this is due to experimental limitations in the determination of the CME speed, or whether there are other physical properties which would need to be measured and included in the algorithm to assess the SEP producing potential of a CME more accurately. False alarms for this type of algorithm tend to be associated with flares of magnitude smaller than M3. There does not seem to be any positional trend in the source location of the false alarms.

An algorithm purely based on the detection of an intense flare (A.2) correctly forecasts almost the same number of SEP events as A.1 but has a much larger false alarm rate (50.6%). Like A.1 it misses a significant fraction of SEP events (also 50.6%). We found that false alarms for this algorithm tend to be flare events of shorter duration, compared to those which did produce SEPs. Of these false alarms, 37% were not associated with a CME. An earlier study has analysed

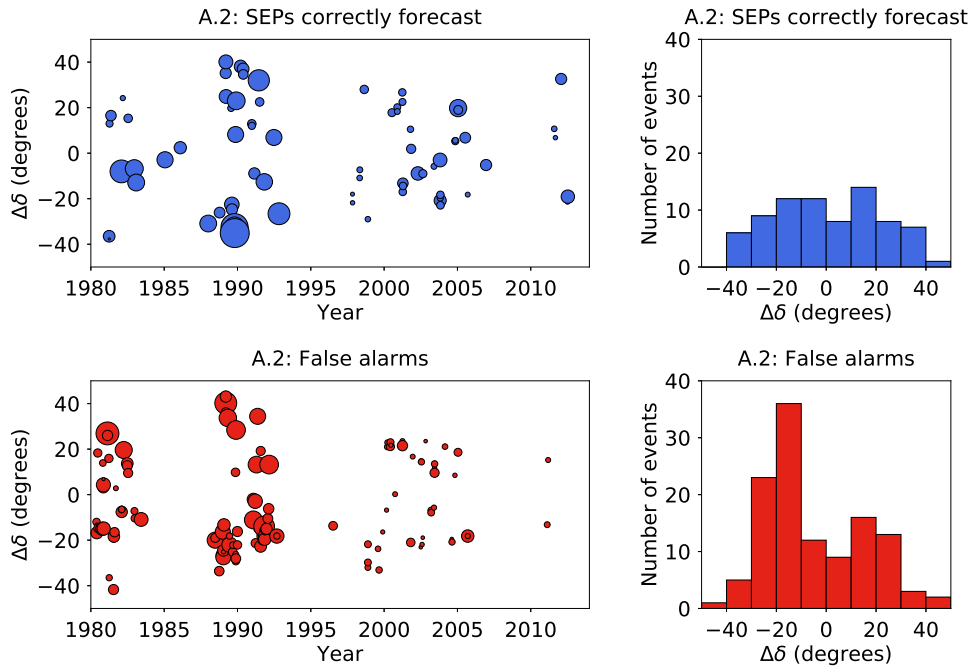


Figure 11. Plots of $\Delta\delta$ against time for algorithm A.2 over time range 2, together with histograms of $\Delta\delta$. The *top plots* present the results for the solar events which were correctly forecast to produce SEPs at Earth (shown in *blue*); the *bottom plots* the false alarms (shown in *red*). The *size of the marker* in the *left hand plots* is representative of the duration of the flare: for example, the flare in October 1989 shown at S35 in the top plot lasted 8 hours 48 minutes, whereas the flare in November 1998 shown at S29 in the same plot lasted 19 minutes

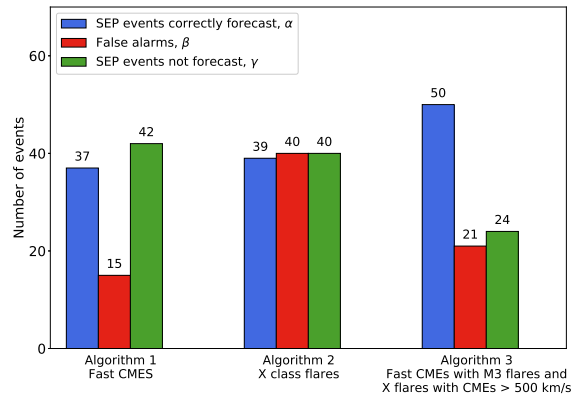


Figure 12. The numbers of correctly forecast SEP events, false alarms and SEP events which were not forecast for the three forecasting algorithms during time range 1.

confined flares (CME-less flares) and emphasized that this kind of event tends not to produce SEPs (Klein, Trottet, and Klassen, 2010). In terms of their longitudinal location, A.2 false alarm events were quite uniformly distributed. We also determined that SEP events not forecast by algorithm A.2 were preferentially located in the well-connected region (between W20 and W80), suggesting that for this region a lower flare magnitude threshold may need to be used.

When evaluated over a longer time range which includes Solar Cycle 21 (time range 2), algorithm A.2 performs less well than over time range 1. This may be due to instrumental effects associated with different GOES detectors being employed at different times, or it may be a real physical effect. We found that there is a systematic trend for flare durations to be larger in Cycle 22 compared with Cycle 23 and this may be an instrumental effect.

It has previously been suggested that the latitudinal separation, $\Delta\delta$, between the flare location and the footpoint of the observing spacecraft plays a role in whether or not high-energy particles are detected (Gopalswamy *et al.*, 2014). In our analysis, carried out over a larger time range, we found that false alarms for algorithm A.2 tended to be associated with a large latitudinal separation $\Delta\delta$, whilst this was not the case for algorithm A.1.

We defined a new forecasting algorithm, A.3, based upon the parameters of both flares and CMEs. This algorithm performed better than the algorithms based solely upon one type of solar event: it correctly forecast 70.4% of SEP events during time range 1 and thus had a false alarm rate comparable to that of algorithm A.1 (29.6%). It also missed many fewer SEP events (32.4%, or 38.3% if eastern events were to be included) than both algorithms A.1 and A.2.

In test particle simulations it has been shown that SEPs may exhibit significant cross-field drift velocities depending on the configuration of the interplanetary magnetic field (Dalla *et al.*, 2013; Marsh *et al.*, 2013). Future work will assess whether the specific polarity of the magnetic field may influence whether or not SEPs were detected at a given location.

We have made available, in electronic form as supplementary material, lists of the >40 MeV proton false alarms according to each of the algorithms we analysed, together with a list of the solar events which produced the >40 MeV SEP events. We hope that these lists can be used as the basis for further studies and comparisons.

Acknowledgments The CDAW catalogue is generated and maintained at the CDAW Data Center by NASA and The Catholic University of America in cooperation with the Naval Research Laboratory. The catalogue may be accessed at http://cdaw.gsfc.nasa.gov/CME_list/index.html. The GOES SXR Flare List can be found at the Heliophysics Integrated Observatory website, <http://hfe.helio-vo.eu>, and we also used data as to heliographic coordinates from the SolarSoft Latest Events Flares List (gevloc) which can be obtained from the same site. Our proton intensity data were downloaded from the SEPTEM website, <http://dev.sepem.oma.be>. We are very grateful to all those who maintain these data repositories as this work could not have been completed without them.

We have also used videos taken by the EIT instrument on board the SOHO spacecraft, and the AIA instrument on board the SDO spacecraft. SOHO is a project of international cooperation between ESA and NASA. We are grateful to them, and to the AIA, EVE, and HMI science teams.

Thanks, too, must go to the anonymous referee for their helpful comments. SD acknowledges support from the UK Science and Technology Facilities Council (STFC, grant ST/M00760X/1).

Disclosure of Potential Conflicts of Interest: the authors declare that they have no conflicts of interest.

References

- Alberti, T., Laurenza, M., Cliver, E.W., Storini, M., Consolini, G., Lepreti, F.: 2017, Solar activity from 2006 to 2014 and short-term forecasts of solar proton events using the ESPERTA model. *Astrophys. J.* **838**(1), 59. [0004-637X-838-1-59]
- Aran, A., Sanahuja, B., Lario, D.: 2006, SOLPENCO: A solar particle engineering code. *Adv. Space Res.* **37**, 1240. DOI. ADS. [2006AdSpR..37.1240A]
- Balch, C.C.: 1999, Sec proton prediction model: Verification and analysis. *Radiat. Meas.*, 231. DOI. [1999RadiatMeas..30..231]
- Balch, C.C.: 2008, Updated verification of the Space Weather Prediction Center's solar energetic particle prediction model. *Space Weather* **6**, S01001. DOI. ADS. [2008SpWea...6.1001B]
- Beck, P., Latocha, M., Rollet, S., Stehno, G.: 2005, TEPC reference measurements at aircraft altitudes during a solar storm. *Adv. Space Res.* **36**, 1627. DOI. ADS. [2005AdSpR..36.1627B]
- Belov, A., Garcia, H., Kurt, V., Mavromichalaki, H., Gerontidou, M.: 2005, Proton Enhancements and Their Relation to the X-Ray Flares During the Three Last Solar Cycles. *Solar Phys.* **229**, 135. DOI. ADS. [2005SoPh..229..135B]
- Bentley, R.D., Csillaghy, A., Abouadarham, J., Jacquey, C., Hapgood, M.A., Bocchialini, K., Messerotti, M., Brooke, J., Gallagher, P., Fox, P., Hurlburt, N., Roberts, D.A., Duarte, L.S.: 2011, HELIO: The Heliophysics Integrated Observatory. *Adv. Space Res.* **47**, 2235. DOI. ADS. [2011AdSpR..47.2235B]
- Brueckner, G.E., Howard, R.A., Koomen, M.J., Korendyke, C.M., Michels, D.J., Moses, J.D., Socker, D.G., Dere, K.P., Lamy, P.L., Llebaria, A., Bout, M.V., Schwenn, R., Simnett, G.M., Bedford, D.K., Eyles, C.J.: 1995, The Large Angle Spectroscopic Coronagraph (LASCO). *Solar Phys.* **162**, 357. DOI. ADS. [1995SoPh..162..357B]
- Cliver, E.W., Ling, A.G., Belov, A., Yashiro, S.: 2012, Size distributions of solar flares and solar energetic particle events. *Astrophys. J. Lett.* **756**, L29. DOI. ADS. [2012ApJ...756L..29C]
- Crosby, N.B., Glover, A., Aran, A., Bonnevie, C., Dyer, C., Gabriel, S., Hands, A., Heynderickx, D., Jacobs, C., Jiggins, P., King, D., Lawrence, G., Poedts, S., Sanahuja, B., Truscott, P.: 2010, SEP-EM -Solar Energetic Particle Environment Modelling. In: *38th COSPAR Scientific Assembly, COSPAR Meeting* **38**, 4. ADS. [2010ocosp...38.4225C]
- Dalla, S., Marsh, M.S., Kelly, J., Laitinen, T.: 2013, Solar energetic particle drifts in the parker spiral. *J. Geophys. Res.* **118**(10), 5979. DOI. <http://dx.doi.org/10.1002/jgra.50589>. [2013JGRA..118.5979D]
- Dierckx, M., Tziotziou, K., Dalla, S., Patsou, I., Marsh, M.S., Crosby, N.B., Malandraki, O., Tsiropoula, G.: 2015, Relationship between Solar Energetic Particles and Properties of Flares and CMEs: Statistical Analysis of Solar Cycle 23 Events. *Solar Phys.* **290**, 841. DOI. ADS. [2015SoPh..290..841D]
- Dumbović, M., Devos, A., Vršnak, B., Sudar, D., Rodriguez, L., Ruždjak, D., Leer, K., Vennerstrøm, S., Veronig, A.: 2015, Geoeffectiveness of Coronal Mass Ejections in the SOHO Era. *Solar Phys.* **290**, 579. DOI. ADS. [2015SoPh..290..579D]
- Feynman, J., Gabriel, S.B.: 2000, On space weather consequences and predictions. *J. Geophys. Res.* **105**, 10543. DOI. ADS. [2000JGR...10510543F]
- Garcia, H.A.: 1994, Temperature and emission measure from GOES soft X-ray measurements. *Solar Phys.* **154**, 275. DOI. ADS. [1994SoPh..154..275G]
- Gopalswamy, N., Yashiro, S., Michalek, G., Stenborg, G., Vourlidas, A., Freeland, S., Howard, R.: 2009, The SOHO/LASCO CME Catalog. *Earth, Moon, and Planets* **104**, 295. DOI. ADS. [2009EM&P..104..295G]
- Gopalswamy, N., Xie, H., Akiyama, S., Mäkelä, P.A., Yashiro, S.: 2014, Major solar eruptions and high-energy particle events during solar cycle 24. *Earth, Planets, and Space* **66**, 104. DOI. ADS. [2014EP&S...66..104G]
- Grubb, R.N.: 1975, The SMS/GOES space environment monitor subsystem. *NASA STI/Recon. Tech. Rep. N.* **76**. ADS. [1975STIN...7628260G]
- Hargreaves, J.K.: 2005, A new method of studying the relation between ionization rates and radio-wave absorption in polar-cap absorption events. *Ann. Geophys.* **23**, 359. DOI. ADS. [2005AnGeo..23..359H]
- Harrison, R.A., Bewsher, D.: 2007, A benchmark event sequence for mass ejection onset studies. A flare associated CME with coronal dimming, ascending pre-flare loops and a transient cool loop. *Astron. Astrophys.* **461**, 1155. DOI. ADS. [2007A&A...461.1155H]
- Hoff, J.L., Townsend, L.W., Zapp, E.N.: 2004, Interplanetary crew doses and dose equivalents: variations among different bone marrow and skin sites. *Adv. Space Res.* **34**, 1347. DOI. ADS. [2004AdSpR..34.1347H]
- Kahler, S.W., Ling, A.: 2015, Dynamic sep event probability forecasts. *Space Weather* **13**(10), 665. DOI. [2015SW001222]. DOI. [SWE:SWE20256]
- Kahler, S.W., Cliver, E.W., Ling, A.G.: 2007, Validating the proton prediction system (PPS). *J. Atmos. Solar-Terr. Phys.* **69**, 43. DOI. ADS. [2007JASTP...69...43K]
- Klein, K.-L., Trottet, G., Klassen, A.: 2010, Energetic Particle Acceleration and Propagation in Strong CME-Less Flares. *Solar Phys.* **263**, 185. DOI. ADS. [2010SoPh..263..185K]
- Klein, K.-L., Trottet, G., Samwel, S., Malandraki, O.: 2011, Particle Acceleration and Propagation in Strong Flares without Major Solar Energetic Particle Events. *Solar Phys.* **269**, 309. DOI. ADS. [2011SoPh..269..309K]
- Kwon, R.-Y., Zhang, J., Vourlidas, A.: 2015, Are Halo-like Solar Coronal Mass Ejections Merely a Matter of Geometric Projection Effects? *Astrophys. J. Lett.* **799**, L29. DOI. ADS. [2015ApJ...799L..29K]

- Laurenza, M., Cliver, E.W., Hewitt, J., Storini, M., Ling, A.G., Balch, C.C., Kaiser, M.L.: 2009, A technique for short-term warning of solar energetic particle events based on flare location, flare size, and evidence of particle escape. *Space Weather* **7**, 4008. DOI. ADS. [2009SpWea...7.4008L]
- Luhmann, J.G., Ledvina, S.A., Odstroil, D., Owens, M.J., Zhao, X.-P., Liu, Y., Riley, P.: 2010, Cone model-based SEP event calculations for applications to multipoint observations. *Adv. Space Res.* **46**, 1. DOI. ADS. [2010AdSpR...46....1L]
- Marqué, C., Posner, A., Klein, K.-L.: 2006, Solar Energetic Particles and Radio-silent Fast Coronal Mass Ejections. *Astrophys. J.* **642**, 1222. DOI. ADS. [2006ApJ...642.1222M]
- Marsh, M.S., Dalla, S., Kelly, J., Laitinen, T.: 2013, Drift-induced Perpendicular Transport of Solar Energetic Particles. *Astrophys. J.* **774**, 4. DOI. ADS. [2013ApJ...774....4M]
- Marsh, M.S., Dalla, S., Dierckxsens, M., Laitinen, T., Crosby, N.B.: 2015, SPARX: A modeling system for solar energetic particle radiation space weather forecasting. *Space Weather* **13**(6), 386. 2014SW001120. DOI. [SWE:SWE20233]
- Papaioannou, A., Anastasiadis, A., Sandberg, I., Georgoulis, M.K., Tziropoula, G., Tziotziou, K., Jiggins, P., Hilgers, A.: 2015, A novel forecasting system for solar particle events and flares (FORSPEF). *J. Phys. Conf. Ser.* **632**(1), 012075. [1742-6596-632-1-012075]
- Papaioannou, A., Sandberg, I., Anastasiadis, A., Kouloumvakos, A., Georgoulis, M.K., Tziotziou, K., Tziropoula, G., Jiggins, P., Hilgers, A.: 2016, Solar flares, coronal mass ejections and solar energetic particle event characteristics. *J. Space Weather Spac.* **6**(27), A42. DOI. ADS. [2016JWSC...6A..42P]
- Park, J., Moon, Y.-J., Gopalswamy, N.: 2012, Dependence of solar proton events on their associated activities: Coronal mass ejection parameters. *J. Geophys. Res.* **117**, A08108. DOI. ADS. [2012JGRA...117.8108P]
- Posner, A.: 2007, Up to 1-hour forecasting of radiation hazards from solar energetic ion events with relativistic electrons. *Space Weather* **5**(5), n/a. S05001. DOI. [SWE:SWE185]
- Reinard, A.A., Andrews, M.A.: 2006, Comparison of CME characteristics for SEP and non-SEP related events. *Adv. Space Res.* **38**, 480. DOI. ADS. [2006AdSpR...38..480R]
- Smart, D.F., Shea, M.A.: 1989, PPS-87 - A new event oriented solar proton prediction model. *Adv. Space Res.* **9**, 281. DOI. ADS. [1989AdSpR...9..281S]
- Vršnak, B., Sudar, D., Ruždjak, D.: 2005, The CME-flare relationship: Are there really two types of CMEs? *Astron. Astrophys.* **435**, 1149. DOI. ADS. [2005A&A...435.1149V]
- Wang, Y., Zhang, J.: 2007, A Comparative Study between Eruptive X-Class Flares Associated with Coronal Mass Ejections and Confined X-Class Flares. *Astrophys. J.* **665**, 1428. DOI. ADS. [2007ApJ...665.1428W]
- Winter, L.M., Ledbetter, K.: 2015, Type II and type III radio bursts and their correlation with solar energetic proton events. *Astrophys. J.* **809**(1), 105. [0004-637X-809-1-105]
- Yashiro, S., Akiyama, S., Gopalswamy, N., Howard, R.A.: 2006, Different Power-Law Indices in the Frequency Distributions of Flares with and without Coronal Mass Ejections. *Astrophys. J. Lett.* **650**, L143. DOI. ADS. [2006ApJ...650L.143Y]

Appendix

A. Association of Solar Flares and CMEs

It has long been accepted that solar flares and CMEs, particularly energetic events, often occur within a short time of each other from the same solar active region, but making associations between them is no trivial exercise. There is no standard approach: for example, Reinard and Andrews, 2006 associate a flare with a CME if the CME occurred within a 2 hour window centred on the time of the peak of the flare; others make associations by using both temporal and spatial criteria (Vršnak, Sudar, and Ruždjak, 2005; Dumbović *et al.*, 2015). Below we describe a method of making associations between CMEs and flares automatically, and evaluate its accuracy.

In the light of the connection between high energy eruptive events and SEPs we decided to look for associations involving CMEs reported by CDAW to have a speed of 1000 km s^{-1} or faster (“rapid CMEs”), and flares reported in the GOES SXR list to be of class M5 or greater (“intense flares”). We examined all such events between 1 July 2011 and 31 August 2012, that period being chosen solely because it provided a data set which was small enough to allow individual observation of each event, yet large enough to allow wider conclusions to be drawn.

There were 55 rapid CMEs and 32 intense flares reported in the 13 month period under investigation. Of these, we did not study further 3 of the rapid CMEs and 1 of the intense flares because they coincided with data gaps. Hence there were 83 events which formed the basis of our study of flare–CME associations.

In order to set a benchmark against which any automated method of associating CMEs and flares could be judged, we needed to know definitively whether any of the 83 energetic events were associated with another solar event. Consequently we watched movies at 193 \AA of each one of these events, each movie having been created from data obtained by the *Atmospheric Imaging Assembly* (AIA) on board the *Solar Dynamics Observatory* (SDO) spacecraft.

For each of the intense flares, identification was done visually from the AIA / SDO movies. We looked for increases in intensity on the solar surface at the time of the flare specified by the GOES SXR list, but in cases where the site of the flare was not obvious we accepted the reported coordinates. Whilst watching the movies of the intense flares, we also searched for evidence of an associated CME. If we were able to see any ejected material, any loop distortion or any coronal dimming consistent with the flare site within 1 hour either side of the reported time of the flare, we associated that flare with a CME (whether or not this was a rapid CME).

Rapid CMEs were identified by searching visually for evidence of any ejected material, any loop distortion or any coronal dimming at the time reported by CDAW. If such evidence was present (and was consistent with a front-side event), the CME was regarded as having occurred on the face of the disk; if there was no such evidence, the CME was regarded as a back-side event. Associations were made between a rapid CME and a flare (whether or not this was an intense flare) if the reported time of the CME (*i.e.* the time the CME was first seen in the LASCO C2 images) fell between 1 hour before the reported start of the flare and 1 hour after its reported end, and the evidence of the CME was consistent with the flare site.

As a result of making the associations manually we found that 35 of the 52 fast CMEs were on the face of the disk. This proportion is slightly higher than might have been expected (given that we can only see one side of the Sun at any one time, we might expect that only half of the CMEs we see would be from the face of the disk), but can be explained by two factors: first, there were large numbers of CMEs from same active regions (two active regions produced five each, and one other eight) and this may slightly distort the figures; secondly 17 of the 52 events were reported to occur very close to the limb, meaning that we may have seen a CME which originated from just behind the limb.

Of the 35 rapid CMEs which occurred on the face of the disk, all were associated with a flare of some kind; 46% (16/35) were associated with an intense flare. Of the 31 intense flares, 84% (26/31) were associated with a CME.

In every instance where we had associated a solar flare with a CME, the flare was reported in the GOES SXR list as having commenced before the CME was first reported in the CDAW catalogue. It should be noted that this is not an indication of actual chronology - as an example of where there is evidence of a CME lifting off before its associated flare, see Harrison and Bewsher, 2007 - but it is of significance when devising a method of automatically making associations between flares and CMEs.

CDAW reports the time of a CME as being when it is first seen in images produced by the LASCO C2 coronagraph. This instrument, however, has a field of view between about 2 and 6 solar radii (as measured from the Sun's centre) and the images used by CDAW have a cadence of, at best, 12 minutes and sometimes much longer. The combination of these factors means that the reported time of the CME may be many minutes after its actual "lift-off" time, t_o .

Any attempt to make an estimate of t_o faces a number of difficulties: there is no information as to the height of the CME when it was first ejected; no information as to whether it has accelerated or decelerated before its first appearance in the C2 images; and no information as to the direction of the CME. Nevertheless, finding a first approximation of t_o is more likely to result in accurate associations between CMEs and flares than using the time of the CME as reported by CDAW.

We make the simple assumptions that by the time the CME reaches the field of view of the C2 coronagraph it has travelled (at least) one solar radius and has undergone neither significant acceleration nor deceleration. An estimate for t_o is then obtained by using the reported speed of the CME.

In order to take into account of the difficulties caused by the cadence of the images, we define Δt as a number of minutes both before and after a flare. For example, if we take $\Delta t = 12$, we compare t_o with a time window opening 12 minutes before the flare began and closing 12 minutes after it ended. Plainly, the greater Δt , the more likely it is that t_o will fall within the window, and hence the greater the likelihood of false associations being made.

We found that a good correlation could be found between those flare-CME associations which had made manually and those using a value of Δt of just 30 minutes. We did investigate whether it may be possible to improve the accuracy of the method by imposing a spatial criterion, for example by requiring the position angle of the CME to agree with the latitude and longitude of the flare to within a particular number of degrees. In fact we found that overall accuracy was not improved by the imposition of such a criterion.

There will, of course, always be a small number of (usually) false associations when using this automatic method given that occasionally apparently unconnected solar events sometimes occur almost simultaneously. Nevertheless, in our sample the method correctly identified 98% (60/61) associations and correctly identified 86% (19/22) non-associations, an overall success rate in 95% (79/83) of cases.

B. Algorithm 1: False alarms in time range 1

Table 5. List of fast CMEs between 1 January 1996 and 31 March 2013 which were false alarms. Column 1 gives the time the CME was first reported, column 2 its speed, and column 3 its acceleration all as reported by CDAW. Column 4 is the position angle at which the height-time measurements had been made (called by CDAW the “measurement position angle”). Column 5 is the CME width. Columns 6 to 10 give the parameters of the associated flare: its start time, heliographic latitude, heliographic longitude, class, and duration.

First reported	CME parameters					Flare parameters				
	V (km s ⁻¹)	Accel. (km s ⁻²)	Mpa (degrees)	Width (degrees)	Time start	Lat	Lon	Class	Duration (hrs: mins)	
1998-11-24T02:30	1798	-12.5	225	360	1998-11-24T02:07	-20	94	X1.0	00:30	
2000-01-06T07:31	1813	10.7	342	67	2000-01-06T06:45	24	35	C5.8	00:21	
2000-05-05T15:50	1594	-103.4	265	360	2000-05-05T15:19	-15	97	M1.5	02:09	
2000-06-25T07:54	1617	-17.5	274	165	2000-06-25T07:17	16	55	M1.9	01:04	
2001-07-19T10:30	1668	-11.6	252	166	2001-07-19T09:52	-8	62	M1.8	00:25	
2002-03-22T11:06	1750	-22.5	259	360	2002-03-22T10:12	-10	95	M1.6	01:40	
2002-05-30T05:06	1625	67.0	275	144	2002-05-30T04:24	5	95	M1.3	01:49	
2002-08-16T12:30	1585	-67.1	121	360	2002-08-16T11:32	-14	-20	M5.2	01:35	
2003-03-18T12:30	1601	-13.3	266	209	2003-03-18T11:51	-15	46	X1.5	00:29	
2003-06-02T00:30	1656	42.5	248	172	2003-06-02T00:07	-8	89	M6.5	00:36	
2003-11-18T08:50	1660	-3.3	206	360	2003-11-18T08:12	-2	-18	M3.9	00:47	
2004-04-11T04:30	1645	-77.6	237	314	2004-04-11T03:54	-16	46	C9.6	00:41	
2005-07-09T22:30	1540	-168.5	328	360	2005-07-09T21:47	12	28	M2.8	00:32	
2005-09-13T20:00	1866	11.5	149	360	2005-09-13T19:19	-11	-3	X1.5	01:38	
2013-02-06T00:24	1867	-8.2	31	271	2013-02-06T00:04	22	-19	C8.7	00:37	

C. Algorithm 2: False alarms in time range 1

Table 6. List of X-class flares between 1 January 1996 and 31 March 2013 which were false alarms. Column 1 gives the time the CME was first reported, column 2 its speed, and column 3 its acceleration all as reported by CDAW. Column 4 is the position angle at which the height-time measurements had been made (called by CDAW the “measurement position angle”). Column 5 is the CME width. Columns 6 to 10 give the parameters of the associated flare: its start time, heliographic latitude, heliographic longitude, class, and duration.

First reported	CME parameters					Flare parameters				
	V (km s ⁻¹)	Accel. (km s ⁻²)	Mpa (degrees)	Width (degrees)		Time start	Lat	Lon	Class	Duration (hrs: mins)
LASCO data gap						1996-07-09T09:01	-10	30	X2.6	00:48
LASCO data gap						1998-11-22T16:10	-30	89	X2.5	00:22
LASCO data gap						1998-11-23T06:28	-28	89	X2.2	00:30
1998-11-24T02:30	1798	-12.5	225	360		1998-11-24T02:07	-20	94	X1.0	00:30
1999-08-02T22:26	292	0.9	264	157		1999-08-02T21:18	-18	46	X1.4	00:20
1999-08-28T18:26	462	1.1	221	245		1999-08-28T17:52	-26	14	X1.1	00:26
1999-11-27T12:54	235	64.2	256	68		1999-11-27T12:05	-15	68	X1.4	00:11
2000-03-02T08:54	776	0.8	233	62		2000-03-02T08:20	-11	70	X1.1	00:11
2000-03-22T19:31	478	-92.0	312	154		2000-03-22T18:34	14	57	X1.1	00:22
						2000-03-24T07:41	16	82	X1.8	00:18
						2000-06-06T13:30	22	-10	X1.1	00:16
2000-06-06T15:54	1119	1.5	47	360		2000-06-06T14:58	21	-9	X2.3	00:42
2000-06-07T16:30	842	59.8	309	360		2000-06-07T15:34	23	-3	X1.2	00:32
2000-06-18T02:10	629	-1.2	318	132		2000-06-18T01:52	23	85	X1.0	00:11
						2000-09-30T23:13	7	91	X1.2	00:15
						2001-04-02T10:04	17	60	X1.4	00:16
2001-04-02T11:26	992	3.0	278	80		2001-04-02T10:58	15	65	X1.1	01:07
2001-10-25T15:26	1092	-1.4	175	360		2001-10-25T14:42	-16	21	X1.3	00:46
2001-12-13T14:54	864	-11.4	37	360		2001-12-13T14:20	16	-9	X6.2	00:15
2002-07-03T02:54	265	-9.9	274	73		2002-07-03T02:08	-20	51	X1.5	00:08

continued ...

Table 6.

First reported	CME parameters				Flare parameters				Duration (hrs: mins)
	V (km s ⁻¹)	Accel. (km s ⁻²)	Mpa (degrees)	Width (degrees)	Time start	Lat	Lon	Class	
2002-07-15T20:30	1151	-25.6	35	360	2002-07-15T19:59	19	1	X3.0	00:15
2002-07-18T08:06	1099	-30.2	354	360	2002-07-18T07:24	19	30	X1.8	00:25
2002-08-03T19:31	1150	-18.8	272	138	2002-08-03T18:59	-16	76	X1.0	00:12
2002-08-21T06:06	268	-19.6	266	66	2002-08-21T05:28	-12	51	X1.0	00:08
2002-10-31T17:06	1061	-33.4	96	43	2002-10-31T16:47	28	87	X1.2	00:08
2003-03-17T19:54	1020	-5.5	264	96	2003-03-17T18:50	-14	39	X1.5	00:26
2003-03-18T12:30	1601	-13.3	266	209	2003-03-18T11:51	-15	46	X1.5	00:29
2003-05-27T23:50	964	-9.6	67	360	2003-05-27T22:56	-7	17	X1.3	00:17
					2003-06-09T21:31	12	34	X1.7	00:12
L/ASCO data gap					2003-06-10T23:19	10	40	X1.3	00:53
L/ASCO data gap					2003-06-11T20:01	14	57	X1.6	00:26
					2004-02-26T01:50	14	14	X1.1	00:20
					2004-08-13T18:07	-13	23	X1.0	00:08
2004-08-18T17:54	602	0.5	250	120	2004-08-18T17:29	-14	90	X1.8	00:25
2004-10-30T12:30	427	12.4	269	360	2004-10-30T11:38	13	25	X1.2	00:12
					2005-01-15T00:22	14	-8	X1.2	00:40
2005-09-13T20:00	1866	11.5	149	360	2005-09-13T19:19	-11	-3	X1.5	01:38
					2005-09-15T08:30	-11	24	X1.1	00:16
2011-02-15T02:24	669	-18.3	189	360	2011-02-15T01:44	-20	10	X2.2	00:22
					2011-03-09T23:13	8	9	X1.5	00:16

D. Algorithm 2: False alarms for time range 2

Table 7. List of X-class flares between 1 April 1980 and 31 December 1995 which were false alarms. Column 1 gives the start time of the flare, column 2 its heliographic latitude, and column 3 its heliographic longitude. Column 4 is the class of the flare and column 5 its duration.

Time start	Flare parameters			Duration (hrs: mins)
	Lat	Lon	Class	
1980-05-21T20:51	-14	15	X1.4	00:35
1980-05-28T19:24	-18	33	X1.1	01:29
1980-06-04T22:57	-14	69	X2.2	00:17
1980-06-21T01:17	20	90	X2.6	00:43
1980-07-01T16:22	-12	38	X2.5	00:49
1980-10-14T05:42	-9	7	X3.3	01:52
1980-10-25T09:42	19	59	X3.9	00:28
1980-11-07T01:56	7	11	X2.7	01:19
1980-11-08T13:33	8	28	X3.3	02:05
1980-11-12T04:46	10	72	X2.5	00:06
1980-11-15T15:40	-12	83	X1.9	01:51
1981-02-17T18:12	20	20	X1	05:30
1981-02-20T06:40	19	49	X2.4	01:07
1981-03-25T20:39	9	89	X2.2	00:44
1981-04-02T11:03	-43	68	X2.2	00:25
1981-07-19T05:32	-37	56	X2.7	01:05
1981-07-26T07:57	-14	18	X1	00:35
1981-07-27T17:24	-13	-11	X1.5	01:24
1981-08-12T06:24	-10	28	X2.6	00:56
1981-09-15T21:13	10	78	X2.3	00:15
1982-02-07T12:50	-14	72	X1	01:21
1982-02-08T12:50	-13	88	X1.4	00:29
1982-02-09T03:57	-13	90	X1.2	00:26
1982-03-30T05:22	13	11	X2.8	03:04
1982-06-26T00:42	16	5	X1.9	01:26
1982-06-26T19:09	15	73	X2.1	01:04
1982-07-17T10:28	14	32	X3.2	00:53
1982-12-22T08:26	-9	82	X2.4	00:31
1982-12-29T06:43	-13	12	X1.9	00:34
1983-06-06T13:31	-11	15	X1.4	02:01
1988-06-23T08:56	-19	34	X1.6	01:07
1988-06-24T04:18	-18	45	X1.3	02:43
1988-06-24T16:03	-17	52	X2.4	00:51
1988-10-03T14:53	-27	16	X3.2	00:49
1988-10-03T23:22	-27	20	X1.1	00:57
1988-12-30T17:25	-19	30	X1.4	02:23

continued ...

Table 7.

Time start	Flare parameters			Duration (hrs: mins)
	Lat	Lon	Class	
1989-01-13T08:29	-31	5	X2.3	02:16
1989-01-14T02:54	-32	10	X2.1	02:25
1989-01-14T21:45	-29	26	X1.1	01:24
1989-01-18T07:02	-30	65	X1.4	00:11
1989-01-27T19:08	-19	-17	X1.1	01:38
1989-03-14T16:46	33	21	X1.1	05:02
1989-03-16T15:24	36	47	X3.6	01:21
1989-03-16T20:35	29	60	X1.4	00:56
1989-05-05T07:23	30	-1	X2.4	03:12
1989-06-15T18:13	-21	-8	X4.1	02:28
1989-06-16T04:19	-17	-3	X3	00:26
1989-09-03T14:28	-18	-16	X1.2	00:32
1989-09-04T08:57	-18	-19	X1.1	00:49
1989-09-09T19:28	-15	67	X1.3	00:28
1989-11-12T06:21	13	39	X1.5	00:46
1989-11-19T06:19	-24	25	X1.1	00:23
1989-11-20T21:25	-27	43	X1	00:36
1989-11-21T13:32	-26	53	X4	00:59
1989-11-25T22:55	30	-5	X1	03:40
1989-12-30T04:09	-19	-9	X1	01:05
1989-12-31T09:32	-25	51	X2.8	00:45
1991-01-30T08:49	-8	34	X1	01:36
1991-01-31T01:58	-17	35	X1.3	03:21
1991-03-16T00:47	-9	-9	X1.8	00:22
1991-03-17T20:54	-10	13	X1	02:11
1991-03-29T06:42	-28	60	X2.4	00:52
1991-03-31T19:11	-22	88	X1	00:08
1991-04-20T08:27	8	50	X1	02:57
1991-05-18T05:06	32	85	X2.8	02:42
1991-07-31T00:46	-17	-11	X2.3	01:29
1991-08-02T03:07	25	-15	X1.5	00:52
1991-09-07T19:11	-11	50	X3.3	01:10
1991-09-08T09:06	-13	58	X1	00:43
1991-10-26T18:53	-9	-20	X1.7	04:32
1991-10-27T02:06	-11	-20	X1.9	00:51
1991-10-27T05:38	-13	-15	X6.1	01:20
1991-11-09T15:32	-16	57	X1.1	01:37
1991-11-15T22:34	-13	19	X1.5	00:43
1991-12-24T10:13	-17	-14	X1.4	01:20
1992-01-26T15:23	-16	66	X1	01:02
1992-02-16T12:32	-13	17	X1.4	01:09
1992-02-27T09:22	6	2	X3.3	03:41
1992-09-06T18:42	-11	41	X1.7	02:09
1992-09-06T20:50	-11	46	X1.3	00:26

Appendix G

Swalwell *et al.* (2017b)

Forecasting Solar Energetic Particle Events and Associated False Alarms

Bill Swalwell¹, Silvia Dalla¹, and Robert Walsh¹

¹Jeremiah Horrocks Institute, University of Central Lancashire,
Preston, Lancashire, PR1 2HE, United Kingdom
email: bswalwell@uclan.ac.uk

Abstract. Because of the significant dangers they pose, accurate forecasting of Solar Energetic Particle (SEP) events is vital. Whilst it has long been known that SEP-production is associated with high-energy solar events, forecasting algorithms based upon the observation of these types of solar event suffer from high false alarm rates. Here we analyse the parameters of 4 very high energy solar events which were false alarms with a view to reaching an understanding as to why SEPs were not detected at Earth. We find that in each case there were present at least two factors which have been shown to be detrimental to SEP production.

Keywords. Sun: flares, coronal mass ejections, particle emission

1. Introduction

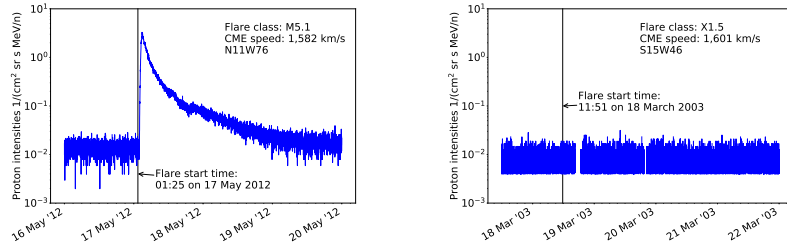
Solar Energetic Particles (SEPs) are a significant component of space weather. They may damage satellites, pose a radiation hazard to astronauts and humans in high-flying aircraft (particularly at high latitudes), and interfere with high-frequency communications' systems. Accurately forecasting their arrival at Earth has become vital.

It has long been known that the detection of SEPs at Earth is associated with solar flares which exhibit high emission in soft X-rays (SXR) and fast Coronal Mass Ejections (CMEs) (*e.g.* Dierckx *et al.* (2015)). The difficulty for SEP forecasting algorithms is, however, that SEPs are not detected at Earth following all such large solar events. For example, Klein *et al.* (2011) investigated all X class flares between longitudes W0° and W90° in the period 1996 to 2006, and they found that 30% did not produce an enhancement of >10 MeV protons above the background level.

Figure 1 shows two plots of proton intensity as measured by the ~40-80 MeV energy channel of the Geostationary Orbital Environmental Satellites' (GOES) Energetic Particle Sensor (EPS) instruments. In Figure 1a, a steep rise is seen following a magnetically well-connected large solar event which occurred on 17 May 2012 as may be expected; by contrast Figure 1b shows that a similarly large event which occurred on 18 March 2003 produced no rise at all. Such an event, which might reasonably have been expected to produce SEPs at Earth, may be termed a "false alarm". Here we examine 4 sample false alarm events with a view to determining why they failed to produce SEPs at Earth.

2. False alarms for simple forecasting algorithms

In Swalwell *et al.* (2017) we defined two simple SEP forecasting algorithms: the first, A.1, is based upon the observation of magnetically well-connected CMEs with a speed greater than 1,500 km/s ("fast CMEs"); the second, A.2, is based upon the observation of well-connected flares of class X. We compared the forecasts of each with historical data sets between January 1996 and March 2013.



(a) A steep rise in energetic proton intensity is seen following a magnetically well-connected M5.1 large solar event as may be expected.

(b) A similarly large solar event produced no rise in energetic proton intensity at all. This event may be termed a “false alarm”.

Figure 1: A comparison of $\sim 40\text{--}80$ MeV proton intensity following two different magnetically-well-connected large solar events.

Algorithm A.1 had a lower false alarm rate (28.8%) than A.2 (50.6%) but both missed a significant number of SEP events (53.2% and 50.6% respectively). We determined that an algorithm which was based upon the parameters of both CMEs and flares produced better results than one based upon the observation of only one type of solar event.

We found a number of factors which are important to SEP production. Fast CMEs were less likely to produce SEPs if they were associated with a flare of class $< M3$, if their associated flare was of relatively short duration, and if they were not reported to be a halo. X class flares were less likely to produce SEPs if either they were not associated with a CME or were associated with a CME slower than 500 km/s, and if they were of relatively short duration (Swalwell *et al.* (2017)).

3. Examples of false alarm events

Table 1 gives four examples of high-energy solar events which it might have been thought would produce SEPs at Earth, but which failed to do so. Examination of some of their parameters sheds some light on why they were false alarms.

3.1. Event 1: 1,813 km/s CME from N24W35 on 6 Jan 2000

This was a very well magnetically-connected, very fast, CME. However, it was associated with a flare which was both short (~ 21 minutes) and of relatively low class (C5.8). Furthermore, the CME itself was reported to have a width of just 67° .

3.2. Event 2: X6.2 flare at N16E09 on 13 Dec 2001

Towards the edge of the best magnetically-connected region, nevertheless this was such a large flare that it might have been expected to produce at least some enhancement of energetic protons. The fact that it did not may be connected to two parameters: (a) it was associated with a CME of relatively low speed (864 km/s), and (b) it was of very short duration (~ 15 minutes).

3.3. Event 3: X1.5 flare at S20W51 on 3 Jul 2002

This very well magnetically-connected flare was associated with a very slow (265 km/s) non-halo (width 261°) CME, and was of very short duration (~ 8 minutes).

Table 1: Example false alarms.

Event no	Date	Event	Coordinates
1	6 Jan 2000	CME speed 1,813 km/s	N24W35
2	13 Dec 2001	X6.2 flare	N16E09
3	3 Jul 2002	X1.5 flare	S20W51
4	18 Mar 2003	X1.5 flare associated with CME speed 1,601 km/s	S15W46

3.4. Event 4: X1.5 flare with 1,601 km/s CME from S15W46 on 18 Mar 2003

This is the event for which the energetic proton intensity is shown in Figure 1b. It was extremely well magnetically-connected to Earth, and in this instance both the flare class and CME speed were high. Flare duration, however, was relatively short (at ~ 29 minutes) and the CME was reported to have a width of 263° .

4. Conclusions

Some very high-energy solar events may fail to produce SEPs at Earth even if they are very well magnetically-connected. Understanding why such events are false alarms may provide an insight as to which of their parameters are important to SEP production.

Swalwell *et al.* (2017) reported that fast CMEs associated with flares of class $<M3$ or of relatively short duration, and fast CMEs which were not reported to be a halo were more likely to be false alarms. X class flares not associated with a CME, or associated with a CME slower than 500 km/s were more likely to be false alarms, as were those of relatively short duration.

Here we considered 4 sample false alarms. In each case 2 or more of the factors which were found to be detrimental to SEP production by Swalwell *et al.* (2017) were found to exist. In event number 1 there were 3: the associated flare was relatively short (~ 21 minutes); it was of class $<M3$ (C5.8); and the CME was not a halo (the width was 67°).

Event number 2 was a less well magnetically-connected flare (from E09) but at X6.2 it was very intense; event 3 was a lower class flare (albeit still large at X1.5) but very well connected. Neither produced SEPs but both had factors likely to result in a false alarm: each flare was short (~ 15 minutes and ~ 8 minutes respectively), and each was associated with a CME of relatively low speed (864 km/s and 265 km/s respectively); and in the case of event 3, the associated CME was not a halo.

Event number 4 illustrates that even a fast CME associated with a high intensity flare may sometimes be a false alarm. In this case, too, however the fact that the CME was not a halo and the short duration of the flare may explain why SEPs were not detected.

The full results and a more detailed analysis are presented in Swalwell *et al.* (2017).

References

- Bentley, R. D., Csillaghy, A., Aboudarham, J., Jacquy, C., Hapgood, M. A., Bocchialini, K., Messerotti, M., Brooke, J., Gallagher, P., Fox, P., Hurlburt, N., Roberts, D. A., & Duarte, L. S. 2011, *Advances in Space Research*, 47, 2235-2239
- Dierckx, M., Tziotziou, K., and Dalla, S., Patsou, I., Marsh, M., Crosby, N., Malandraki, O., & Tsiropoula, G. 2015, *Solar Physics*, 290, 841-874
- Gopalswamy, N., Yashiro, S., Michalek, G., Stenborg, G., Vourlidas, A., Freeland, S., & Howard, R. 2009, *Earth Moon and Planets*, 104, 295-313
- Klein, K.-L., Trottet, G., Samwel, S., & Malandraki, O. 2011, *Solar Physics*, 269, 309-333
- Swalwell, B., Dalla, S., & Walsh, R. 2017, *Solar Physics*, submitted

Appendix H

Battarbee *et al.* (2017)

Multi-spacecraft observations and transport simulations of solar energetic particles for the May 17th 2012 GLE event

M. Battarbee¹, J. Guo², S. Dalla¹, R. Wimmer-Schweingruber², B. Swalwell¹, and D. J. Lawrence³

¹ Jeremiah Horrocks Institute, University of Central Lancashire, PR1 2HE, Preston, UK
e-mail: mbattarbee@uclan.ac.uk

² Institut fuer Experimentelle und Angewandte Physik, University of Kiel, Germany
e-mail: guo@physik.uni-kiel.de

³ Johns Hopkins University Applied Physics Laboratory, MD, USA

Final draft, ready for submission, 26th June 2017

ABSTRACT

Context. The injection, propagation and arrival of solar energetic particles (SEPs) during eruptive solar events is an important and current research topic of heliospheric physics. During the largest solar events, particles may have energies up to a few GeVs and sometimes even trigger ground-level enhancements (GLEs) at Earth. These large SEP events are best investigated through multi-spacecraft observations.

Aims. We study the first GLE-event of solar cycle 24, from 17th May 2012, using data from multiple spacecraft (SOHO, GOES, MSL, STEREO-A, STEREO-B and MESSENGER). These spacecraft are located throughout the inner heliosphere, at heliocentric distances between 0.34 and 1.5 astronomical units (au), covering nearly the whole range of heliospheric longitudes.

Methods. We present and investigate sub-GeV proton time profiles for the event at several energy channels, obtained via different instruments aboard the above spacecraft. We investigate issues due to magnetic connectivity, and present results of three-dimensional SEP propagation simulations. We gather virtual time profiles and perform qualitative and quantitative comparisons with observations, assessing longitudinal injection and transport effects as well as peak intensities.

Results. We distinguish different time profile shapes for well-connected and weakly connected observers, and find our onset time analysis to agree with this distinction. At select observers, we identify an additional low-energy component of Energetic Storm Particles (ESPs). Using well-connected observers for normalisation, our simulations are able to accurately recreate both time profile shapes and peak intensities at multiple observer locations.

Conclusions. This synergetic approach combining numerical modeling with multi-spacecraft observations is crucial for understanding the propagation of SEPs within the interplanetary magnetic field. Our novel analysis provides valuable proof of the ability to simulate SEP propagation throughout the inner heliosphere, at a wide range of longitudes. Accurate simulations of SEP transport allow for better constraints of injection regions at the Sun, and thus, better understanding of acceleration processes.

Key words. Sun: activity – Sun: magnetic field – Sun: particle emission – Sun: heliosphere – methods: numerical – Instrumentation: detectors

1. Introduction

The Sun releases vast amounts of energy through its activity, which mostly follows a periodic 11-year cycle. These eruptions can accelerate protons, electrons and heavier ions to relativistic energies and release them into interplanetary space. These solar energetic particles (SEPs) are guided by the interplanetary magnetic field (IMF), and in some cases result in intensive particle fluxes near the Earth. SEP events take place much more frequently during solar maximum, and can affect atmospheric and space-related activities in many ways, and as such, their investigation has been recognized as extremely important.

During extreme solar events, protons can be accelerated into the GeV range, and, when directed at the Earth, may lead to neutron monitors (NMs) detecting events at the Earth's surface. These ground-level enhancements (GLEs) are the most extreme of solar events, and thus are of special interest to the heliophysics community. Our understanding of energetic solar events and specifically GLEs increased dramatically during solar cycle 23 (Gopalswamy et al. 2012) due to advances in instrumentation and an abundance of events to observe. Solar cycle 24, being

much quieter, has so far provided only a single unambiguous GLE, designated as GLE71, on May 17th 2012.

We present sub-GeV proton observations of GLE 71, utilizing multiple vantage points throughout the inner heliosphere to better understand the spatial extent of SEP intensities in GLEs. We present new observations from the Mars Science Laboratory (MSL) Radiation Assessment Detector (RAD) and the MESSENGER Neutron Spectrometer (NS), together with energetic particle data from STEREO and near-Earth missions. We use a fully three-dimensional test particle model to simulate the transport of SEPs, originating from an acceleration region in the solar corona, generating virtual time profiles at various observer locations. The model includes, for the first time, the effects of a wavy Heliospheric Current Sheet (HCS) and of the two opposite polarities of the IMF. We compare intensity time profiles and peak intensities of data from both observations and simulations, at the different observer locations.

In section 1.1, we introduce the event along with previously published analysis. In section 2, we introduce the instruments used in our multi-spacecraft observations. We then present intensity time profiles and solar release times, and discuss magnetic

arXiv:1706.08458v1 [astro-ph.SR] 26 Jun 2017

connectivity and energetic storm particles (ESPs). In section 3, we describe our particle transport simulation method. We then proceed to present simulated intensity time profiles, and compare them and deduced peak intensities with observations. Finally, in section 4 we present the conclusions of our work. In Appendix A, we discuss calibration of our MESSENGER NS observations.

1.1. The May 17th 2012 GLE event

On May 17, 2012 at 01:25 UT, the NOAA active region 11476, located at N11 W76 in Earth view, produced a class M5.1 flare starting, peaking, and ending at 01:25, 01:47, and 02:14 UT, respectively (e.g., Gopalswamy et al. 2013; Shen et al. 2013). The type II radio burst indicating the shock formation was reported by Gopalswamy et al. (2013) to start as early as 01:32 UT using the dynamic spectra from Hiraiso, Culgoora and Learmonth observatories. Based on this, they also determined the coronal mass ejection (CME) driven shock formation height as 1.38 solar radii (R_{\odot} , from the centre of the Sun). The CME reached a peak speed of $\sim 1997 \text{ km s}^{-1}$ at 02:00 UT. They reasoned that although the May 17th flare is rather small for a GLE event, the associated CME was directed toward near-ecliptic latitudes, facilitating good connectivity between the most efficient particle acceleration regions of the shock front and the Earth. Despite the flare exhibiting relatively weak x-ray flux, Firoz et al. (2014, 2015) suggested that both the flare and the CME had a role in particle acceleration. Ding et al. (2016) agreed with this, based on velocity dispersion analysis (VDA) of proton arrival.

Gopalswamy et al. (2013) further estimated, using NM data, that the solar particle release time was about 01:40, slightly later than the shock formation time of 01:32. Papaioannou et al. (2014) reported the type III radio bursts which signified the release of relativistic electrons into open magnetic field lines starting at around 01:33 UT and ending at 01:44 UT. Using a simple time-shifting analysis, they derived the release of 1 GeV protons from the Sun at about 01:37 UT, slightly earlier but broadly agreeing with the onset time obtained by Gopalswamy et al. (2013).

This event was later directly detected at Earth by several NMs¹ with slightly different onset times (between 01:50 and 02:00), with the strongest signal detected at the South Pole (Papaioannou et al. 2014) where the rigidity cutoff is the lowest. Within the magnetosphere, proton energy spectra were measured by the PAMELA instrument (Picozza et al. 2007) as reported by Adriani et al. (2015), indicating that protons with energies of up to one GeV and helium of up to 100 MeV/nucleon were accelerated and transported to the vicinity of Earth. The GeV proton detection has also been corroborated later by Kühl et al. (2015) using an inversion technique exploring the response functions of the Electron Proton Helium Instrument (EPHIN, Müller-Mellin et al. 1995) aboard the SOHO spacecraft. The event was also detected aboard the international space station (Berrilli et al. 2014). Analysis of NM and PAMELA observations, using comparisons of peak and integral intensities, can be found in Asvestari et al. (2016).

Utilizing lower particle energies for release time analysis, Li et al. (2013) compared Wind/3DP and GOES 13 particle fluxes with NM and solar disk observations, concluding that electrons at this event appear to be flare-accelerated, with proton acceleration happening mainly at the CME-driven shock. The ERNE/HED detector (Torsti et al. 1995) aboard SOHO detected

a strong event, but suffered from data gaps during the event, which poses additional challenges to analysis.

During this event, the STEREO Ahead (STA) and STEREO Behind (STB) spacecraft were leading and trailing Earth by 114.8 and 117.6 degrees, respectively, both at a heliocentric distance of approximately 1 au. Lario et al. (2013) studied the 15–40 MeV and 25–53 MeV proton channels of this event using GOES and the high energy telescope (HET) on STB. For the 15–40 MeV channel, they obtained an enhancement rate (peak intensity/pre-event intensity) of 2.64×10^3 at GOES and only 35.0 at STB. For the 25–53 MeV channel, they obtained an enhancement rate of 1.94×10^4 at GOES and only 13.4 at STB. Unfortunately they did not determine the peak intensity of this event as measured by STA. This event has previously been included in a STEREO event catalogue (Richardson et al. 2014), and multi-spacecraft observations of electrons have been analysed in Dresing et al. (2014). Heber et al. (2013) included STA and STB proton time profiles for a single energy range in a figure, displaying the longitudinal extent of the event.

The event was also observed by the MESSENGER (MES) spacecraft orbiting around Mercury which, at the time of the event, was at a heliocentric distance of 0.34 au (Lawrence et al. 2016). The longitudinal connectivity of MES was similar to that of STA, as shown in Figure 1. In this paper, we investigate the time-series of proton measurements from MES using its neutron spectrometer (NS, Lawrence et al. 2016).

Beyond 1 au, this event was also observed by the Radiation Assessment Detector (RAD, Hassler et al. 2012) on board the Mars Science Laboratory (MSL) on its way to Mars (Zeitlin et al. 2013). We derive the proton intensities measured by RAD at different energy ranges and compare them with Earth-based observations and simulated particle intensities at the same location. We note that the RAD detector did not measure original proton intensities in space, but rather a mix of primary and secondary particles due to primaries experiencing nuclear and electromagnetic interactions as they traverse through the inhomogeneous flight-time shielding of the spacecraft. To retrieve the original particle flux outside the spacecraft is rather challenging and is beyond the scope of the current paper.

2. Multi-spacecraft observations

The heliospheric locations of five different spacecraft whose measurements are employed in the current study are shown in Figure 1 and also listed in Table 1. For this study, we estimated the average solar wind speed from measurements made by the CELIAS/MTOF Proton Monitor on the SOHO Spacecraft during Carrington rotation 2123. The average radial solar wind speed value was 410 km s^{-1} , which was rounded down to 400 km s^{-1} for the purposes of this research. Table 1 also includes calculated Parker spiral lengths using this solar wind speed.

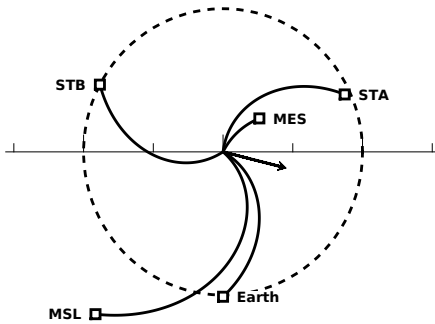
In order to effectively analyse the heliospheric and temporal extent of the May 17th 2012 GLE, we assess proton time profiles from multiple instruments throughout the inner heliosphere. The energy-dependent time profiles of SEPs measured at five different heliospheric locations are shown in Figure 2.

For STA and STB, we analyse 1-minute resolution data from HET of the In situ Measurements of Particles and CME Transients (IMPACT) investigation aboard both STEREOs. The protons are measured between 13 and 100 MeV in 11 different energy channels. For our purpose of comparing the STEREO measurement to those at other locations, we combine the energy channels into four different bins: 13–24 MeV, 24–40 MeV, 40–60 MeV, and 60–100 MeV.

¹ <http://www.nmdb.eu>

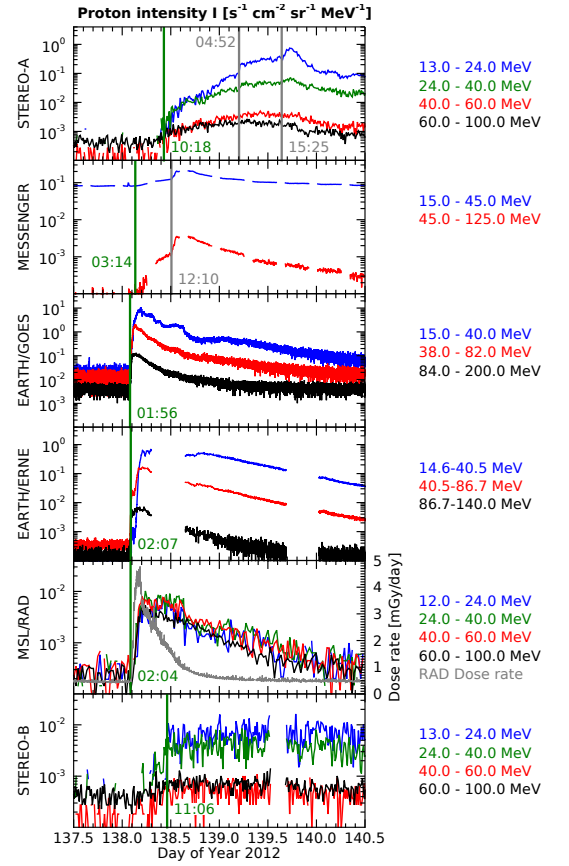
Table 1. Heliospheric location, Parker spiral length and onset time of the event seen at different spacecraft. The flare source region at the Sun is NOAA active region 11476 with coordinate of N11 W76 and the flare onset time is 01:25 on 17th May 2012.

	HGI latitude	HGI longitude	distance to the Sun	Parker spiral length	shortest travel time	SEP onset time	estimated SRT (1 GeV p)	Observed SEP event type
STA	7.3 °	275.4 °	0.96 au	1.11 au	631.4 s	10:18	10:07	slowly rising
MES	2.1 °	290.9 °	0.35 au	0.36 au	204.8 s	03:14	03:11	slowly rising
Earth	-2.4 °	160.7 °	1.01 au	1.18 au	671.2 s	01:56	01:45	rapidly rising
MSL	-7.3 °	121.8 °	1.46 au	1.92 au	1092 s	02:04	01:46	rapidly rising
STB	-4.7 °	42.7 °	1.00 au	1.16 au	659.8 s	11:06	10:55	slowly rising


Fig. 1. The heliospheric locations of MES, Earth, MSL, STA and STB. The Parker spiral configuration is calculated using a constant solar wind speed of $u_{sw} = 400 \text{ km s}^{-1}$. The 1 au distance is shown with a dashed circle. The arrow is placed along the radial direction at the flare location.

For MES data at Mercury, we use the neutron spectrometer which contains one borated plastic (BP) scintillator sandwiched between two Li glass (LG) scintillators. To account for the shielding of particles by the magnetosphere of Mercury and by the geometric shadowing of the planet itself, we selected only observations where the orbit altitude of MES is larger than 5000 km. The energy thresholds for triggering each type of charged particle were simulated and derived using particle transport codes (Lawrence et al. 2014) and are as follows: single coincidence, ≥ 15 MeV protons (or ≥ 1 MeV electrons); double coincidences, ≥ 45 MeV protons (or ≥ 10 MeV electrons); and triple coincidences, ≥ 125 MeV protons (or ≥ 30 MeV electrons). Since ≥ 10 MeV electrons are fairly rare in SEPs, we assume these channels measure mainly protons during the event. For the single-coincidence channel, contamination by many different sources is possible. We converted single, double, and triple coincidence counts into fluxes according to methods explained in detail in Appendix A.

We solve the intensity profile for 15–45 MeV and 45–125 MeV protons in the following way: We subtract the ≥ 45 MeV flux from the ≥ 15 MeV flux, and the ≥ 125 MeV flux from the ≥ 45 MeV flux. These two fluxes, now bounded from both above and below in energy, are then divided with the energy bin widths, i.e., 30 and 80 MeV, resulting in intensities in units $\text{protons s}^{-1} \text{sr}^{-1} \text{cm}^{-2} \text{MeV}^{-1}$. The ≥ 125 MeV flux is not shown in Figure 2, as it shows little enhancement for this time period. We emphasize that the 15–45 MeV flux calibration is uncertain. The time profiles in Figure 2 indeed show a very high intensity in the 15–45 MeV channel, likely due to non-proton background contamination.


Fig. 2. The proton intensity time profiles, in units $\text{s}^{-1} \text{cm}^{-2} \text{sr}^{-1} \text{MeV}^{-1}$, for different proton energy ranges at various spacecraft. The green vertical lines mark the onset times of the first arriving particles while the grey vertical lines mark the possible onsets of ESP events. SOHO/ERNE has two large data gaps but is located close to GOES, allowing cross-comparison of the data. The 17th of May is DOY 138.

Close to Earth, we employed two separate detectors. GOES 13, situated within the Earth's magnetosphere, provided us with 15–40 MeV, 38–82 MeV, and 84–200 MeV proton channels, with 32 second resolution. The SOHO/ERNE HED detector at L1 was used to construct two sets of energy channels with 1 minute time resolution. The first set was to match the GOES channels with energy ranges of

14.6–40.5 MeV, 40.5–86.7 MeV, and 86.7–140 MeV, whereas the second set was to match the STA/STB channels with energy ranges of 12.6–24.1 MeV, 24.0–40.5 MeV, 40.5–62.2 MeV, and 59.2–101 MeV. GOES provided uninterrupted observations, allowing us to constrain the time of peak flux, but the flux was contaminated and enhanced due to magnetospheric effects. ERNE/HED provided uncontaminated fluxes, but with data gaps during the event.

At MSL, during the cruise phase, the RAD instrument provided radiation dose measurements with a high time resolution of 64 seconds, and particle spectra with a time resolution of ~ 32 minutes. The radiation dose measurements were used to determine the event onset time. The particle spectra are provided by a particle telescope consisting of silicon detectors and plastic scintillators, with a viewing angle of $\sim 60^\circ$ (Hassler et al. 2012), and providing proton detections up to a stopping energy of 100 MeV. The original energy of the particle, E , is solved through analyzing E versus dE/dx correlations for each particle. Since RAD transmits the deposited energy in each triggered detector layer for almost all stopping protons, the particle identification is done in post-processing and is very accurate. Protons stopping inside RAD can thus be selected and their intensities have been obtained in four energy channels: 12–24 MeV, 24–40 MeV, 40–60 MeV, and 60–100 MeV. The particles detected by RAD are a combination of primaries and secondaries resulting from spallation and energy losses as particles travel through the flight-time spacecraft shielding. The shielding distribution around RAD is very complex: most of the solid angle was lightly shielded with a column density smaller than 10 g/cm^2 , while the rest was broadly distributed over a range of depths up to about 100 g/cm^2 (Zeitlin et al. 2013). Due to this shielding, deducing the exact incident energies of particles as they reach the spacecraft is a challenging process. We briefly discuss correcting for these effects in section 3.2.

Celestial mechanics dictate that a spacecraft on a Hohmann transfer to Mars remain magnetically well connected to Earth during most of its cruise phase (Posner et al. 2013). This connection is also shown in Figure 1. Due to this reason, the intensity profiles seen at Earth and MSL are expected to show similar time evolutions.

2.1. First arrival of particles and solar release time

Intense energy release at the surface of the Sun or in the corona can accelerate SEPs to relativistic energies, allowing them to propagate rapidly along the Parker spiral (Parker 1958) to heliospheric observers. If the observer is magnetically well-connected to the acceleration site and particle transport is unhindered, the arrival time of first particles can be used to infer the travel distance, i.e., the Parker spiral length.

As each heliospheric location will see the first arrival of energetic protons at a different time, we have defined onset times separately for each spacecraft, listed in Table 1. In Figure 2, the green vertical lines mark the onset times of the highest-energy channel corresponding to the arrivals of fastest protons. For STA and MES observations, we also define onset times of possible ESP events in low-energy channels, marked by grey lines, as will be discussed in more detail later. For STA, we find two distinct jumps, which may both be due to an ESP event. These times were defined from the raw data through subjective analysis of rise over a background level.

The nominal Parker spirals connecting the spacecraft to the Sun are shown in Figure 1 assuming an average solar wind speed of 400 km s^{-1} and their lengths have also been calculated and

listed in Table 1. Given a Parker spiral length of 1.18 au for an observer at Earth, 1 GeV protons (with a speed of $\sim 2.6 \times 10^5 \text{ km/s}$) propagating from the flare site without scattering would arrive after ~ 670 s or 11 minutes. A particle onset time at Earth at 01:56 would indicate a solar release time (SRT) of about 01:45 UT for these protons, which is consistent with radio burst observations (Gopalswamy et al. 2013; Papaioannou et al. 2014), considering the 8-min propagation time of radio signals from the Sun to Earth. Table 1 also lists the 1 GeV proton travel times and estimated associated SRTs, for each of the location considered, based on the calculated Parker spiral lengths. The observed MSL onset time is in good agreement with that at Earth and with the estimated proton release time, likely due to the good magnetic connection between the acceleration region and Earth/MSL. However, SRT values derived from MES, STA, and STB are very different from each other and hours later than the time of flare onset and shock formation. This indicates that these spacecraft were not magnetically well-connected to the solar acceleration site, and that particle transport to these locations was not due to propagation parallel to the magnetic field lines but was affected by drift motion, co-rotation, cross-field diffusion and turbulence effects.

2.2. Magnetic connectivity

The multi-spacecraft observations available for the SEP event on May 17th 2012 provide an exemplary chance to investigate magnetic connectivity between the Sun and observation platforms at a wide variety of longitudes and radial distances. We model magnetic connectivity by assuming the IMF to follow a Parker spiral. We use a constant solar wind speed of 400 km s^{-1} for our modelling, based on the averaging described in Section 2.

In Figure 3, we plot the Carrington Rotation 2123 solar synoptic source surface map (Hoeksema et al. 1983) for $r = 2.5 R_\odot$, resulting from potential field source surface (PFSS) modelling, provided by the Wilcox Solar Observatory. The model assumes a radial magnetic field at the solar surface and at $r = 2.5 R_\odot$. The plot shows the location of the flare on May 17th 2012 (indicated by a triangle) relative to the central meridian, along with estimated Parker spiral footpoints for the five observation platforms. As the plot shows, Earth (labelled 1) and MSL (2) are connected to regions on the Sun's surface very close to each other, with STA (3) and MES (5) connected to more western longitudes, close to each other. STB (4) is connected to more eastern longitudes.

Figure 3 also includes, as a thick white solid curve, a depiction of the PFSS neutral line between hemispheres of outward and inward pointing magnetic field. A model of a simple parametrized wavy neutral line is fitted to this PFSS line using a least squares fit method, as described in Battarbee & Dalla (2017). This neutral line parametrisation is the $r = 2.5 R_\odot$ anchor point for our model wavy HCS, and the wavy HCS parameters are described in section 3. Finally, figure 3 shows a rectangular region of width 180° , extending to latitudes $\pm 60^\circ$, which we use as a model injection region for SEPs. The width of the injection region was iterated upon, until an agreement between observations and simulations, for as many heliospheric observers as possible, was achieved.

As the solar wind flows outward and the solar surface rotates, magnetic structures at a given heliocentric distance are co-rotated westward. In Figure 3, this would be described by the PFSS polarity map including the HCS moving to the right. We validate the synoptic source and Parker spiral model through simple radial magnetic field observations. MES and STA are in regions of inward-pointing magnetic field throughout the anal-

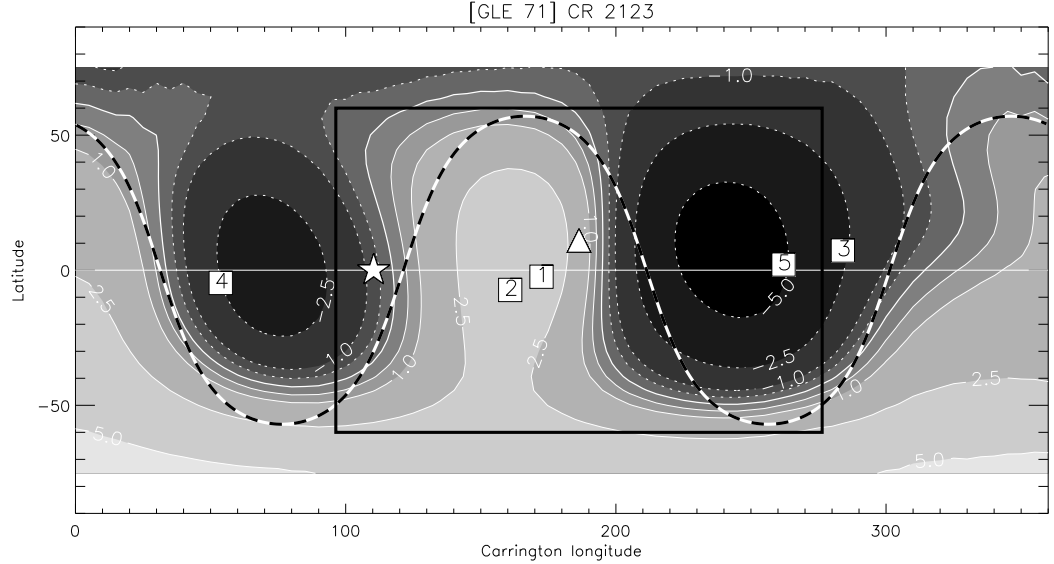


Fig. 3. Synoptic source surface map computed for $r = 2.5 R_{\odot}$ using photospheric measurements for Carrington rotation 2123. The location of the flare on May 17th, 2012, is indicated with a triangle. The central meridian at the time of the flare is indicated with a star. The Parker spiral connecting footpoints for each observer, assuming a solar wind speed of 400 km s^{-1} , are shown with squares, numbered as 1: Earth, 2: MSL, 3: STA, 4: STB, 5: MES. Pale regions indicate outward-pointing magnetic fields, dark regions inward-pointing magnetic fields, and the boundary line is shown as a solid white curve. Contour values are given in microtesla. A fit for a simple wavy current sheet is shown as a black dashed curve, and the boundary of the injection region used in particle transport simulations is shown with a black rectangle. PFSS data is provided by the Wilcox Solar Observatory.

used time period, in agreement with the map. Up until the time of the flare, Earth is connected to outward-pointing field lines, after which a strong interplanetary CME (ICME) is detected and the field orientation flips. STB is initially connected to inward-pointing field lines, but from the 19th of May onward, the direction points inward, in agreement with the spacecraft crossing the HCS.

2.3. Interplanetary shocks and energetic storm particles

In addition to SEPs accelerated close to the Sun during the initial, strong phase of the solar eruption, particle acceleration can happen throughout the inner heliosphere at propagating interplanetary (IP) shocks, driven by ICME fronts. Depending on the heliospheric location relative to the flare site and the ICME, different spacecraft see different properties of the event. The time profiles of *in-situ* measurements in Figure 2 and estimated SRTs in Table 1 suggest that the particle intensities at Earth and MSL (with estimated SRTs of 01:45 and 01:46) are dominated by coronally accelerated SEPs, but at MES and STA, there is an additional population of energetic storm particles (ESPs) accelerated by an IP shock from those accelerated early on in the corona, we turn to ICME and shock catalogues.

For MES, the circum-Mercurial orbital period of only 8 hours and related magnetospheric disturbances make identification of ICMEs challenging. Winslow et al. (2015) were able to detect an ICME at MES, lasting from 12:09 until 15:38 on May 17th. The shock transit speed was identified as 1344 km s^{-1} . SEPs usually peak at lower energies than coronally accelerated SEPs, and are found only in the vicinity of the IP shocks due to

turbulent trapping. At MES shown in Figure 2, we notice a clear intensity peak, likely due to SEPs, starting around 12:10 marked by a grey line right after the arrival of the ICME.

A comprehensive catalogue of ICMEs, IP shocks, and streaming interactive regions (SIRs) for the STEREO spacecraft has been compiled by Jian et al. (2013)². A shock was detected at STA on May 18th at 12:43, followed by an ICME until 09:12 on May 19th. The deka-MeV proton channels at STA show major enhancements starting at about 15:25 on May 18th (marked by a grey line), which can be attributed to IP shock accelerated SEPs. A smaller enhancement is seen at 04:52, possibly due to a foreshock of SEPs escaping in front of the IP shock.

STB is reported to be within a SIR from 23:48 on May 18th until 16:35 on May 22nd, well after the weak increase in proton flux. Upon further inspection of relevant solar wind measurements on between the 18th and 19th of May cannot be ruled out, but the data are ambiguous. An alternative explanation for the particle enhancement at STB, which begins less than 12 hours after the flare, is for coronally accelerated particles to drift there along the HCS, which co-rotates over the position of STEREO-B. We include this HCS drift in our simulations and assess this possibility in section 3.1.

Many spacecraft are available for observing near-Earth transients. Both Wind and ACE databases report the Earth as within an ICME already from the 16th of May, being thus unrelated to the GLE 71 eruption. The Wind ICME list³ lists the ICME start-

² http://www-ssc.igpp.ucla.edu/forms/stereo/stereo_level_3.html

³ <https://wind.nasa.gov/2012.php>

B. Algorithm 1: False alarms in time range 1

Table 5. List of fast CMEs between 1 January 1996 and 31 March 2013 which were false alarms. Column 1 gives the time the CME was first reported, column 2 its speed, and column 3 its acceleration all as reported by CDAW. Column 4 is the position angle at which the height-time measurements had been made (called by CDAW the “measurement position angle”). Column 5 is the CME width. Columns 6 to 10 give the parameters of the associated flare: its start time, heliographic latitude, heliographic longitude, class, and duration.

First reported	CME parameters					Flare parameters				
	V (km s ⁻¹)	Accel. (km s ⁻²)	Mpa (degrees)	Width (degrees)	Time start	Lat	Lon	Class	Duration (hrs: mins)	
1998-11-24T02:30	1798	-12.5	225	360	1998-11-24T02:07	-20	94	X1.0	00:30	
2000-01-06T07:31	1813	10.7	342	67	2000-01-06T06:45	24	35	C5.8	00:21	
2000-05-05T15:50	1594	-103.4	265	360	2000-05-05T15:19	-15	97	M1.5	02:09	
2000-06-25T07:54	1617	-17.5	274	165	2000-06-25T07:17	16	55	M1.9	01:04	
2001-07-19T10:30	1668	-11.6	252	166	2001-07-19T09:52	-8	62	M1.8	00:25	
2002-03-22T11:06	1750	-22.5	259	360	2002-03-22T10:12	-10	95	M1.6	01:40	
2002-05-30T05:06	1625	67.0	275	144	2002-05-30T04:24	5	95	M1.3	01:49	
2002-08-16T12:30	1585	-67.1	121	360	2002-08-16T11:32	-14	-20	M5.2	01:35	
2003-03-18T12:30	1601	-13.3	266	209	2003-03-18T11:51	-15	46	X1.5	00:29	
2003-06-02T00:30	1656	42.5	248	172	2003-06-02T00:07	-8	89	M6.5	00:36	
2003-11-18T08:50	1660	-3.3	206	360	2003-11-18T08:12	-2	-18	M3.9	00:47	
2004-04-11T04:30	1645	-77.6	237	314	2004-04-11T03:54	-16	46	C9.6	00:41	
2005-07-09T22:30	1540	-168.5	328	360	2005-07-09T21:47	12	28	M2.8	00:32	
2005-09-13T20:00	1866	11.5	149	360	2005-09-13T19:19	-11	-3	X1.5	01:38	
2013-02-06T00:24	1867	-8.2	31	271	2013-02-06T00:04	22	-19	C8.7	00:37	

to use a near-Earth peak intensity as the reference intensity. For this normalisation, we required a peak intensity at ERNE, as GOES intensities suffered from magnetospheric contamination. Due to the ERNE channels having data gaps, we compared the GOES and ERNE proton channels as seen in Figure 2. The 15–40 MeV GOES channel has some irregular structure during the first 12 hours of the event, but the 38–82 MeV channel has a smoother time profile. Comparing this channel with the 40.5–86.7 MeV channel from ERNE allows us to posit that the peak intensity has been reached before the data gap. Thus, the ERNE 40.5–86.7 MeV channel peak intensity was used as the anchor point. Using our simulations, we then generated a virtual time profile for an Earth observer, using a 40.5–86.7 MeV energy channel, and found its peak intensity. Hereafter, for all time profile and peak intensity analysis, results from our simulations were multiplied by a single normalisation constant, which resulted in agreement between peak intensities deduced from the 40.5–86.7 MeV channels at Earth from both simulations and observations.

3.1. Comparison with observations: time profiles

In this section, we compare the intensity time profiles of simulations and observations. Figure 5 displays results of both observations and simulations, with intensity time profiles for selected energy bins at each location, actual observations on the top row and simulation results on the bottom row. Panels are ordered according to observer footpoint longitude, as shown in Figure 3. For this comparison, instead of using the energy ranges utilised by GOES, the ERNE and Earth-located simulation energy channels were selected as to give a good match to MSL, STA and STB channels. We first focus on the shape of the time profiles, proceeding from west to east (right to left) in observer footpoint longitude.

At STA, observations show a gradually increasing flux, and SRTs calculated from onset times in Table 1 are many hours after the flare time. This suggests that the location of STA does not have good magnetic connectivity to the injection region. However, the numerical simulation is able to provide a proton time profile in agreement with observations, using the 01:40 UT release time. Protons fill the well-connected field lines with a population which isotropizes, and this population is then co-rotated over the STA position. STA observations in the lowest two energy bins show an additional feature, with bumps in intensity at approximately 04:52 and 15:25 on DOY 139. Both these bumps are designated with grey vertical lines in Figure 5. As described in section 2.3, an IP shock is detected at STA, and these enhancement at low energies can be explained as ESPs related to a passing IP shock. The first bump would indicate the arrival of an enhanced foreshock region, and the second bump would occur during the actual shock crossing. The simulated results do not show these bumps as ESP particles were not modeled by the SEP transport simulations.

Our confidence in the time evolution of the MES measurements is high, yet the observed time profile of particle intensity at MES does not agree with the rapid increase in intensity seen in the numerical simulation. The simulated time profile shows a simple abrupt event due to an efficient connection to the injection region, although it does drop off fast as the observer is rotated westward around the Sun with a rapid 88 day orbital period. Observations seem to suggest that coronally accelerated particles were not propagated efficiently to MES, as the enhancement over background intensities is small and happens too late. Shielding effects due to Mercury or its magnetic field were ac-

counted for by masking out measurements with altitudes below 5000 km. Thus, if an abrupt coronally accelerated component had been present at the position of MES, we should have seen it. A delayed enhancement, possibly due to ESPs, has a good match with the reported ICME crossing at 12:09, preceded by a foot of particles accelerated at the IP shock. This enhancement appears stronger in the 45–125 MeV channel, which might indicate that the signal at MES is strongly influenced by particle drifts, as the magnitude of particle drifts scales with energy. Alternatively, the signal in the 15–45 MeV channel might be hidden behind a strong background contamination signal. We note again that ESPs were not modeled in our transport simulations.

From the observed discrepancies between simulations and observations, we deduce that the structure of field lines in the inner heliosphere at the longitudes of STA and MES may be non-trivial. We examine magnetic footpoints and the PFSS modeling shown in Figure 3. The SEP signal at STA, with a footpoint further away from the flare location than MES, suggests a very wide shock and injection region. This injection region should have led to a strong signal at MES, however, the observations at MES do not support this.

One possible explanation is that the magnetic connectivity between STA and the corona is different from that of our model. STA is in a fast solar wind stream prior to the event, and additionally a SIR was detected there on May 16th (Jian et al. 2013), with a maximum solar wind speed of 660 km s^{-1} , well above the value of 400 km s^{-1} used in our simulations. This SIR may have primed the background solar wind conditions, leading to a shorter Parker spiral length and a more radial field than what we have used in the model, and resulting in a connected footpoint closer to the flare location. Due to lack of solar wind measurements at Mercury, the Parker spiral shape connected to MES remains an open question.

Other possibilities for explaining this disparity include various more complicated transport effects such as field-line meandering (see, e.g., Laitinen et al. 2016). Recent research, shown in panel a) of Figure 6 in Laitinen et al. (2017), suggests that the early-time cross-field variance of a particle distribution is strongly dependent on radial distance. Thus, during the early phase of the event, STA could be connected to the injection region through widely meandering field lines, whereas MES at a distance of only $0.34 R_{\odot}$ would remain outside this region. Later during the event Mercury would have continued westward on its orbit, remaining outside the region of field lines filled with accelerated particles.

At the location of Earth, we compare four ERNE/HED energy channel time profiles with observations. The highest energy channel at 59.2–101 MeV provides an excellent match between simulations and observations, suggesting acceleration was near-instantaneous in the corona, and that Earth was well-connected to the acceleration region. At lower energies, a reasonable match is also found, although the data gaps provide some challenge in assessing the time period between 07:00 and 15:00 UT on May 17th. As we investigate lower energies, the observed time profiles show an increasingly long plateau before decaying, especially in the 12.6–24.1 MeV energy channel. A possible explanation for this would be that low-energy proton injection from the CME-driven shock front was extended in time, whereas the simulated injection was instantaneous.

At MSL, with a similar magnetic connection to Earth, time profiles also agree well with simulations. The observations at MSL seem to show similar intensities for all the different channels, resulting in a near-flat spectrum. The total intensities observed at the detector are more than an order of magnitude lower

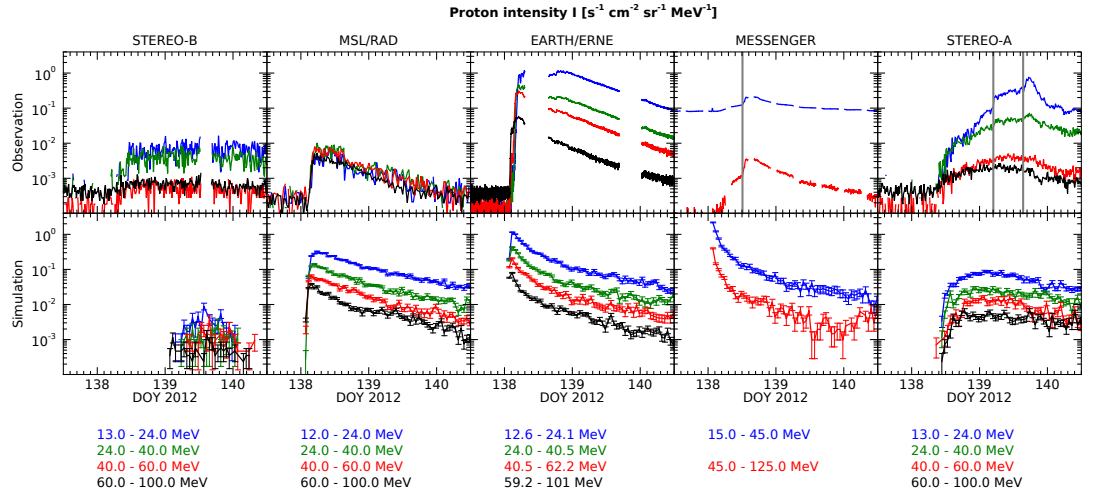


Fig. 5. Top row: proton time profiles at five heliospheric locations. Bottom row: corresponding virtual time profiles generated through SEP transport simulations. The locations are ordered according to connected footpoint longitude: STB, MSL, Earth, MES, and STA. MES and STA observations are also marked with the onsets of ESP-related proton effects with grey lines. For STA, the first grey line designates the estimated onset of foreshock ESP flux.

than the simulated intensities. However, as the general shape of the time profile agrees well with that of simulations, we suggest that transport and connectivity is not the primary cause of the discrepancy, but rather, that is due to the flight-time spacecraft shielding around MSL/RAD, causing particles to decelerate, fragment, or be deflected away. Modelling this effect in detail and performing inversion on the measured particle flux is rather challenging. We present preliminary corrections accounting for the energy loss of protons in section 3.2.

Although the footpoint of STB is separated from the flare region by almost 180 degrees, a weak enhancement in proton flux is seen both in observations and in simulation results. There was a SIR in the vicinity of STB in the time period following the event (Jian et al. 2013). Due to this and complicated solar wind observations, a weak ICME-driven shock cannot be ruled out. However, the most likely candidate for explaining the SEP flux enhancements at STB is coronally accelerated particles transported along the HCS. The successful simulation of this signal at STB is only possible through the results of our newly improved SEP transport simulation, supporting an IMF with two magnetic polarities separated by a wavy HCS. Particles propagate along the HCS, which is co-rotated over the position of STB (see Figure 3). The difference in onset time and signal duration between simulations and observations can be explained by inaccuracies in the exact position and tilt of the HCS at the position of STB.

3.2. Comparison with observations: peak intensities

In order to further assess longitudinal accuracy of our SEP transport simulations, we gathered peak intensities for both simulations and observations for each channel and plotted them according to estimated footpoint location (see also Figure 3). The peak intensities for STB, MSL, ERNE, MES, and STA are shown in Figure 6, along with peak intensities deduced from simulations. In determining observational peak intensities for STA

and MES, we excluded time periods deemed to be enhanced by ESP effects. For STA, this exclusion extended to 04:52 UT on the 18th of May, corresponding with the foreshock region of the IP shock. This foreshock region is visible especially in the 13–24 MeV channel, but somewhat also in the 24–40 MeV channel.

Comparing the 12–24 MeV, 24–40 MeV and 40–62 MeV observed and simulated peak intensities at Earth results in a good match due to a 40.5–86.7 MeV energy channel being used for the normalisation of simulation results. However, observations at 59–101 MeV show smaller intensities than the respective simulation results, suggesting our simulated injection power-law wasn't completely correct.

At STB, observed peak intensities are in agreement with simulated intensities. All channels at STB show only a weak increase over background intensities, which is modeled well by the HCS-transported particles in the simulation. At the highest two energy channels, the observed peak intensities are somewhat lower than the simulated ones, similar to what was seen at Earth.

At STA, after excluding all ESP-enhanced regions from observations, observed and simulated peak intensities are in very good agreement. However, similar to STB, the observations in the two highest energy channels exhibit slightly weaker peak intensities than what the simulations suggest.

Neither the time profiles nor the peak fluxes of simulations and observations at MES agree with each other, which indicates that the true magnetic connectivity to MES is more complicated than the one used in our simulations. Based on our calibrations, we believe this is not an instrumental effect. The simulated injection region was set to a width of 180° in order to provide a good time profile match at STA, however, CME modeling from observations produced shocks fronts of only 100° width. A narrower injection region might prevent coronally accelerated particles from reaching MES. The question of magnetic connectivity from the corona to STA and MES was explained in detail in section 3.1. If the CME transitions to an ICME, and further out,

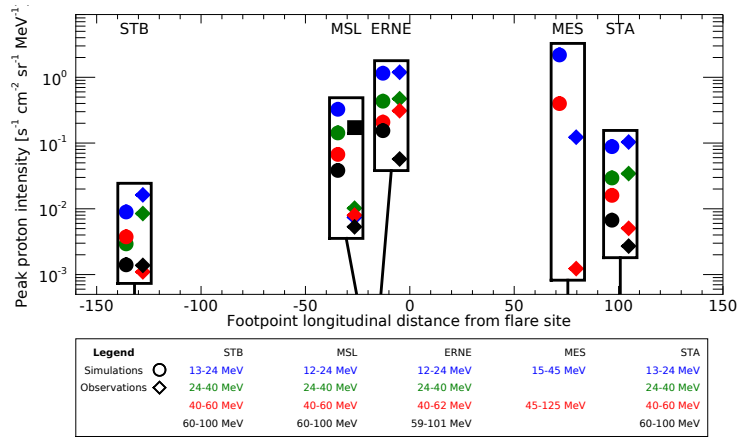


Fig. 6. Peak intensities of time profiles, recorded from observations (circles) and numerical simulations (diamonds). Observers are placed on the x-axis according to footpoint longitudinal distance from the flare. Peak intensities inferred from observations excluded time periods with ESP effects. For MSL/RAD, in addition to the recorded intensities, we show as a black square a version of the 60-100 MeV proton channel, with preliminary first-order corrections for energy losses due to spacecraft shielding.

expands in width, this could be seen as ESPs at MES, thus explaining the observations.

At MSL, the observed peak intensities are much lower than those of simulations, possibly due to the in-flight shielding covering much of the detector. As a first step toward correcting particle fluxes at MSL/RAD, we performed calculations of the energy loss of protons traversing a model of the spacecraft shielding. Proton energy losses in matter are primarily due to ionization, which is characterized by the Bethe-Bloch equation, which was used in our calculations. We considered the distribution of aluminium equivalent shielding depth within RAD’s viewing angle (Zeitlin et al. 2013). Due to the involved complexity, we did not account for generation of secondary particles, which play a major role at low energies. Thus, we produced a corrected peak intensity only for the 60-100 MeV channel, shown in Figure 6 as a black square. This value appears to be a good match with both simulation results and ERNE observations. Recreating original particle intensities at all channels of MSL/RAD will be the topic of future investigations.

4. Conclusions

We have presented extensive, detailed multi-spacecraft observations of proton intensities for GLE 71, which occurred on May 17th, 2012. We have shown the event to encompass a large portion of the inner heliosphere, extending to a wide range of longitudes, with a strong detection at Earth, MSL, and STA. We were able to analyse SEP transport and magnetic connectivity based on a new improved 3D test particle model.

Our SEP transport model solves the full-orbit 3D motion of test particle SEPs within heliospheric electric and magnetic fields. The model naturally accounts for co-rotation, particle drifts and deceleration effects. Our new improved model includes, for the first time, effects due to a solar magnetic field of two different polarities, separated by a wavy HCS. We model proton injection with a shock-like structure near the Sun, and model interplanetary transport in accordance with a particle mean free path of $\lambda_{\text{mfp}} = 0.3$ au.

At Earth, we successfully combine observations from two different types of instruments and two distinct observation platforms, namely SOHO/ERNE and GOES-13, in order to resolve problems related to data gaps and magnetospheric contamination.

We present novel multi-spacecraft analysis of an SEP event, encompassing all heliolongitudes and radial distances ranging from 0.35 au to 1.46 au. We compare results from multiple spacecraft and particle detectors with virtual observers placed within a large-scale numerical simulation. We improve upon previous studies, usually focused on a single observation platform, with our analysis, providing very good agreement between simulations and observations at multiple heliospheric locations.

We show that for GLE 71, observers magnetically connected to regions close to the flare location exhibit a rapid rise in proton intensity, followed by a prolonged fall-off. We report how STEREO-A observations are explained through a combination of co-rotation of an SEP-filled flux tube across the spacecraft in combination with an ESP event, and how STEREO-B observations can be explained through HCS drift of coronally accelerated protons.

For four out of five observer locations, we are able to find a good match in both the qualitative intensity time profiles and the quantitative peak intensities when comparing observations and numerical simulations. Our results suggest modern modeling of large-scale events and GLEs has improved, and has benefited greatly from the opportunities provided by the two STEREO spacecraft, as well as other heliospheric and even planetary missions such as MESSENGER and MSL. SEP forecast tools such as those presented in Marsh et al. (2015) should play an important role in furthering our understanding of solar activity.

Our study shows that magnetic connectivity to the injection region as well as the perpendicular propagation of particles in interplanetary space are important factors when assessing the risk of SEP events. Solar wind streams, interacting regions, and concurrent coronal mass ejections with associated magnetic structures alter the IMF and particle transport conditions, yet modern computation methods are capable of impressive modelling

of SEP events. Further improvements in modelling of the background conditions for SEP simulations are required, with 3-D magnetohydrodynamic models a likely candidate for future studies.

Acknowledgements. This work has received funding from the UK Science and Technology Facilities Council (STFC; grant ST/M00760X/1) and the Leverhulme Trust (grant RPG-2015-094). We acknowledge the International Space Science Institute, which made part of the collaborations in this paper through the ISSI International Team 353 "Radiation Interactions at Planetary Bodies". RAD is supported by the National Aeronautics and Space Administration (NASA, HEOMD) under Jet Propulsion Laboratory (JPL) subcontract 1273039 to Southwest Research Institute and in Germany by DLR and DLR's Space Administration grant numbers 50QM0501 and 50QM1201 to the Christian Albrechts University, Kiel. The RAD data used in this paper are archived in the NASA Planetary Data Systems Planetary Plasma Interactions Node at the University of California, Los Angeles. The PPI node is hosted at <http://ppi.pds.nasa.gov/>. Wilcox Solar Observatory data used in this study was obtained via the web site <http://wso.stanford.edu> at 2017:01:12_05:40:05 PST courtesy of J.T. Hoeksema. The Wilcox Solar Observatory is currently supported by NASA. MESSENGER data were calibrated using measurements from Neutron monitors of the Bartol Research Institute, which are supported by the National Science Foundation. Work from D. J. Lawrence is supported by the NASA's MESSENGER Participating Scientist Program through NASA grant NNX08AN30G. All original MESSENGER data reported in this paper are archived by the NASA Planetary Data System (<http://pdsgeosciences.wustl.edu/missions/messenger/index.htm>).

References

- Adriani, O., Barbarino, G., Bazilevskaya, G., et al. 2015, *The Astrophysical Journal Letters*, 801, L3
- Afanasyev, A., Vainio, R., Rouillard, A. P., et al. 2017, submitted to *Astronomy & Astrophysics*
- Asvestari, E., Willamo, T., Gil, A., et al. 2016, *Advances in Space Research*
- Battarbee, M. & Dalla, S. 2017, in preparation
- Battarbee, M., Dalla, S., & Marsh, M. S. 2017, *The Astrophysical Journal*, 836, 138
- Berrilli, F., Casolino, M., Del Moro, D., et al. 2014, *Journal of Space Weather and Space Climate*, 4, A16
- Bieber, J. W., Evenson, P., & Pyle, R. 2014, Bartol Research Institute neutron monitor data, <http://neutronm.bartol.udel.edu>
- Castagnoli, G. & Lal, D. 1980, *Radiocarbon*, 22, 133–158
- Ding, L.-G., Jiang, Y., & Li, G. 2016, *The Astrophysical Journal*, 818, 169
- Dresing, N., Cohen, C. M. S., Gómez-Herrero, R., et al. 2014, *Brazilian Journal of Physics*, 44, 504
- Feldman, W. C., Lawrence, D. J., Goldsten, J. O., et al. 2010, *Journal of Geophysical Research: Space Physics*, 115, n/a
- Firoz, K. A., Gan, W. Q., Li, Y. P., & Rodríguez-Pacheco, J. 2015, *Solar Physics*, 290, 613
- Firoz, K. A., Zhang, Q. M., Gan, W. Q., et al. 2014, *The Astrophysical Journal Supplement Series*, 213, 24
- Gopalswamy, N., Xie, H., Akiyama, S., et al. 2013, *The Astrophysical Journal*, 765, L30
- Gopalswamy, N., Xie, H., Yashiro, S., et al. 2012, *Space Science Reviews*, 171, 23
- Hassler, D., Zeitlin, C., Wimmer-Schweingruber, R., et al. 2012, *Space science reviews*, 170, 503
- Heber, B., Dresing, N., Dröge, W., et al. 2013, in *Proceedings, 33rd International Cosmic Ray Conference (ICRC2013) (Rio de Janeiro: Braz.J.Phys.)*, paper 0746
- Hoeksema, J. T., Wilcox, J. M., & Scherrer, P. H. 1983, *Journal of Geophysical Research*, 88, 9910
- Jian, L. K., Russell, C. T., Luhmann, J., Galvin, A. B., & Simunac, K. D. C. 2013, in *SOLAR WIND 13: Proceedings of the Thirteenth International Solar Wind Conference*, 191–194
- Kühl, P., Banjac, S., Dresing, N., et al. 2015, *Astronomy & Astrophysics*, 576, A120
- Laitinen, T., Dalla, S., & Marriott, D. 2017, *Monthly Notices of the Royal Astronomical Society*, stx1509 [arXiv:1706.06580]
- Laitinen, T., Kopp, A., Effenberger, F., Dalla, S., & Marsh, M. S. 2016, *Astronomy & Astrophysics*, 591, A18
- Lario, D., Aran, A., Gómez-Herrero, R., et al. 2013, *The Astrophysical Journal*, 767, 41
- Lawrence, D. J., Feldman, W. C., Goldsten, J. O., et al. 2014, *Journal of Geophysical Research: Space Physics*, 119, 5150
- Lawrence, D. J., Peplowski, P. N., Beck, A. W., et al. 2017, *Icarus*, 281, 32
- Lawrence, D. J., Peplowski, P. N., Feldman, W. C., Schwadron, N. A., & Spence, H. E. 2016, *Journal of Geophysical Research: Space Physics*, 121, 7398
- Li, C., Firoz, K. A., Sun, L. P., & Miroshnichenko, L. I. 2013, *The Astrophysical Journal*, 770, 34
- Marsh, M. S., Dalla, S., Dierckxsens, M., Laitinen, T., & Crosby, N. B. 2015, *Space Weather*, 13, 386
- Marsh, M. S., Dalla, S., Kelly, J., & Laitinen, T. 2013, *The Astrophysical Journal*, 774, 4
- Masarik, J. & Reedy, R. C. 1996, *Journal of Geophysical Research: Planets*, 101, 18891
- McComas, D., Bame, S., Barker, P., et al. 1998, *Space Science Reviews*, 86, 563
- McKinney, G. W., Lawrence, D. J., Prettyman, T. H., et al. 2006, *Journal of Geophysical Research*, 111, E06004
- Müller-Mellin, R., Kunow, H., Fleißner, V., et al. 1995, *Solar Physics*, 162, 483
- Papaiounou, A., Souvatzoglou, G., Paschalis, P., Gerontidou, M., & Mavromichalaki, H. 2014, *Solar Physics*, 289, 423
- Parker, E. N. 1958, *The Astrophysical Journal*, 128, 664
- Picozza, P., Galper, A., Castellini, G., et al. 2007, *Astroparticle physics*, 27, 296
- Posner, A., Odrščil, D., MacNeice, P., et al. 2013, *Planetary and Space Science*, 89, 127
- Richardson, I. G. & Cane, H. V. 2010, *Solar Physics*, 264, 189
- Richardson, I. G., von Rosenvinge, T. T., Cane, H. V., et al. 2014, *Solar Physics*, 289, 3059
- Rouillard, A. P., Plotnikov, I., Pinto, R. F., et al. 2016, *The Astrophysical Journal*, 833, 45
- Shen, C., Li, G., Kong, X., et al. 2013, *The Astrophysical Journal*, 763, 114
- Smith, C., L'Heureux, J., Ness, N., et al. 1998, *Space Science Reviews*, 86, 613
- Torsti, J., Valtonen, E., Lumme, M., et al. 1995, *Solar Physics*, 162, 505
- Winslow, R. M., Lugaz, N., Philpott, L. C., et al. 2015, *Journal of Geophysical Research: Space Physics*, 120, 6101
- Zeitlin, C., Hassler, D., Cucinotta, F., et al. 2013, *Science*, 340, 1080

Appendix A: MESSENGER flux calibration

As the MESSENGER NS instrument was not originally designed with SEP proton measurements in mind, calibration and validation of derived fluxes is necessary. Absolute flux profiles of protons for the $MES \geq 45$ MeV and ≥ 125 MeV energy thresholds were determined using the modeled response and validated with measures of the galactic cosmic ray (GCR) flux. Following Feldman et al. (2010), the measured count rate, C , is related to the proton flux, F_0 , (in units of protons $\text{sec}^{-1} \text{sr}^{-1} \text{cm}^{-2}$) using $C = GAF_0$, where G is the geometry factor in sr, and $A = 100 \text{cm}^2$ is the detector area. For the two highest energy ranges, the values for G are $G_{\geq 125 \text{ MeV}} = 1.1 \text{ sr}$ and $G_{\geq 45 \text{ MeV}} = 4.25 \text{ sr}$ (Lawrence et al. 2014). For borated plastic singles, the geometry factor is approximately $G_{\text{singles}} \approx 4\pi - 2G_{\geq 45 \text{ MeV}}$. However, the singles count rate likely contains a substantial fraction of contamination and non-proton background counts, such that its absolute calibration for energetic protons is highly uncertain. The measured count rates (Lawrence et al. 2016, 2017) are converted to fluxes using the above relation with the appropriate geometry factors.

The derived fluxes for the ≥ 45 MeV and ≥ 125 MeV thresholds were validated based on a comparison with Earth-based neutron monitor counts that were converted to particle flux using the process given by McKinney et al. (2006). Specifically, neutron monitor counts from McMurdo (Bieber et al. 2014) were empirically converted to a solar modulation parameter, which is used as input to a GCR flux parameterization of Castagnoli & Lal (1980) and Masarik & Reedy (1996). The total GCR flux accounts for both protons and proton-equivalent alpha particles using the formulation given by McKinney et al. (2006). When the NS-measured fluxes are compared to the fluxes derived through the neutron monitor data, we find an average absolute agreement of $<10\%$ for the ≥ 125 MeV flux and $<20\%$ for the ≥ 45 MeV flux, which validates the modeled response of Lawrence et al. (2014). The flux rates for the time period of March 26th 2011 to April 30th 2015 are plotted in Figure A.1.

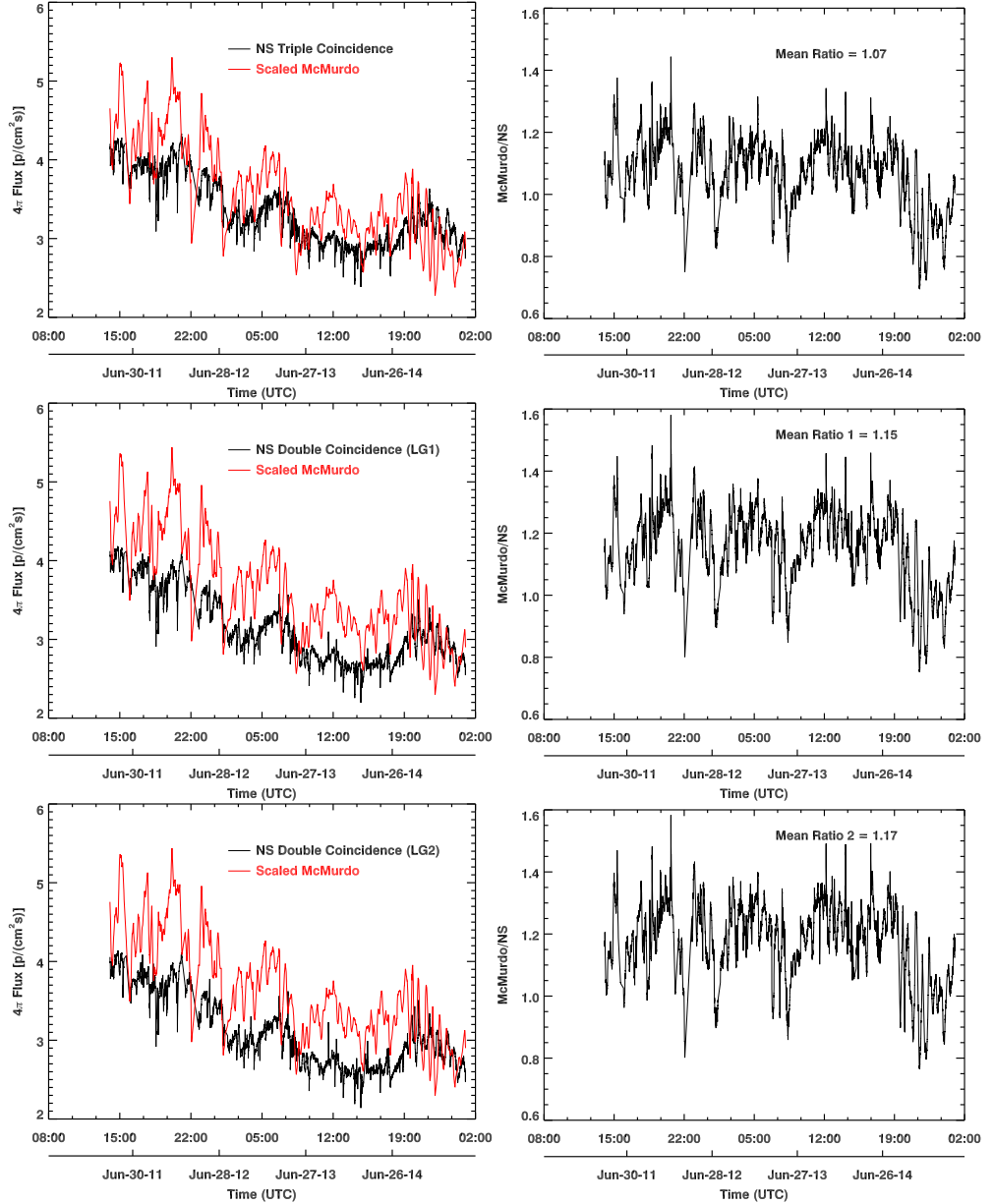


Fig. A.1. Validation for MESSENGER NS observations: GCR flux obtained via MESSENGER NS counts, and from McMurdo neutron monitor observations (left column). Shown are GCR fluxes obtained via NS Triple Coincidence counts (top panel), NS LG1 double coincidence counts (middle panel), and NS LG2 double coincidence counts (bottom panel). The flux ratios (right column) had mean values of 1.07, 1.15, and 1.17, respectively. The time period assessed was March 26th 2011 to April 30th 2015.

The mean validation ratios of 1.07 for triple coincidences, 1.15 for double coincidence channel LG1 and 1.17 for double coincidence channel LG2 were applied as correction coefficients to the extracted MES proton fluxes.

Appendix I

Dalla *et al.* (2017)

Application of Test Particle Simulations to Solar Energetic Particle Forecasting

S. Dalla¹, B. Swalwell¹, M. Battarbee¹, M.S. Marsh²,
T. Laitinen¹ and S.J. Proctor¹

¹University of Central Lancashire, Preston, PR1 2HE, UK

²Met Office, Exeter, UK

Abstract. Modelling of Solar Energetic Particles (SEPs) is usually carried out by means of the 1D focused transport equation and the same approach is adopted within several SEP Space Weather forecasting frameworks. We present an alternative approach, based on test particle simulations, which naturally describes 3D particle propagation. The SPARX forecasting system is an example of how test particle simulations can be used in real time in a Space Weather context. SPARX is currently operational within the COMESEP Alert System. The performance of the system, which is triggered by detection of a solar flare of class >M1.0 is evaluated by comparing forecasts for flare events between 1997 and 2017 with actual SEP data from the GOES spacecraft.

Keywords. Sun: particle emission

1. The SPARX forecasting system

A number of physics-based forecasting models are currently being developed to predict the particle intensities and radiation risk associated with SEPs. The traditional approach is spatially 1D, meaning that particles are assumed to remain tied to the magnetic field line on which they were originally injected, with no propagation across the field [e.g. Aran et al. (2006); Luhmann et al. (2010)]. However, high energy SEPs have a strong influence on the radiation dose and these particles are affected by drifts due to the gradient and curvature of the Parker spiral, requiring a 3D description [Marsh et al. (2013); Dalla et al. (2013)].

The SPARX forecasting system is based upon a 3D test particle model that accounts for drift and deceleration effects [Marsh et al. (2015)]. It is currently operational within the COMESEP alert system [www.comesep.eu, Crosby et al. (2012)]. In real time operation, SPARX is triggered by the detection of a solar flare of magnitude >M1.0. The system makes use of a database of runs of the test particle model to combine the contribution of many injection tiles near the Sun, describing an extended CME-driven shock structure. A profile of SEP intensities versus time at Earth for protons >10 MeV and >60 MeV is produced. Peak intensities are normalised by means of an empirical relationship between flare peak flux and particle peak intensities [Dierckx et al. (2015)]. Further details about SPARX may be found in Marsh et al. (2015).

2. Evaluating model performance

To assess the performance of the SPARX model in forecasting SEP events and their parameters, we proceeded as follows. We started from a list of X-class solar flares that took place in the time range between 1 September 1997 and 30 April 2017, covering solar cycles 23 and 24 up to the present time. The initial list consisted of 169 flares.

hits = 20	false alarms = 27	47
misses = 20	correct negatives = 58	78
40	85	125

Table 1. Contingency table for SPARX forecasts for F_N threshold.

Bias	1.18
POD	0.5
FAR	0.57
POFD	0.32
CSI	0.30

Table 2. SPARX scores for F_N threshold.

For each flare, SPARX was run as it would have been in a forecast mode, i.e. with a fixed set of model input parameters which remained the same for all events. The output was then examined and a forecast constructed as follows: if the peak flux for protons >10 MeV over the entire duration of the event exceeded a specified threshold F , then a positive forecast of SEP event was made, otherwise a no event situation was predicted.

In the analysis below, we considered two thresholds: the first one is the standard NOAA threshold, $F_N=10$ pfu (where pfu is particles $\text{cm}^{-2} \text{s}^{-1} \text{sr}^{-1}$) and the second is a lower threshold $F_1=1$ pfu.

We then examined data from the >10 MeV proton channel of the GOES Energetic Particle Sensor (EPS) to verify whether an actual event took place following each of the flares in our list. To define the occurrence of an SEP event, we used in the first instance the threshold F_N and subsequently F_1 . The methodology for associating an SEP event with a given flare is described in Swalwell et al. (2017). At the start time of 36 flares in our list, the EPS detector already had an enhanced flux from a previous event, making it impossible to verify whether or not an SEP event occurred: these flares were removed from the list. In addition, for 8 flares no EPS data was available. Therefore the total number of flares used in the analysis below is 125.

2.1. NOAA threshold

The contingency table for the NOAA threshold, F_N , is shown in Table 1. A correct negative is any X class flare which was not forecast to produce SEPs and which did not do so. From a contingency table, it is possible to derive a number of indicators that assess the performance of the model. They are defined as follows.

The bias score gives an indication of whether there is a tendency to under-forecast (bias < 1) or over-forecast (bias > 1) events. The perfect score is 1. The bias is given by:

$$\text{BIAS} = \frac{\text{hits} + \text{false alarms}}{\text{hits} + \text{misses}} \quad (2.1)$$

The probability of detection (POD) score gives the fraction of observed “yes” events which were correctly forecast. The perfect score is 1. The POD is given by:

$$\text{POD} = \frac{\text{hits}}{\text{hits} + \text{misses}} \quad (2.2)$$

The false alarm ratio (FAR) gives the fraction of predicted “yes” events which did not occur. The perfect score is 0. The FAR is given by:

hits = 40	false alarms = 31	71
misses = 12	correct negatives = 42	54
52	73	125

Table 3. Contingency table for SPARX forecasts for F_1 threshold.

Bias	1.37
POD	0.77
FAR	0.44
POFD	0.43
CSI	0.48

Table 4. SPARX scores for F_1 threshold.

$$FAR = \frac{\text{false alarms}}{\text{hits} + \text{false alarms}} \quad (2.3)$$

The probability of false detection (POFD), also called false alarm rate, is the fraction of “no” events incorrectly forecast as “yes”. The perfect score is 0. It is given by:

$$POFD = \frac{\text{false alarms}}{\text{correct negatives} + \text{false alarms}} \quad (2.4)$$

Finally the critical success index (CSI) shows how well the forecast “yes” events correspond to the observed “yes” events. The perfect score is 1. The CSI is given by:

$$CSI = \frac{\text{hits}}{\text{hits} + \text{misses} + \text{false alarms}} \quad (2.5)$$

For the SPARX model with F_N threshold, the values of the scores defined in eqs.(2.1)–(2.5) are given in Table 2.

2.2. 1 pfu threshold

The contingency table is shown in Table 3 for the SPARX forecasts for the F_1 threshold. The various scores as defined in eqs.(2.1)–(2.5) are shown in Table 4 for the F_1 threshold.

3. Comparison between forecast and actual SEP profile characteristics

For those events which were correctly forecast by SPARX to occur, we can compare the properties of the forecast flux profiles with those of the observed GOES profiles.

Fig. 1 shows the peak fluxes forecast by the SPARX model versus actual peak fluxes from GOES EPS data. The colour scale of the symbols reflects the longitude of the flare.

Fig. 2 presents a comparison of times to maximum intensity, defined as the time between the start of the flare and the time of peak flux. SPARX times to maximum versus actual GOES EPS ones are plotted. As in Fig. 1 the colour scale gives the longitude of the flare.

4. Discussion

SPARX performs much better if a lower threshold than that used by NOAA is used to define an SEP event. For both thresholds, the BIAS score is above 1, meaning that

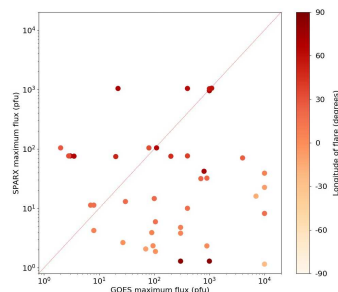


Figure 1. Peak fluxes forecast by the SPARX model versus actual GOES peak fluxes, for >10 MeV protons. The gray line is the 1:1 line.

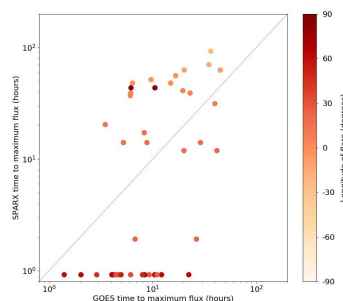


Figure 2. Time to peak intensity forecast by the SPARX model versus actual GOES time to peak intensity, for >10 MeV protons.

SPARX over-forecasts SEP events, more so for the lower threshold. All of the remaining scores are better for the lower threshold: the POD score for the lower threshold is much higher than for the lower (0.77 versus 0.5); the FAR is lower for the lower threshold (0.44 versus 0.57); and the CSI is higher for the lower threshold (0.48 versus 0.30).

Regarding the characteristics of the profiles of SEP fluxes, SPARX appears to significantly underestimate the time to peak intensity for well connected Western flares, while for Eastern flares reasonable agreement between forecast and actual times to peak are seen. Peak fluxes for Eastern flares tend to be underestimated.

References

- Aran, A., Sanahuja, B., and Lario, D., 2006, *Adv. Space Res.*, 37, 1240
 Crosby, N. B., et al., 2012, in *AIP Conference Series*, vol. 1500, ed. Q. Hu, et al, p. 159.
 Dalla, S., Marsh, M.S., Kelly, J. and Laitinen, T., 2013, *J. Geophys. Res.*, 118, 5979
 Dierckxens, M., et al., 2015, *Solar Phys.*, 290, 841
 Luhmann, J. G., et al., 2010, *Adv. Space Res.*, 46, 1
 Marsh, M. S., Dalla, S., Kelly, J., and Laitinen, T., 2013, *Ap. J.*, 774, 4
 Marsh, M. S., Dalla, S., Dierckxens, M., Laitinen, T., & Crosby, N. B. 2015, *Space Weather*, 13, 386
 Swalwell, B., Dalla, S., & Walsh, R.W., 2017, *Solar Phys.*, submitted